

Charge transport in two-dimensional materials and their electronic applications

DISSERTATION

zur Erlangung des akademischen Grades

Doctor rerum naturalium
(Dr. rer. nat.)

vorgelegt

dem Bereich Mathematik und Naturwissenschaften
der Technischen Universität Dresden

von

Himani Arora
geboren am 22. Januar 1989 in Neu-Delhi, Indien

Eingereicht am 18. Februar 2020

Die Dissertation wurde in der Zeit von Oktober 2015 bis Februar 2020
am Institut für Ionenstrahlphysik und Materialforschung
am Helmholtz-Zentrum Dresden-Rossendorf angefertigt.

Charge transport in two-dimensional materials and their electronic applications

DISSERTATION
zur Erlangung des akademischen Grades
Doctor rerum naturalium (Dr. rer. nat.)

Vorgelegt von
Himani Arora
geboren am 22. Januar 1989 in Neu-Delhi, Indien

Wissenschaftliche Betreuer
PD Dr. habil. Artur Erbe
Prof. Dr. Gianaurelio Cuniberti

Gutachter
Prof. Dr. Gianaurelio Cuniberti
PD Dr. habil. Artur Erbe
Prof. Dr. Manfred Helm

Eingereicht am 18. Februar 2020
Verteidigt am 09. Dezember 2020

Abstract

Semiconducting two-dimensional (2D) materials have gained considerable attention in recent years owing to their potential in future electronics. On the one hand, the conventional 2D semiconductors, such as transition metal dichalcogenides (TMDCs) (MoS_2 , WS_2 , etc.) are being exhaustively studied, on the other hand, search for novel 2D materials is at a rapid pace. In this thesis, we explore 2D materials beyond graphene and TMDCs in terms of their intrinsic electronic properties and underlying charge transport mechanisms. We introduce 2D semiconducting materials of indium selenide (InSe) and gallium selenide (GaSe), and a novel π -d conjugated $\text{Fe}_3(\text{THT})_2(\text{NH}_4)_3$ metal-organic framework (MOF) as potential candidates for their use as active elements in (opto)electronic applications.

Owing to the air-sensitivity of InSe and GaSe , their integration into active devices has been severely constrained. Here, we report a hexagonal boron nitride (hBN) based encapsulation, where 2D layers of InSe and GaSe are sandwiched between two layers of hBN; top hBN passivating the 2D layer from the environment and bottom hBN acting as a spacer and suppressing charge transfer to the 2D layer from the SiO_2 substrate. To fabricate the devices from fully encapsulated InSe and GaSe layers, we employ the technique of lithography-free via-contacts, which are metal contacts embedded within hBN flakes. Based on our results, we find that full hBN encapsulation preserves InSe in its pristine form and suppresses its degradation with time. Consequently, the electronic properties of encapsulated InSe devices are significantly improved, leading to a mobility of $30\text{--}120 \text{ cm}^2 \text{ V}^{-1} \text{ s}^{-1}$ as compared to a mere $\sim 1 \text{ cm}^2 \text{ V}^{-1} \text{ s}^{-1}$ obtained for unencapsulated devices. In addition, encapsulated InSe devices are stable for a prolonged period of time, overcoming their limitation to be air-sensitive. On employing full hBN encapsulation to GaSe , a high photoresponsivity of 84.2 A W^{-1} at 405 nm is obtained. The full hBN encapsulation technique passivates the air-sensitive layers from various degrading factors and preserves their unaltered properties. In the future, this technique can be applied to other 2D materials that have been restricted so far in their fundamental study and applications due to their environmental sensitivity.

MOFs are another emerging class of semiconducting 2D materials investigated in this thesis. They are hybrid materials that consist of metal ions connected with organic ligands via coordination bonds. In recent years, advances in synthetic approaches have led to the development of electrically conductive MOFs as a new generation of electronic materials. However, to date, poor mobilities and hopping-type charge transport dominant in these materials have prevented them from being considered for electronic applications. In this work, we investigate a newly developed π -d conjugated $\text{Fe}_3(\text{THT})_2(\text{NH}_4)_3$ (THT: 2,3,6,7,10,11-hexathioltriphenylene) MOF. The MOF films are characterized with a direct bandgap lying in the infrared (IR) region. By employing Hall-effect measurements, we demonstrate band-like transport and a record-high mobility of $230 \text{ cm}^2 \text{ V}^{-1} \text{ s}^{-1}$ in $\text{Fe}_3(\text{THT})_2(\text{NH}_4)_3$ MOF films. The temperature-dependent conductivity confirms a thermally activated charge carrier population in the samples induced by the small bandgap of the analyzed MOFs.

Following these results, we demonstrate the feasibility of using this high-mobility semiconducting MOF as an active material in thin-film optoelectronic devices. The MOF photodetectors fabricated in this work are capable of detecting wavelengths from UV to NIR (400–1575 nm). The narrow IR bandgap of the active layer constrains the performance of the photodetector at room temperature by band-to-band thermal excitation of the charge carriers. At 77 K, the device performance is significantly improved; two orders of magnitude higher voltage responsivity, lower noise equivalent power and higher specific detectivity of $7 \times 10^8 \text{ cm Hz}^{1/2} \text{ W}^{-1}$ are achieved at 785 nm excitation, which is a direct consequence of suppressing the thermal generation of charge carriers across the bandgap. These figures of merit are retained over the analyzed spectral region (400–1575 nm) and are comparable to those obtained with the first demonstrations of graphene and black phosphorus based photodetectors, thus, revealing a promising application of MOFs in optoelectronics.

Kurzfassung

Zweidimensionale (2D) Halbleiter haben dank ihres Potenzials für elektronische Anwendungen in den letzten Jahren grosse Aufmerksamkeit erregt. Dabei werden einerseits konventionelle 2D-Materialien, wie die Übergangsmetall-Chalkogenide (TMDCs) (MoS_2 , WS_2 , usw.) intensiv erforscht. Andererseits schreitet auch die Suche nach neuen 2D-Materialien rasch voran. Diese Dissertation stellt Forschungsergebnisse zu elektrischen Eigenschaften und den zugrundeliegenden Ladungstransportmechanismen von 2D-Materialien jenseits von Graphen und TMDCs vor. Untersucht wurden die 2D-Halbleiter Indiumselenid (InSe) und Galliumselenid (GaSe), sowie eine neuartige π -d konjugierte Metallorganische Gerüstverbindung (Metal-Organic Framework, MOF) $\text{Fe}_3(\text{THT})_2(\text{NH}_4)_3$. Diese Materialien sind vielversprechende Kandidaten für elektronische und optoelektronische Anwendungen.

InSe und GaSe sind besonders lufempfindliche Materialien. Aus diesem Grund ist ihre Verwendung für aktive Bauteile trotz ihrer hervorragenden elektrischen Eigenschaften bis heute sehr begrenzt. In dieser Arbeit wird ein effektives Verkapselungsverfahren vorstellt, bei dem InSe - oder GaSe -2D-Schichten zwischen zwei Schichten aus hexagonalem Bornitrid (hBN) eingebettet werden. Die untere Schicht hBN isoliert das Material vom Substrat Siliziumdioxid (SiO_2), während die obere Schicht das 2D-Material luftdicht isoliert. Um Bauteile aus komplett eingekapseltem InSe oder GaSe herzustellen, wurden lithographiefreie, sogenannte via-Kontakte hergestellt. Dies sind Metallkontakte, die bereits vor der Verkapselung in die hBN-Schichten integriert werden. Die hBN-Verkapselung erhält InSe in seiner ursprünglichen Form. Die hier vorgestellten Ergebnisse zeigen, dass sich die elektronischen Eigenschaften von InSe durch Verkapselung signifikant verbessern, was zu elektrischen Mobilitäten von $30\text{--}120 \text{ cm}^2 \text{ V}^{-1} \text{ s}^{-1}$ gegenüber nur rund $\sim 1 \text{ cm}^2 \text{ V}^{-1} \text{ s}^{-1}$ in unverkapselten Bauteilen führt. Darüber hinaus bleiben die Eigenschaften der verkapselten InSe -Bauteile über einen langen Zeitraum erhalten und degradieren nicht mehr bei Kontakt mit Luft. Die Verkapselung von GaSe ermöglicht den Einsatz in Fotodetektoren, bei einer Wellenlänge von 405 nm wird eine Fotoempfindlichkeit von 84.2 A W^{-1} gemessen; auch hier bewahrt die Verkapselung die empfindlichen Schichten vor schädlichen Einflüssen und konserviert so ihre unveränderten Eigenschaften. In der Zukunft kann diese Technik auch für andere 2D-Materialien eingesetzt werden, insbesondere für solche, deren Erforschung und Anwendung durch die grosse Empfindlichkeit bis heute eingeschränkt ist.

Darüber hinaus untersucht diese Dissertation mit Metallorganischen Gerüstverbindungen (MOFs) eine zweite Klasse halbleitender 2D-Materialien. MOFs sind hybride Materialien aus Metallionen, die mit organischen Molekülen als Verbindungselementen eine meist kristalline Struktur bilden. In den letzten Jahren haben Fortschritte in der synthetischen Herstellung zur Entwicklung von elektronisch leitfähigen MOFs geführt. Die niedrige Mobilität und der sogenannte hopping-Ladungstransport der gängigsten MOFs haben jedoch verhindert, dass diese für Anwendungen betrachtet wurden. In dieser Arbeit wird eine kürzlich neu entwickelte, π -d-konjugierte $\text{Fe}_3(\text{THT})_2(\text{NH}_4)_3$ (THT: 2,3,6,7,10,11-hexathioltriphenylene)

MOF vorgestellt. Der MOF Film hat eine direkte Bandlücke im Infrarot(IR)-Bereich liegend. Mithilfe von Hall-Effekt-Messungen wurde gezeigt, dass der Transport in den $\text{Fe}_3(\text{THT})_2(\text{NH}_4)_3$ MOF Filmen mit dem Drude-Modell konsistent ist. Darüber hinaus wird eine bis jetzt nicht übertroffene Mobilität von $230 \text{ cm}^2 \text{ V}^{-1} \text{ s}^{-1}$ gemessen. Die Temperaturabhängigkeit der Leitfähigkeit bestätigt, dass die kleine Bandlücke zu thermisch aktivierten Ladungsträgerdichten in den Proben führt.

Auf Grundlage dieser Ergebnisse wird die Machbarkeit von hochmobilen halbleitenden $\text{Fe}_3(\text{THT})_2(\text{NH}_4)_3$ MOFs als aktives Material in dünnen optoelektronischen Bauteilen gezeigt. Die hier vorgestellten MOF Fotodetektoren reagieren auf Wellenlängen im UV- bis Nahinfrarotspektrum (400–1575 nm). Die schmale Bandlücke schränkt die Leistung des Fotodetektors bei Raumtemperatur durch thermische Band-zu-Band-Anregung der Ladungsträger ein. Bei einer Temperatur von 77 K verbessert sich die Leistung des Detektors signifikant: Bei 785 nm wird eine um zwei Größenordnungen erhöhte Spannungsempfindlichkeit, eine niedrigere äquivalente Rauschleistung sowie eine höhere spezifische Empfindlichkeit von $7 \times 10^8 \text{ cm Hz}^{1/2} \text{ W}^{-1}$ erhalten. Dies ist eine direkte Konsequenz der Unterdrückung thermischer Anregung von Ladungsträgern über die Bandlücke. Diese Leistungszahlen sind über das analysierte Spektrum (400–1575 nm) gültig und vergleichbar mit den ersten Fotodetektoren auf Grundlage von Graphen und Schwarzen Phosphor. Die Ergebnisse zeigen deutlich das Potenzial von MOFs für optoelektronische Anwendungen.

Acknowledgements

The past four years of the PhD have been an incredible experience that propelled my professional and personal development. There are many people whom I would like to thank for their support and affection throughout this time. As a physicist, we learn to pay attention to the fundamentals. So let me start by thanking the people who gave me the foundation at an early age to be able to pursue this career today. I would like to thank my parents for nurturing my curiosity from a young age of 5–6 years. Their enormous support and love encouraged me to move forward continuously in all aspects of life. My sister and brother for being the most lovable persons in the world for me. I would also like to thank my grandmother for being a constant support to us in all these years. A special person whom I would like to mention at this stage would be my science teacher from primary school, Ms. Meenakshi, who generated enough interest in me to wonder and learn about the mysteries of the Universe.

Coming to this professional endeavor, first and foremost, I would like to express my gratitude by thanking Dr. Artur Erbe, my immediate supervisor. Throughout my PhD years, Artur has been a great mentor and inculcated professionalism in me which will be treasured for next stages of my career. He was always available for detailed discussions on the subject matter and provided immense guidance and support when needed. I am thankful for his trust in me with the topic of two-dimensional materials, which motivated me to use all my abilities to do my best in this PhD project. Next, I would like to thank Prof. Dr. Gianaurelio Cuniberti for being my official supervisor and guiding me through this journey. His wise advises at professional and personal fronts were valuable and helpful. I am very grateful to Prof. Dr. Manfred Helm for supporting this project throughout and for being available for many discussions whether technical or administrative. Special thanks to Dr. Harald Schneider for fruitful discussions on the photodetection in thin-film semiconductors, which only motivated me to learn more. I also wish to thank Tommaso Venanzi for being an excellent colleague to work with. The long and hilarious talks during our Bus 261 rides were re-energizing (as much as two shots of an Italian espresso). Many thanks to Yara Alsaadawi for being a trusted “PDMS supplier” to the 2D group. We fabricated many wonderful stacks with her help. I would also like to thank Shima Jazavandi Ghamsari for being a wonderful friend and support in these last months. Special thanks to Dr. Peter Zahn for his exceptional support in simplifying various administrative processes, and for organizing NanoNet courses and get-togethers. I thank Dr. Yordan Georgiev for bringing positive energy every time I talked with him. I will remember our endless discussions on culture, food, politics, travel, and what not. I would also like to thank Prof. Dr. Sibylle Gemming for her encouragement and motivation in tough times. Her enthusiasm and love for research is an inspiration for every women pursuing science as their career.

During the course of this thesis, a lot has been accomplished and this would not have been possible without the support of our collaborators. Firstly, I would like to thank Prof. Dr. James Hone for giving me an opportunity to learn and carry out research at his

research facilities in Columbia University (New York, USA). During my research stay at his group, I learned state-of-the-art status of 2D materials. Working in their highly equipped laboratories and learning from the experts was a wonderful scientific experience. Next, I heartily thank Dr. Enrique Cánovas, who has not just been a collaborator but a mentor to me. He always encouraged me to delve deeper into the subject to understand the physics at a fundamental level. I am deeply grateful to Dr. Renhao Dong and Prof. Dr. Xinliang Feng for being brilliant collaborators to work with. Their expertise in synthesizing novel materials combined with our expertise in nanofabrication and characterization produced some groundbreaking results published in very high impact factor journals.

I heartily thank Claudia Neisser for her help and support during cryogenic measurements. I will cherish our initial struggles with the He-Dewar and probe station. It is because of Claudia's efforts that the cryogenic probe station is well-maintained and that we all can measure our devices uninterrupted. I also would like to thank to Tommy Schönherr for introducing me to e-beam lithography and for hours spend together trying to contact tiny 2D flakes. My gratitude to Holger Lange for teaching me how to perform electrical characterization of 2D devices, and not to forget, also for practicing German with me. Thanks to him, I now know some German scientific vocabulary. Finally, thanks to Jens Zscharschuch for his help in laser installations, even at short notices. His optimistic view even during complex measurements was much needed during this time.

I gratefully acknowledge the IHRS NanoNet and HZDR for funding my research, and for providing excellent infrastructure. I am incredibly grateful to the FWIO group for their constant support and love in the times of ups and downs in last 4 years, and believe me there were many. In last years, not just work colleagues but some great friendships were founded.

I would also like to thank my friends outside science, who have listened to me blabbering about my research, without understanding much. Without their love and care, this journey would have been much tougher. And last but not the least, my deepest thanks to Jonathan Old, who has been by my side throughout this journey with his unconditional support. Thanks for believing in me and constantly encouraging me to move forward. I believe his involvement in my practice talks, proofreading papers and this thesis has made him quite versed in my research by now.

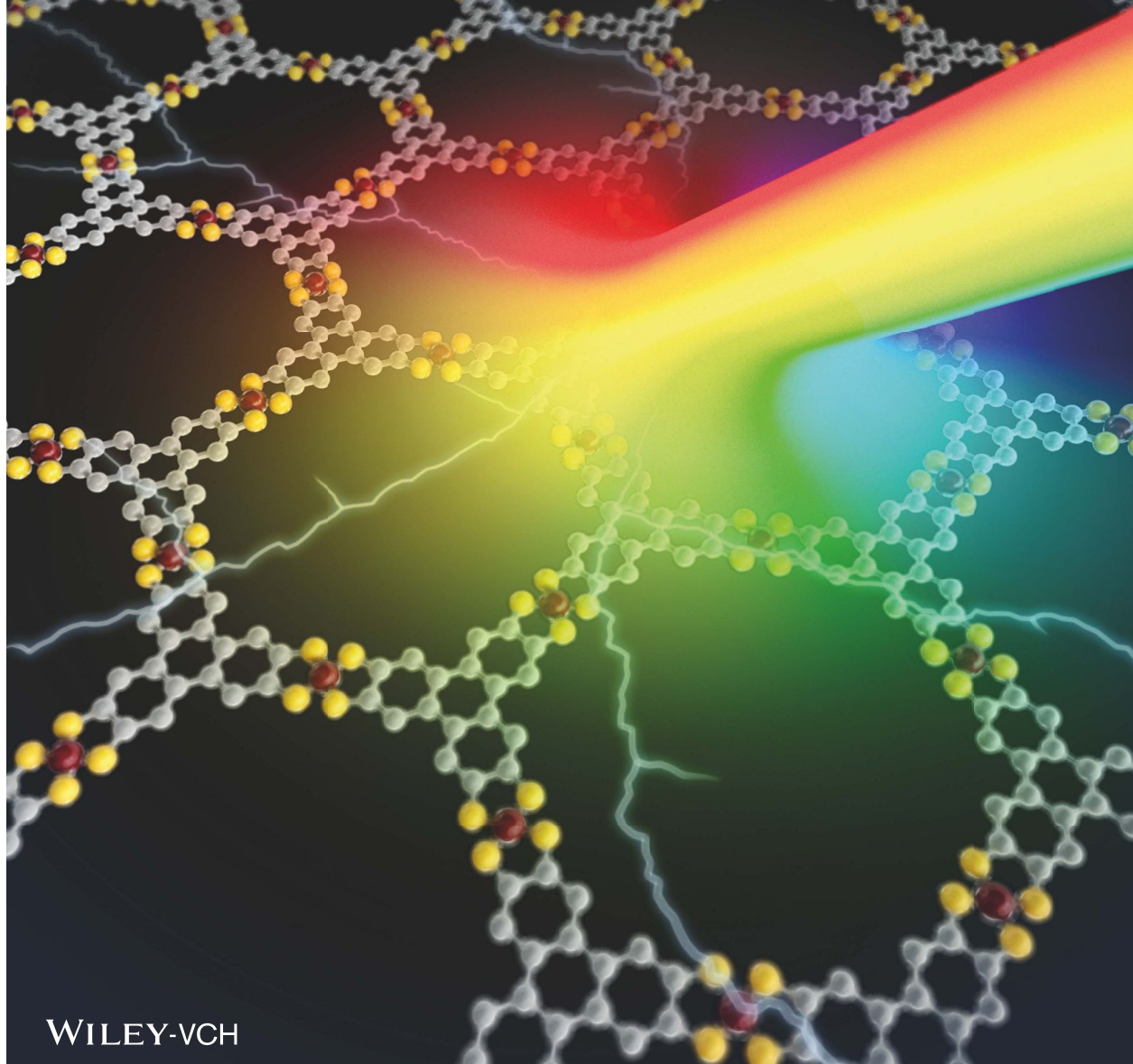
List of Publications

1. **H. Arora** and A. Erbe, “Recent progress in contact, mobility, and encapsulation engineering of InSe and GaSe”, InfoMat, 10.1002/inf2.12160 (2020).
2. **H. Arora**, S. Park, R. Dong, and A. Erbe, “2D MOFs: A New Platform for Optics?”, Optics and Photonics News **31**, 36–43 (2020).
3. **H. Arora**, R. Dong, T. Venanzi, J. Zscharschuch, H. Schneider, M. Helm, X. Feng, E. Cánovas, and A. Erbe, “Demonstration of a Broadband Photodetector Based on a Two-Dimensional Metal–Organic Framework”, Advanced Materials **32**, 1907063 (2020).
4. T. Venanzi, **H. Arora**, S. Winnerl, A. Pashkin, P. Chava, A. Patanè, Z. D. Kovalyuk, Z. R. Kudrynskyi, K. Watanabe, T. Taniguchi, A. Erbe, M. Helm, and H. Schneider, “Photoluminescence dynamics in few-layer InSe”, Physical Review Materials **4**, 044001 (2020).
5. F. Kern, M. Linck, D. Wolf, N. Alem, **H. Arora**, S. Gemming, A. Erbe, A. Zettl, B. Büchner, and A. Lubk, “Autocorrected off-axis holography of two-dimensional materials”, Physical Review Research **2**, 043360 (2020).
6. **H. Arora**, Y. Jung, T. Venanzi, K. Watanabe, T. Taniguchi, R. Hübner, H. Schneider, M. Helm, J. C. Hone, and A. Erbe, “Effective Hexagonal Boron Nitride Passivation of Few-Layered InSe and GaSe to Enhance Their Electronic and Optical Properties”, ACS Applied Materials & Interfaces **11**, 43480–43487 (2019).
7. F. Kern, M. Linck, D. Wolf, T. Niermann, **H. Arora**, N. Alem, A. Erbe, S. Gemming, and A. Lubk, “Direct Correction of Residual Symmetric Aberrations in Electron Holograms of Weak Phase Objects”, Microscopy and Microanalysis **25**, 98–99 (2019).
8. T. Venanzi, **H. Arora**, A. Erbe, A. Pashkin, S. Winnerl, M. Helm, and H. Schneider, “Exciton localization in MoSe₂ monolayers induced by adsorbed gas molecules”, Applied Physics Letters **114**, 172106 (2019).
9. R. Dong, P. Han, **H. Arora**, M. Ballabio, M. Karakus, Z. Zhang, C. Shekhar, P. Adler, P. S. Petkov, A. Erbe, S. C. B. Mannsfeld, C. Felser, T. Heine, M. Bonn, X. Feng, and E. Cánovas, “High-mobility band-like charge transport in a semiconducting two-dimensional metal-organic framework”, Nature Materials **17**, 1027–1032 (2018).
10. **H. Arora**, T. Schönherr, and A. Erbe, “Electrical characterization of two-dimensional materials and their heterostructures”, IOP Conference Series: Materials Science and Engineering **198**, 12002 (2017).

Vol. 32 • No. 9 • March 5 • 2020

www.advmat.de

ADVANCED MATERIALS



WILEY-VCH

Figure 1: Our image is featured on the back cover of the March issue of **Advanced Materials**. The image demonstrates our work, “Demonstration of a Broadband Photodetector Based on a Two-Dimensional Metal-Organic Framework”.

Contents

Abstract	I
Kurzfassung	III
Acknowledgements	V
List of publications	VII
Symbols and Physical Constants	XVII
List of Abbreviations	XVIII
1 Introduction	1
2 Overview	5
1 Two-dimensional materials	5
1.1 Graphene	6
1.2 2D vdW semiconductors	9
2 Novel 2D semiconductors: III–VI chalcogenides	11
2.1 Indium selenide	12
2.2 Electronic properties of InSe	14
2.3 Encapsulation of InSe to suppress ambient degradation	19
2.4 Gallium selenide and its (opto)electronic properties	20
3 2D dielectric: hexagonal boron nitride	25
4 Van der Waals heterostructures	27
5 Metal-organic frameworks	29
5.1 Structure	29
5.2 Properties and applications	31
5.3 Semiconducting MOFs for (opto)electronic applications	31
3 Van der Waals heterostructures and their fabrication	37
1 Exfoliation of 2D layers and their transfer	38
1.1 Mechanical exfoliation	38
1.2 Deterministic transfer	40
2 Microfabrication and device assembly	48
2.1 VdW heterostructures using hBN	48
2.2 Free-standing hBN on a TEM grid	51
3 Conclusions	53

4 Devices based on few-layered InSe and GaSe	55
1 Introduction	56
2 Material characterization	56
3 Planar metal-InSe devices	58
3.1 Device fabrication	58
3.2 Electrical characterization	58
4 Planar metal-InSe devices inside a glovebox	61
4.1 Device fabrication	61
4.2 Device characterization	62
5 Devices based on hBN encapsulated InSe and GaSe	63
5.1 Device fabrication	64
5.2 Micro-photoluminescence measurements	66
5.3 Electronic properties of InSe-via devices	68
5.4 Optoelectronic properties of GaSe-via devices	74
5.5 Conclusions	77
5 Charge transport in 2D metal-organic frameworks	79
1 Introduction	79
2 A novel 2D MOF: $\text{Fe}_3(\text{THT})_2(\text{NH}_4)_3$	80
2.1 Synthesis	80
2.2 Structural characterization	81
3 Electronic transport in $\text{Fe}_3(\text{THT})_2(\text{NH}_4)_3$ 2D MOF films	82
3.1 Two-probe conductivity measurements	85
3.2 Four-probe and Hall-effect measurements	88
3.3 Conclusions	95
6 Broadband photodetectors based on $\text{Fe}_3(\text{THT})_2(\text{NH}_4)_3$ 2D MOF	97
1 Introduction	97
2 Photodetector operation and its figures of merit	98
2.1 Photovoltaic	98
2.2 Photoconductor	99
2.3 Figures of merit of a photodetector	100
3 Broadband photodetectors based on $\text{Fe}_3(\text{THT})_2(\text{NH}_4)_3$ 2D MOF films	104
3.1 Principle of operation	104
3.2 Experimental section	104
3.3 Photoresponse in the near-infrared region	107
3.4 Photoresponse in the visible region	113
4 Conclusions	116
7 Summary and outlook	117
Bibliography	123
Appendices	141
A Material characterization	143
B Device fabrication	144
C Device characterization	145

List of Figures

2.1	Thickness scaling in bulk versus 2D semiconductor for FET application	6
2.2	Schematic of the structure of graphite and graphene	7
2.3	Band structure and corresponding electronic properties of graphene	8
2.4	Chart illustrating the evolution of the family of 2D materials	9
2.5	Crystal and band structure of MoS ₂ and corresponding electronic properties	10
2.6	Structural schematics of top and side views of MX compounds	11
2.7	Stacking arrangements of three different polytypes of III–VI chalcogenides .	12
2.8	Crystal structure of mono- and few-layered γ -InSe	13
2.9	Micro-PL study of different thicknesses of exfoliated InSe	14
2.10	Raman study of different thicknesses of exfoliated InSe	15
2.11	Literature review of InSe FETs: bottom substrate engineering	17
2.12	Literature review of InSe FETs: contact engineering	18
2.13	Different encapsulation techniques employed for InSe to prevent ambient degradation	20
2.14	GaSe crystal structure and electronic band structure	21
2.15	Raman measurements to study the oxidation dynamics of GaSe in air	22
2.16	Electrical characterization of an FET based on GaSe channel	22
2.17	GaSe photodetector device structure and performance characterization .	23
2.18	Optoelectronic performance of partially hBN encapsulated GaSe photodetectors	24
2.19	Schematic of the hexagonal structure of hBN monolayer	25
2.20	Principle of building vdW heterostructures	28
2.21	Assembly of graphene-hBN vdW heterostructures	28
2.22	Schematic of a MOF unit cell where metal ions are connected via organic linkers	30
2.23	Reaction schematic for the synthesis of MOF-5 from its constituents	30
2.24	Schematics of 1D, 2D and 3D forms of MOF structures	31
2.25	Graphical representation of properties of MOFs and their applications. The roadmap for the progress and integration of MOFs into device applications over years	32
2.26	Schematic illustrations of charge transport routes in MOFs	34
3.1	The procedure of mechanical exfoliation of the bulk crystal to obtain 2D layers	39
3.2	Identification of different thicknesses of exfoliated InSe using optical contrast and AFM	40
3.3	Micromanipulator installed in our lab used for stacking different 2D layers to form vdW heterostructures	41
3.4	Schematic representation of the PDMS dry transfer method for vdW heterostructure assembly	43
3.5	PDMS/PPC stack on a glass slide used for pick-up and drop-down of 2D layers	44
3.6	Schematic representation of the PPC vdW assembly technique	45

3.7	Schematic representation of fabrication of graphene/hBN vdW heterostructure using PVA transfer technique	46
3.8	The process steps showing dissolution of the PVA layer in DI water and lifting up of the PMMA membrane from the bottom substrate	47
3.9	Identification of flat and clean hBN flakes for the bottom substrate using optical contrast and AFM	49
3.10	Optical micrograph of hBN/InSe/hBN vdW heterostructure employed for low-temperature time-resolved PL studies	50
3.11	Optical image of vdW heterostructure of monolayer MoSe ₂ and hBN	50
3.12	Schematic of a Si-based TEM grid	52
3.13	Optical contrast of hBN few layers resting on PDMS stamp under white and yellow light	52
3.14	Few layers of hBN free-standing on the TEM window	52
4.1	Bulk single crystals of InSe and GaSe used in this study for mechanical exfoliation	57
4.2	EDS and Raman spectra of InSe	57
4.3	EDS and Raman spectra of GaSe	58
4.4	FET based on few-layered InSe, fabricated by depositing metal contacts directly on top of exfoliated InSe	59
4.5	<i>I</i> – <i>V</i> characteristics of the planar metal-InSe FET	60
4.6	A nitrogen-filled glovebox at Columbia University, used rigorously for fabricating the devices based on air-sensitive materials	61
4.7	Planar metal-InSe FET, fabricated from 9.6 nm thick InSe layer exfoliated inside a nitrogen-filled glovebox	62
4.8	<i>I</i> – <i>V</i> characteristics of the planar metal-InSe FET fabricated inside a nitrogen-filled glovebox	63
4.9	Step-wise illustration of the fabrication of Pd/Au via-contacts	65
4.10	hBN flakes with different via-contact configurations that can be used to perform various electrical characterizations	65
4.11	Optical image of a hBN flake containing Pd/Au via-contacts, lying on a PDMS/PPC stamp after a successful pick-up from SiO ₂ /Si substrate	66
4.12	Photoluminescence spectra at 297 K and 4.2 K for encapsulated and unencapsulated InSe, demonstrating high quality of encapsulated InSe	67
4.13	Photoluminescence spectra at 4.2 K for different stack configurations of hBN-InSe to demonstrate the role of hBN encapsulation	68
4.14	Photoluminescence spectra measured for encapsulated and unencapsulated InSe over time, demonstrating ambient stability of encapsulated InSe	69
4.15	Device configurations of encapsulated and unencapsulated InSe-based FETs, analyzed and compared in this study	70
4.16	Transfer and output characteristics of the InSe-via device and its comparison with the unencapsulated InSe device	71
4.17	<i>I</i> – <i>V</i> characteristics of another InSe-via device, revealing a mobility of 85 cm ² V ⁻¹ s ⁻¹	72
4.18	Transfer characteristics and FET parameters of mobility and on/off ratio measured over time, revealing the stability of via-encapsulated devices over unencapsulated InSe devices.	73

4.19	Low-temperature micro-PL measurements of few-layered GaSe, demonstrating the suppression of degradation on using full hBN encapsulation	75
4.20	Electronic and optoelectronic properties of fully encapsulated GaSe devices	76
5.1	Structural characterization of $\text{Fe}_3(\text{THT})_2(\text{NH}_4)_3$ 2D MOF films	81
5.2	Lorentz forces acting on the charge carriers in a magnetic field	83
5.3	Principle of four-probe conductivity measurements of a rectangular conductor	84
5.4	Hall bar geometry consisting of six electrical contacts	85
5.5	Two-terminal device based on a large-area MOF film	86
5.6	$I\text{-}V$ curves measured at room temperature for Fe-THT MOF films with varying film thicknesses	86
5.7	Temperature-dependent $I\text{-}V$ curves for the 70 nm thick Fe-THT MOF film, displaying ohmic response between -1 and 1 V	87
5.8	Logarithmic dependence of the two-probe conductivity on the reciprocal temperature	88
5.9	$I\text{-}V$ curve at 5 K for the Fe-THT MOF film, demonstrating a non-ohmic response and large hysteresis	88
5.10	Hall bar geometry developed by laser ablation of 1.7 μm thick MOF film	90
5.11	Temperature-dependent $I\text{-}V$ characteristics of the Hall bar device based on 1.7 μm thick MOF film, demonstrating ohmic behavior in the temperature range of 100–300 K	90
5.12	Logarithmic dependence of four-probe conductivity on the reciprocal temperature	91
5.13	Hall-effect measurements on two Fe-THT MOF samples	92
5.14	Temperature dependence of transport properties of Fe-THT MOFs measured by Hall-effect	93
5.15	Zabrodskii plots for Ge and Fe-THT MOF to understand their conduction mechanism	94
6.1	Device structure and characteristic curves of a photodiode under illumination	99
6.2	Device structure, band diagram and characteristic curves of a photoconductor under illumination	100
6.3	FTIR characterization of the MOF film and photodetector fabrication	105
6.4	Effect of MOF thickness on light absorption characteristics	106
6.5	Electrical characterization of the MOF photodetector at 785 nm	108
6.6	Figures of merit calculated at 785 nm to characterize the performance of the MOF photodetector as a function of temperature	109
6.7	Photoswitching behavior of the MOF photodetector at 785 nm	110
6.8	Performance characterization of the MOF photodetector at 1575 nm as a function of temperature	112
6.9	Photoresponse of the MOF photodetector at 405 nm as a function of temperature	113
6.10	Performance characterization of the MOF photodetector at 633 nm	114
6.11	Photoswitching behavior of the MOF photodetector at 633 nm	115
6.12	Responsivity at 100 K as a function of photon energy at a constant laser power density	116

List of Tables

2.1	Comparison of (opto)electronic properties obtained for InSe and MoS ₂	16
4.1	Key FET properties obtained for different metal-InSe FETs	60
4.2	Comparison of the key parameters for GaSe-photodetectors	77
C.1	Summary of Hall data	147

Physical Constants

Quantity	Symbol	Value	Unit
Boltzmann constant	k	8.617×10^{-5}	eV K ⁻¹
Electron charge	e	1.602×10^{-19}	C
Electron rest mass	m_0	9.109×10^{-31}	kg
Permittivity in vacuum	ϵ_0	8.854×10^{-12}	F m ⁻¹
Planck constant	h	6.626×10^{-34}	J s
Speed of light	c	2.998×10^8	m s ⁻¹

List of Abbreviations

2DM	Two-dimensional material
AFM	Atomic force microscopy
CMOS	Complementary metal-oxide semiconductor
CVD	Chemical vapor deposition
DFT	Density functional theory
EDS	Energy-dispersive X-ray spectroscopy
FET	Field-effect transistor
FTIR	Fourier-transform infrared spectroscopy
FWHM	Full width at half maximum
GaSe	Gallium selenide
hBN	Hexagonal boron nitride
HOMO	Highest occupied molecular orbital
InSe	Indium selenide
IR	Infrared
LUMO	Lowest unoccupied molecular orbital
MIBK	Methyl isobutyl ketone
MOF	Metal-organic framework
MoS ₂	Molybdenum disulfide
MoSe ₂	Molybdenum diselenide
NEP	Noise equivalent power
NIR	Near-infrared
PDMS	Polydimethylsiloxane

PL	Photoluminescence
PMMA	Polymethyl methacrylate
PPC	Poly propylene carbonate
PVA	Polyvinyl alcohol
SEM	Scanning electron microscopy
TEM	Transmission electron microscopy
THT	2,3,6,7,10,11-triphenylenehexathiol
TMDC	Transition metal dichalcogenide
UV	Ultraviolet
vdW	van der Waals
VIS	Visible

Chapter 1

Introduction

One of the key trends of this century in the area of microelectronics has been the search for new materials that could replace silicon (Si) to carry on further miniaturization as per Moore’s Law. The successful isolation of graphene in 2004 has brought a novel class of materials, so called two-dimensional (2D) materials, into the limelight. Because of quantum confinement in one direction, the properties of 2D materials are much different from those of their bulk. This led to an early speculation of 2D materials being a potential alternative to Si in electronics at sub-10 nm dimensions. Today the 2D family has expanded to comprise inorganic, organic and even hybrid organic-inorganic materials. Extensive researches are being carried out to characterize various 2D materials, each offering a unique set of intrinsic properties and covering a wide range of applications; e.g. semi-metals (graphene), semiconductors (MoS_2 , InSe and black phosphorus), dielectrics (hexagonal boron nitride), superconductors (NbSe_2), and topological insulators (Bi_2Se_3). However, for applications in electronic and optoelectronic devices including transistors, photodetectors, photovoltaic, sensors, and light-emitting diodes, semiconducting 2D materials with a finite bandgap, excellent transport properties and mechanical flexibility are required. Within the 2D limit, transition metal dichalcogenides (TMDCs) have gained considerable attention and demonstrated their potential as active elements in (opto)electronics. Among TMDCs, molybdenum disulfide (MoS_2) is the most researched material, owing to its relatively high mobility ($>100 \text{ cm}^2 \text{ V}^{-1} \text{ s}^{-1}$), large FET switching ratio ($>10^8$), and reduced short-channel effects. For these reasons, it is being monitored by International Technology Roadmap for Semiconductors since 2012 as a promising candidate for device scaling. However, the growing interest in 2D semiconductors is not limited to TMDCs, but has expanded beyond these conventional materials. In the last years, search for new 2D materials which could demonstrate graphene-like properties, i.e. high mobility at atomic thicknesses, delocalized charge transport, and ambient stability while possessing a finite (preferably direct) bandgap, has been the main focus.

Joining this quest for new materials, this thesis presents a comprehensive investigation of electronic properties and underlying charge transport mechanisms of two novel semiconducting classes of materials: (a) the family of III–VI chalcogenides, of which indium

selenide (InSe) and gallium selenide (GaSe) are of main interest, and (b) metal-organic frameworks (MOFs), where a newly developed π -d conjugated $\text{Fe}_3(\text{THT})_2(\text{NH}_4)_3$ 2D MOF is discussed. Field-effect transistors (FETs) and two-terminal devices are fabricated with the material of interest as the channel to understand its conduction mechanisms. Taking advantage of their layered structures, van der Waals (vdW) heterostructures have been assembled by carefully controlling the substrate and metal contacts, in order to reach their intrinsic mobility limits. As the contacts play a vital role in determining the properties of the 2D channel layer, immense focus has been placed on establishing reliable and efficient contacts to the underlying channel layer.

Around the same time as the beginning of this PhD project, the first reports on electronic properties of InSe and GaSe were published. The early reports on InSe demonstrated a two-probe mobility of $\sim 1000 \text{ cm}^2 \text{ V}^{-1} \text{ s}^{-1}$ (an order of magnitude higher than MoS₂) for layers with thicknesses of more than 30 nm.^[11,12] However, it was later established that InSe and GaSe are air-sensitive materials, which degrade rapidly on exposure to oxygen and water.^[13,14] During the course of this PhD project, very few reports were published to address the ambient degradation of InSe and GaSe, while measuring two-probe mobilities of few hundreds for thicknesses of 6–40 nm.^[15–17] Despite previous reports on encapsulation, a systematic study on long-term stability and high performance of encapsulated InSe (and GaSe) devices was missing, which has been accomplished in this work. By employing an effective encapsulation technique based on hexagonal boron nitride (hBN) for air-sensitive materials of InSe and GaSe, we achieved both good performance and long-term stability, which could not be obtained until now. Our encapsulation technique is robust and easily transferable to other complex air-sensitive 2D materials. We believe that this technique can open ways for fundamental studies as well as towards the integration of these materials in technological applications.

Another set of emerging 2D materials with potential applications in optoelectronics are MOFs. In contrast to inorganic 2D materials, MOFs provide a high degree of structural and chemical tunability achieved by varying the constituents. Because of their manifold benefits, such as low-cost production, large-area coverage, ambient stability, and flexibility, MOFs can be *the* materials for future electronics. However, to exploit these benefits, their electronic properties should meet state-of-the-art performance of inorganic materials. To this end, significant efforts have been made to synthesize semiconducting MOFs, but owing to the fact that the majority of MOFs revealed poor mobility associated with localized hopping transport, their exploitation in electronics and optoelectronics has remained severely constrained. In this work, we investigate electronic properties of a novel 2D semiconducting MOF film of $\text{Fe}_3(\text{THT})_2(\text{NH}_4)_3$ (THT: 2,3,6,7,10,11-triphenylenehexathiol), synthesized and provided by the group of Prof. Xinliang Feng at Technische Universität Dresden. To understand the charge transport mechanisms, we performed the very first Hall-effect measurements on a MOF system. The results revealed a record-high mobility of $230 \text{ cm}^2 \text{ V}^{-1} \text{ s}^{-1}$ at room temperature and band-like charge transport operative in the MOF films. In addition, the intrinsic mechanisms affecting the electrical conductivity of the MOF films as a function

of temperature are investigated. The findings reveal the presence of a thermally activated charge carrier population in the samples, induced by the small bandgap of the MOFs. Following this work, we demonstrated the first-ever proof-of-concept photodetector based on $\text{Fe}_3(\text{THT})_2(\text{NH}_4)_3$ MOF film. The small bandgap of the MOF film causes thermally excited band-to-band charge carrier population that is suppressed by cooling the device to cryogenic temperatures. The figures of merit obtained for the MOF photodetector are improved at 77 K as compared to room temperature, and are comparable to those obtained with the first demonstrations of graphene and black phosphorus based photodetectors. This work presents the feasibility of integrating conjugated MOFs as an active element into functional photodetectors, thus bridging the gap between materials' synthesis and technological applications.

Thesis overview The next chapter (chapter 2) provides a review of the literature, including the fundamental concepts of 2D materials and their importance for future electronics. A brief introduction to graphene and MoS_2 is provided for the context. Next, the materials under investigation, i.e. InSe and GaSe, their crystal structure, material characterization and key findings on their (opto)electronic properties are provided. Special focus has been placed on various encapsulation techniques and their effect on intrinsic properties of InSe and GaSe. An introduction to hBN and its properties as a dielectric is discussed. Since vdW assembly is an important part of this thesis, its working principle and importance in the 2D field is discussed. The later part of this chapter provides an overview of the MOF materials, with special focus on semiconducting 2D MOFs. The fundamentals of charge transport mechanisms are discussed. The results reported until now for the electronic properties of MOFs are highlighted.

The sample preparation procedures and experimental setups used during this work are discussed in chapter 3. The techniques of fabricating vdW heterostructures as well as other complex stacks for the purposes of charge transport studies, time-resolved micro-photoluminescence, low-temperature photoluminescence, and transmission electron microscopy investigations are detailed.

In chapter 4, the electronic properties of InSe and GaSe as obtained from their FET devices are discussed. The initial attempts to fabricate InSe FETs included using bare InSe as the channel. However, the devices became non-functional over time because of degradation of InSe in air. To circumvent this issue, techniques for the passivation of InSe and GaSe are discussed. A part of this work has been carried out during my research visit at the group of Prof. James Hone at Columbia University (New York, USA). Using their glovebox and nanofabrication facilities, an effective encapsulation technique based on hBN for air-sensitive materials is developed. The hBN based encapsulation preserved InSe and GaSe flakes in their pristine form, while giving us an opportunity to understand their unaltered properties and transport mechanisms in greater detail. My training at their labs helped us to set up our own lab at Helmholtz-Zentrum Dresden-Rossendorf (HZDR), which boosted our research on

2D materials as well as attracted several collaborations.

The electrical investigation of 2D MOF films of $\text{Fe}_3(\text{THT})_2(\text{NH}_4)_3$ is presented in chapter 5. The MOF films are obtained from the group of Prof. Xinliang Feng at Technische Universität Dresden. To elucidate conduction mechanisms, conductivity measurements (two-probe and four-probe) and Hall-effect measurements are performed. The findings revealed a record-high charge mobility of $230 \text{ cm}^2 \text{ V}^{-1} \text{ s}^{-1}$ at room temperature and band-like charge transport operating in these films. With these attractive properties, proof-of-concept photodetectors based on 2D MOF films are demonstrated in chapter 6. Temperature dependence of various figures of merit of the photodetector is presented. Also, the photoresponse at various wavelengths in the UV-to-NIR range is measured and discussed. So far, only a handful of reports have addressed the photodetection properties of MOFs, and our work reports the first proof-of-concept MOF-based photodetector, revealing MOFs as promising candidates for optoelectronic applications.

The last chapter (chapter 7) concludes the thesis with a summary of the key results. It also provides an outlook on further research with respect to ongoing developments and the recent literature.

Chapter 2

Overview

1 Two-dimensional materials

Two-dimensional materials, often abbreviated as 2DMs or 2D materials, are a sub-class of thin-film materials with thicknesses at the nm-level and lateral dimensions ranging several times greater than their thicknesses. Due to quantum confinement in one direction, their properties are much different from their bulk. Most 2D materials are layered structures, with strong covalent bonds within each layer and weak vdW forces acting between the layers separated by an interlayer distance. Because of these vdW forces, they are easily exfoliated from their bulk crystal into mono- to few-layers, with thicknesses ranging from less than 1 nm to few μm .

The field of 2D materials is known since the 1940s,^[18–21] however, for a long time it was believed that 2D materials could not exist because of their thermodynamic instability.^[22–24] It was only in 2004 when for the first time a two-dimensional one-atom thick layer of carbon, named as graphene, was experimentally isolated at the University of Manchester by the two physicists Konstantin Novoselov and Andre Geim.^[25,26] The discovery led them to win the Nobel Prize in Physics in 2010 and prompted the scientific community to isolate and employ other 2D materials in various applications. Today the 2D family has expanded to comprise more than 600 vdW materials,^[27] ranging from inorganic materials like graphene to organic structures and plate-like polymers, each offering a unique set of intrinsic properties and covering a wide range of applications.

Due to the atomic scale thicknesses, high electrical and thermal conductivity, and mechanical flexibility, 2D materials have always been envisioned as an alternative to silicon for future's fast, flexible and miniaturized electronics. It is well-known that conventional bulk semiconductors, such as silicon (Si) and germanium (Ge) are unsuitable for device scaling because of short-channel effects, leading to poor mobility and device performance. In this regard, atomically thin 2D materials are advantageous, as they do not suffer from these issues and provide an atomically smooth and dangling bonds-free surface. Though Si and Ge can also be processed into thin films, 2D materials are naturally existing atomically thin materials due to weak vdW interlayer interactions. Furthermore, thinning down bulk semiconductors can

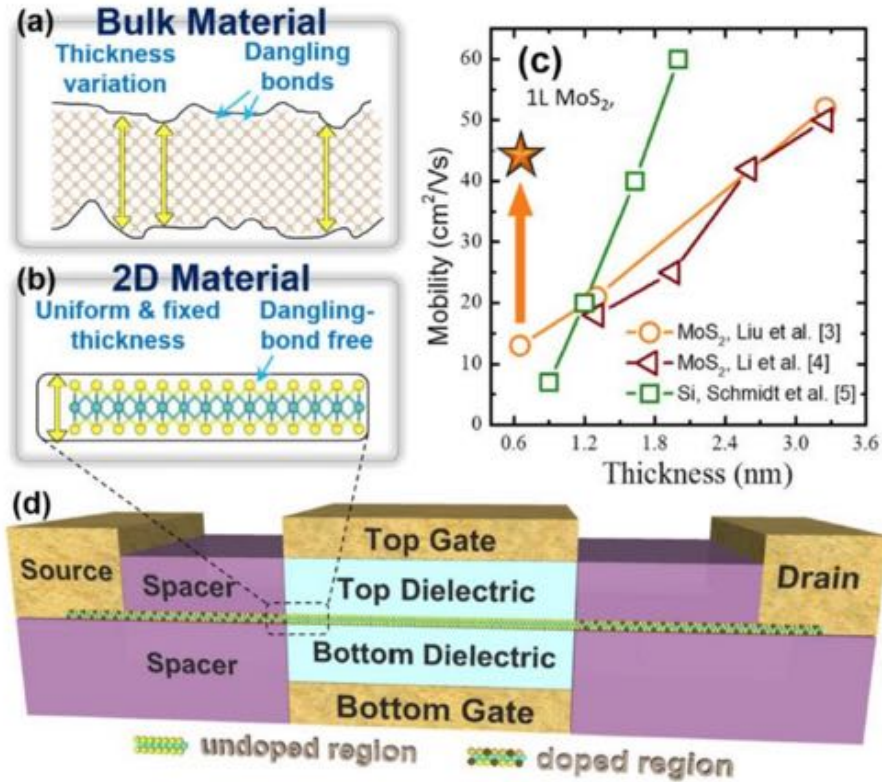


Figure 2.1: Thickness scaling in bulk versus 2D semiconductor for FET application. (a) Non-uniform thickness and dangling bonds on the surface of the bulk semiconductor when thinned down, (b) uniform thickness and flat surface of the intrinsically thin 2D material, (c) carrier mobility variation on decreasing the thickness of Si and MoS₂, (d) schematic of a 2D FET with top and back gates.^[28]

lead to thickness (and hence, bandgap) variations, whereas 2D semiconductors have uniform thicknesses associated with the number of layers present. In addition, because of strong quantum confinement in the vertical direction, electronic structure and bandgap of 2D materials are highly tunable by varying their thicknesses. The schematic in Figure 2.1 shows the advantages of 2D materials over bulk semiconductors. An interesting study in Figure 2.1c shows the carrier mobility degradation in Si and MoS₂ during thickness scaling. It is found that the mobility degradation rate with decreasing thickness is slower in MoS₂ compared to Si.^[28] Since this report in 2015 until today, the reported mobility of monolayer MoS₂ has reached $\sim 100 \text{ cm}^2 \text{ V}^{-1} \text{ s}^{-1}$, attributed to continuous improvement in the material's quality, gate dielectric and contact engineering.^[29,30] These mobilities are maintained even in strained MoS₂ layers, indicating the possibility of venturing into flexible electronics. These advantages of 2D materials in addition to charge trap-free surfaces, guarantee a robust device performance at sub-10 nm dimensions.^[28]

1.1 Graphene

Graphene, a 2D form of graphite, is composed of a single layer of sp^2 hybridized carbon atoms arranged in a honeycomb lattice (Figure 2.2). It is the thinnest material system discovered

to date (one atom thick, i.e. ~ 0.335 nm) and is the fundamental building block of all other sp^2 carbon allotropes, such as three-dimensional (3D) graphite, one-dimensional (1D) carbon nanotubes, and zero-dimensional (0D) fullerenes. Graphene was originally obtained by micro-mechanical exfoliation of its bulk crystal graphite by Scotch-tape. To date, several top-down and bottom-up approaches have been optimized to produce high-quality graphene films with large areas extending up to few cm.

Due to the extraordinary electronic, optoelectronic, and mechanical properties of graphene, it is a promising candidate for a large variety of applications. Many excellent properties, such as its 2.3% absorption in the white light spectrum,^[31] high Young's modulus of 1 TPa and tensile strength of 130 GPa,^[32] high thermal conductivity ($\sim 2\text{--}5.3$ kW m $^{-1}$ K $^{-1}$)^[33] and electrical conductivity (higher than copper), flexibility, and impermeability to gases, have all been reported.^[34] These remarkable properties have inspired extensive research on its potential applications in a wide range of areas, including fast electronic and photonic device, energy generation and storage, chemical sensors, and even DNA sequencing.^[35]

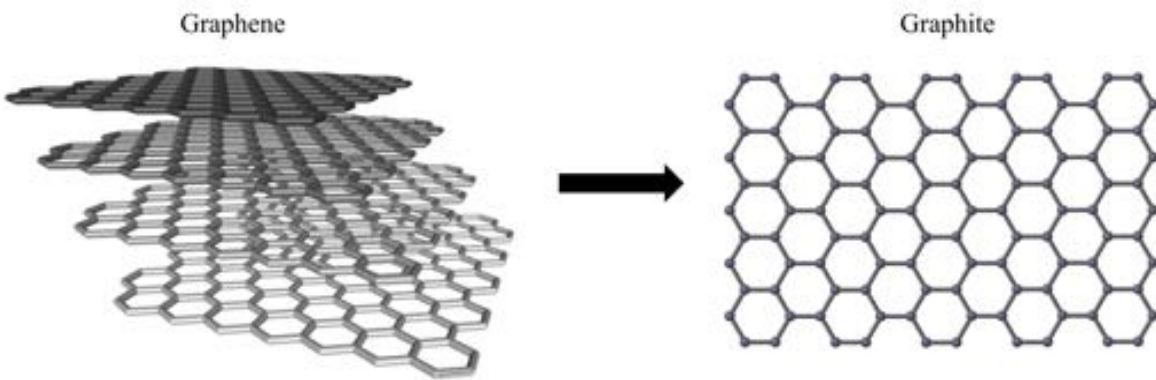


Figure 2.2: Schematic of the structure of graphite and graphene.

The properties of graphene differ from its parent graphite in many ways because of its atomic and electronic configuration. The sp^2 hybridization of carbon atoms in a graphene sheet form strong in-plane σ covalent bonds that gives graphene its mechanical strength. The unaffected, half-filled π -orbitals provide delocalized π -electrons, acting as a 2D electron gas across its surface.^[36] The honeycomb lattice of graphene with lattice vectors a_1 and a_2 is shown in Figure 2.3a, while the corresponding reciprocal lattice with vectors b_1 and b_2 is shown in Figure 2.3b. For electronic properties of graphene, the two points of the first Brillouin zone, K and K' , (charge neutrality points, also known as Dirac-points) play a major role. In contrast to the parabolic dispersion of graphite, graphene shows a linear energy-momentum relation (Figure 2.3c,d). The conduction and valence bands intersect at the K and K' points, leading to no bandgap. Around these points, the electrons behave as massless Fermi-Dirac particles and are governed by the Dirac equation instead of the Schrödinger equation. This gives rise to record-high carrier mobilities of 2.5×10^5 cm 2 V $^{-1}$ s $^{-1}$ at room temperature, which is two orders of magnitude higher than Si.^[37-39] This mobility can vary further depending on the quality of the film and the bottom substrate because of the extreme sensitivity of the delocalized π -orbitals to the surroundings.^[36,40] Though graphene demonstrates high intrinsic

mobilities, its gap-less electronic structure is not suitable for device applications where a defined bandgap is required. The absence of bandgap makes the switching of graphene FETs very difficult and gives rise to a poor on/off ratio.

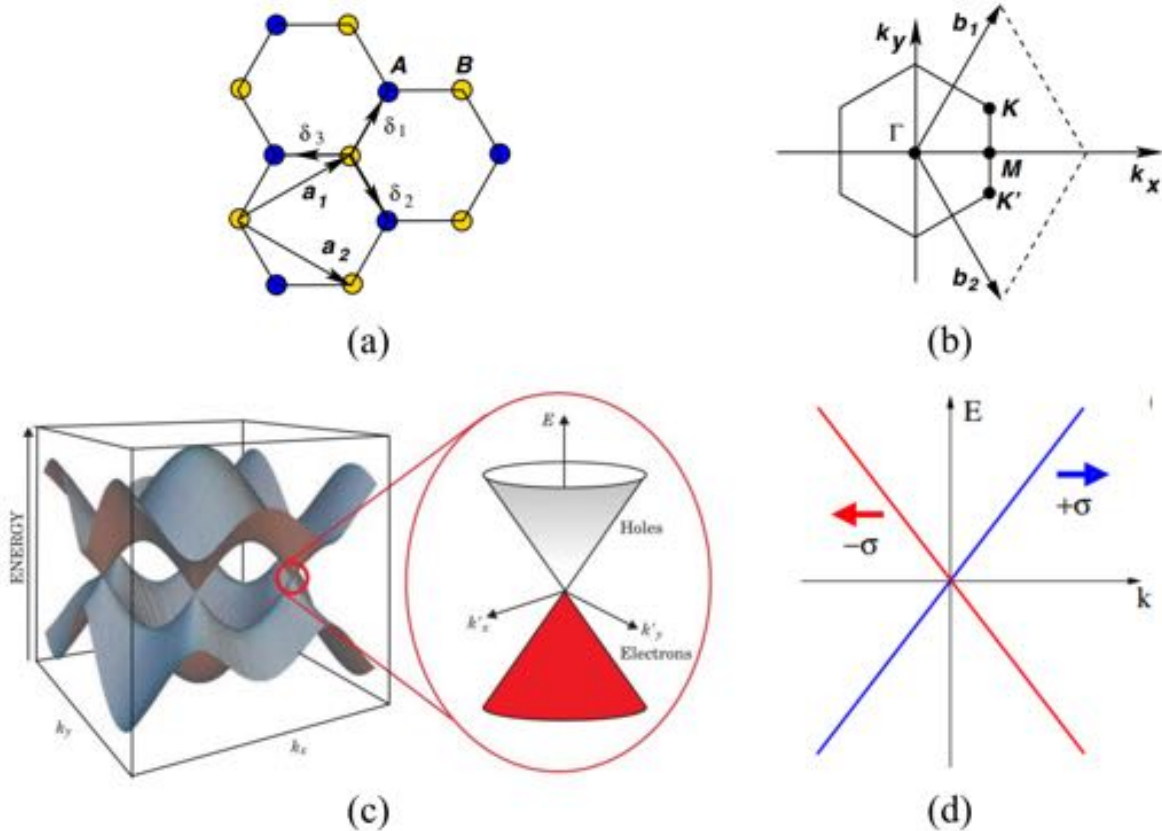


Figure 2.3: Band structure and corresponding electronic properties of graphene. (a) Schematic of the honeycomb lattice of graphene with a_1 and a_2 as lattice vectors, (b) first Brillouin zone of graphene with corresponding reciprocal lattice vectors b_1 and b_2 , (c) the valence and conduction bands of graphene with a zoomed in view of the band structure around the Dirac points K and K' , (d) the linear and gap-less energy dispersion in graphene.^[36]

Nevertheless, such interesting properties of graphene encouraged the isolation and investigation of other 2D materials. The easy exfoliation of 2D layers from their bulk crystals has facilitated discovery of more than 600 2D materials currently known, consisting of semi-metals, semiconductors, insulators and superconductors (Figure 2.4).^[41,42] This growing interest in 2D materials is not only limited to fundamental research, but has also taken a serious turn in industrial applications in the areas of electronics, optoelectronics, photovoltaics, spintronics, sensing, and energy storage. From the vast family of 2D materials, this work focuses on 2D vdW semiconductors and their heterostructures, while exploring their potential applications in the areas of electronics and optoelectronics.

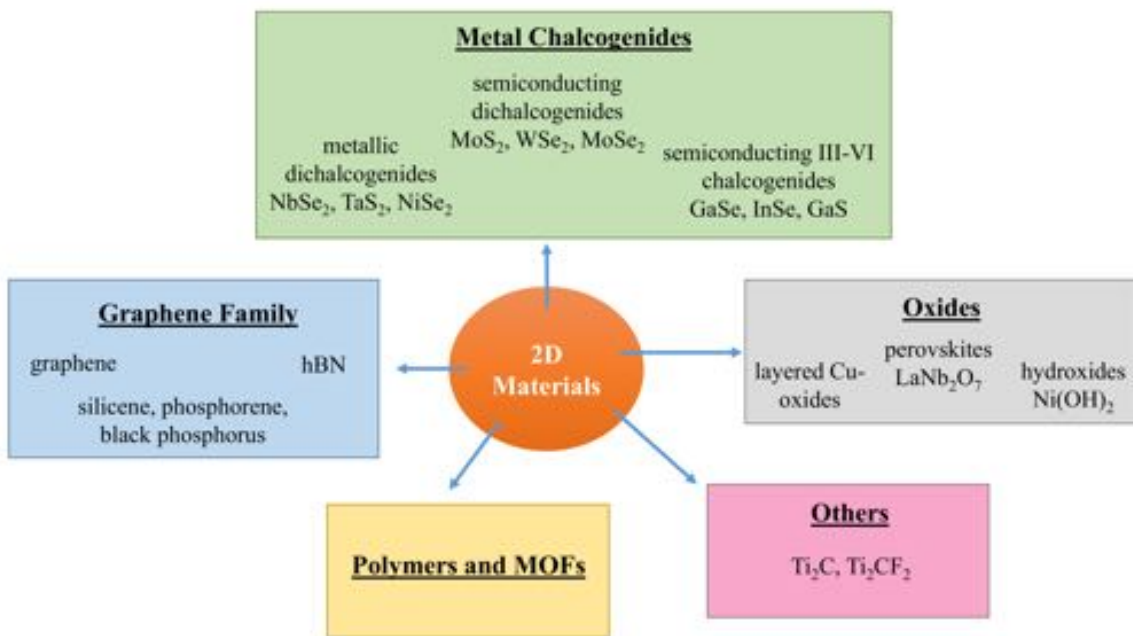


Figure 2.4: Chart illustrating the evolution of the family of 2D materials categorically. Adapted from Geim et al.^[43]

1.2 2D vdW semiconductors

The presence of a bandgap in a material is essential for its application in electronic and logic circuits that are based on FETs. One of the key requirements for a functional FET is its ability to switch-off by modulating the gate voltage. Semiconducting 2D materials with a finite bandgap and excellent transport properties are of particular interest for such applications. In this regard, the family of TMDCs with the general formula MX_2 , where M is the transition metal from the d -block (group 4–12 in the periodic table) and X is the chalcogen atom from group 16 (S, Se, Te), is the most popular class of 2D vdW semiconductors. Another class of semiconducting 2D materials rapidly gaining interest is the family of III–VI chalcogenides. These are layered materials with the formula MX , where M is the metal from group 13 (Ga, In) and X is the chalcogen atom (S, Se, Te). While TMDCs take dichalcogenides (MX_2) stoichiometry, III–VI chalcogenides are monochalcogenides (MX). Other than these, mixed stoichiometric compositions, e.g. sesquichalcogenides (M_2X_3) and trichalcogenides (MX_3) are also found. Beyond metal chalcogenides, other 2D semiconductors, such as black phosphorus, phosphorene, are also emerging class of materials.

In the case of metal chalcogenides, their electronic band structure is found to evolve rapidly as their dimensionality is reduced towards a 2D nanosheet. Accordingly, the intrinsic electronic properties evolve as well on decreasing the thickness to few layers from the bulk. MoS₂, a member of the TMDC family, offers a prime example to demonstrate this. The crystal structure of MoS₂ consists of two hexagonal planes of sulfur (S) atoms sandwiching the hexagonal plane of molybdenum (Mo) atoms. These three atomic layers stacked together yield one monolayer of MoS₂ as shown in Figure 2.5a. Strong covalent bonding exists between Mo and

S atoms within the monolayer, while weak vdW forces act between the layers, thus holding them together. Figure 2.5b shows the evolution of the band structure of MoS₂ from bulk to monolayer. Significant changes are revealed in the shapes of valence and conduction bands when bulk MoS₂ is reduced to a monolayer. An interesting feature of MoS₂ is its indirect to direct bandgap transition in monolayers. Bulk MoS₂ has an indirect bandgap of ~ 1.2 eV, whereas monolayer MoS₂ possess a direct bandgap of ~ 1.89 eV, which enables its wide use in optoelectronics. This striking contrast between monolayer and bulk MoS₂ is a consequence of decoupled interlayer interaction and electron confinement in a single plane. In terms of electronic transport, FETs based on MoS₂ have shown an intrinsic *n*-type conduction with a peak electron mobility of ~ 100 cm² V⁻¹ s⁻¹ in a 5-layer structure.^[44,45] Mobility in MoS₂ FETs follows a Gaussian distribution with the maximum for layer thicknesses between 5 (~ 3.6 nm) and 10 layers (~ 7 nm), as shown in Figure 2.5d.

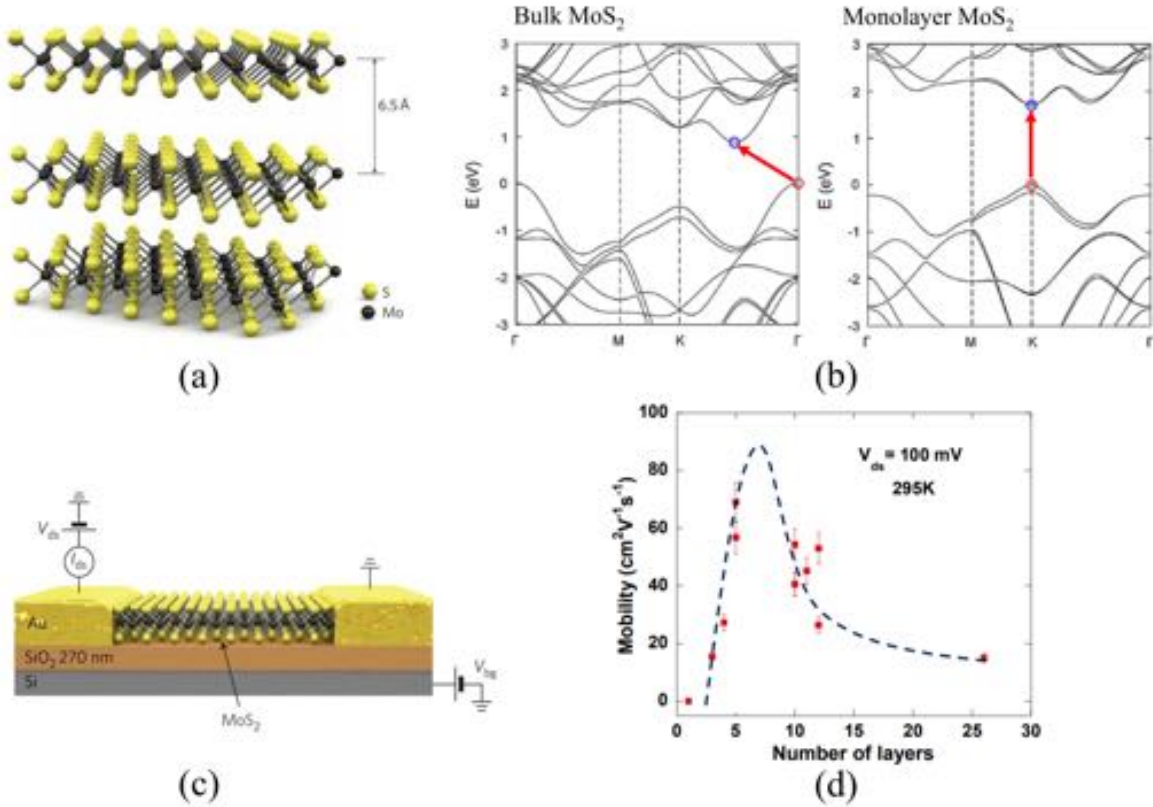


Figure 2.5: Crystal and band structure of MoS₂ and corresponding electronic properties. (a) Schematic representation of the structure of MoS₂ showing two S layers (yellow) sandwiching one Mo layer (black).^[46] (b) electronic band structures of bulk and monolayer MoS₂ calculated from first principles using density functional theory (DFT). Bulk MoS₂ shows an indirect bandgap with the maximum of valence band located at the Γ point and conduction band minimum at a low-symmetry point of the Brillouin zone. Monolayer MoS₂ shows a direct bandgap with valence band maximum and conduction band minimum located at K point.^[47] (c) schematic of an FET based on monolayer MoS₂,^[30] (d) evolution of mobility for various thicknesses of MoS₂ at 295 K. The distribution indicates an optimal thickness between 5 and 10 layers for maximum mobility in back-gated MoS₂ FET devices.^[44]

Owing to its good mobility, high on/off ratio and relative stability, MoS₂ is a popular candidate for electronic applications. However, the unavailability of a direct bandgap has constrained its use in optoelectronics to only monolayers. Recently, other 2D materials exhibiting even higher mobilities of $\sim 1000 \text{ cm}^2 \text{ V}^{-1} \text{ s}^{-1}$ at room temperature have been reported. These novel 2D semiconductors could exceed TMDCs in various applications in the future. The following section introduces one such emerging class of semiconducting 2D materials, the family of III–VI semiconductors, which has the potential to contribute significantly to the development of future technologies.

2 Novel 2D semiconductors: III–VI chalcogenides

The family of III–VI chalcogenides comprising of vdW semiconductors has gained considerable attention in recent years owing to its intriguing properties and underlying physics at low dimensions. The family consists of layered semiconductors with the formula MX; M is a metal from group 13 (Ga, In) and X is a chalcogen atom (S, Se, Te). The stoichiometric composition is M₂X₃, arranged in X–M–M–X fashion, i.e. two metal layers sandwiched between two chalcogen planes. The top and side views of the layer arrangement of MX compounds are shown in Figure 2.6. The top view shows the hexagonal lattice structure and the side view reveals the four atomic layers covalently bonded to produce a monolayer of the MX compound. Similar to TMDCs, strong in-plane covalent bonds exist between M and X atoms, while vdW forces hold the layers together. Depending on the stacking pattern, three main polytypes including two two-hexagonal (2H) phases and one three-rhombohedral (3R) phase are found. The three polytypes differ in the stacking patterns as shown in Figure 2.7. 2H-phases of ϵ and β polytypes consist of AB stacking by repeating the bilayer structure, whereas the γ -polytype (3R-phase) has ABC stacking by repeating the trilayer arrangement in the direction perpendicular to the in-plane layers.^[48]

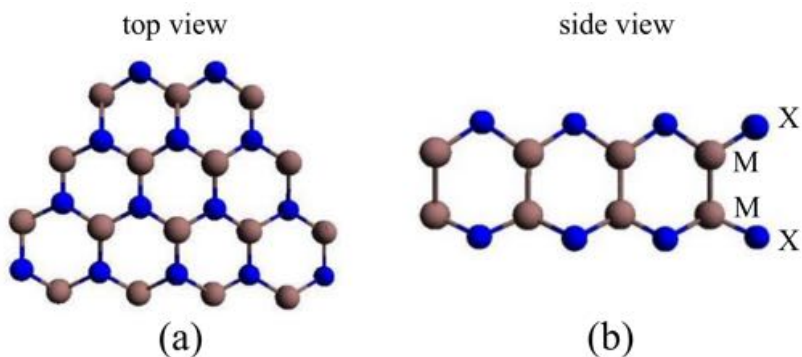


Figure 2.6: Structural schematics of (a) top, and (b) side views of MX compounds. Blue spheres represent chalcogen atoms and brown represent metal atoms. Adapted from Arora et al.^[10]

Bulk crystals of III–VI compounds are produced by a range of top-down and bottom-up techniques. The Bridgman method is one of the commonly used techniques for growing high-quality crystals of InSe and GaSe. The crystals are mechanically exfoliated into mono- and

few-layers using an adhesive tape. Another synthesis technique is liquid phase exfoliation and has an advantage in producing large-area sheets. Bottom-up approaches, such as chemical vapor deposition (CVD), physical vapor deposition and vapor phase mass transport have also been reported for producing single layers of III–VI compounds. In the last years, molecular beam epitaxy has also been demonstrated for the growth of III–VI nanosheets.^[49]

The two most prominent members of the III–VI chalcogenide family are indium selenide (InSe) and gallium selenide (GaSe), owing to their appealing electronic properties. An intrinsic mobility of $\sim 1000 \text{ cm}^2 \text{ V}^{-1} \text{ s}^{-1}$ in InSe at quantum confinement thicknesses is the highest mobility reported so far in an *n*-type 2D material.^[50] In addition, InSe has a direct bandgap of 1.26 eV in bulk that is retained at all thicknesses above 6 nm.^[51] This makes InSe advantageous over MoS₂ for several applications, including high-speed electronics,^[11,12,52] and optoelectronics.^[15,53,54] GaSe, on the other hand, has shown potential for single-photon emission^[55] and terahertz applications^[56], owing to its nonlinear optical properties.^[57]

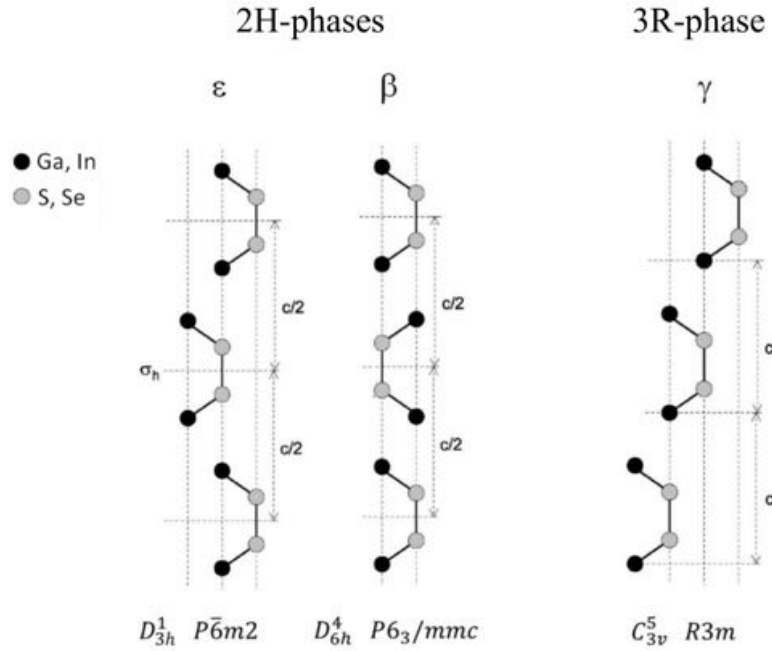


Figure 2.7: Stacking arrangements of three different polytypes of III–VI chalcogenides. 2H-phase consists of ϵ and β polytypes and 3R-phase consists of γ polytype.^[58]

2.1 Indium selenide

InSe single crystals grown by the Bridgman method crystallize at ambient conditions in the γ -InSe polytype, which belongs to the space group C_{3v} .^[58] Figure 2.8 illustrates schematically the crystal structure of γ -InSe. The top and side views of a monolayer of InSe are shown in Figure 2.8a,b, respectively.

Each monolayer consists of four covalently bonded atoms in the sequence Se–In–In–Se. The primitive unit cell consisting of three monolayers has an out-of-plane lattice parameter

$c = 2.492$ nm (along the c -axis). In a plane, atoms form a hexagonal lattice with parameters $a = b = 0.4$ nm.^[51] When these covalently bonded monolayers interact through vdW forces, multilayered structures are formed with an interlayer distance of ~ 0.88 nm as shown in Figure 2.8c,d. The patterns in which the layers are stacked define the phase of the crystal. The γ -phase of InSe has ABC stacking mode, i.e. three layers in the unit cell are stacked with an offset in the a - b plane, as shown in the side view of few-layered InSe in Figure 2.8d.^[6]

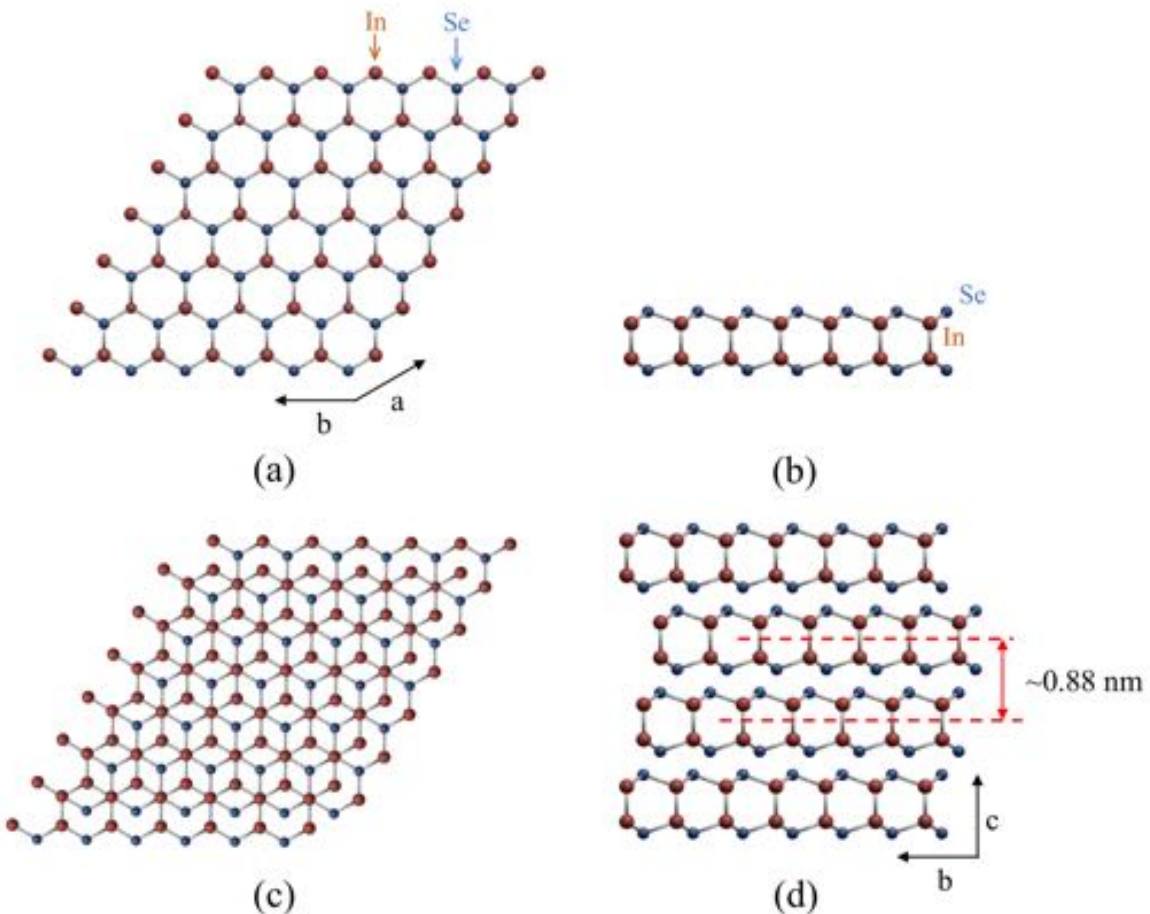


Figure 2.8: Crystal structure of mono- and few-layered γ -InSe. (a) Top view of hexagonal lattice structure of monolayer InSe, (b) side view of monolayer InSe, covalently bonded in the sequence Se-In-In-Se, (c) top view of few layers of InSe along a - and b -axis, (d) side view of few layers of InSe held together by vdW forces with an interlayer distance of 0.88 nm. Adapted from Arora et al.^[6]

In bulk, InSe has a direct bandgap of 1.26 eV, which increases significantly for thicknesses less than 15 nm, where strong quantum confinement effects come into play.^[51] InSe retains its direct band gap up to a thickness of 6 nm, below which it exhibits an indirect transition and the bandgap increases up to 2.35 eV for monolayer InSe.^[51,52] Figure 2.9 shows the evolution of the bandgap as a function of layer thickness for γ -InSe.^[51] For thicknesses more than 15 nm, the photoluminescence (PL) peak is centered at ~ 1.26 eV, which shifts to higher energies on decreasing the thickness below 15 nm, consistent with quantum confinement of photo-excited carriers by the external surfaces of the flakes.^[51] The PL intensity also decreases

progressively for thicknesses less than 10 nm, and quenches for thicknesses below 6 nm, i.e. 7-layer InSe. The strong decrease in the PL signal at thicknesses below 6 nm is attributed to a direct-to-indirect bandgap crossover.

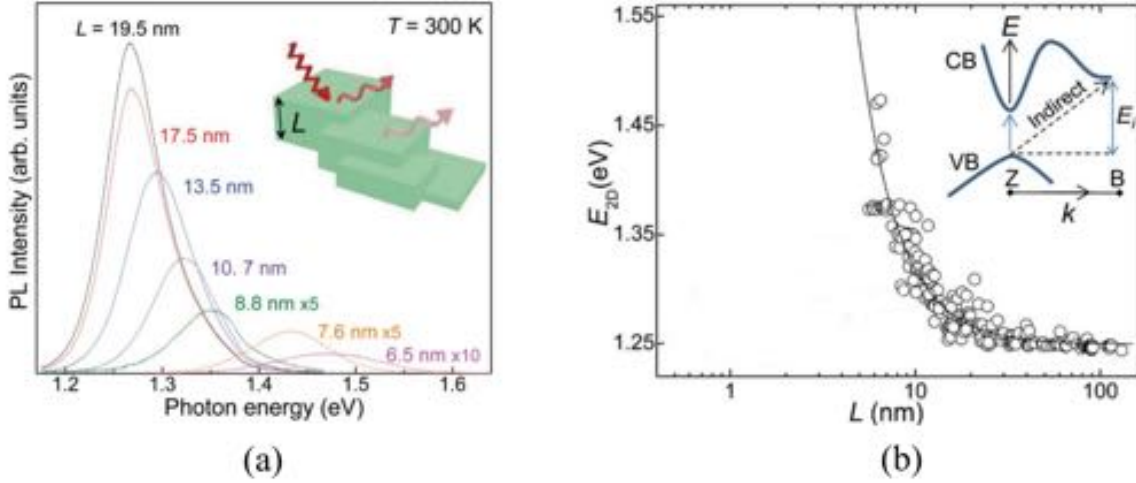


Figure 2.9: Micro-PL study of different thicknesses of exfoliated InSe. (a) Micro-PL spectra of InSe layers at 300 K , showing strong dependence of PL peak position on the layer thickness. The inset sketches the PL emission from flakes of different thickness. (b) The peak energy of the micro-PL emission versus the thickness L of the InSe layer at 300 K . The inset shows the direct and indirect gap.^[51]

The Raman spectrum of InSe is shown in Figure 2.10. In one unit cell of γ -InSe, there are 12 atoms. For 12 atoms there will be 3×12 , i.e. 36 vibrational modes.^[59] The Mulliken symbols A and B are used to refer to vibrational modes along the c -axis, i.e. perpendicular to the in-plane layers, while for modes along the basal plane, E is used.^[59] According to crystal symmetry and Raman selection rules, not all modes are active and visible in the Raman spectra.^[60] For InSe, four modes have been observed experimentally, A'_1 (117 cm^{-1}), E'' (179 cm^{-1}), $A''_2(\text{LO})$ (201 cm^{-1}) and A'_1 (227 cm^{-1}). For bulk InSe, the $A''_2(\text{LO})$ peak is relatively weak. As the thicknesses decreases, this mode becomes stronger in intensity. For 3 to 5 layers, all Raman modes disappear leaving behind a broad envelope, indicating a major change in the electronic band structure, i.e. direct to indirect transition.^[60]

2.2 Electronic properties of InSe

One of the simplest and most efficient methods to determine the electronic properties of 2D semiconductors is to measure an FET based on the 2D layer as the channel material. In an FET, the 2D channel is separated from the gate electrode by an insulating gate dielectric. Source and drain electrodes are fabricated in contact with the 2D channel for injection and collection of the charge carriers. The channel area is defined by the length L and width W , which also defines the area between source and drain. Two important figures of merit used to characterize the performance of the 2D semiconductors are carrier mobility (μ) and responsivity (R) (for photosensitive FETs).

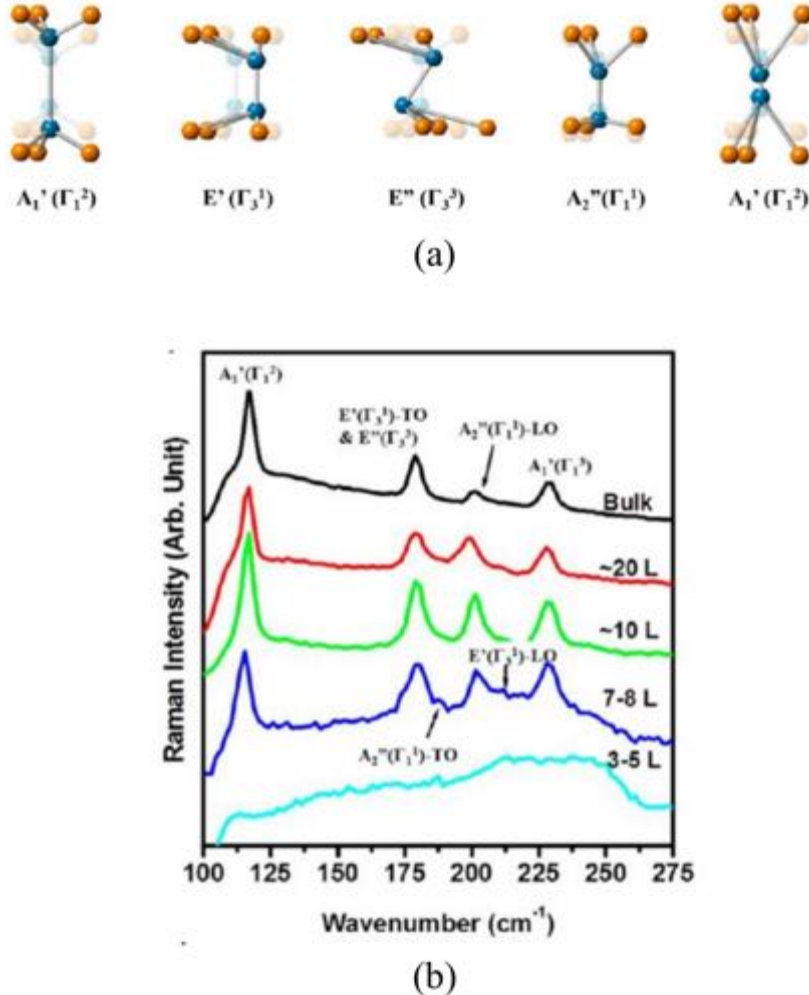


Figure 2.10: Raman study of different thicknesses of exfoliated InSe. (a) Vibrational modes for γ -InSe, (b) thickness-dependent Raman spectra of InSe flakes measured using 514 nm laser excitation.^[60]

The carrier mobility in an FET, also known as field-effect mobility (μ_{FE}), is calculated using the following equation:

$$\mu_{FE} = \frac{dI_{DS}}{dV_G} \frac{L}{WC_i V_{DS}} \quad (2.1)$$

where I_{DS} is the source-drain current, V_G is the applied gate voltage and $\frac{dI_{DS}}{dV_G}$ is the transconductance measured in the linear region of the transfer curve. C_i is the capacitance per unit area of the dielectric and V_{DS} is the applied bias. The capacitance per unit area of the gate dielectric is calculated using the equation:

$$C_i = \frac{\epsilon_0 \epsilon_d}{d} \quad (2.2)$$

where $\epsilon_0 = 8.854 \times 10^{-12} \text{ F m}^{-1}$ is the permittivity in vacuum, ϵ_d is the relative permittivity of the dielectric, and d is the thickness of the dielectric layer. In addition to transconductance measurements, four-probe and Hall-effect measurements are other methods for obtaining a more precise estimate of the intrinsic mobility by excluding the contribution of contact

resistances. The methodologies of four-probe and Hall-effect measurements are discussed in detail in chapter 5.

InSe shows a high electron mobility of $\sim 1000 \text{ cm}^2 \text{ V}^{-1} \text{ s}^{-1}$, resulting from its low electron effective mass ($m_e^* = 0.143 m_0$).^[11,61] In contrast to TMDCs, where the mobility drops severely on decreasing the layer thickness, InSe retains high mobility even at small layer thicknesses.^[52] In optoelectronics, InSe is particularly beneficial because of its direct bandgap at all thicknesses above 6 nm. Moreover, the spectral response of InSe is much broader than MoS₂ and expands from visible (VIS) to near-infrared (NIR). Table 2.1 compares the (opto)electronic properties of MoS₂ and InSe, indicating the potential of InSe for high-performance electronic devices.

Table 2.1
Comparison of (opto)electronic properties obtained for InSe and MoS₂

	Direct bandgap (eV)	Effective mass (m_e^*)	Mobility (cm^2 $\text{V}^{-1} \text{ s}^{-1}$)	Intrinsic doping	Spectral response	Responsivity (A W^{-1})
MoS ₂	1.89 (in monolayer)	$0.45 m_0$	$\sim 200^{[30]}$	<i>n</i> -type	VIS	$880^{[62]}$
InSe	1.26–1.42 (> 6 nm)	$0.143 m_0$	$\sim 1000^{[52]}$	<i>n</i> -type	VIS-to- NIR	$10^7^{[17]}$

Early InSe FETs were fabricated with multilayered InSe channel, exfoliated directly onto highly doped Si substrates with a SiO₂ layer serving as the bottom dielectric. These FETs were characterized with *n*-type conduction and low carrier mobility of $\sim 0.1 \text{ cm}^2 \text{ V}^{-1} \text{ s}^{-1}$.^[54,60] Such low mobility values can be attributed to coulomb scattering at charged interfaces, scattering from surface roughness of the bottom substrate, and surface polar phonon scattering from the dielectric.^[63]

The dielectric/semiconductor interface, where various carrier scattering centers and charge traps exist, can affect the device performance severely. Conventional dielectric substrates based on oxide layers, such as SiO₂, Al₂O₃, HfO₂ etc., are associated with a lot of hydroxyl groups and other charge trap disorders at the surface,^[11] which can hamper the carrier mobilities. On using PMMA/Al₂O₃ bilayer as the bottom dielectric, Feng et al.^[11] and Sucharitakul et al.^[12] demonstrated significant improvement in the mobility values of multilayered InSe (Figure 2.11a,b). The FETs showed a maximum mobility of $1055 \text{ cm}^2 \text{ V}^{-1} \text{ s}^{-1}$ for a 33 nm thick InSe flake (Figure 2.11c), which is comparable to strained-Si thin-film FETs,^[64] and also to black phosphorus transistors.^[65] This improved mobility is a consequence of the suppression of interfacial coulomb impurities scattering. In addition, the device showed a high on/off ratio of 10^8 , demonstrating its applicability with complementary metal-oxide semiconductor (CMOS) technology. Four-probe mobility and Hall mobility are also extracted for these devices as a function of temperature. Hall mobility is found to increase with decreasing temperature because of the suppression of phonon scattering. With PMMA dielectric, a maximum Hall mobility of $\sim 2400 \text{ cm}^2 \text{ V}^{-1} \text{ s}^{-1}$ is obtained for temperatures below 100 K.

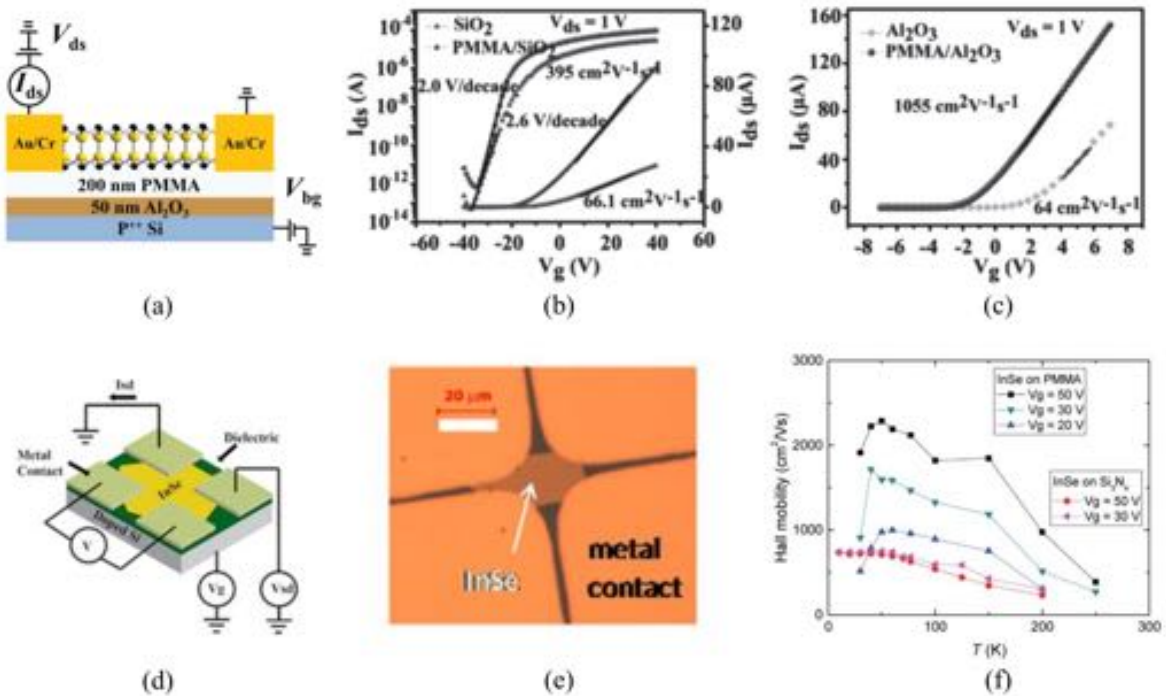


Figure 2.11: Substrate engineering: (a) Schematic of a back-gated InSe FET with PMMA/Al₂O₃ bilayer dielectric, (b) linear and semi-log transfer characteristics of two InSe FETs with SiO₂ and PMMA/SiO₂ as dielectric. The latter shows better performance, (c) transfer characteristics of two InSe FETs; better performance is obtained when PMMA/Al₂O₃ bilayer dielectric is used,^[11] (d) schematic of a four-terminal InSe FET with Si back gate and bottom dielectric, (e) optical micrograph of a four-terminal InSe FET, (f) temperature-dependent Hall mobility of InSe FETs on PMMA and Si₃N₄ dielectric surface.^[12]

Another approach to improve the carrier mobility is by selecting an appropriate metal for contacting the InSe layers, as reported by Feng et al.^[66] Metal contacts play a vital role in determining the performance of the FET devices. An ohmic contact with low contact resistance is desirable for an efficient injection of the charge carriers into the semiconducting film. Metals can be chosen based on their work function as per the relation: $\phi_b = \phi - \chi$, where ϕ is the work function and χ is the semiconductor electron affinity.^[66] Among all analyzed metal contacts, Feng et al.^[66] found In and Al to have the smallest work function (Figure 2.12b) and are thus, expected to yield the highest performance. By using In metal, μ_{FE} of $162 \text{ cm}^2 \text{ V}^{-1} \text{ s}^{-1}$ is obtained for 33 nm thick InSe flake, which surpasses the performance by other metal contacts, including Al, Ti, Au, and Cr, as shown in Figure 2.12c. The authors explain the reason to be a strong interaction between In and InSe, resulting in the formation of an intimate contact, which could not be achieved with Al and other metals. In another study by Yang et al.^[15], focused ion beam is used to fabricate metal electrodes to the InSe with thicknesses much beyond the quantum confinement scale ($>45 \text{ nm}$). These FETs showed a high mobility of $450 \text{ cm}^2 \text{ V}^{-1} \text{ s}^{-1}$ and a high responsivity of 10^7 A W^{-1} at room temperature.^[15]

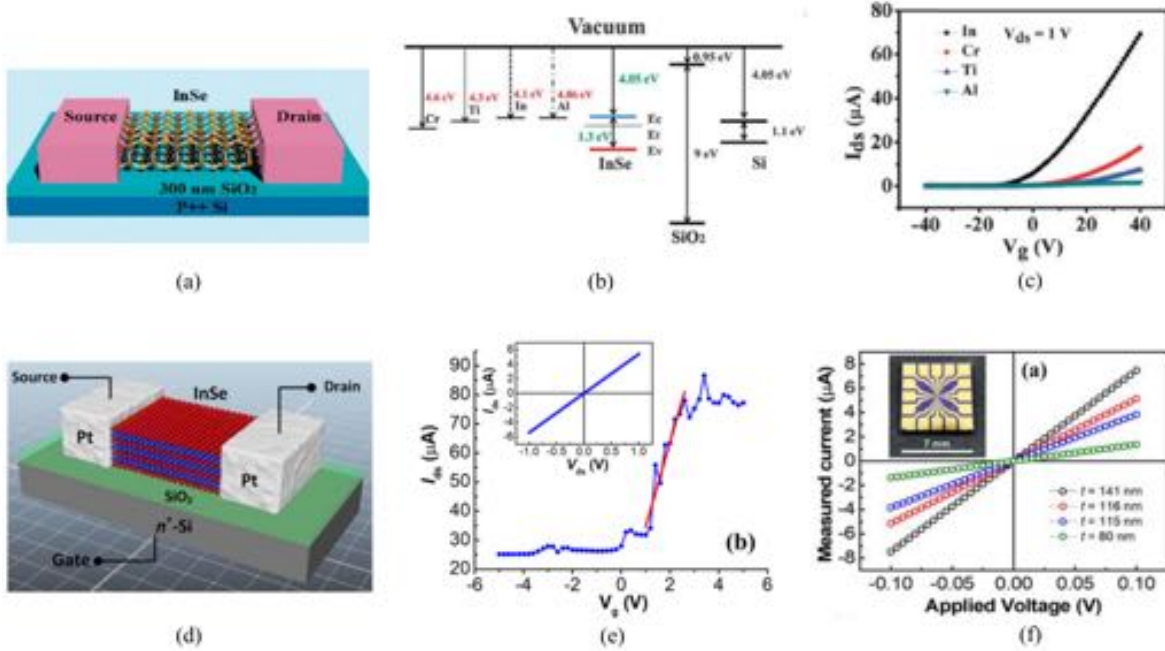


Figure 2.12: Contact engineering: (a) Schematic of a back-gated InSe FET with SiO₂ as bottom dielectric, (b) work functions of various metals as compared to band edges of InSe, (c) transfer characteristics of 33 nm thick InSe FET with different metal contacts,^[66] (d) schematic of a back-gated InSe FET with Pt FIB contacts, (e) transfer curve of the InSe FET, revealing μ_{FE} of $450 \text{ cm}^2 \text{ V}^{-1} \text{ s}^{-1}$. The inset shows the output curve and the formation of ohmic contacts, (f) two-terminal I–V measurements for InSe flakes with different thicknesses. The inset depicts a chip template with patterned Ti/Au multiple electrodes used for the InSe FET fabrication by FIB.^[15]

Around the time of publication of aforementioned studies, we also started investigating into the transport mechanisms of few-layered InSe (8–20 nm). The FET devices fabricated with bare InSe as the channel yielded low mobility and poor transport characteristics. The reason was attributed to the poor chemical stability of InSe layers under ambient conditions, which further intensifies as the thickness reduces to atomic scale. Shi et al.^[13] stated that a defect-free InSe will have an excellent ambient stability against O₂ and H₂O. However, when Se vacancies are present, the adsorbents of O₂ and H₂O in the air are chemisorbed at the Se vacancies, leading to the formation of In₂O₃ with insulating properties. Since Se vacancies are numerous on the surface, the oxidation starts there and propagates through the entire sheet by substituting the Se atoms from the InSe structure and forming In–O bonds.^[14,16] These morphological changes in InSe on adsorption of oxygen atoms causes serious hampering of the electronic properties with mobility and other FET parameters to decrease by several orders of magnitude.^[14] Though InSe degrades faster than MoS₂, it still has higher environmental stability than black phosphorous. It is worth mentioning that most previous reports which reported high mobility on bare InSe used thicker layers (>30 nm) and shadow masks to fabricate their devices.^[11,12,15,66] However, as InSe layer thickness approaches the quantum confinement limit, it becomes increasingly sensitive to environmental influences such as oxygen, moisture, charge traps in the dielectric and chemical contamination, leading to fast and uncontrollable morphological changes and poor device performance. Therefore, more recent

works on thinner layers of InSe demonstrated the necessity of encapsulating InSe against environmental influences to achieve high-performance and stable devices.

2.3 Encapsulation of InSe to suppress ambient degradation

The first report on the encapsulation of InSe was presented by Bandurin et al.^[52] by using the inert layers of hexagonal boron nitride (hBN). The source and drain to encapsulated InSe layers were fabricated using graphene flakes as shown in the schematic of Figure 2.13a. A field-effect mobility of $0.02 \text{ cm}^2 \text{ V}^{-1} \text{ s}^{-1}$ was obtained in these devices, attributed to high contact resistance of graphene contacts. However, a high Hall mobility of $\sim 1000 \text{ cm}^2 \text{ V}^{-1} \text{ s}^{-1}$ was achieved at room temperature, which increased further on decreasing the temperature because of reduced phonon scattering. In addition, the devices showed the quantum Hall-effect, including Shubnikov de Haas oscillations under strong magnetic fields. The mobilities of InSe reported in this work are the highest values reported for an *n*-type material so far. Though high performance was obtained, an analysis of long-term ambient stability of the devices was missing. Reliability issues could arise in these devices because hBN does not perfectly seal around the protruding graphene contact, allowing air or moisture to enter through small open pockets and initiating the degradation process that eventually penetrates into the deeper parts of the layer. Long-term stability, thus, could not be guaranteed in these stacks.

Another approach to passivate InSe is the dry oxidation technique by Ho et al.^[16], shown in Figure 2.13b. It involves exposing multilayer InSe to pure oxygen at room temperature to form a dense capping layer on top of InSe. A high two-probe mobility of $\sim 400 \text{ cm}^2 \text{ V}^{-1} \text{ s}^{-1}$ at room temperature and on/off ratio of $\sim 10^8$ were demonstrated in an FET based on a 13 nm thick InSe layer. Despite high performance of these FETs, ambient degradation could be suppressed for short timescales of only four days. With time, direct oxidation eventually perturbs the electronic structure of InSe, making the devices non-functional. Furthermore, the dry oxidation technique is only compatible with shadow-mask-defined devices and results in inferior device performance when paired with e-beam lithography.^[17]

Recently, Wells et al.^[17] demonstrated the technique of seeded atomic layer deposition (ALD) of alumina (Al_2O_3) for encapsulating InSe as shown in Figure 2.13c. The alumina encapsulated InSe FETs revealed a room temperature mobility of $8\text{--}40 \text{ cm}^2 \text{ V}^{-1} \text{ s}^{-1}$, high responsivities of 10^7 A W^{-1} and long-term stability of up to 6 months. It was found that the morphology of the deposited ALD alumina films depends sensitively on the surface preparation of InSe nanosheets. For example, ALD performed on freshly exfoliated InSe resulted in rough and discontinuous alumina films with isolated islands of $\sim 50 \text{ nm}$ diameter. Thus, to obtain uniform film growth, InSe had to undergo a chemical treatment, which is detrimental for its structural integrity and for device reproducibility.

While both techniques of dry oxidation and ALD use oxides-based encapsulation, they encapsulate only the top surface of InSe, whereas the bottom part rests on SiO_2 . The unsuitability of SiO_2 as a bottom dielectric in 2D electronics is discussed in later sections of this chapter. In short, SiO_2 deteriorates the performance of FETs by inducing charge disorder at the

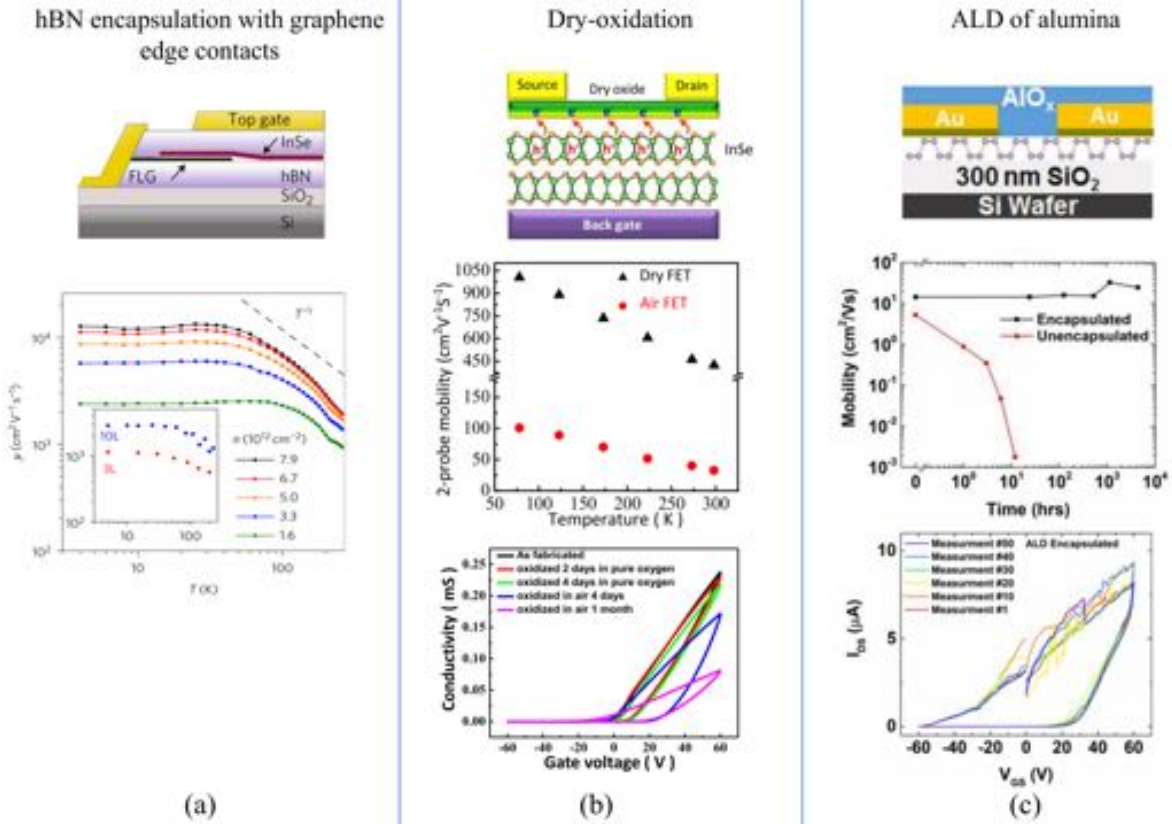


Figure 2.13: Different encapsulation techniques employed for InSe to prevent ambient degradation. (a) hBN based encapsulation with graphene contacts at the edges of the InSe flake.^[52] The devices showed high performance but long-term stability was missing, (b) encapsulation of InSe using the technique of dry oxidation.^[16] High mobility was achieved, but the devices became non-functional after few days. (c) ALD of Al₂O₃ on top of InSe to suppress environmental degradation.^[17]

interface because of scattering from charge traps, impurities, and surface roughness.^[40,67] The substantial hysteresis and unreliability in the I - V characteristics of the InSe FETs fabricated in both reports prove the existence of charge traps at SiO₂/InSe interface and hydration on SiO₂ surface.^[12] These shortcomings emphasize the importance of developing an effective approach to encapsulate InSe against ambient degradation while maintaining high performance and long-term stability of the devices.

2.4 Gallium selenide and its (opto)electronic properties

Being a member of the III–VI chalcogenide family, GaSe is a layered structure with tetra-layer arrangement in the sequence of Se–Ga–Ga–Se. It is commonly found in the β - or ϵ -phase with hexagonal lattice structure shown in Figure 2.14a,b and the unit cell parameters $a = b = 0.374$ nm and $c = 1.592$ nm. β -GaSe belongs to the space group D_{6h}^4 and has an inversion symmetry because of the stacking sequence. On the other hand, ϵ -GaSe is generated from one primitive layer by translations, is non-centrosymmetric and belongs to the space group D_{3h}^1 .^[57] Due to weak vdW forces between the planes of the crystals, few-layered structures can be easily produced by mechanical exfoliation.

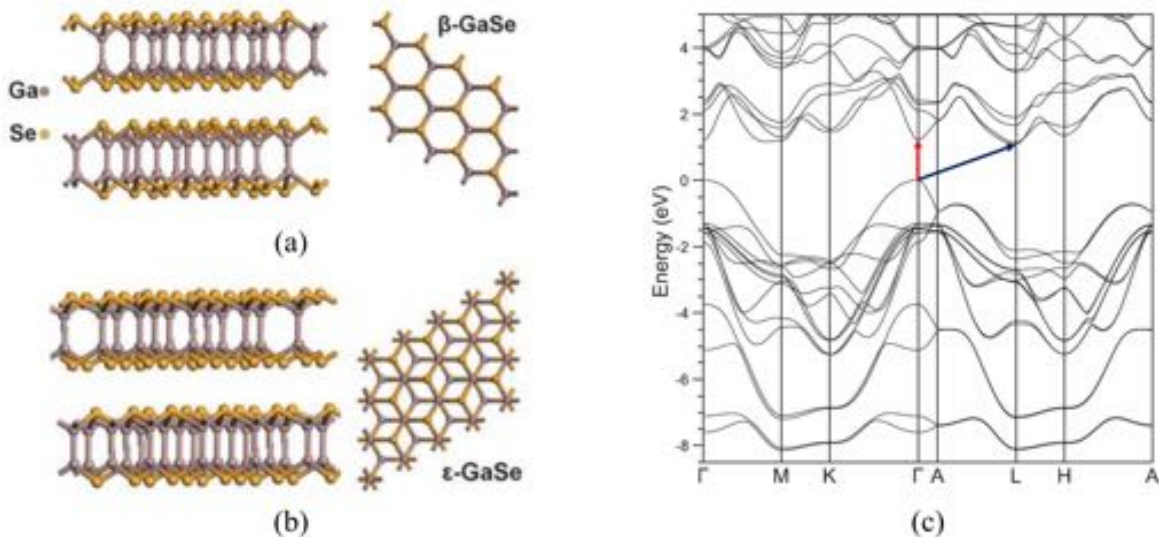


Figure 2.14: *GaSe* crystal structure and electronic band structure. (a) Side and top views of β -GaSe, (b) side and top views of ϵ -GaSe,^[57] (c) electronic band structure of bulk GaSe calculated using DFT. The red arrow shows the direct bandgap and the blue arrow shows the indirect transition.^[68]

GaSe is known to be a *p*-type material with a tunable bandgap of 2.11 eV in bulk, which increases to 3.5 eV for monolayers.^[69–71] Many reports state that GaSe has an indirect bandgap in bulk form^[72], however, theoretical studies pointed out that a direct bandgap also exists at a small energy difference of 25 meV as shown in Figure 2.14c.^[73,74] Due to this small energy difference between the direct and indirect bandgap, the photoexcited carriers can easily transfer between these two bands using thermal fluctuations.^[41,75]

GaSe is much more air-sensitive than InSe, such that a 45 nm thick GaSe layer oxidizes fully within a 30 min of time period. GaSe forms a native oxide when exposed to air, furthermore, thermal- and photo-induced oxidation has been reported as well.^[71,76] This oxidation process induces morphological and chemical changes in the structure and is highly detrimental to intrinsic optical and electronic properties. Raman spectroscopy has been frequently employed to study the oxidation dynamics of GaSe. Figure 2.15 shows the effect of oxidation on the Raman spectrum of GaSe. Freshly exfoliated pristine GaSe reveals five major Raman modes: E'' at 59.2 cm^{-1} , A_1'' at 134 and 308 cm^{-1} , $E_1''(\text{TO})$ at 214 cm^{-1} , and $E_1''(\text{LO})$ at 246 cm^{-1} .^[71,77] The Raman spectrum evolves significantly as a function of exposure time. The intensity of all features decreases rapidly and several additional Raman modes appear at frequencies of 155, 161, 257 and 282 cm^{-1} as shown in Figure 2.15. These additional modes are attributed to chemical transformation of GaSe on air and laser exposure, forming products of Ga_2Se_3 , a-Se , and $\beta\text{-Ga}_2\text{O}_3$. Given our interest in using few-layered GaSe for electronic and optoelectronic applications, it becomes essential to passivate its air-sensitive layers in order to extract its unaltered intrinsic properties.

In terms of electronic transport, bulk GaSe has been demonstrated with a mobility of $210\text{ cm}^2\text{ V}^{-1}\text{ s}^{-1}$ at room temperature, calculated using the time-of-flight technique.^[78] However, in an FET configuration when integrated as a channel, few-layered GaSe revealed much

lower mobility of $0.1\text{--}0.6 \text{ cm}^2 \text{ V}^{-1} \text{ s}^{-1}$, as shown in Figure 2.16.^[79,80] Unlike InSe, GaSe is not a high-mobility material because of the presence of heavy holes, but it is still very appealing for a variety of optical applications. Because of the absence of an inversion symmetry, GaSe is widely used in nonlinear optics.^[57] Other interesting applications include photodetectors,^[79] single-photon emitters^[55], and terahertz applications^[56].

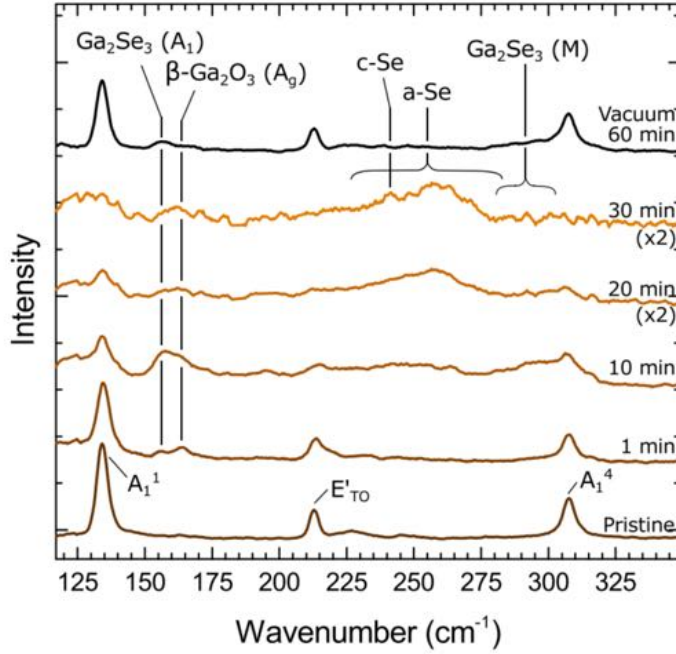


Figure 2.15: Evolution of the Raman spectrum of a 45 nm thick GaSe sample in air as a function of exposure time at 532 nm irradiation. “Pristine” refers to the sample measured in vacuum immediately after exfoliation. The topmost curve is a spectrum of the same sample obtained after 60 min of laser exposure at $6 \text{ mW } \mu\text{m}^{-2}$ in vacuum.^[71]

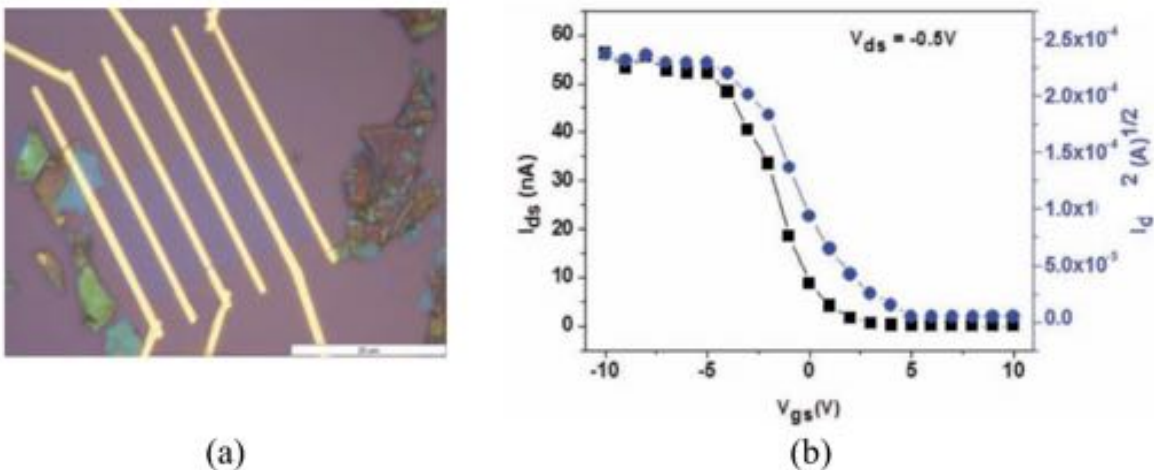


Figure 2.16: Electrical characterization of an FET based on GaSe channel. (a) Optical image of a GaSe FET, with Si as the back gate and SiO_2 as the gate dielectric, (b) transfer characteristics, i.e. gate dependence of the source-drain current (I_{ds}) at source-drain voltage (V_{ds}) of 0.5 V, revealing μ_{FE} of $0.6 \text{ cm}^2 \text{ V}^{-1} \text{ s}^{-1}$.^[80]

Many reports have demonstrated photoactive transistors based on GaSe with high responsivities in excess of 1200 A W^{-1} , indicating its potential applications in optoelectronics.^[73,79,81] Responsivity (R), similar to mobility, is an essential figure of merit to quantify the performance of a photodetector operating in the transistor mode. The responsivity is a measure of the output signal per unit watt of incident radiation. It is calculated as the ratio of the photocurrent (I_{ph}) and the optical power (P) incident on the photodetector:

$$R = \frac{I_{ph}}{P} \quad (2.3)$$

A high responsivity is an indication of a high output at a certain optical power. In early reports, a responsivity of $\sim 1.7 \text{ A W}^{-1}$ was achieved with CVD grown GaSe crystals.^[82] For photodetectors based on exfoliated few-layered GaSe, a responsivity of 2.8 A W^{-1} at zero gate bias, high quantum efficiency of 1367% and a fast response of 20 ms were achieved.^[73]

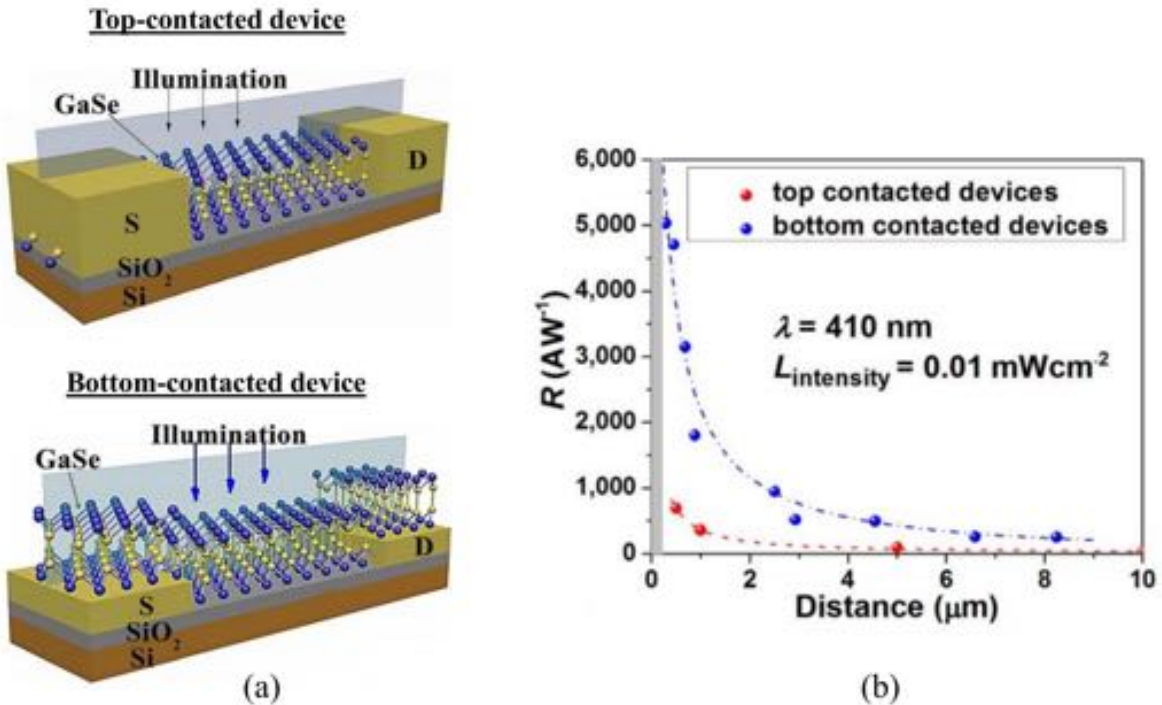


Figure 2.17: *GaSe photodetector device structure and performance characterization.* (a) Schematics of two different photodetector geometries, first with contacts on top of the GaSe layer and second with pre-patterned bottom contacts, (c) responsivity as a function of the electrode spacing distance for top contacted (red) and bottom contacted (blue) photodetectors. The latter shows much higher responsivity.^[75]

A strong enhancement in the responsivity is later realized by contact engineering and device geometry optimization.^[75] For example, by shrinking the electrode spacing distance (before tunneling begins), the responsivity is found to increase monotonically. Further enhancement is achieved by using pre-patterned bottom contacts (metal contacts deposited on Si substrate before GaSe transfer) as opposed to the conventional top contact geometry, as shown in Figure 2.17a. A high responsivity of up to 5000 A W^{-1} is achieved by using pre-patterned Au contacts at a reduced electrode spacing (Figure 2.17b). This major improvement in

bottom contacted devices is attributed to the generation of photo-excited charge carriers in the channel as well as in the material lying on top of the metal contacts. The charge carriers generated in this area travel only the vertical distance to get collected by the electrodes, unlike planar transported carriers generated in the channel area, which are likely to recombine before getting collected. Thus, bottom contacted device geometry generates more photocurrent, leading to higher responsivity.

2.4.1 Encapsulation of GaSe against ambient degradation

Encapsulation of GaSe is more challenging than that of InSe, as it is not compatible with the techniques of dry-oxidation and ALD of alumina, which have been successfully demonstrated for InSe previously. Thus, developing an encapsulation technique for GaSe is a demanding process. To the best of our knowledge, only one report has addressed the degradation of GaSe so far. In this report by Zhao et al.,^[81] the top surface of GaSe was encapsulated by hBN, while the bottom surface rested on SiO₂ dielectric, as shown in Figure 2.18a. Electrical connections to the GaSe channel were achieved by fabricating pre-patterned bottom Au contacts. These partially encapsulated devices revealed long-term stability (Figure 2.18b), however, the performance remained inferior to previously reported GaSe photodetectors.

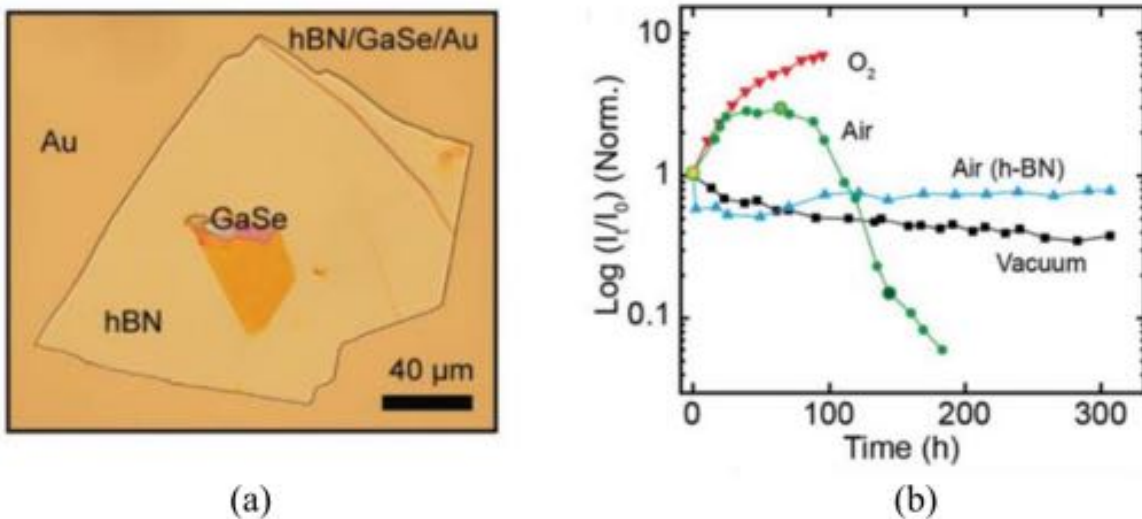


Figure 2.18: Optoelectronic performance of partially hBN encapsulated GaSe photodetectors. (a) Microscopic image of a GaSe flake deposited onto Au and then covered by a hBN flake, (b) evolution of normalized photocurrent versus time for GaSe photodetectors in the dry-oxygen (red), air (green), and vacuum (black) atmosphere. The blue curve represents the top-encapsulated GaSe photodetector measured in air and shows a stable performance for a prolonged period of time.^[81]

The electronic transport in InSe and GaSe is quite sensitive to the local environment and can be significantly enhanced by optimizing contacts, bottom substrate and top encapsulation. hBN as a bottom substrate and as a top encapsulation has been frequently employed for several 2D vdW semiconductors. The very first report on using hBN as a bottom gate dielectric for graphene was published by Dean et al.^[40] These hBN/graphene FETs revealed a mobility of 60,000 cm² V⁻¹ s⁻¹, three times larger than the carrier mobility of SiO₂/graphene

devices. Advancing on this idea, Mayorov et al.^[83] sandwiched graphene between top and bottom hBN layers, enabling a record mobility of $\sim 2.5 \times 10^5 \text{ cm}^2 \text{ V}^{-1} \text{ s}^{-1}$ at room temperature. On encapsulating few-layer MoS₂ in hBN layers, a low-temperature mobility exceeding $10^4 \text{ cm}^2 \text{ V}^{-1} \text{ s}^{-1}$ and a room-temperature mobility of $\sim 100 \text{ cm}^2 \text{ V}^{-1} \text{ s}^{-1}$ (limited by optical phonons) were achieved.^[84]

3 2D dielectric: hexagonal boron nitride

Boron nitride (BN) can be found in different forms, such as cubic, wurtzite, hexagonal, and amorphous, however, the most stable crystalline form of BN is the hexagonal. Hexagonal boron nitride or hBN has emerged as a valuable material in 2D electronics. It is also known as “white graphene” because of its white appearance and structural similarity to graphene.^[85] The structure of hBN is obtained by replacing the carbon atoms at the *K* and *K'* positions in graphene with boron and nitrogen atoms.^[86] Figure 2.19 shows alternatively arranged boron and nitrogen atoms in a hexagonal lattice of hBN. Within a layer, boron and nitrogen atoms are bonded via strong σ bonds, while adjacent layers are held by weak vdW forces. Therefore, hBN is also a vdW layered material and can be exfoliated into thin layers from its bulk crystal. The lattice constant of hBN is 2.5 Å, which is 1.8% larger than that of graphene.^[87,88] The interlayer spacing in hBN is 0.333 nm, slightly less than that of graphene (0.335 nm). While graphene is a semi-metal with zero bandgap, hBN is a wide bandgap insulator (~ 5.7 eV), resulting from the strong electronegativity difference between boron and nitrogen atoms.^[89,90]

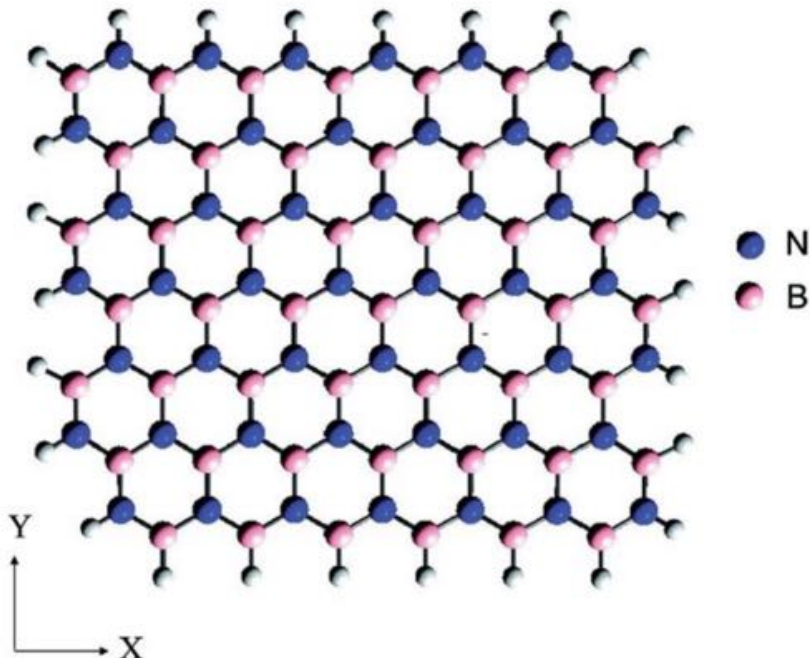


Figure 2.19: Schematic of the hexagonal structure of hBN monolayer. Blue spheres represent nitrogen, pink spheres boron atoms.^[85]

Because of the intrinsically flat and defect-free surface of hBN, it can be combined with other 2D materials to form vdW heterostructures. hBN itself does not participate in electronic transport because of its insulating nature, rather it is used as a substrate dielectric and/or an encapsulant for 2D semiconducting layers. Though SiO_2 is a popular choice of dielectric in CMOS technology, hBN has evolved as a better dielectric material in 2D electronics owing to its superior properties as listed below.

- **Dielectric properties:** hBN is an insulator with a bandgap of ~ 5.7 eV, a dielectric constant (ϵ) of 3.5, and a breakdown voltage of ~ 0.7 V nm $^{-1}$.^[40,90]
- **Low charge trap and defect density:** In 2D electronics, the requirement of low defect density is more stringent than traditional in CMOS devices. High amount of defect density and charge traps leads to unreliability in electronic transport and underestimation of electronic properties (detailed discussion in chapter 4). Even in high-quality SiO_2 , a significant amount of defect density could be present, inducing charge disorder at the insulator/semiconductor interface and hampering the electronic properties of the device.^[12,91,92] Therefore, SiO_2 is typically not favorable as a substrate for investigating the intrinsic properties of 2D materials. On the other hand, because of strong, in-plane, ionic bonding between boron and nitrogen atoms, hBN is inert and free from dangling bonds and surface charge traps.^[40] High-quality crystalline hBN has very low concentration of the defect density (few orders less than those in SiO_2). This eliminates the charge trap states at the interface of the semiconductor and the dielectric, leading to a more accurate estimation of the intrinsic properties of the semiconductor. This is one of the reasons that the mobility of graphene on hBN is found to be $60,000$ cm 2 V $^{-1}$ s $^{-1}$, three times higher than that on SiO_2/Si substrate.^[40]
- **Atomically flat surfaces:** Unlike SiO_2 where atoms are chemically bonded in a 3D network, hBN consists of atomically thin 2D sheets held together by vdW forces. Because the vdW forces are much weaker than the interatomic forces, each sheet of hBN is isolated from perturbations from adjacent layers. This results in an atomically flat surface of hBN, making it an ideal substrate for nanosheets of 2D semiconductors. The flatness of hBN helps suppressing the thermodynamic ripples in 2D materials. For example, the roughness of graphene on hBN (~ 70 pm) has found to be three times less than that on SiO_2 (~ 185 pm).^[40,93]
- **Chemical and thermal inertness:** Depending on the application, a substrate might be exposed to high temperatures or extreme conditions, where it is expected to be chemically and thermodynamically stable. Owing to its high thermal conductivity of ~ 400 W m $^{-1}$ K $^{-1}$ and low thermal expansion coefficient of 2.6×10^{-4} K $^{-1}$, hBN is quite stable over a wide temperature range.^[88] The chemical inertness of hBN is especially beneficial for air-sensitive materials in order to passivate them from the environment for a prolonged period of time. In addition, hBN is oxidation and corrosion resistant.^[88,94]

- The optical phonons in hBN are twice higher in energy than those in SiO₂, which opens ways to high-temperature and high-electric-field devices using hBN as dielectric.^[89]

Because of the above stated properties, hBN is one of the most widely used substrate for fabricating 2D (opto)electronic devices. hBN encapsulation has also proved its worth by enabling devices of high quality that do not deteriorate under ambient conditions. In optoelectronics, the large bandgap of hBN is advantageous, as it does not interfere with the performance of the devices. However, to fabricate stacks from diverse 2D materials, heterostructure assembly techniques are required. Thanks to the vdW nature of 2D materials, different 2D layers can be easily combined to form vdW heterostructures for the realization of new technologies.

4 Van der Waals heterostructures

A major advancement in the field of 2D materials came with the possibility of stacking multiple layers on top of each other, giving rise to the area of 2D vdW heterostructures. These vdW heterostructures provide intriguing possibilities for controlling and manipulating the individual properties of participating 2D layers to facilitate the design of unique devices. The basic principle involves stacking mono- or few-layers of one 2D material on top of another, which is then stamped onto another, and so on. The resulting stack is equivalent to an artificial material assembled in a desired sequence, similar as building with Lego blocks (Figure 2.20). The strong covalent bonds within the layer provide in-plane stability, whereas relatively weak vdW-like forces keep the stack together.^[95] These vdW heterostructures with diverse 2D layers are expected to show novel properties with unprecedented characteristics and unique functionalities. From an application point of view, they can be exploited in emerging designs of electronic devices, including tunneling transistors and flexible electronics, as well as in optoelectronic devices, including photodetectors, photovoltaics, and light-emitting devices.

Experimentally, vdW heterostructures can be obtained by either growing nanosheets of different materials epitaxially or by manually stacking different exfoliated layers on top of each other. Bottom-up synthesis of different layers grown directly on top of each other using CVD of graphene, hBN, and TMDCs has been demonstrated as well.^[96–98] However, due to the complexity of the process, only a few selective heterostructures can be produced epitaxially. Manual assembly, on the other hand, offers a large degree of flexibility to mix and match different 2D layers. Because of its high throughput and many possibilities of stacking sequences, it is the most used approach for fabricating vdW stacks.

A stacking procedure typically starts by isolating few layers of a 2D crystal on top of a thin transparent film (usually a polymer film) acting as a transfer medium. The isolated 2D layer is put face down onto another 2D layer resting on a chosen substrate. Similarly, subsequent layers are stamped on top of the previous layer and the transfer is repeated until a desired stack is assembled. Conceptually, the method is simple, but to master it experimentally takes months of practice and experience. To align multiple layers with micrometer precision, an experimental setup called micromanipulator is required.

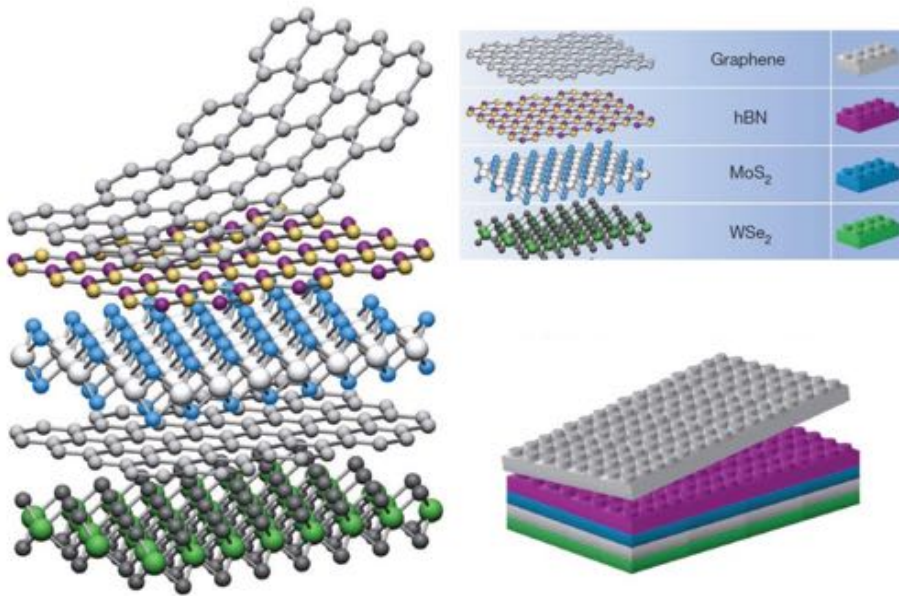


Figure 2.20: Principle of building vdW heterostructures. One can visualize 2D layers to be analogous to Lego blocks (right side). A huge variety of layered structures can be constructed by stacking different layers on top of each other.^[43]

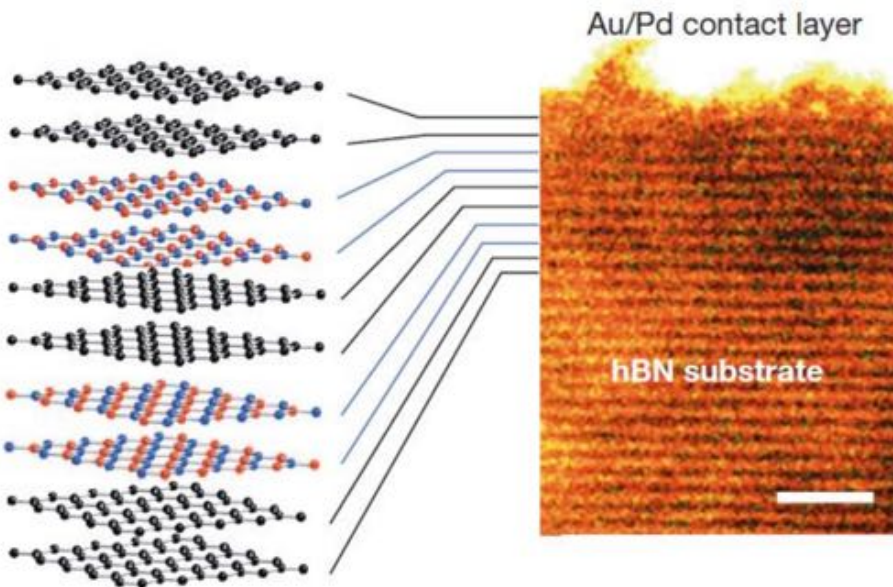


Figure 2.21: High-resolution cross-sectional scanning transmission electron microscopy image of a graphene/hBN superlattice, consisting of six stacked bilayers (right) and a corresponding schematic representation (left). Scale bar: 2 nm.^[99]

A detailed description of the micromanipulator installed in our lab and various transfer methods used in this project for fabricating vdW heterostructures is provided in chapter 3. Using these transfer methods, we produced several heterostructures, which otherwise would have been impossible to realize by bottom-up techniques. It is conceivable that by using vdW stacking, air-sensitive materials (such as, InSe and GaSe) could be encapsulated in inert hBN layers, which has been one of the main focuses of this work and is discussed in

detail in chapter 4. The micromanipulator not only facilitates position accuracy, but also crystallographic alignment. Two layers can be twisted at certain angles relative to each other to obtain interesting properties, such as Moiré patterns. An important challenge in vdW fabrication is to keep the interfaces as clean as possible without any contamination from the environment. Figure 2.21 shows a vdW superlattice assembled in air from six alternating bilayers of graphene and hBN.^[43,99] The vdW stack shows that complex heterostructures with sharp and clean interfaces can be fabricated manually. To keep the contamination to the lowest, the vdW stacking can be performed inside an argon or nitrogen-filled glovebox. Further advances to perform full vdW heterostructure fabrication inside a vacuum chamber is also an upcoming technique.

5 Metal-organic frameworks

Metal-organic frameworks (commonly denoted as MOFs) have attracted considerable attention in recent years, owing to their highly-tailorable properties and potential applications in (opto)electronics. MOFs represent a class of hybrid materials consisting of metal ions or clusters in coordination bond with organic linkers. One of the main advantages of MOFs over conventional inorganic 2D materials is their structural tunability, which makes it possible to tailor their intrinsic properties while retaining a particular framework topology. This versatility of MOFs can be visualized similar to vdW heterostructure assembly of 2D materials. By appropriately choosing the 2D layer sequence, new functionalities can be achieved in a vdW stack, similarly, by tuning the components of a MOF structure, novel properties can be obtained. This high degree of synthetic flexibility of MOFs allows fine tuning of their intrinsic properties, allowing a wide range of applications in the areas of electronics, optics, sensing, and magnetic devices.

5.1 Structure

Figure 2.22 shows the simplest schematic representation of a MOF structure, where metals are connected via organic linkers in a cubic arrangement. The empty space created inside the cube is called “pore” and is one of the key features of the MOF structure producing up to 90% of free volume.^[100–102] Depending on the constituents, the pore sizes are tunable ranging from less than 1 nm up to 10 nm.^[103]

A coordination network or framework is formed when MOF unit cells are repeated in space, generating crystalline structures with long-range order.^[104] Due to the crystallinity of MOFs, well-defined pore systems are present throughout the material, enabling better reproducibility and uniformity of the properties as compared to organic and amorphous materials. A well-known MOF structure is MOF-5, prepared by reacting Zn-metal centers with carboxylate ligands as shown in Figure 2.23.^[105,106] The unit cell of MOF-5 shows a cubic arrangement which bonds in all directions to form a 3D framework. The yellow sphere represents the microporous cavity.

Though most MOFs are bulk materials, i.e. 3D frameworks, recently, efforts have been made to synthesize their low-dimensional forms. Depending on the coordination geometry of their

building blocks, 1D, 2D and 3D MOF structures can be synthesized. The schematics of different dimensionalities of MOFs are shown in Figure 2.24. A chain-like 1D MOF structure is produced when the constituents bond along one direction. A 2D MOF has bonding along two directions which results in a sheet or a monolayer of MOF. Similar to inorganic 2D materials, superimposition of 2D layers via vdW interactions in a preferred stacking pattern leads to a multilayer MOF structure. A 3D MOF, as shown earlier, is formed when the constituents bond in all directions, which produces bulk material rather than single sheets or chains.

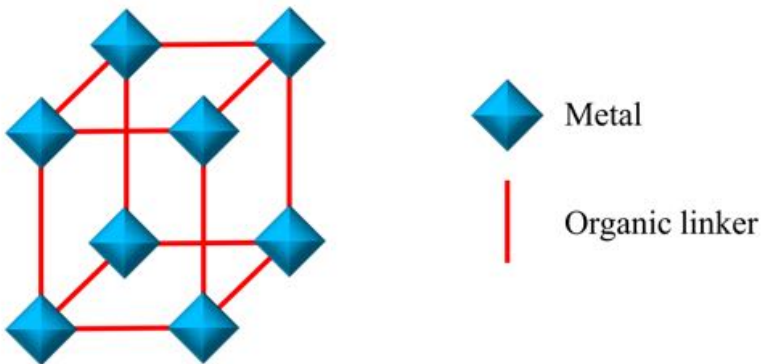


Figure 2.22: Schematic of a MOF unit cell where metal ions are connected via organic linkers.

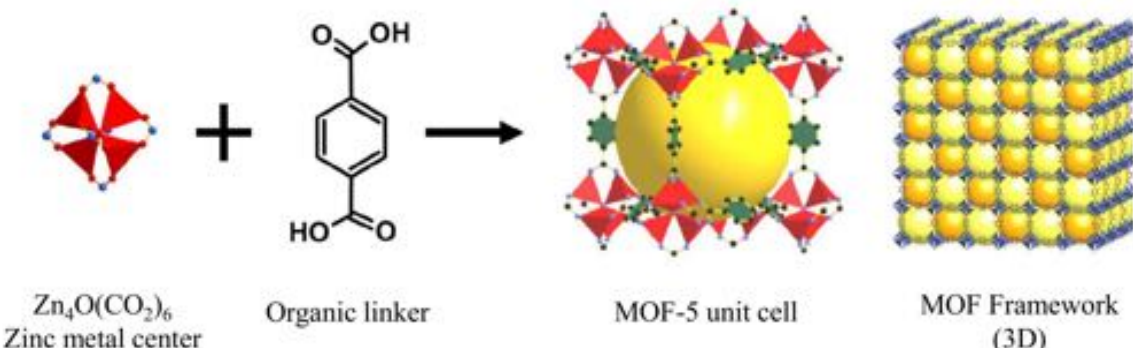


Figure 2.23: Reaction schematic for the synthesis of MOF-5 from its constituents. The unit cell when repeated in all three dimensions forms a 3D framework.^[106]

In addition to multiple dimensionalities, MOFs are well-known for their synthetic tunability, i.e. by combining different metal ions and organic linkers, a variety of MOFs can be produced. The selection of metal centers is limited by the periodic table, whereas ligands with various chemical formulae, oxidation, and spin states are easily available. Interestingly, more than 20,000 different MOFs, depending on the constituents' geometry, size, and dimensionality, have been reported so far, while theoretical studies predict more.^[107] Such extraordinary degree of synthetic versatility allows fine tuning of their intrinsic properties as desired.

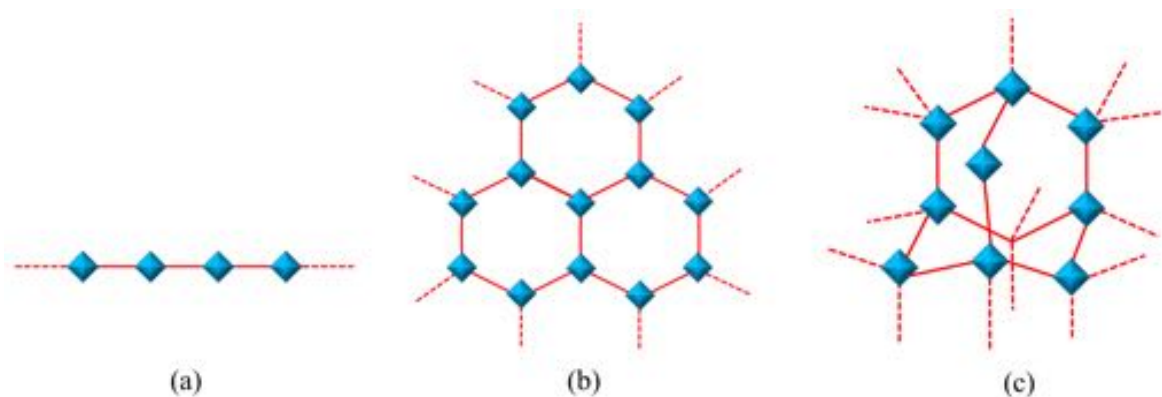


Figure 2.24: Schematics of different dimensionalities of MOF structures. Bonding between the metal and organic linker in (a) 1D MOF, (b) 2D MOF, and (c) 3D MOF structure.

5.2 Properties and applications

Presence of voids and empty volume yield large and permanent porosity (up to 90% of free volume) in MOF structures.^[100–102] This ultrahigh porosity and the large internal surface areas extending beyond $7000 \text{ m}^2 \text{ g}^{-1}$,^[101] have enabled MOFs prominently for applications in gas storage and separations.^[108,109] Other applications include drug delivery^[110,111] and catalysis,^[112,113] owing to their diverse metallic centers acting as a catalytically active site. Several studies also demonstrated MOFs as a potential candidate to store fuels of H_2 and CH_4 , while advances have been made to use them for CO_2 capture for clean energy and environmental protection. Though early reports on MOFs discussed their properties and applications as gas vessels, the focus has gradually shifted towards their integration into electronics. The synthetic flexibility allows fine tuning of their intrinsic electrical, optical and mechanical properties while maintaining high-crystalline order. This has enabled a wide range of applications in the areas of electronics, photonics, magnetics, low- κ dielectrics, proton- and ion-conduction, luminescence, and nonlinear optics, as shown in Figure 2.25a. Their integration into electronics and related applications as an integral element gained interest only recently, as evident from the evolution of publications over past years (Figure 2.25b). This work focuses only on the semiconducting properties of 2D MOFs and their implementation as an active element into (opto)electronics. With “active element”, it is meant that the MOF layer is the main conducting channel, controlling the flow of charge carriers through the circuit. In the next sections, the discussion will be only from the perspective of semiconducting properties of MOFs and the aspects for their utilization into functional devices will be considered.

5.3 Semiconducting MOFs for (opto)electronic applications

Due to the presence of both rigid metal ions and flexible organic ligands, MOFs have a number of interesting properties. They are crystalline solids with long-range order and are highly stable and robust under ambient conditions. Some MOFs have also demonstrated high thermal stability up to 500–600 °C, which is challenging to achieve in general.^[115,116]

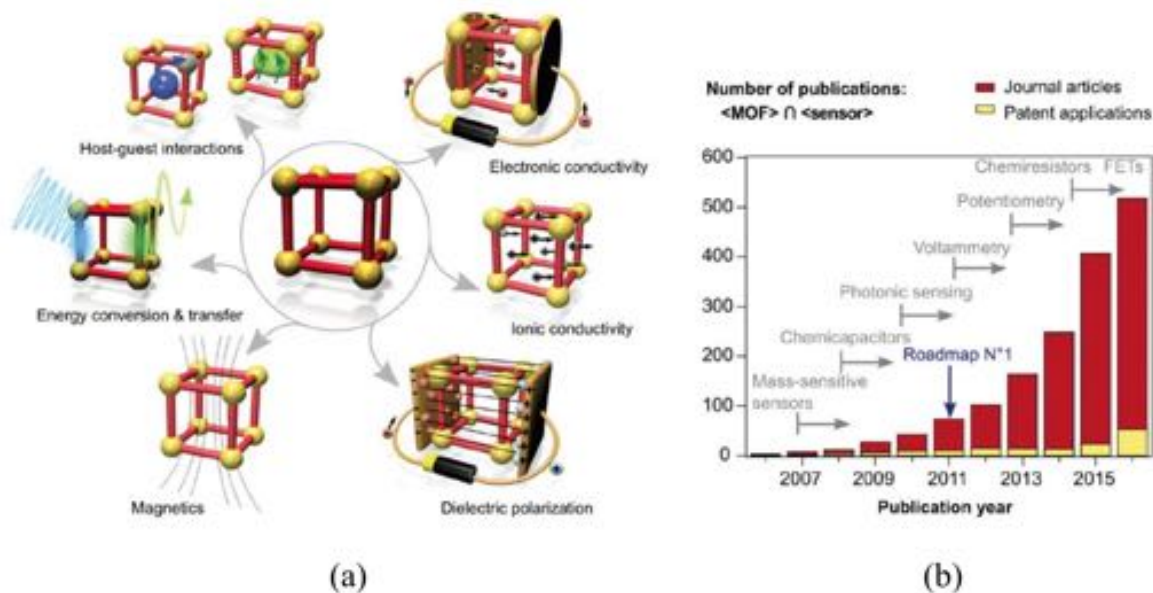


Figure 2.25: (a) Graphical representation of properties of MOFs and their applications. Some key properties of MOFs that may lead to applications in electronic devices, (b) the roadmap for the progress and integration of MOFs into devices and their evolution into yearly publications.^[114]

All these properties combined with an appropriate bandgap would yield a near-ideal material for various applications in electronics and optoelectronics. On the contrary, their utilization in applications requiring long-range charge transport has been very limited compared to their applications as porous materials. One of the main reasons for this setback is their insulating nature ($E_g > 3.5$ eV), arising from the presence of redox-inactive organic groups and small π -orbital conjugation.

It was only in 2012 when the first electrically conductive 2D MOF was synthesized by introducing the ligands with delocalized π -bonds, thereby, triggering its semiconducting properties.^[117] A room-temperature conductivity of 0.1 S cm^{-1} was reported. Later Sun et al.^[118] reported a novel approach in which the oxygen atoms in metal-oxygen chains of the existing MOFs were replaced isomorphically with sulfur atoms, giving rise to infinite metal-sulfur chains and providing electrical conduction paths. Followed by the development of electrically conductive MOFs, Talin et al.^[119] demonstrated that the electrical conductivity of $\text{Cu}_3(\text{BTC})_2$ (BTC: benzene-1,3,5-tricarboxylic acid) MOF films can be tuned by infiltrating redox-active conjugated 7,7,8,8-tetracyanoquinodimethane (TCNQ) molecule into the nanopores. To date, 2D MOFs with electrical conductivity as high as 1580 S cm^{-1} have been reported, the majority of which are Cu-, Ni- and Fe-based. Such drastic improvement within a short time span indicates the rapid progress in the field of MOF materials in terms of synthesis, characterization, and application.^[120-122]

5.3.1 Charge transport mechanisms

A material with high electrical conductivity (σ) as well as high charge carrier mobility (μ) is desirable for its successful implementation into electronic devices. While mobility is an

intrinsic property of the material, conductivity is a function of both mobility and charge carrier density (N) as per Drude's law:

$$\sigma = eN\mu \quad (2.4)$$

where e is the electronic charge.

Charge carrier density represents the loosely bound charge carriers per unit volume participating in the conduction mechanism. In an intrinsic semiconductor at finite temperatures, thermal agitation results in continuous excitation of electrons from the valence band to the conduction band, leaving an equal number of holes behind in the valence band. This process accounts for the charge carrier density in the material and is determined by an activation energy (E_a). Since it is a thermally activated process, charge carrier density increases exponentially with temperature as per the following relation:

$$N(T) = N_0 \exp\left(\frac{-E_a}{kT}\right) \quad (2.5)$$

where N_0 is the prefactor, k is the Boltzmann constant, T is the absolute temperature and E_a is the activation energy of the free charge carrier generation.

In an intrinsic semiconductor, the Fermi-level lies close to the center of the bandgap and thermal transitions occur across the bandgap. In this case, the activation energy is $E_g/2$, where E_g is bandgap of the material. Thus, for a high charge density, a narrow bandgap is preferred, which can be engineered in MOF structures. By increasing the conjugation of the linkers, the highest occupied molecular orbital (HOMO) can be raised in energy, which will reduce the bandgap. Selecting appropriate metal centers with unoccupied d -orbitals below the lowest unoccupied molecular orbital (LUMO) of the organic linker will also decrease the bandgap. Further control of the bandgap can be attained by modifying the organic linker with various functional groups ($-\text{NH}_2$, $-\text{OH}$, $-\text{CH}_3$, $-\text{Cl}$), which may donate $2p$ electrons to the linker, resulting in a band shift.^[123,124]

Charge carrier mobility (μ) is an intrinsic property of a material and gives a measure of the efficiency of charge transport. In hopping transport^a, mobility is proportional to hopping probability (P_H), which in turn is dependent on spatial distance (D) and energy difference (E) between neighboring hopping sites.^[125,126]

$$\mu \propto P_H = \exp\left(-\alpha D - \frac{E}{kT}\right) \quad (2.6)$$

where α is a constant that depends on the nature of hopping, k is the Boltzmann constant and T is the absolute temperature.

^a **Hopping-type charge transport:** As the name suggests, this conduction mechanism involves hopping of the charge carriers from one state to another. The charge carriers (electrons and/or holes) are localized at specific sites with discrete energy levels and conduct only by hopping between neighboring sites. A thermal barrier must be overcome for their motion, making hopping-type charge transport a thermally activated process. Disordered materials (e.g. organic semiconductors) predominantly exhibit this transport mechanism, which results in poor mobility and low charge carrier density. Due to incoherent motion of charge carriers, properties like mobility and conductivity become anisotropic.

In a band-like transport^b, mobility is governed by effective mass (m^*) of the charge carriers and mean-free time between two scattering events (τ) as:

$$\mu = \frac{e\tau}{m^*} \quad (2.7)$$

Equation 2.7 shows clearly that for achieving high mobility, τ should be increased. τ is the mean time between two successive scattering events of the charge carriers with scattering centers which could be disorder, defects, impurities, vacancies, and grain boundaries. Thus, a high τ can be achieved in an ordered crystalline material with low density of these charge scattering sites. Smaller m^* will also enhance the mobility, which is fundamentally related to the band dispersion. In MOFs, by appropriately choosing the metal ions and organic linkers, their electronic coupling can be increased, making the band dispersion larger and m^* smaller. Large band dispersion energetically favors delocalized charge carriers, making electron-electron repulsion insignificant and giving rise to band-like charge transport.^[114,125] Band-like transport is, therefore, usually associated with higher mobility and consequently, higher conductivity than the hopping mechanism. Thus, achieving band-like charge transport is the ultimate goal when designing new electrically conductive MOFs for device applications.

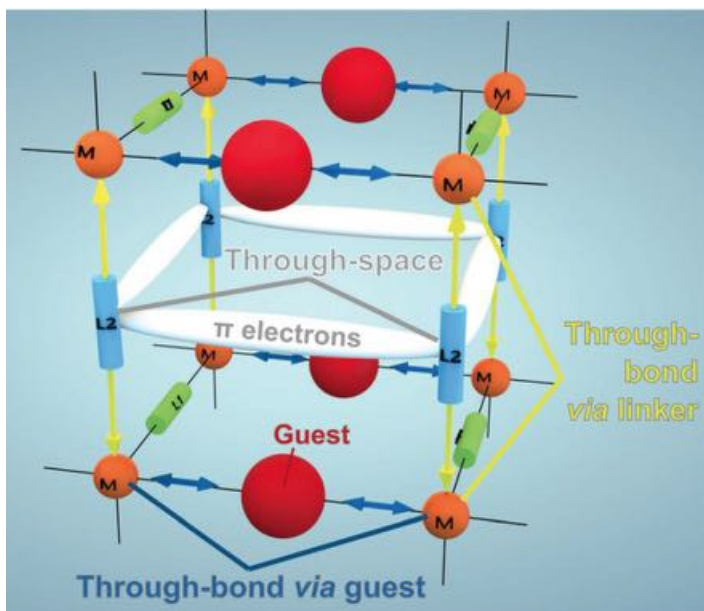


Figure 2.26: Schematic illustrations of charge transport routes in MOFs. Three possible mechanisms have been observed in MOFs for charge transport: through-bond conduction via metal nodes and linkers, through-space conduction via charge delocalization through adjacent aromatic linkers, and through-guest molecules conduction via guests that function as bridging units.^[114]

Nevertheless, both hopping and band transport mechanisms require charge transport pathways. In a MOF structure, there are three possible conduction pathways: (a) through-bond

^b **Band-like charge transport:** This transport mechanism occurs when charge carriers move coherently via fully delocalized electronic states. Unlike hopping transport, temperature destroys the band transport because of various scattering phenomena (phonons and impurities). Therefore, this transport mechanism is favored at lower temperatures where phonons die out.

conduction, (b) through-space conduction, and (c) through-guest molecules, as illustrated in the schematic in Figure 2.26.^[114] In “through-bond” conduction, charges move through the continuous chains of covalent and coordination bonds in the MOF material. This mechanism is found in graphene-like MOF analogues that exhibit extended π -conjugation. “Through-space” conduction occurs via charge delocalization through adjacent aromatic linkers. When interplanar linker separation is small (few Å), inter-linker charge transfer is enabled. The charge transport through guest molecules occurs when a guest molecule is infiltrated into the pores that bounds strongly to the framework. An example has been discussed before, with TCNQ incorporation into Cu₃(BTC)₂ MOF films, leading to an enhanced conductivity.

5.3.2 Role of MOF morphology in charge transport mechanisms

A key factor for accurately measuring the electronic properties of MOF samples is the physical form or morphology in which the MOF sample is measured. MOFs are commonly produced as pressed pellets, polycrystalline films, single-domain films, and single crystals, which may all be used as samples, but naturally give different values of the intrinsic properties. Pressed pellets is the most measured form of MOFs, obtained by compressing the powder under high pressure. Despite easy handling, pressed pellets suffer from serious drawbacks, such as high number of grain boundaries, variation of grain sizes because of variation in applied pressure, and random orientation of crystallites within the pellet, giving rise to anisotropic charge transport.^[125] These drawbacks result in high density of defects especially grain boundaries and thus, underestimation of intrinsic properties of conductivity and mobility. In this regard, a polycrystalline film provides more reliable evaluation of electrical properties. Films have been demonstrated with higher conductivity as compared to pellets because of their denser structures.^[125]

Chapter 3

Van der Waals heterostructures and their fabrication

In this chapter, the techniques of fabricating vdW heterostructures from different 2D materials on a variety of substrates are discussed. The fabricated heterostructures are employed for charge transport studies in the presence of electric fields and under illumination, time-resolved micro-PL, low-temperature PL, and transmission electron microscopy (TEM) investigations. The bulk crystals of InSe and GaSe are bought commercially from *2dSemiconductors* and *hq graphene*, respectively. The bulk crystals of hBN are provided by our collaborators Dr. Kenji Watanabe and Dr. Takashi Taniguchi from the National Institute for Materials Science, Japan. The vdW heterostructures are produced using the micromanipulator setup bought from *Graphene Industries*.

The vdW heterostructures discussed in the next chapters are fabricated by myself. During my research stay at the group of Prof. James Hone at Columbia University (New York, USA), I learned the intricate processes of vdW heterostructure assembly. To deal with air-sensitive materials of InSe and GaSe, the heterostructure fabrication process was further optimized to be performed inside a glovebox. Some of the transfer techniques discussed in this chapter have been mastered during my training with the experts from the University of Manchester. Acquiring these skills from the top-notch experts in the field of 2D materials helped us to set up our own lab fully dedicated to electrical characterization of 2D materials and their heterostructures at Technische Universität Dresden.

The results discussed in this chapter are published as:

1. T. Venanzi, **H. Arora**, S. Winnerl, A. Pashkin, P. Chava, A. Patanè, Z. D. Kovalyuk, Z. R. Kudrynskyi, K. Watanabe, T. Taniguchi, A. Erbe, M. Helm, and H. Schneider, “Photoluminescence dynamics in few-layer InSe”, *Physical Review Materials* **4**, 044001 (2020).
2. F. Kern, M. Linck, D. Wolf, N. Alem, **H. Arora**, S. Gemming, A. Erbe, A. Zettl, B. Büchner, and A. Lubk, “Autocorrected off-axis holography of two-dimensional materials”, *Physical Review Research* **2**, 043360 (2020).

3. T. Venanzi, **H. Arora**, A. Erbe, A. Pashkin, S. Winnerl, M. Helm, and H. Schneider, “Exciton localization in MoSe₂ monolayers induced by adsorbed gas molecules”, Applied Physics Letters **114**, 172106 (2019).
4. F. Kern, M. Linck, D. Wolf, T. Niermann, **H. Arora**, N. Alem, A. Erbe, S. Gemming, and A. Lubk, “Direct Correction of Residual Symmetric Aberrations in Electron Holograms of Weak Phase Objects”, Microscopy and Microanalysis **25**, 98–99 (2019).

1 Exfoliation of 2D layers and their transfer

1.1 Mechanical exfoliation

Obtaining high-quality nanosheets of a 2D material is an essential step in fabricating high-performance devices. Mono- and few-layers of 2D materials can be obtained by both top-down exfoliation of bulk materials (mechanical and liquid-phase exfoliation) and bottom-up synthesis from precursors using CVD, solvothermal process etc.^[127]

Of all the techniques, mechanical exfoliation or micromechanical cleavage is by far the most used technique to produce 2D layers. It is done by repetitively peeling of the bulk crystal with the help of an adhesive tape until thin layers are obtained. This simple and efficient technique was the one which led to the isolation of graphene in 2004 and later on many other 2D materials, such as MoS₂, hBN, and black phosphorus etc. Unlike other techniques, it is considerably less destructive, produces high-quality layers, yields large monolayers of $\sim 20\text{ }\mu\text{m}$ in size, and is a low-cost method with minimal investments.

In this work, the majority of 2D layers are obtained by mechanical exfoliation of their bulk single crystals, unless stated otherwise. Figure 3.1 elaborates the process of mechanical exfoliation to obtain 2D layers of InSe from its bulk crystal. The adhesive tapes with low organic contamination (model: BT-50E-FR and BT-130E-SL) are bought from *TELTEC GmbH*. The bulk crystal of InSe shown in Figure 3.1a is placed on the blue tape (preferably model BT-50E-FR) and peeled off slowly. This transfers some parts of the crystal onto the tape as shown in Figure 3.1b. Next, the tape containing the bulk is repetitively stripped to obtain thin layers of the material (Figure 3.1c). Finally, the tape containing the thin flakes is adhered to an intermediate transfer polymer or directly onto a substrate, e.g. a highly doped Si chip with 285 nm thick SiO₂ layer, as shown in Figure 3.1d.

Mechanical exfoliation produces flakes with lateral dimensions up to few μm and varying thicknesses from less than 1 nm to μm -thick sheets. The thickness of the 2D layer can be verified by atomic force microscopy (AFM), Raman spectroscopy, and optical microscopy. AFM captures the topography and the monatomic steps in the samples at atomic resolution by tip-sample interaction. The probe tip remains in constant physical contact with the sample surface and records a vertical deflection of the cantilever. While AFM is a reliable technique and provides thickness estimation with high accuracy, it is time consuming and unsuitable when thicknesses are measured over large area and on a frequent basis. In addition, AFM measurements are adversely affected in the presence of an absorbed water layer or other

contaminants on the 2D layer surface. Raman spectroscopy, on the other hand, is relatively fast and relies on inelastic scattering of light from phonons to characterize the thickness and number of layers in the 2D flake. Raman spectroscopy is employed frequently for graphene and MoS₂ to identify mono-, bi- and tri-layer systems from the rest. However, for InSe and GaSe, Raman spectroscopy is not a helpful technique as the spectrum hardly changes with the number of layers.^[128] In such scenarios, optical microscopy is advantageous as it provides a fast, efficient and non-destructive thickness identification of the 2D layer. This method depends on the optical contrast between the 2D layer and the underlying substrate, and hence, the thickness is estimated within a range rather than a precise value.

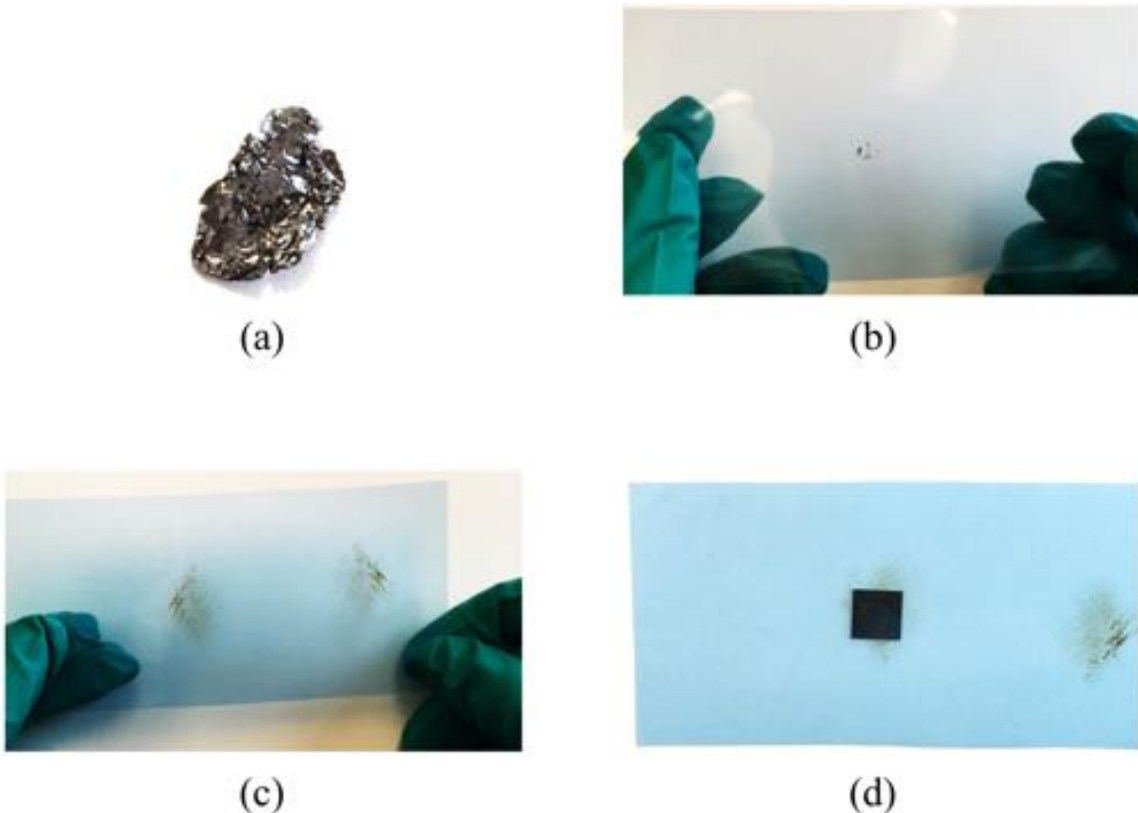


Figure 3.1: Mechanical exfoliation of the bulk crystal of InSe to obtain 2D layers. (a) InSe bulk crystal, (b) flakes on the blue tape after peeling off from the bulk crystal, (c) repetitive peeling to obtain thin layers of InSe, (d) blue tape in contact with the SiO₂/Si substrate for transferring the flakes.

In this work, thickness identification of few layers of InSe and GaSe is performed by the means of optical microscopy (*Olympus BX51*) and AFM (*Bruker*) attached with a MultiMode 8 scanning probe microscope. A good contrast and visibility of the exfoliated layers depend on the incident illumination wavelength and the underlying substrate. Highly doped Si substrate with 285–300 nm thick SiO₂ is chosen as the bottom substrate throughout the project. This thickness of SiO₂ produces a strong contrast for the 2D layers of InSe, GaSe, and hBN under white light illumination. Figure 3.2a shows an InSe flake on 285 nm SiO₂/Si substrate, revealing different color contrasts corresponding to different layer numbers as indicated on the image. As the thickness of InSe increases, the color changes from translucent blue (3 layers)

to blue (15 layers), and finally, yellow for 37 layers. After initial identification under the optical microscope, 2D layers are characterized by contact mode AFM in air. The AFM image and height profile are shown in Figure 3.2b,c, respectively. Considering that the interlayer distance in InSe is ~ 0.88 nm, the number of layers are determined and indicated in Figure 3.2a. Along with thickness, AFM also provides information on surface topography, especially the presence of residues which should be prevented during the assembly of vdW heterostructures.

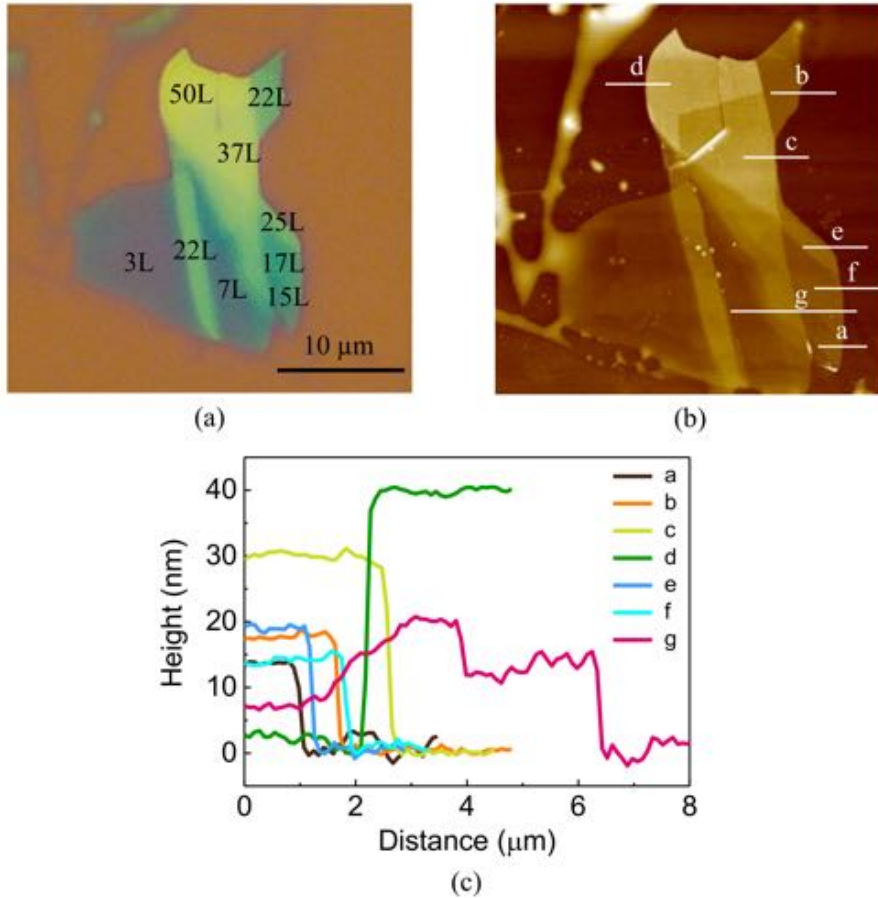


Figure 3.2: Identification of different thicknesses of exfoliated InSe using optical contrast and AFM. (a) Optical microscopic image of a multi-terraced InSe flake. Different color contrasts correspond to different layer numbers of InSe as indicated on the image, (b) AFM topography of the same flake, (c) height profiles measured by AFM at the marked places.

The same procedure of exfoliation and thickness identification is followed for other 2D materials. Exfoliation of high-quality, residue- and crack-free 2D layers is the first step towards the fabrication of vdW heterostructures. In the following section, the techniques and experimental setup for heterostructure assembly are discussed.

1.2 Deterministic transfer

Once the few layers of a 2D material are isolated, they can either be utilized directly or stacked onto each other to obtain vdW heterostructures. The probability of obtaining these heterostructures by randomly depositing different 2D materials onto the substrate is too low. Hence, novel transfer approaches are required, which can guarantee precise control over the position and alignment of the layers. One approach to achieve this is by using a micromanipulator which offers an easy transfer of multiple layers irrespective of the bottom substrate. A micromanipulator is an experimental setup equipped with a movable stage, a microscope, a transfer arm, and a heating system. During the course of this work, one such setup is installed in our lab (shown in Figure 3.3) and is optimized by myself for the fabrication of complex heterostructures. The components of the micromanipulator are controlled by a Labview interface and are described below.

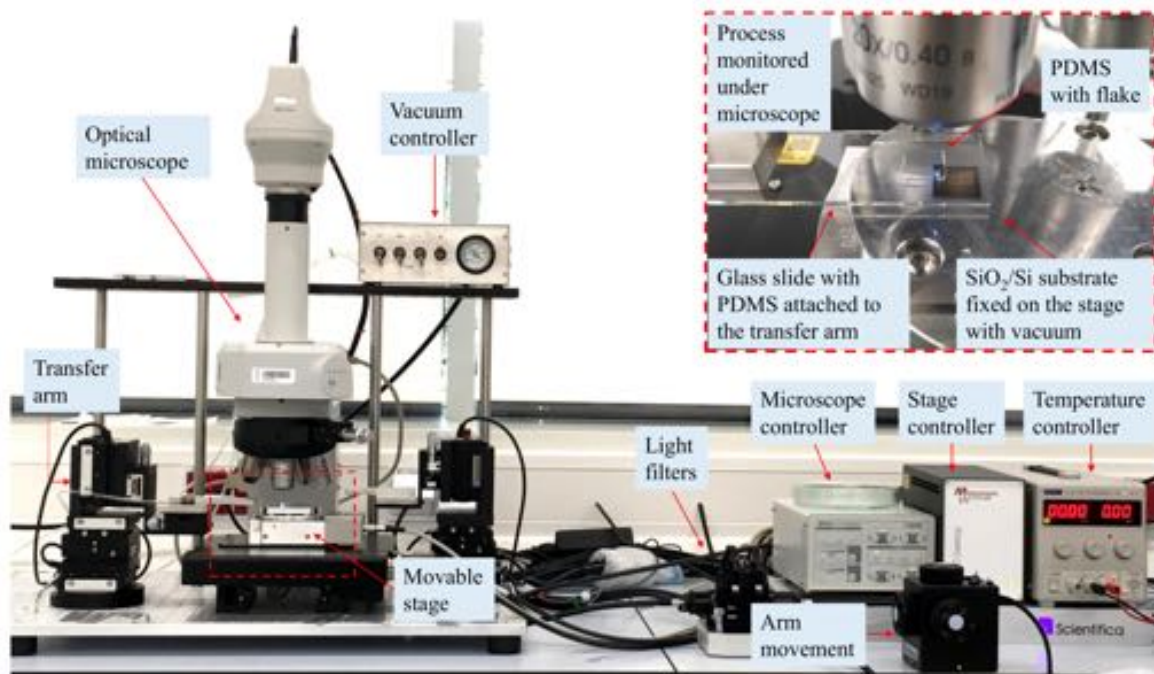


Figure 3.3: Photograph of the micromanipulator setup installed in our lab and its major components. Zoomed image shows the stage and an ongoing transfer to make a vdW stack using PDMS.

- **Movable stage:** The movable stage (SCAN^{plus} 75 × 50 mm from *Märzhäuser Wetzlar GmbH*) is an essential component of the micromanipulator. The substrate is fixed via vacuum line and can be moved in *x*- and *y*-direction with a resolution of 0.05 μm. In addition, the stage also provides a controlled rotary movement of 330° in clockwise and anticlockwise direction.
- **Microscope:** A DS-Ri2 and DS-Qi2 monochrome camera along with a C-HGFI fiber illuminator (mercury lamp) from *Nikon* are used in the microscope setup. The camera is capable of capturing color as well as monochrome images. Another important

purpose of the camera is to monitor the alignment of the layers and progress of the transfer process.

- **Transfer arm:** The transfer arm used in the micromanipulator is bought from *Scientifica* and consists of three identical motorized movements along the three axis (*x*-axis: left-right movement, *y*-axis: front-back movement, *z*-axis: vertical up-down movement). The arm has a height resolution of 0.1 μm and is controlled manually with the help of a joystick.
- **Heating system:** To control the temperature of the sample during transfer, a power supply (TTI-EL302P-USB) is connected to the stage. A set of commands through Labview allow remote control of the temperature from room temperature to a maximum of 175 °C.

The functioning of the micromanipulator is shown in the zoomed image of Figure 3.3. The substrate is fixed on the movable stage. The exfoliated 2D layers are held on the transfer arm and aligned with the bottom substrate at the desired location. Thanks to the controlled movement of the arm, the 2D layer is positioned with high accuracy over the targeted substrate and is slowly brought down. The layer at some point touches the substrate and gets transferred onto it. The whole process is monitored and controlled under the optical microscope at various magnifications. Though the basic principle of vdW assembly is same, a number of transfer techniques can be used to produce a variety of heterostructures on arbitrary substrates. Some of these techniques optimized in our lab and used throughout the project are: (a) PDMS dry transfer,^[129] (b) PPC vdW assembly technique,^[130] and (c) PVA method.^[40]

1.2.1 PDMS dry transfer

Polydimethylsiloxane (PDMS), a viscoelastic material has found its uses in many areas. In the field of 2D materials, it plays an important role in the fabrication of 2D vdW heterostructures. It can either be used as a transfer medium for 2D layers or as a carrier for other polymer based transfer membranes, such as PPC, PC, or PMMA. Among all available techniques for stacking 2D materials, PDMS dry transfer is most versatile, deterministic, and fairly simple to perform. In this technique, PDMS acts as a substrate for the exfoliated 2D layers, and subsequently, transfers them onto a desired substrate by first adhering to the substrate and then slowly detaching and leaving the 2D layer behind.

PDMS preparation PDMS stamps are prepared in-house because it allows us to control its adhesiveness and thickness as required. However, ready-made PDMS stamps (Gel-Film® PF-40-X4 or DGL film 50/17-X4) are also easily available to purchase.

To prepare the PDMS, the silicone elastomer and the curing agent (*Sylgard 184, Dow Corning*) are weighed in the ratio of 10:1 in a plastic mug. The components are mixed using a hand blender until the solution turns cloudy white. It is then poured into a plastic Petri dish up to a thickness of ~1 mm and placed in a desiccator (for around 1 hour) to remove the air-bubbles. If they still persist, the solution is mixed and placed again in the

desiccator. Once all air-bubbles are gone, the Petri dish is placed in an oven at 60 °C for 2 days. On complete polymerization, the Petri dish is removed from the oven, covered with a lid and stored in a glovebox or desiccator.

The thickness of the polymerized PDMS stamp is very important as it can affect the stacking process. A thickness of ~1 mm is optimum for our micromanipulator because it is neither too thin to crash into the movable stage nor too thick to affect the visibility. During polymerization, PDMS neither shrinks nor swells, therefore, it is advisable to fill the Petri dish up to a height which is the desired thickness of the cured PDMS. A fully cured PDMS is transparent and flat without any corrugations and non-uniformities, which is required for a successful transfer process.

PDMS assisted transfer The vdW assembly of 2D layers using PDMS transfer method is presented schematically in Figure 3.4 and described below.

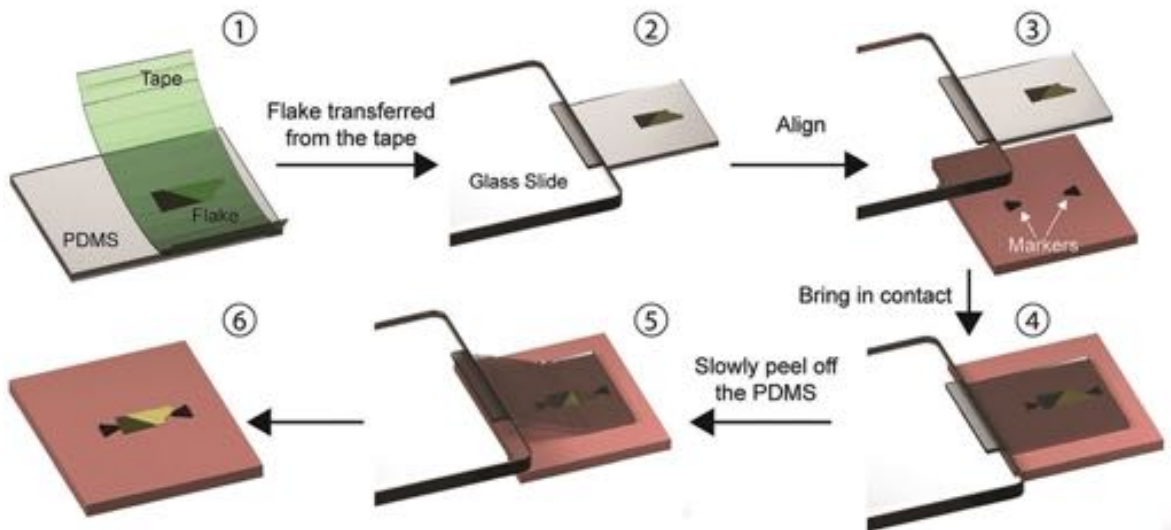


Figure 3.4: Schematic representation of the PDMS dry transfer method for vdW heterostructure assembly.^[131]

Step 1. The cured PDMS stamp is cut into individual blocks of about $1 \times 1 \text{ cm}^2$ using a sharp blade. The 2D layers are exfoliated from their bulk crystals using the adhesive tape as discussed before. The tape is placed onto the PDMS stamp resting on a standard microscopic glass slide for support. It is pressed gently with a flat tweezers and left on the PDMS for 1–2 min, allowing the flakes to adhere better to the PDMS.

Step 2. The tape is peeled off very quickly and preferably at an angle of 45°. The flakes are retained on the PDMS stamp.

Step 3. The exfoliated flakes are identified under the optical microscope. The glass slide carrying the PDMS is mounted on the transfer arm of the micromanipulator and positioned over the targeted substrate, such as SiO₂/Si chip with markers or TEM grid, etc.

Step 4. The arm is brought down until the 2D layer touches the bottom substrate and then left in contact for few minutes.

Step 5. The PDMS is slowly retracted back by pulling the transfer arm up. The retraction should be as slow as $\sim 2 \mu\text{m}/\text{min}$, which favors the adhesion of the 2D layers onto the bottom substrate.

Step 6. The transfer is now complete and a stack with different 2D layers is obtained.

A controlled and slow movement of the z -micrometer usually ensures a good transfer of 2D layers from PDMS stamp to the substrate. Different layers can be transferred onto each other in a similar fashion. Though the PDMS transfer process is easy and fast, it generates residues compromising the cleanliness of the 2D interfaces.^[132] In addition, fabrication of complex heterostructures is difficult to realize with this technique. To address these limitations, other techniques involving a sacrificial polymer layer are discussed next.

1.2.2 PPC vdW assembly technique

The vdW heterostructure assembly using a polymer membrane of polypropylene carbonate (PPC) is a challenging yet popular method. One of the major advantages of this technique is the small amount of residues and contamination, resulting in very clean interfaces between different 2D layers.

PPC transfer slide preparation PPC films or membranes are prepared by spinning PPC (*Sigma-Aldrich*) (15% in anisole) at 3600 rpm for 1 min on bare Si chips, followed by a post-baking at 90 °C for 2 min. This produces clean and uniform PPC films of $\sim 1 \mu\text{m}$ thick. The PPC film is then peeled off the Si substrate and placed carefully onto the cured PDMS stamp ($2 \times 2 \text{ mm}^2$) taped to a microscopic glass slide (Figure 3.5). The PDMS stamp provides support to the thin PPC film and prevents its delamination during the transfer process. The assembled glass slide is baked at 90 °C for 2 min to remove wrinkles and bubbles which may have originated during the slide preparation steps.

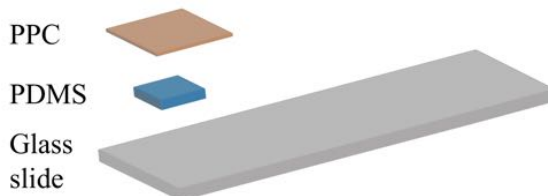


Figure 3.5: PDMS/PPC stack on a glass slide used for pick-up and drop-down of 2D layers.

PPC assisted transfer Unlike in the PDMS transfer technique, here the 2D materials are not exfoliated onto the PPC film but picked up from the SiO_2/Si substrate. The schematic shown in Figure 3.6 details the PPC assisted transfer process used frequently in this project.

Step 1. At the micromanipulator, the PDMS/PPC slide is aligned onto the targeted flake through the optical microscope. The slide is lowered slowly until the contact between the PPC film and the flake is established.

Step 2. Once the contact is made, the temperature of the stage is raised to 40 °C and maintained for 5–6 min. This ensures good adhesion between the PPC film and the 2D flake. To pick up the flake, the slide is slowly pulled up. Because of the strong adhesive forces between the PPC film and the flake, the yield is nearly 100%.

Step 3. The process is repeated with the same slide to pick up the next 2D layers. Successive pick-up of multiple layers forms a stack onto the PPC film.

Step 4. To transfer the stack, the PPC film carrying the stack is brought in contact with the bottom substrate.

Step 5. The temperature of the stage is raised to 90 °C, i.e. above glass transition temperature of PPC (~45 °C), which weakens the adhesion between the polymer and the 2D stack. As this point, the adhesion between the substrate and 2D stack dominates, and thus, 2D stack is left behind when the PPC arm is lifted up.

Step 6. The sample is left to cool down to room temperature to obtain the final stack for further processing.

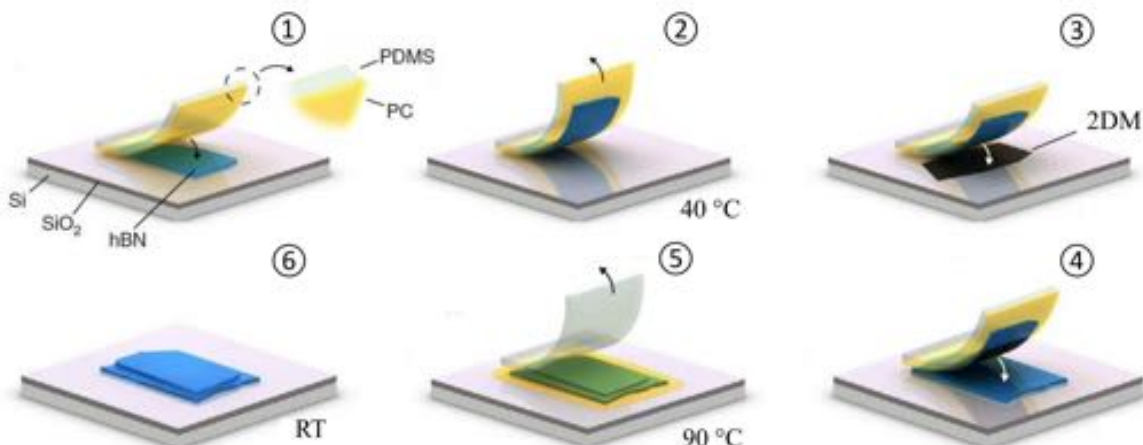


Figure 3.6: Schematic representation of the PPC vdW assembly technique.^[133]

Since different 2D layers are picked up successively, they do not come in direct contact with PPC polymer. Thus, the interfaces remain utmost clean without any residues or trapped contamination. In addition, this technique allows pick-up and integration of lithographically patterned 2D materials, CVD grown flakes and “via-contacts” into vdW heterostructures (details in chapter 4), which is very difficult to achieve with the PDMS technique.

1.2.3 PVA method

Another popular technique for assembling vdW heterostructures layer-by-layer is the PVA method. A two-polymer stack is used as the transfer system in which bottom layer of polyvinyl

alcohol (PVA) is sacrificed to obtain a freely floating membrane of polymethyl methacrylate (PMMA) carrying the 2D layers. The PMMA layer is eventually picked up and the 2D layers are transferred to the substrate.

PVA and PMMA preparation PVA and PMMA (*Sigma-Aldrich*) are dissolved in deionized (DI) water and anisole, respectively, to make a 3% solution by weight. The solution container is sealed with a spin-stirrer magnet inside and is placed on a magnetic hotplate at 60 °C for 24 hours. The solution is then filtered to remove any undissolved particles before using it for the transfer process.

PVA transfer technique The PVA transfer technique is explained schematically in Figure 3.7 with the help of a graphene/hBN stack.

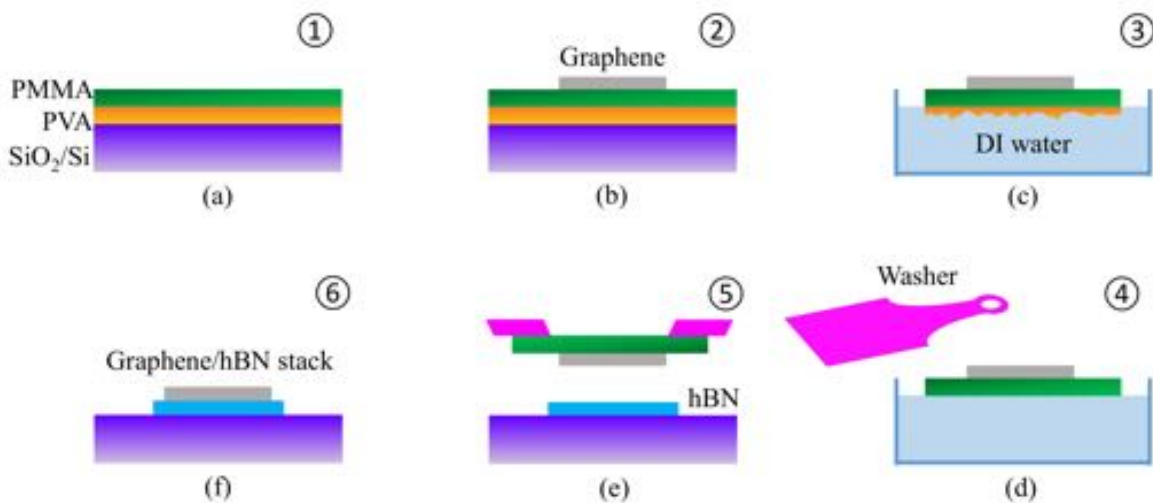


Figure 3.7: Fabrication of graphene/hBN vdW heterostructure using PVA transfer technique. (a) A SiO_2/Si substrate is coated with consecutive layers of PVA and PMMA, (b) graphene is exfoliated onto the coated substrate, (c) the hydrophilic PVA layer is dissolved in DI water, (d) freely-floating PMMA membrane carrying the graphene flake is captured by the washer, (e) graphene flake is positioned over a hBN flake resting on SiO_2/Si substrate, (f) final graphene/hBN stack on the SiO_2/Si substrate is obtained.

Step 1. To prepare the substrate for exfoliation, SiO_2/Si chip is cleaned in acetone and isopropanol followed by nitrogen blow dry. PVA is spin-coated onto the SiO_2/Si chip at 3500 rpm for 2 min to obtain a thickness of ~ 180 nm. The substrate is post-baked at 130 °C for 5 min and left to cool down to room temperature. Next, PMMA layer is spin-coated onto the PVA layer at 2200 rpm for 2 min and post-baked at 130 °C for 5 min to obtain a ~ 280 nm thick layer. This thickness of the PMMA layer is ideal for producing a good optical contrast of the 2D layers for successful identification by optical means.

Step 2. The 2D material (here, graphene) is exfoliated onto the PVA/PMMA coated SiO_2/Si substrate and identified under the optical microscope.

Step 3. Once a flake is selected, a circle (~ 3 mm in diameter) is marked around it with tweezers, cutting deep into the polymer layers. This disconnects the marked area from rest of the polymer film and defines the size of the PMMA membrane. Few drops of DI water are placed around the carved circle to dissolve the underlying PVA layer. As the PVA layer dissolves, the PMMA membrane carrying the flake also detaches from the bottom substrate. This process is captured sequentially through optical microscope and is shown in Figure 3.8.

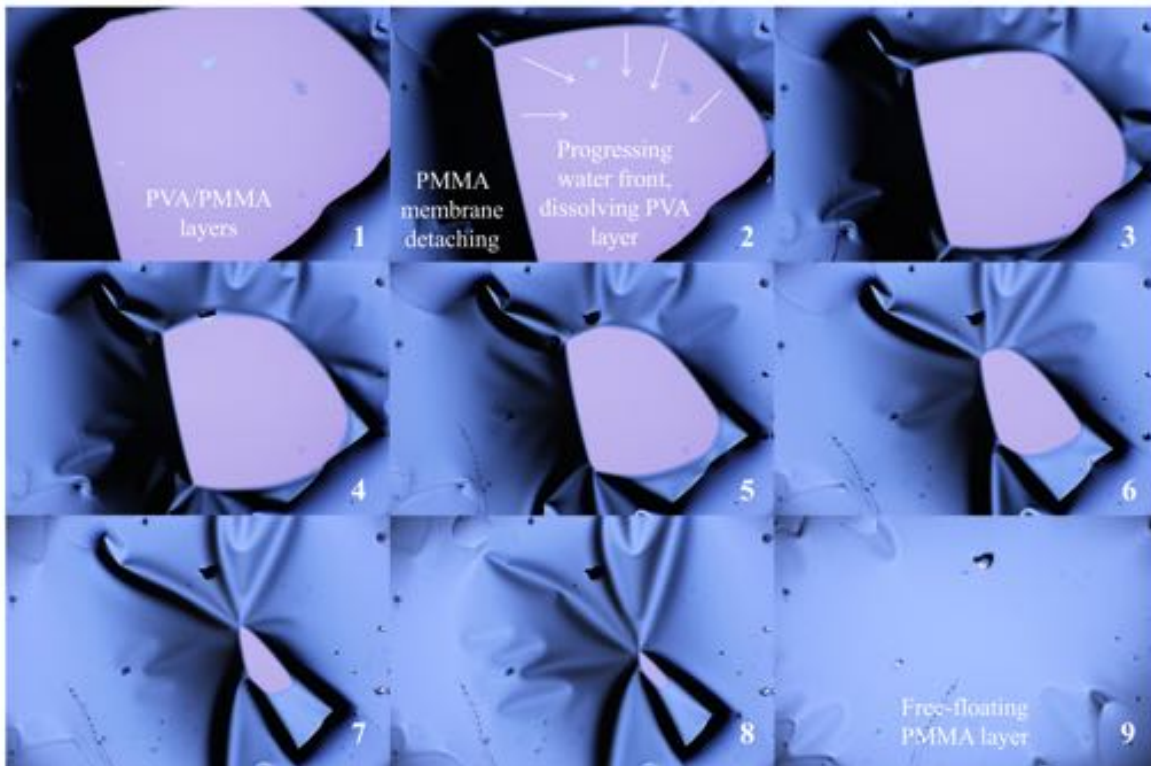


Figure 3.8: The process steps numbered 1 to 9 show dissolution of the PVA layer on coming in contact with DI water and lifting up of the PMMA membrane from the bottom substrate.

Step 4. The free-standing PMMA membrane is carefully transferred to a beaker filled with DI water. With the help of a metallic washer, the free-floating PMMA layer is “fished out”. If the layer has wrinkles, the washer can be baked at $120\text{ }^{\circ}\text{C}$ for 2–3 min.

Step 5. The metallic washer is then attached to the transfer arm at the micromanipulator with the 2D layers facing downwards. At this point, it is very important that the arm is leveled, otherwise a uniform contact with the substrate cannot be made.

Step 6. The 2D layer is then brought in contact with the bottom substrate where it needs to be transferred. As soon as the contact is made, the temperature of the stage is raised to $60\text{ }^{\circ}\text{C}$. The arm is then slowly lifted up, leaving the flake behind.

This method produces residue-free stacks, but relies largely on vdW interactions between different 2D layers. For example, the adhesion between graphene and hBN should be stronger

than between graphene and PMMA for the graphene flake to get transferred. Without bottom hBN, the transfer would be difficult because the adhesion between graphene and PMMA is stronger than graphene and SiO₂. To favor the transfer in such cases, oxygen-plasma treatment of the SiO₂ surface can be done, which will improve its adhesion to graphene. All of the above discussed transfer techniques can also be carried out under controlled atmospheres, such as inside a glovebox. A glovebox keeps the contaminants to the lowest and thus, clean vdW heterostructures with strong interlayer adhesion are obtained.

2 Microfabrication and device assembly

During this project, a variety of device structures are fabricated, serving the purpose of (opto)electronic characterization, micro-PL studies, and TEM investigations. For the fabrication of such elaborated structures, the aforementioned assembly techniques in conjunction with e-beam lithography and metal deposition are used. The TEM study of hBN and micro-PL study of hBN-encapsulated MoSe₂ and InSe are carried out by our collaborators in Leibniz Institute for Solid State and Materials Research (IFW Dresden) and HZDR, respectively. The preparation and fabrication of the vdW heterostructures under investigation are performed by myself. This section discusses the vdW heterostructures of 2D semiconductors of monolayer MoSe₂ and few-layered InSe combined with 2D dielectric hBN. Next, the fabrication of TEM grid samples carrying mono- and few-layers of free-standing hBN is described.

2.1 VdW heterostructures using hBN

As discussed before, hBN is frequently used in vdW heterostructures to serve two major roles.

1. **Bottom substrate dielectric:** Because of its atomically flat surface and low density of trapped charges, hBN is an ideal substrate for 2D layers. Unlike SiO₂, it provides a defect-free and homogeneous dielectric environment for the 2D channel.
2. **Top encapsulant:** The chemical inertness of hBN is beneficial for using it as a top encapsulant for 2D materials; especially air-sensitive materials can be prevented from environmental degradation once encapsulated in hBN.

2.1.1 VdW heterostructure of hBN/InSe/hBN

As discussed earlier, thin layers of InSe suffer from considerable degradation in air. This fast and uncontrollable degradation results in morphological changes, making it difficult to investigate its intrinsic properties. In order to preserve InSe against environmental degradation, it is encapsulated in top and bottom hBN. Upon full encapsulation, the stack stays intact in air and can be characterized further.

The stacks of hBN/InSe/hBN are fabricated by PPC vdW assembly technique, where hBN and InSe are exfoliated from their bulk crystals onto two different 285 nm SiO₂/Si substrates with markers. Markers are necessary to locate the flakes easily and are used in patterning the substrates later with e-beam lithography. After exfoliation, the flakes are identified by

optical means. It is important that the flakes are free from residues and cracks, and have uniform thickness and no steps. This is particularly required for achieving good interlayer adhesion and to prevent corrugations or distortions at the interfaces. A series of steps are followed for the selection of atomically flat hBN flakes, as detailed in Figure 3.9. The hBN flakes with a thickness of 30–40 nm are identified by optical contrast. Wide cracks and big chunks of residues are easily distinguishable under the optical microscope, e.g. the residues at the top edge of the flake in Figure 3.9. Steps and surface contamination are hardly visible in the optical image, but recognizable in a gamma corrected image (Figure 3.9b) where they get intensified. From the optical images, these surface features are recognized and avoided in the vdW assembly process. The flakes meeting these requirements are then investigated under AFM to obtain exact thickness and surface topography. AFM can measure the surface roughness in the range of few Å and thus, is an effective quality-check of the surface from adsorbents and contaminants. Figure 3.9c shows an AFM image of the flake, which appears to be clean over a large area (except the top edge) and hence, qualifies as a bottom substrate for the incoming 2D layer.

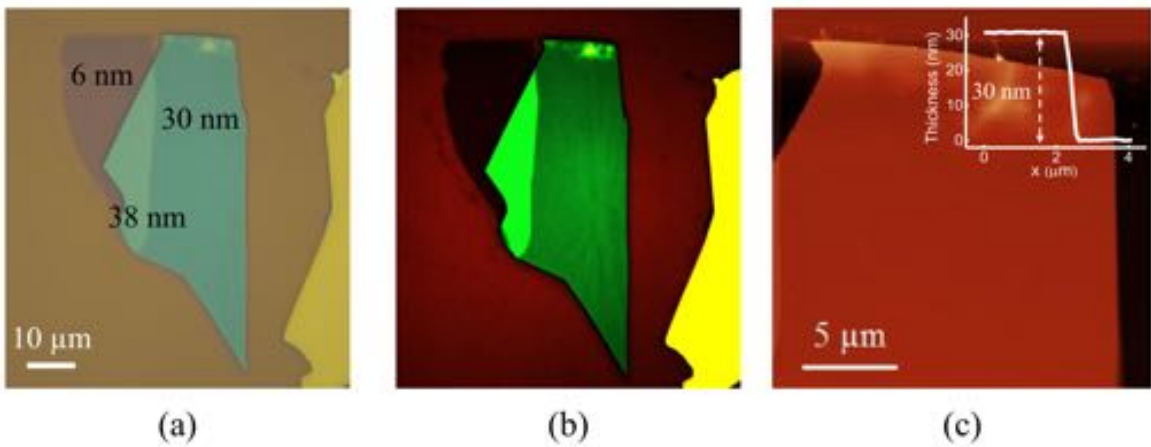


Figure 3.9: Identification of flat and clean hBN flakes for the bottom substrate: (a) Optical micrograph of a hBN flake. Different colors correspond to different thicknesses as indicated on the image, (b) gamma corrected image of the same flake to show clean and flat surface of hBN, (c) AFM topography revealing a thickness of ~ 30 nm and no surface residues and contamination except at the top edge.

To fabricate the stacks, the top hBN flake is picked up by PDMS/PPC transfer slide, as described before. At the micromanipulator, the top hBN is aligned with the InSe flake and slowly brought in contact. Due to strong vdW forces between hBN and InSe, the 2D flake is picked up. The transfer slide now carrying a stack of hBN and InSe is brought in contact with the bottom hBN flake resting on a 285 nm SiO₂/Si substrate. The temperature of the stage is raised to 90 °C which softens the PPC and transfers the stack onto the bottom hBN. A fully encapsulated stack of InSe is shown in Figure 3.10, which is utilized for time-resolved micro-PL studies of InSe at room- and low-temperatures. The effect of full hBN encapsulation in enhancing the electrical properties of InSe is one of the major findings of this work and is discussed in detail in chapter 4.

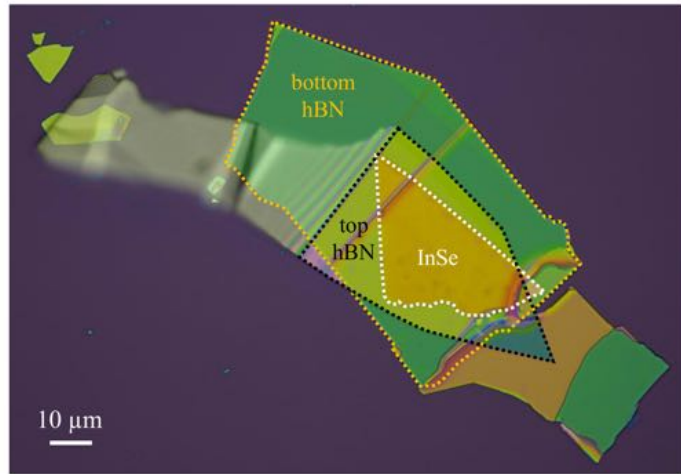


Figure 3.10: Optical micrograph of $h\text{BN}/\text{InSe}/h\text{BN}$ vdW heterostructure. InSe is sandwiched between two layers of $h\text{BN}$ and hence, fully encapsulated from the environment. White dotted line marks $\sim 15 \text{ nm}$ thick InSe , black dotted line marks $\sim 50 \text{ nm}$ thick top $h\text{BN}$, orange dotted line represents bottom $h\text{BN}$ of $\sim 42 \text{ nm}$ thickness.

2.1.2 VdW heterostructure of $h\text{BN}/\text{MoSe}_2/\text{hBN}$

Another interesting vdW heterostructure fabricated is $h\text{BN}/\text{MoSe}_2/\text{hBN}$, where monolayer MoSe_2 is sandwiched between top and bottom $h\text{BN}$. The stack is employed for low-temperature PL studies to understand the effect of the physisorbed gas molecules on the optical properties of monolayer MoSe_2 . Similar to other TMDCs, MoSe_2 has a direct bandgap only in monolayer, thus, only monolayers are relevant for optical characterization. The monolayers of MoSe_2 are easily identified because of strong color contrast on 285 nm SiO_2 substrate, as seen in Figure 3.11a.

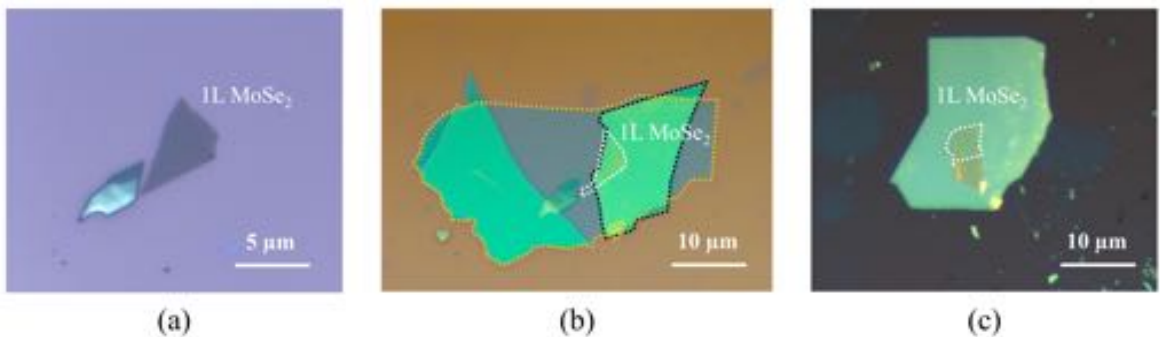


Figure 3.11: (a) Optical micrograph of monolayer MoSe_2 ($\sim 0.8 \text{ nm}$ thick), (b) $h\text{BN}/\text{MoSe}_2/\text{hBN}$ vdW heterostructure fabricated by PPC transfer technique. White dotted line marks monolayer MoSe_2 , black dotted line marks $\sim 40 \text{ nm}$ thick top $h\text{BN}$, orange dotted line represents bottom $h\text{BN}$ of $\sim 25 \text{ nm}$ thickness, (c) top $h\text{BN}$ encapsulation of monolayer MoSe_2 .

It should be noted that the adhesion of monolayer MoSe_2 to the oxide surface is so strong that very few successful attempts could be made to pick up the monolayers using $h\text{BN}$. In most of the cases, only the part of the monolayer covered by $h\text{BN}$ could be picked up, while the rest

stayed on SiO₂. Figure 3.11b shows the fully encapsulated stack of the MoSe₂ flake shown in Figure 3.11a, prepared by PPC transfer technique. Since MoSe₂ is relatively stable than InSe, only top hBN is sufficient to preserve monolayer MoSe₂ from adsorption of molecular contamination from air. The hBN/MoSe₂ stack is fabricated by PDMS transfer technique, where hBN exfoliated on PDMS is transferred directly onto the monolayer MoSe₂ (final stack shown in Figure 3.11c). The low-temperature PL results confirm that the top hBN encapsulation prevents physisorption of gas molecules and preserves the optical properties of monolayer MoSe₂.

2.2 Free-standing hBN on a TEM grid

TEM is used intensively for 2D materials to study their crystal structure, edge states, formation of defects, and grain boundaries. An electron holographic technique is developed at IFW Dresden, which facilitates high spatial resolution compared to conventional imaging techniques in the TEM. As a collaborator on this study, our task was to prepare samples where free-standing mono- and few-layers of hBN are deposited on a TEM grid. The substrates employed for TEM studies are hollow in order to allow the stream of electrons to pass through. Therefore, when 2D materials are deposited on TEM grids, they do not experience any vdW attraction from the bottom substrate, which makes their transfer quite challenging. In this section, these fabrication challenges are addressed. After several attempts, free-standing layers of hBN are deposited on TEM grids, which are subsequently employed for developing the electron holographic method.

For sample fabrication, a variety of TEM grids are tested including the conventional carbon-mesh grid. Of all the tested grids, Si-based TEM grids work the best. After optimization of the transfer process, the hBN flakes could be transferred onto these grids with nearly 100% yield. The Si-based TEM grid (bought from *TEM windows*) is ~3 mm in diameter with a window size of 30 × 30 μm² as shown in the Figure 3.12. The window comes with a 5 nm thick Si₃N₄ membrane which is removed by ultrasonic. The hBN is transferred to the TEM grids by both PDMS and PVA method successfully. While PDMS technique is faster and easier, the PVA method is challenging because of strong adhesion between PMMA and hBN. For a successful transfer, it is important to place the flake in such a way that the edges reside on the Si substrate. In this way, the vdW forces acting around the edges of the flake will make the transfer easier while maintaining the structural integrity of the flake.

Sample preparation The first step is to exfoliate hBN flakes onto the PDMS stamp. Unlike 2D semiconductors, few layers of hBN are hardly visible under the white light, attributed to a contrast of a mere 1.5%.^[134] On using a yellow filter ($\lambda = 590$ nm), the atomically thin layers of hBN could be seen on PDMS. The optimum color contrast obtained with the yellow filter is shown in Figure 3.13. Once the flake is identified on PDMS, it is brought down onto the TEM window in a way that the edges of the flake make contact with the Si substrate. Figure 3.14 shows the final sample consisting of hBN flakes on the TEM window. A monolayer to 12-layer thick hBN layers are identified under TEM for this sample.

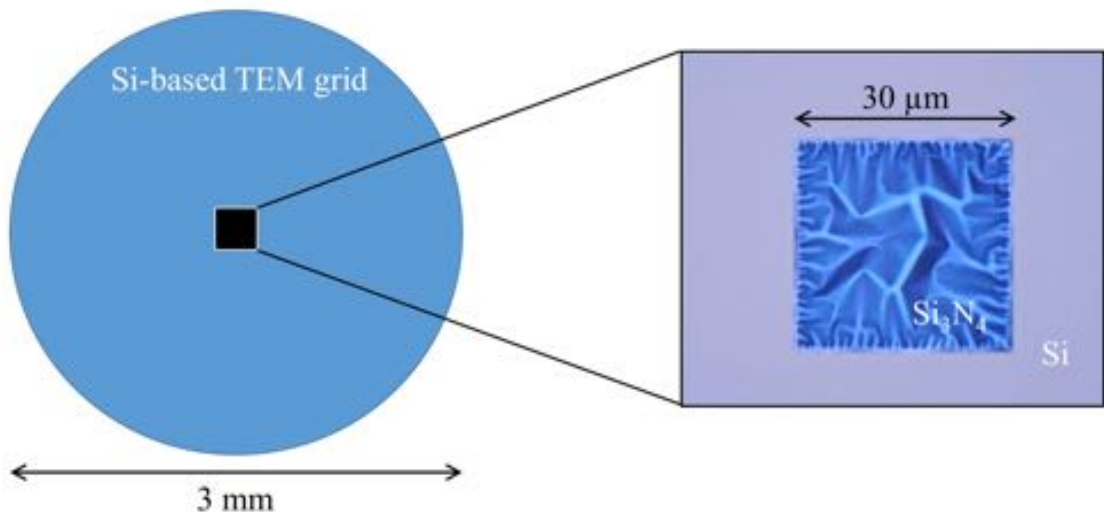


Figure 3.12: Schematic of a Si-based TEM grid of ~ 3 mm in diameter. The window where the flake should be deposited is zoomed in (right) and shows the Si_3N_4 membrane.

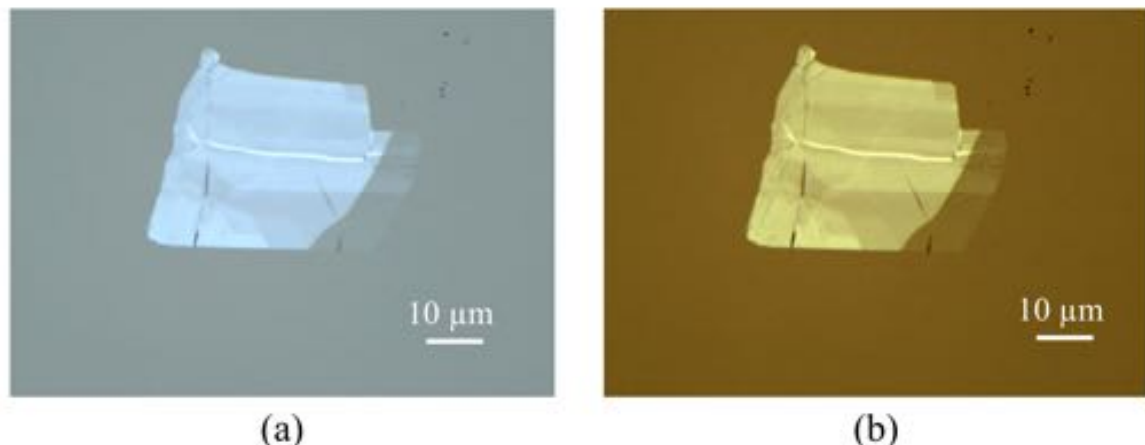


Figure 3.13: Optical contrast of hBN few layers resting on PDMS stamp under (a) white light, and (b) yellow light ($\lambda = 590$ nm).



Figure 3.14: Few layers of hBN free-standing on the TEM window.

3 Conclusions

The vdW heterostructure is an upcoming field in 2D research and provides new avenues to venture into in terms of properties and underlying physics. In this chapter, a step-by-step description for the assembly of 2D materials to fabricate a vdW heterostructure is provided. Various transfer techniques are discussed, which are optimized and utilized during the course of this work. Depending on the requirements of the final structure, the appropriate transfer technique is chosen. Though different kinds of vdW stacks, homo- and heterojunctions can be fabricated from the vast family of 2D materials, the focus here is majorly on hBN encapsulation of air-sensitive materials. The heterostructures based on InSe and GaSe are studied in great length for their electronic and optoelectronic properties, which will be discussed in the next chapter.

Chapter 4

Devices based on few-layered InSe and GaSe

This chapter focuses on electronic and optical properties of vdW semiconductors of InSe and GaSe. To perform electrical characterization, FETs are fabricated in back-gate configuration with InSe or GaSe as the channel. The first part of the chapter discusses initial attempts of fabricating InSe-based FETs with metal electrodes deposited directly on top of the exfoliated InSe layers. These FETs revealed poor properties along with a Schottky barrier to the charge injection, attributed to the oxidation of InSe and GaSe channel in air. This brought us to the conclusion that in order to investigate intrinsic properties of InSe and GaSe, their passivation from environment is necessary.

The second part of the chapter focuses on developing effective passivation techniques for InSe and GaSe to achieve high-performance and ambient-stable devices. A major part of this work is carried out during my research visit at the group of Prof. James Hone at Columbia University (New York, USA), where I learned the intricate processes of vdW heterostructure assembly, i.e. stacking multiple layers to produce new functionalities. By using their nanofabrication facilities, a hBN-based encapsulation technique is developed for air-sensitive layers of InSe and GaSe. The fabrication of vdW heterostructures is carried out inside a nitrogen-filled glovebox, which provides a contamination-free and inert atmosphere. The electrical connections to the encapsulated layers of InSe and GaSe are formed by using a novel contacting scheme called “via-contacts”.

The results assimilated in this chapter are published as:

1. **H. Arora**, Y. Jung, T. Venanzi, K. Watanabe, T. Taniguchi, R. Hübner, H. Schneider, M. Helm, J. C. Hone, and A. Erbe, “Effective Hexagonal Boron Nitride Passivation of Few-Layered InSe and GaSe to Enhance Their Electronic and Optical Properties”, ACS Applied Materials & Interfaces **11**, 43480–43487 (2019).
2. **H. Arora**, T. Schönherr, and A. Erbe, “Electrical characterization of two-dimensional materials and their heterostructures”, IOP Conference Series: Materials Science and Engineering **198**, 12002 (2017).

1 Introduction

In recent years, InSe-based devices have seen many advances owing to high electron mobility,^[11,12,52] resulting from its low electron effective mass ($m_e^* = 0.143 m_0$) and a direct bandgap lying in the NIR region.^[51,61] In contrast to TMDCs, where the mobility drops severely on decreasing the layer thickness, InSe retains high mobility and direct bandgap even for few layers. The electron mobility of $\sim 1000 \text{ cm}^2 \text{ V}^{-1} \text{ s}^{-1}$ demonstrated at room temperature in InSe devices is the highest value reported for an *n*-type 2D material so far.^[11,12,52] In optoelectronics, InSe-based photodetectors have demonstrated broadband operation from VIS to NIR region with responsivities as high as 10^7 A W^{-1} .^[17,54,60,135] Some advances have also been made in the area of flexible electronics based on InSe, where successful photodetection in its strained configuration is demonstrated.^[54] With these excellent merits, InSe can be easily envisioned as an active element in high-performance (flexible) electronics as well as to produce versatile 2D heterostructure devices.

GaSe, on the other hand, is a *p*-type material with a bandgap of 2.11 eV in bulk.^[69,70,78] In terms of electronic transport, few-layered GaSe has revealed mobilities of 0.1–0.6 $\text{cm}^2 \text{ V}^{-1} \text{ s}^{-1}$ when integrated as a channel into FETs.^[79,80] Unlike InSe, GaSe is not a high-mobility material because of the presence of heavy holes, but it is still very appealing for optoelectronics,^[73,79,81] single-photon emission,^[55] nonlinear optics^[57] and terahertz applications.^[56] The photodetectors based on GaSe have seen tremendous progress in the past decade, reaching high responsivities of $\sim 1200 \text{ A W}^{-1}$ along with a stable and fast photoswitching behavior with response times of 10–20 ms.^[73,75]

2 Material characterization

Single crystals of InSe used in this study are bought commercially from *2dSemiconductors*. As confirmed by the supplier, InSe crystals are grown by Bridgman growth process which guarantees highly crystalline crystals of large sizes of $\sim 1 \text{ cm}$ and 99.9999% purity. The XRD characterization data provided by the supplier shows the growth of γ -phase InSe, which has a rhombohedral (3R) crystal structure. Single crystals of GaSe are bought from *hq graphene*. The XRD measurements performed by the supplier confirms 2H-phase of GaSe with hexagonal structure. The produced crystals have a typical lateral size of 0.6–0.8 cm and a dark-copper metallic appearance. The bulk crystals of InSe and GaSe are shown in Figure 4.1.

Since the properties of the exfoliated 2D layers depend strongly on the quality and composition of the bulk crystal, further characterization is carried out to confirm structural and compositional integrity of the crystals. The chemical composition of InSe is analyzed by energy-dispersive X-ray spectroscopy (EDS). The details of the EDS measurement are provided in Appendix A.1. Figure 4.2a shows the EDS spectrum and compositional analysis of InSe bulk. Only In and Se peaks are present in the spectrum without any traces of impurities, which confirms high purity of the InSe crystals. The atomic ratio of In:Se is found to be 1:1. Figure 4.2b shows the Raman spectra measured at room temperature for various InSe thicknesses of 7–22 nm. In all spectra, four major vibrational modes are recognized, which

are typical modes for γ -InSe.^[60,136] For the 10 nm InSe layer, the peaks at 113 cm^{-1} and 223 cm^{-1} correspond to the non-polar A'_1 mode and those at 176 cm^{-1} and 193 cm^{-1} to the polar E'' and A''_2 (LO) modes, respectively.



Figure 4.1: Bulk single crystals of (a) InSe bought from 2dSemiconductors (image from www.2dsemiconductors.com/InSe). (b) GaSe bought from hq graphene (image from www.hqgraphene.com/GaSe).

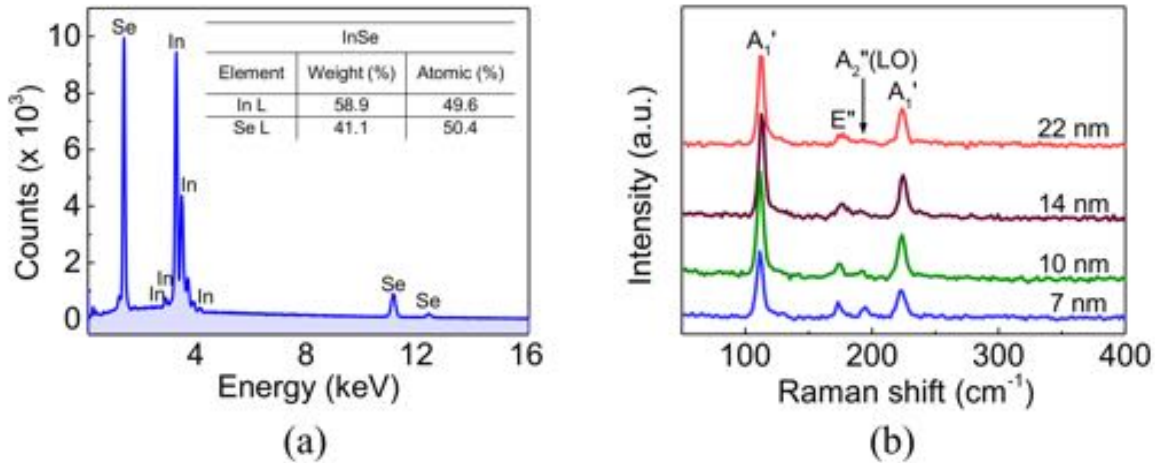


Figure 4.2: (a) EDS analysis of InSe bulk crystal to determine its chemical composition, (b) Raman spectra of few-layered InSe (7–22 nm) showing characteristic peaks of γ -InSe. Adapted from Arora et al.^[6]

For GaSe, the EDS and Raman spectra are measured as well (details of the measurements are provided in Appendix A.1 and A.2). The scanning electron microscopy (SEM) image of GaSe employed for EDS characterization is shown in Figure 4.3a. The peaks of Ga and Se in the EDS spectra (Figure 4.3b) confirms that the crystal is free from impurities and contamination. Raman spectrum of GaSe in Figure 4.3c shows five prominent peaks at 57.3 , 132.8 , 211.5 , 245 and 307.1 cm^{-1} , which are characteristic Raman modes for pristine 2H-GaSe.^[71–73,77,82]

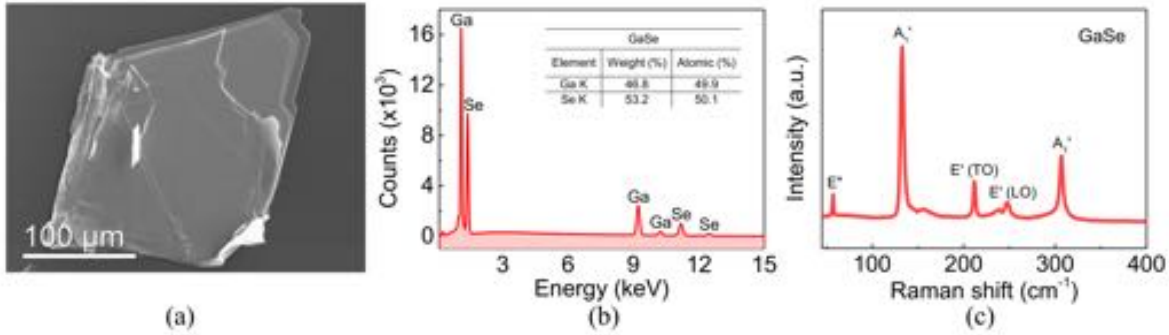


Figure 4.3: (a) SEM image of GaSe flake, (b) EDS analysis of GaSe confirming its chemical purity, (b) Raman spectrum of GaSe showing five characteristic Raman modes. Adapted from Arora et al.^[6]

3 Planar metal-InSe devices

3.1 Device fabrication

Few layers of InSe are obtained by micromechanical cleavage of its bulk crystal using an adhesive tape. The exfoliated layers are deposited directly onto a highly *p*-doped Si substrate with 285 nm thick SiO₂ layer serving as the back gate for the fabricated devices. The identification of the desirable layers of InSe is first performed under an optical microscope followed by AFM as discussed in chapter 3. The focus of this work is on few-layered structures of InSe and GaSe, i.e. thicknesses ranging between 8–30 nm. After the desired layers are identified, metal electrodes (source and drain) are patterned using high-precision e-beam lithography. The whole process of metal electrodes fabrication, beginning from e-beam lithography to metal lift-off is discussed in detail in Appendix B.1. The electrodes are fabricated by depositing 5 nm Ti or Cr metal as an adhesive layer, followed by 100 nm Au layer.

3.2 Electrical characterization

The optical image of an InSe flake (white dashed line) on a 285 nm SiO₂/Si substrate is shown in Figure 4.4a. An FET device is fabricated by depositing Ti/Au metal electrodes (source and drain) directly onto the InSe flake as shown in Figure 4.4b. The gate voltage is applied at the Si substrate which acts as the bottom gate for the device and the SiO₂ layer as the gate dielectric, as shown in the schematic in Figure 4.4c. The channel length *L*, i.e. the distance between the two electrodes is \sim 2 μ m. The current–voltage (*I*–*V*) characteristic of the FET device is measured by applying a drain-source voltage (*V*_{DS}) and a back-gate voltage (*V*_G).

The measured output characteristic, *I*_{DS} versus *V*_{DS} (Figure 4.5a), shows the formation of Schottky barrier at the Au/InSe interface. The transfer characteristic, *I*_{DS} versus *V*_G (Figure 4.5b), shows the semiconducting *n*-type behavior as expected. The field-effect mobility (μ_{FE}) is estimated using Equation 2.1, also mentioned below.

$$\mu_{FE} = \frac{dI_{DS}}{dV_G} \frac{L}{WC_i V_{DS}} \quad (4.1)$$

The capacitance per unit area of the SiO_2 dielectric is calculated using Equation 2.2, with the relative permittivity $\epsilon_{\text{SiO}_2} = 3.9$,^[67,137] and the thickness of the SiO_2 layer $d_{\text{SiO}_2} = 285 \text{ nm}$. Substituting these values in Equation 2.2, the C_{SiO_2} is calculated to be $0.121 \times 10^{-7} \text{ F cm}^{-2}$. Once C_i is known, μ_{FE} of $2.1 \times 10^{-4} \text{ cm}^2 \text{ V}^{-1} \text{ s}^{-1}$ is extracted at $V_{DS} = 20 \text{ V}$ using the above expression. The mobility value is much lower than expected, which is attributed to very high contact resistance and formation of Schottky barrier between Au and InSe.

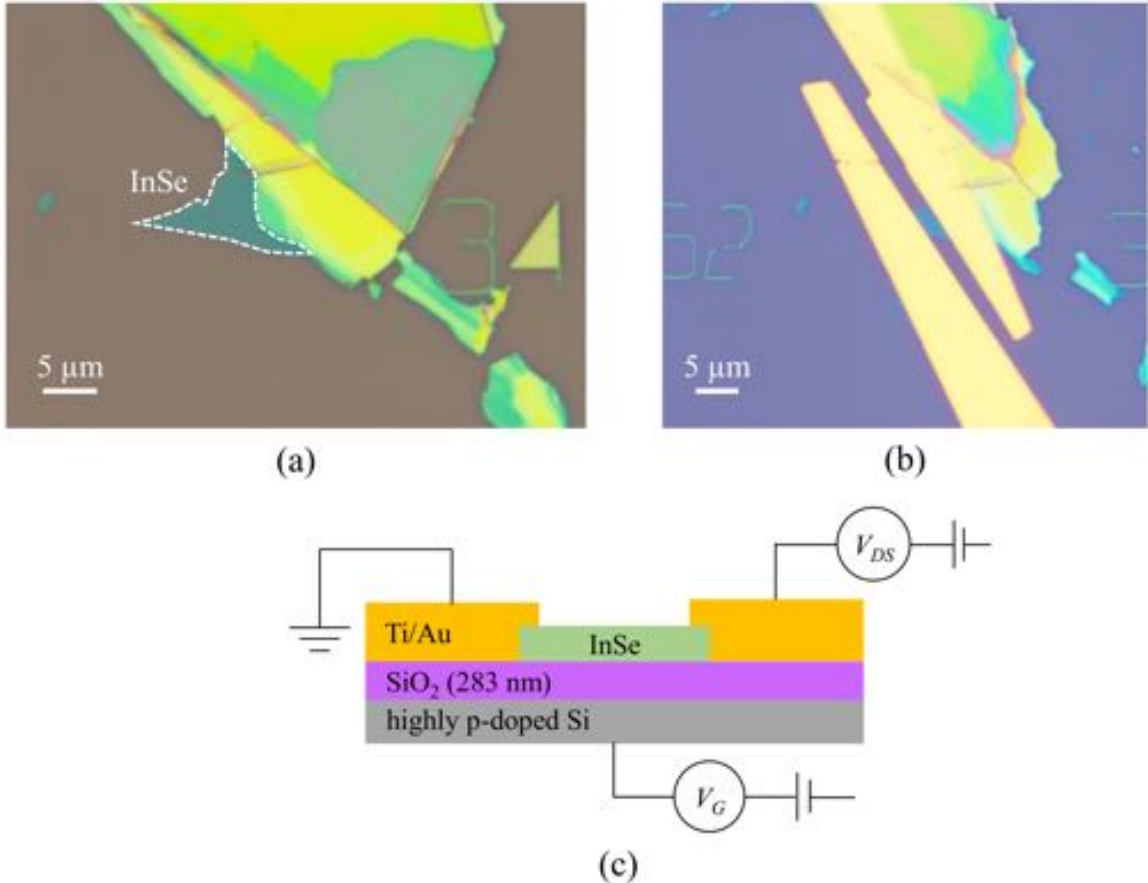


Figure 4.4: (a) Optical image of InSe flake on SiO_2/Si substrate, (b) FET device fabricated by depositing Ti/Au on the InSe flake, (c) schematic of the bottom-gate FET device based on InSe channel and Ti/Au electrodes.

In order to minimize the contact resistance, different metals, such as aluminum (Al), chromium (Cr) and titanium (Ti) are further tested. All metal contacts are $\sim 10 \text{ nm}$ thick and deposited directly onto the InSe flake followed by deposition of $\sim 40 \text{ nm}$ Au capping layer to prevent the oxidation of the underlying metal. The Al contacts have an extra layer of platinum (Pt) deposited between Al and Au layers as a diffusion barrier layer, in order to prevent the formation of an insulating alloy when Al diffuses into Au. The performance of InSe based FETs fabricated with different metal configurations is characterized electrically and compared in Table 4.1. As evident from the results, Cr forms the least resistive contact among all tested metal contacts. To further improve the mobility, the devices are annealed under argon atmosphere for 1 hour at 200°C . Slightly higher I_{DS} is obtained after annealing, however, the mobility is still much lower than the theoretical predictions.

The FETs based on GaSe are fabricated in the same fashion as InSe and characterized electrically. The measured I - V curves, even at large biases, showed no conduction whatsoever.

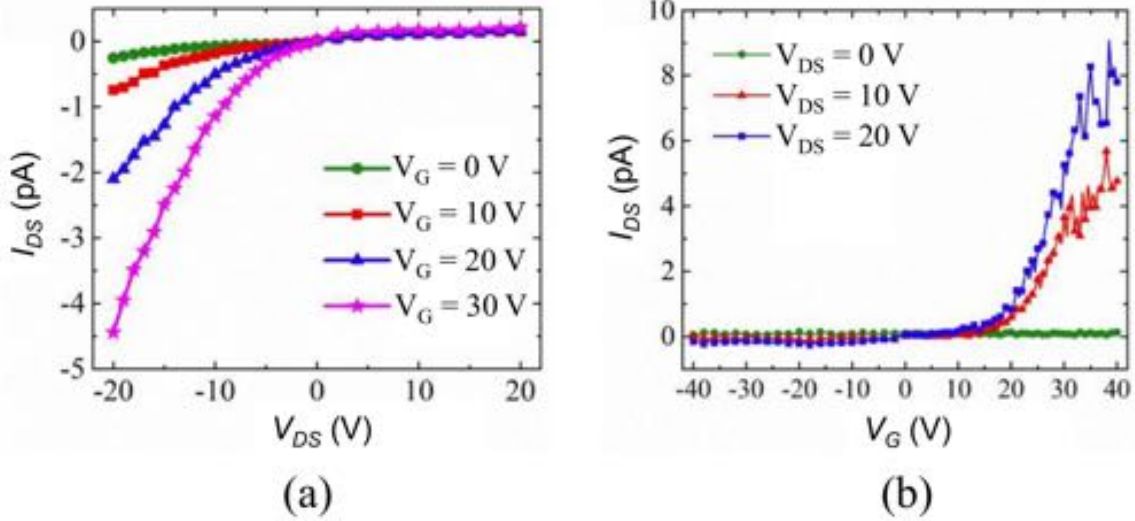


Figure 4.5: I - V characteristics of the planar metal-InSe FET. (a) Output characteristic at various V_G ranging 0–30 V, (b) transfer characteristic at V_{DS} of 0–20 V. Adapted from Arora et al.^[10]

Table 4.1
Key FET properties obtained for different metal-InSe FETs

Metal	on/off	μ_{FE} ($\text{cm}^2 \text{V}^{-1} \text{s}^{-1}$)
Ti(5 nm)/Au(100 nm)	80	2.1×10^{-4}
Ti(10 nm)/Au(40 nm)	44	2.1×10^{-4}
Cr(10 nm)/Au(40 nm)	500	2.8×10^{-3}
Al(10 nm)/Pt(5 nm)/Au(40 nm)	300	9.1×10^{-6}

A major reason for the poor performance of the devices is the chemical instability of InSe and GaSe in air and moisture as discussed in chapter 2. The results further indicate their sensitivity towards device fabrication processes as well. During the lithographic patterning process, the layers come in contact with several solvents and patterning resists, which further accelerates the oxidation process. This compromises the structural integrity of the layers and induces tunnel barriers and Fermi-level pinning, both of which can increase the contact resistance. In case of GaSe, the degradation is much faster than InSe and happens at a time scale of few hours. It is highly probable that by the time metal contacts are fabricated, the surface has already degraded and oxidation is penetrating into deeper layers. The metal/InSe interface thus has an oxide layer as a tunnel barrier which worsens with time because of continuously ongoing oxidation. Therefore, in order to characterize InSe and GaSe, their passivation is necessary. In the next sections, such passivation techniques will be discussed.

4 Planar metal-InSe devices inside a glovebox

In the previous section, it has been established that to investigate intrinsic properties of InSe and GaSe, their ambient degradation should be prevented. One technique to do so is to fabricate the devices inside a glovebox. A glovebox is a sealed container that provides a controlled atmosphere with very low oxygen and water content (<1 ppm), along with very low amount of impurities and contamination. The layers exfoliated inside a glovebox remain intact for much longer time than in air, which gives us an opportunity to study their unaltered properties in great detail. A nitrogen-filled glovebox installed at Columbia University and used in this work for the fabrication of InSe and GaSe devices is shown in Figure 4.6.



Figure 4.6: A nitrogen-filled glovebox at Columbia University used rigorously for fabricating the devices based on air-sensitive materials.

4.1 Device fabrication

To prevent the degradation of samples, the devices are fabricated inside the glovebox and spin-coated immediately with PMMA to avoid ambient exposure. The first step of the fabrication involves the exfoliation of InSe and GaSe onto a 285 nm SiO₂/Si substrate inside the nitrogen-filled glovebox. PMMA A6 (*MicroChem Co.*) layer is spin-coated onto the SiO₂/Si substrate at 2000 rpm for 1 min. The PMMA layer minimizes the exposure of the 2D layers to ambient conditions and is an e-beam resist for further processing. The substrate is then removed from the glovebox and processed further to make metal contacts by using e-beam lithography. After e-beam exposure, the sample is developed by dipping in the solution of methyl isobutyl ketone (MIBK) and isopropanol (3:1) for 1 min followed by nitrogen blowing. The metals in the order of Cr (2 nm)/Pd (20 nm)/Au (40 nm) are deposited using e-beam evaporator at a deposition rate of 1 Å s⁻¹. For the lift-off process, the sample is dipped into acetone followed by isopropanol rinsing and nitrogen blowing to obtain the final device.

4.2 Device characterization

Figure 4.7 shows one of the InSe devices fabricated inside the glovebox. The AFM reveals ~ 9.6 nm or 12 layers thick InSe flake, used here as the channel. The device is measured in back-gate configuration for its transfer and output characteristics. The electrical characterization is performed under ambient conditions and in the dark to exclude the effect of light on conduction.

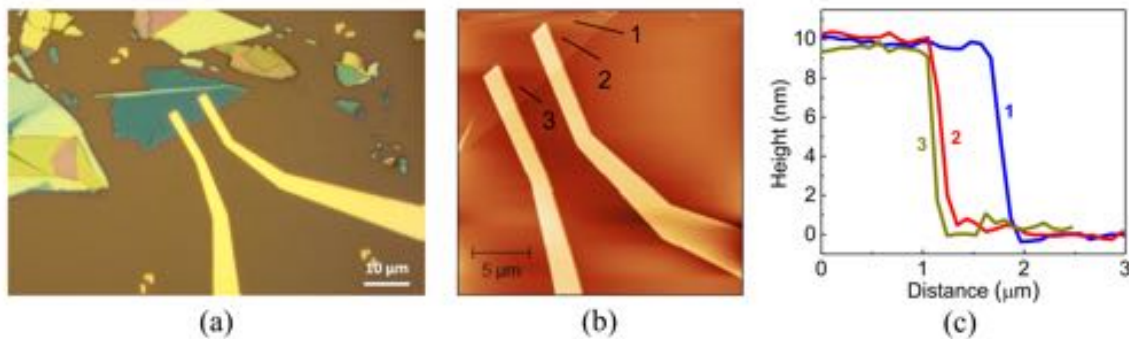


Figure 4.7: Planar metal-InSe FET. (a) Optical image of a device fabricated with an InSe flake exfoliated inside the nitrogen-glovebox, (b) AFM image of the device, (c) AFM height profiles confirming ~ 9.6 nm (12 layers) thick InSe flake.

The $I-V$ characteristics measured for the device is presented in Figure 4.8. Higher current levels and more reliable device performance are obtained as compared to the device fabricated in air (discussed in the previous section). The transfer curve (Figure 4.8a) shows an n -type behavior because of intrinsic doping of InSe as predicted previously.^[11,12,66] The room temperature μ_{FE} is calculated using Equation 2.1 and found to be $\sim 0.47 \text{ cm}^2 \text{ V}^{-1} \text{ s}^{-1}$ in forward sweep direction. On testing multiple devices, the highest mobility of $\sim 1.2 \text{ cm}^2 \text{ V}^{-1} \text{ s}^{-1}$ is obtained with an on/off ratio of 500.

The transfer curve of the device also reveals large hysteresis, which is attributed to trapped charge carriers at the InSe/SiO₂ interface.^[12,67,138] Large hysteresis can give rise to several unreliability issues, e.g. extraction of field-effect mobility. In a hysteretic curve, on sweeping towards the positive gate voltage, a portion of the gate-induced electrons are transferred to the substrate to fill the trap sites, leading to a slower rate change of the electron density in the channel, thus a reduced transconductance $\frac{dI_{DS}}{dV_G}$. The scenario reverses when the gate voltage is swept towards the negative direction. As a result, the field-effect mobility estimate becomes strongly dependent on the gate sweep direction.^[139] The output characteristics shown in Figure 4.8b shows higher I_{DS} levels than the device discussed in the previous section, however, the Schottky nature of the contacts is still present. The tendency of InSe to form Schottky contacts with several metals contacts has been reported previously.^[10,12,21,140] This could be attributed to surface degradation of InSe leading to the formation of tunnel barriers and Fermi-level pinning at the metal/semiconductor interface.

In summary, the key properties of an FET device, such as mobility and on/off ratio show an improvement when InSe layers are exfoliated inside a glovebox as compared to air. A PMMA layer spin-coated immediately on freshly exfoliated InSe prevents its degradation further.

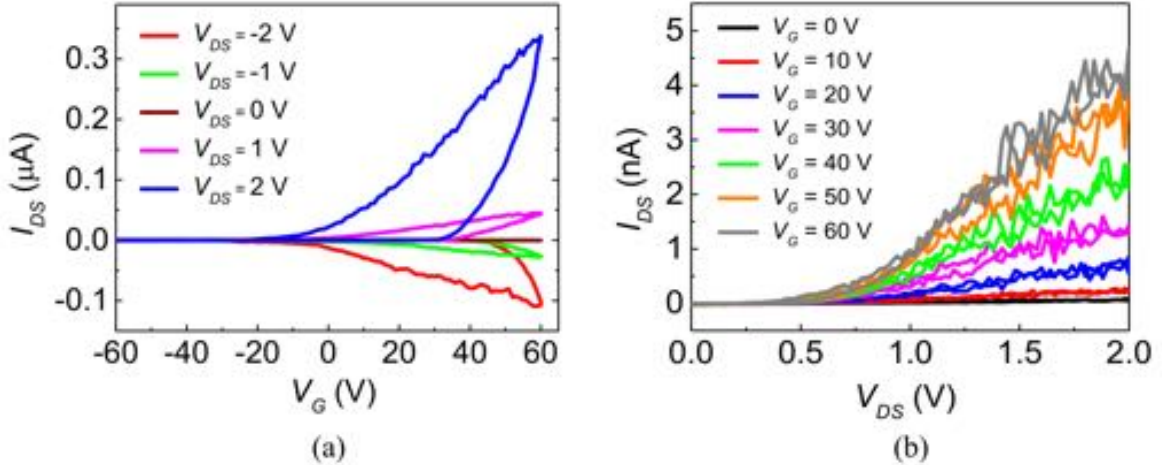


Figure 4.8: *I–V characteristics of the planar metal-InSe FET fabricated inside a nitrogen-filled glovebox. (a) Transfer curve measured for the InSe FET device shown in Figure 4.7 at various V_{DS} , (b) output curve measured at V_G from 0 to 60 V at regular intervals of 10 V.*

However, the chemical inertness of PMMA is not sufficient to provide long-term stability and high performance of the InSe devices. Due to porous structure of the PMMA layer, once the samples are removed from the glovebox, the degradation initiates and accelerates further during the lithographic patterning of metal contacts. Thus, to obtain high-performance devices with long-term stability, an efficient and robust encapsulation technique, which is inert to these degrading factors, is strongly needed.

5 Devices based on hBN encapsulated InSe and GaSe

Despite many promising properties of InSe and GaSe, limited work has been done exploiting them into devices because of their instability under ambient conditions. Though GaSe has been demonstrated to degrade rapidly on interaction with ambient air,^[71,81,141] the question whether InSe is air-sensitive or not is yet unclear within the scientific community. While some reports have claimed it to be relatively stable with no observable degradation over time,^[66,142,143] and extracted high mobilities under normal atmospheric conditions^[11,12], others observed that it degrades in air on coming in contact with water and oxygen.^[13,14,16] As demonstrated in the previous section, even standard process steps of device fabrication involving lithographic patterning, resist spinning and solvents' dips can cause considerable structural damage, degrading the quality of the material and resulting in poor performance of the devices.^[10,54] It is thus safe to say that InSe has better air-stability than GaSe, nevertheless thin layers of InSe tend to suffer from considerable degradation when exposed to air as compared to its bulk. Therefore, in order to achieve high performance and stable devices, effective encapsulation techniques should be developed to protect InSe and GaSe layers against degradation and maintain their structural integrity.

In this work, a hBN-based encapsulation is reported, where 2D layers of InSe and GaSe are sandwiched between two layers of hBN; top hBN passivating the 2D layer from the environment and bottom hBN acting as a spacer and suppressing charge transfer to the 2D layer from the SiO_2 substrate. To fabricate the devices from fully encapsulated InSe and GaSe layers, a novel contacting scheme of lithography-free via-contacts is employed.^[144] Based on our results, it is found that full hBN encapsulation preserves InSe in its pristine form and suppresses its degradation with time under ambient conditions. Consequently, the electronic properties of the encapsulated InSe are significantly improved, leading to a room temperature μ_{FE} in the range of $30\text{--}120 \text{ cm}^2 \text{ V}^{-1} \text{ s}^{-1}$ and an on/off ratio of 10^4 as compared to μ_{FE} of a mere $\sim 1 \text{ cm}^2 \text{ V}^{-1} \text{ s}^{-1}$ obtained for the unencapsulated InSe devices discussed in the previous section. In addition, the encapsulated InSe devices are stable for a prolonged period of time, overcoming their limitation to be air-sensitive. On employing full hBN encapsulation to GaSe, PL is dramatically improved and a high photoresponsivity of 84.2 A W^{-1} at 405 nm is obtained. The full hBN encapsulation technique passivates the air-sensitive layers from various degrading factors and preserves their unaltered properties. We believe that this technique can open ways for fundamental studies as well as towards the integration of these materials in technological applications.

5.1 Device fabrication

5.1.1 Via-contacts fabrication

Via-contacts are metal electrodes embedded within hBN flakes. They allow us to simultaneously achieve encapsulation and an electrical connection to the underlying 2D layer without any direct lithographic patterning. The fabrication of the via-contacts employed in this study is shown in the schematic of Figure 4.9. hBN flakes are exfoliated onto a 285 nm SiO_2/Si substrate using an adhesive tape. Crack- and residue-free hBN flakes with uniform thicknesses of $30\text{--}40 \text{ nm}$ are identified using optical contrast. The SiO_2/Si substrate is then spin-coated with PMMA A6 at 2000 rpm , followed by post-baking at 180°C for $5\text{--}6 \text{ min}$. The PMMA layer serves as the resist layer for the subsequent patterning of hBN using e-beam lithography. To develop the patterns, the substrate is dipped into the developer solution of MIBK and isopropanol (3:1) for 1 min followed by nitrogen blow dry. To etch holes into patterned hBN flakes, reactive ion etching (*Oxford RIE*) is used. A gas mixture of SF_6/O_2 is supplied at 60 W for 1 min to generate the plasma. The advantage of the SF_6/O_2 gas mixture is its high etch selectivity between hBN and SiO_2 , resulting in successful etching of hBN without damaging the bottom SiO_2 substrate. The etched holes are then filled with 20 nm Pd followed by 40 nm Au using e-beam evaporator at a deposition rate of 1 \AA s^{-1} . To obtain the via-contacts, the final step is metal lift-off, where the sample is dipped into acetone for $2\text{--}3 \text{ hours}$, followed by isopropanol rinsing and nitrogen blow dry.

Due to versatility of the fabrication process, via-contacts can be fabricated into different shapes, sizes, and patterns to offer variable channel lengths and device areas as shown in Figure 4.10. This is highly advantageous for exfoliated flakes, which irrespective of their sizes and shapes can be easily contacted by multi-electrode via-contacts. Having multiple

via-contacts on one InSe flake also gives us an opportunity to obtain multiple devices and characterize the best one. Though not the focus of this work, but an appropriate via-contact geometry can also be fabricated for carrying out Hall-effect and four-probe conductivity measurements.

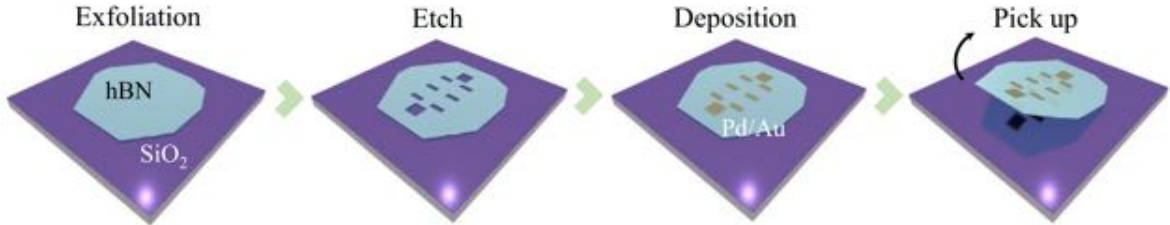


Figure 4.9: Step-wise illustration of the fabrication of Pd/Au via-contacts. Adapted from Arora et al.^[6]

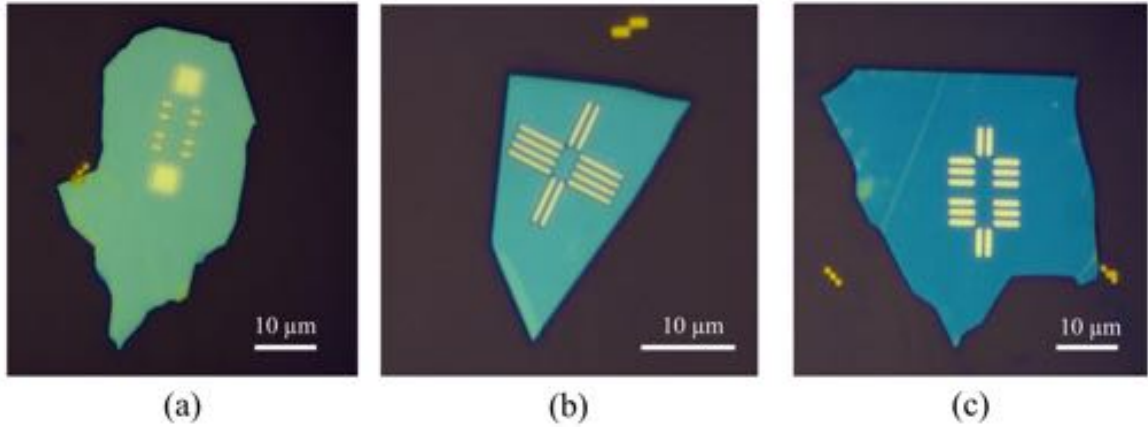


Figure 4.10: (a)–(c) hBN flakes with different via-contact configurations that can be used to perform various electrical characterizations.

5.1.2 VdW assembly of hBN/InSe/via-hBN

Heterostructure assembly plays a crucial role in achieving high-performance devices. The 2D vdW heterostructure is required to have clean interfaces, because if contamination and residues are present between the interfaces, they act as “blisters” for the 2D layers and deteriorate their intrinsic properties. Two main sources of blisters are residues from the transfer process and wrinkles/bubbles formed from trapped air molecules and organic adsorbates. The latter is common if the stacking is performed in air. To minimize these contamination, the exfoliation and encapsulation of InSe and GaSe is done in a nitrogen-filled glovebox, which prevents ambient degradation of the 2D layers and keeps the hBN/2DM interfaces clean. Further cleanliness of the interfaces is assured by using the PPC transfer technique (discussed in chapter 3) for fabricating via-devices, as it guarantees a residue-free stacking. The first step of the fabrication involves picking up of a via-hBN (hBN flake carrying via-contacts) using a PDMS/PPC transfer slide at the micromanipulator. The exact steps described for the PPC transfer method in chapter 3 are followed. The via-hBN lying on a

PDMS/PPC stamp after a successful pick-up is shown in Figure 4.11. Next, InSe is exfoliated from its bulk crystal inside a nitrogen-filled glovebox and transferred onto a hBN flake (bottom dielectric) resting on a 285 nm SiO₂/Si substrate. To form the hBN/InSe/via-hBN heterostructure, the PDMS/PPC stamp containing the via-hBN is stacked onto the InSe flake in such a way that the metal electrodes cover it entirely. The substrate is then removed from the glovebox and processed further to make extended metal bars to the via-contacts and contact pads where probes could be placed (the process of fabricating metal bars and contact pads is discussed in Appendix B.2).

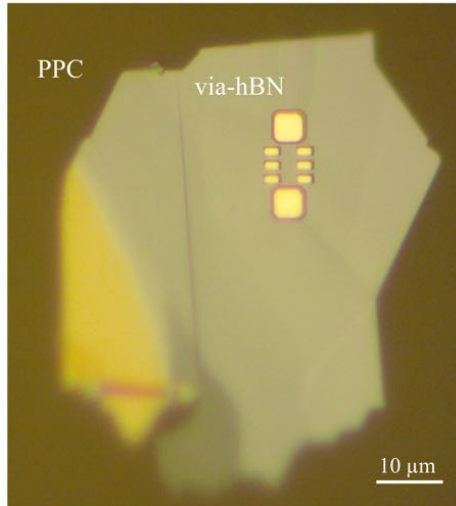


Figure 4.11: Optical image of a hBN flake containing Pd/Au via-contacts, lying on a PDMS/PPC stamp after a successful pick-up from SiO₂/Si substrate.

5.2 Micro-photoluminescence measurements

To demonstrate the effect of full hBN encapsulation on the stability of InSe, we performed micro-PL measurements to adjacent surfaces of exposed and protected InSe (see Appendix A.2 for detailed PL specifications). Figure 4.12a,b show the PL spectra obtained for both samples at 297 K and 4.2 K, respectively. It is evident that at both temperatures hBN encapsulation significantly enhances the PL spectra by yielding narrower and more intense peaks as compared to the unencapsulated InSe because of crystalline and atomically flat layers of hBN. The prominent effect of hBN encapsulation is seen at 4.2 K (Figure 4.12b), where the PL linewidth narrows down to give a full width at half maximum (FWHM) of ~12 meV in contrast to 36–38 meV obtained for the exposed InSe of the same thickness. This significant reduction of the PL linewidth in the encapsulated sample indicates fabrication of a high-quality hBN/InSe/hBN vdW heterostructure. As compared to PL at 4.2 K, the linewidth of both samples broadens at 297 K and shows a red-shift of ~50 meV from ~1.30 (at 4.2 K) to ~1.25 eV (at 297 K) as seen in Figure 4.12 because of the interaction with acoustic and optical phonons.^[91,145] Furthermore, the encapsulated InSe shows higher PL intensity, which further confirms the suppression of surface charge traps and defects by using bottom hBN substrate.^[67,91]

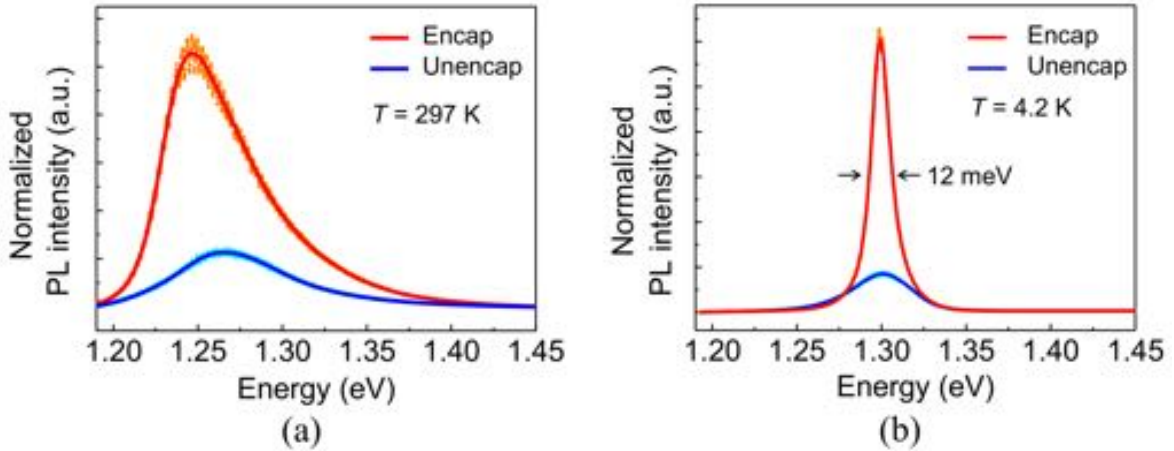


Figure 4.12: PL spectra measured for encapsulated and unencapsulated InSe samples at (a) 297 K, (b) 4.2 K. The encapsulated sample shows higher intensity at both temperatures. At 4.2 K, a narrow linewidth with FWHM of 12 meV for encapsulated InSe is obtained. Adapted from Arora et al.^[6]

To understand the role of hBN encapsulation, the PL emissions of three different stack configurations: (a) a fully hBN encapsulated InSe flake, (b) an InSe flake on a SiO_2 bottom substrate, and (c) an InSe flake on a hBN bottom substrate, are compared. For best comparison, all three configurations are produced on a single InSe flake of uniform thickness as shown in the Figure 4.13a. On measuring multiple stacks, a mix of red- and blue-shifts in the PL peak position is obtained when full hBN encapsulation is used (Figure 4.13b). The ambiguity in the shift direction is attributed to multi-layered structures of InSe and GaSe employed in this study. Unlike monolayers of TMDCs where a reproducible red-shift because of a strong effect of hBN dielectric is observed, here, the effect is much less pronounced.^[91,145,146] While the red-shift can be attributed to a stronger effect of the hBN dielectric, the blue-shift may arise because of various reasons, such as the presence of shallow defect states, compositional fluctuations, interface inhomogeneities, and/or due to the relative population of neutral and charged excitons as demonstrated in TMDCs.^[147–149] A recent study shows that in multi-layered InSe, hBN initiates stronger charge confinement than SiO_2 , shifting the optical bandgap to higher energies.^[150] Hence, the shift direction in multi-layers of InSe and GaSe is governed by several factors and cannot be associated only with the dielectric environment. Nevertheless, the superiority of full hBN encapsulation is evident in other PL features of intensity and FWHM. It is clearly seen in Figure 4.12 and Figure 4.13b that the unencapsulated InSe on SiO_2 substrate shows the lowest intensity. When InSe is deposited on a bottom hBN flake, PL intensity similar to the unencapsulated InSe is obtained. A major enhancement in the peak intensity is only seen when InSe is sandwiched between bottom and top hBN. In addition, a statistical analysis of various stacks (Figure 4.13c) confirms an overall narrowing down of the PL linewidth by 2–3 times when 2D layers are fully encapsulated as compared to other two configurations. These findings thus show that the best results are obtained when the bottom hBN which protects the InSe layers from the charge disorder at the SiO_2 surface is used in conjunction with top hBN which avoids exposure of the top surface to air.^[8,151]

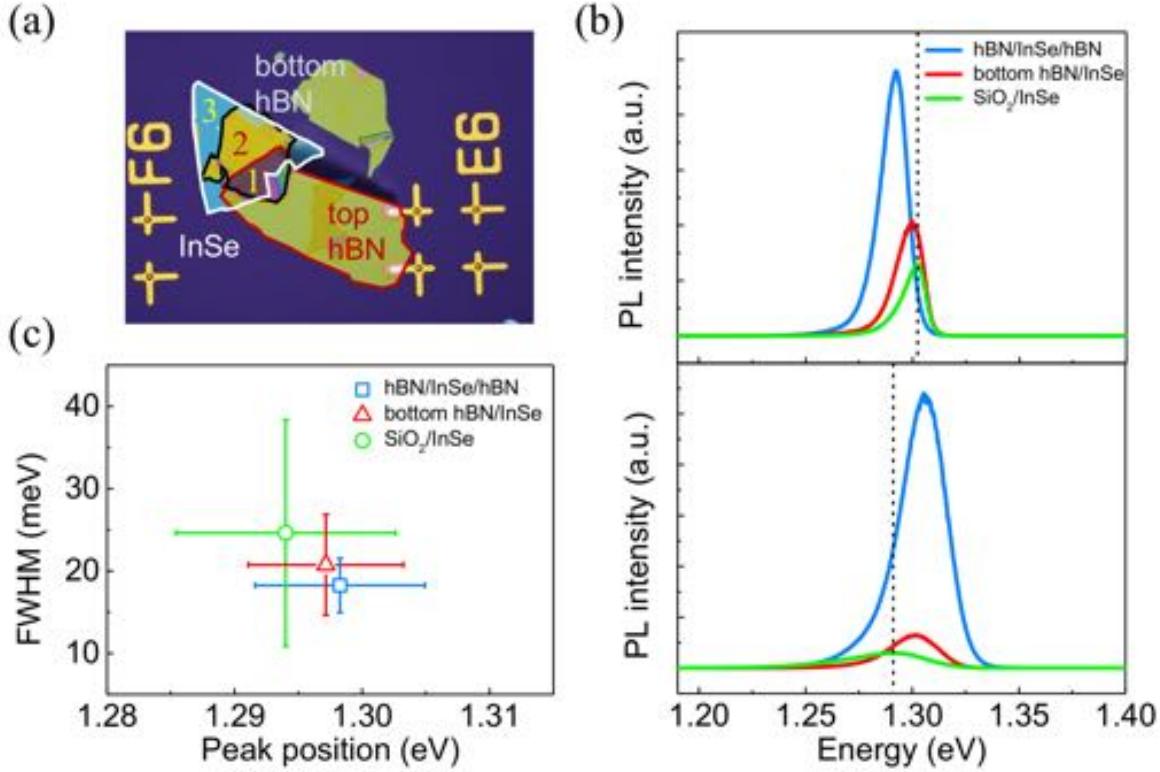


Figure 4.13: PL spectra at 4.2 K for different stack configurations of hBN-InSe to demonstrate the role of hBN encapsulation. (a) Optical image of the InSe-hBN stack. The stack has three configurations fabricated from a single InSe flake: a fully hBN encapsulated InSe (area marked as 1), InSe on hBN (area marked as 2), and InSe on the SiO₂ (area marked as 3), (b) PL spectra of two different InSe flakes, showing maximum PL yield obtained in fully encapsulated InSe, (c) statistical analysis of various stacks, showing narrower FWHM in fully encapsulated InSe as compared to other two configurations.

Subsequently, the samples are measured over time to test their long-term stability under ambient conditions. Figure 4.14a,b reveal the PL spectra measured at room temperature under normal atmospheric conditions for a time period of 8 weeks. Between consecutive measurements, both samples are stored in the dark and under ambient conditions, allowing the ambient exposure to affect both devices in the same manner. Figure 4.14c shows that the PL peak intensity of the encapsulated InSe is intact for almost 4 weeks after which it starts to decline gradually, whereas for the unencapsulated sample the PL intensity has almost vanished after 2 weeks. The PL peak position, however, is not significantly affected over time (Figure 4.14d). Balakrishnan et al.^[142] have attributed the reduction in the PL intensity to the formation of In₂O₃ as InSe thin layers are exposed to air under high temperatures and focused lasers. The trend in Figure 4.14 indicates that the stability of the InSe layers is greatly enhanced by using hBN encapsulation which preserves InSe from the complex physical and chemical changes occurring when it comes in contact with air.

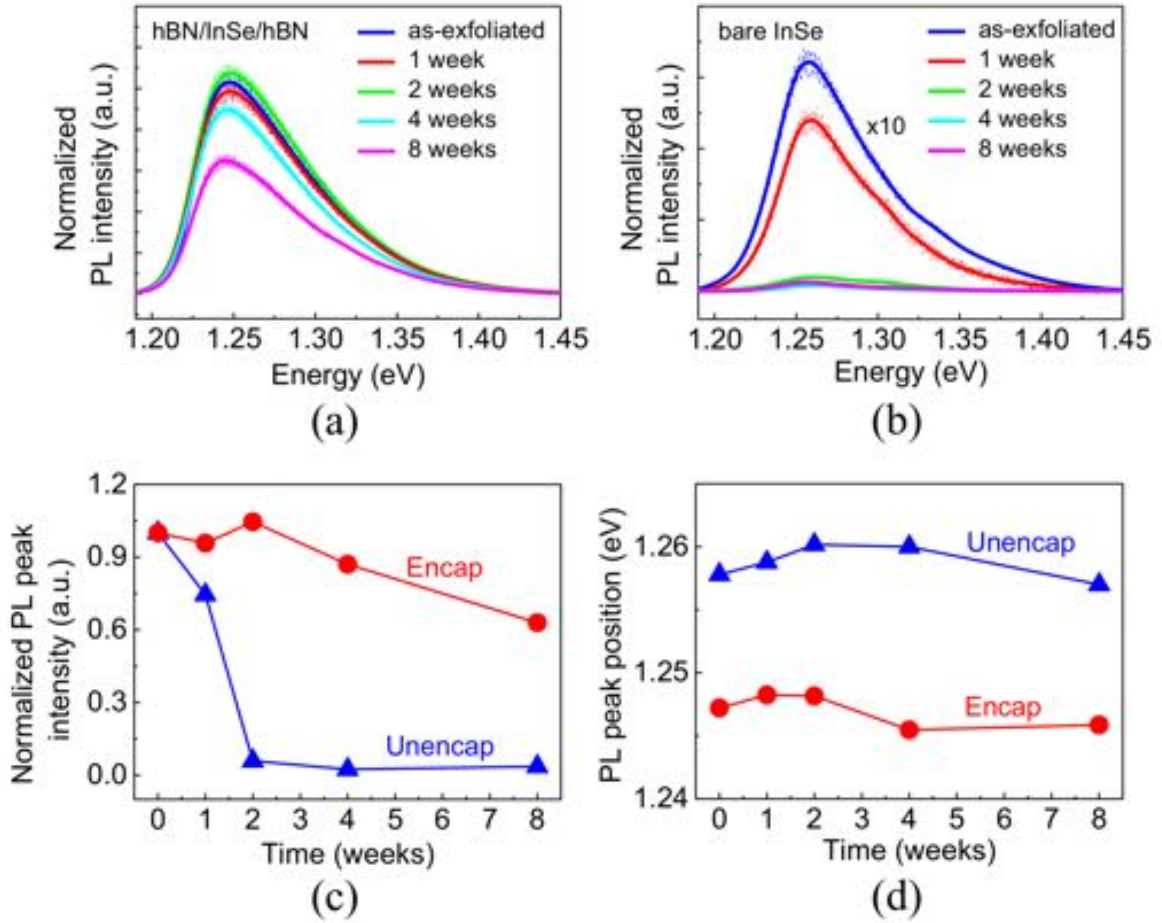


Figure 4.14: PL spectra measured for encapsulated and unencapsulated InSe over time, demonstrating ambient stability encapsulated InSe. (a),(b) Evolution of the PL spectra at room temperature with time for encapsulated and unencapsulated InSe, respectively, stored under ambient conditions. (c),(d) Normalized PL peak intensity and PL peak position measured over time, showing structural instability of InSe when exposed to air, whereas the encapsulated sample stays intact over 4 weeks. Adapted from Arora et al.^[6]

5.3 Electronic properties of InSe-via devices

The FET device based on encapsulated InSe channel is electrically characterized and compared with its unencapsulated counterpart to analyze the effect of hBN encapsulation on its performance. Figure 4.15 compares the two configurations of InSe-based device geometries investigated in this work. Figure 4.15a,b show the schematic and the optical micrograph of a fully encapsulated InSe-via device, respectively, where black solid lines (in the enlarged image of Figure 4.15b) show the via-metal in an intimate contact with the underlying InSe layer. The multi-electrode via-contact in one hBN flake allows us to produce and measure multiple devices on one single InSe flake. The heterostructure is fabricated in a contamination-free environment, so that the layers have clean and impurity-free interfaces. Figure 4.15c,d show the schematic and the optical image of the unencapsulated InSe device discussed in the previous section. For a consistent comparison, both encapsulated and unencapsulated devices

are fabricated with the same thickness of InSe, i.e. ~ 9.6 nm or 12 layers. The metal contact configuration is also kept same in both devices, i.e. 20 nm Pd capped with 40 nm Au, deposited by e-beam evaporation.

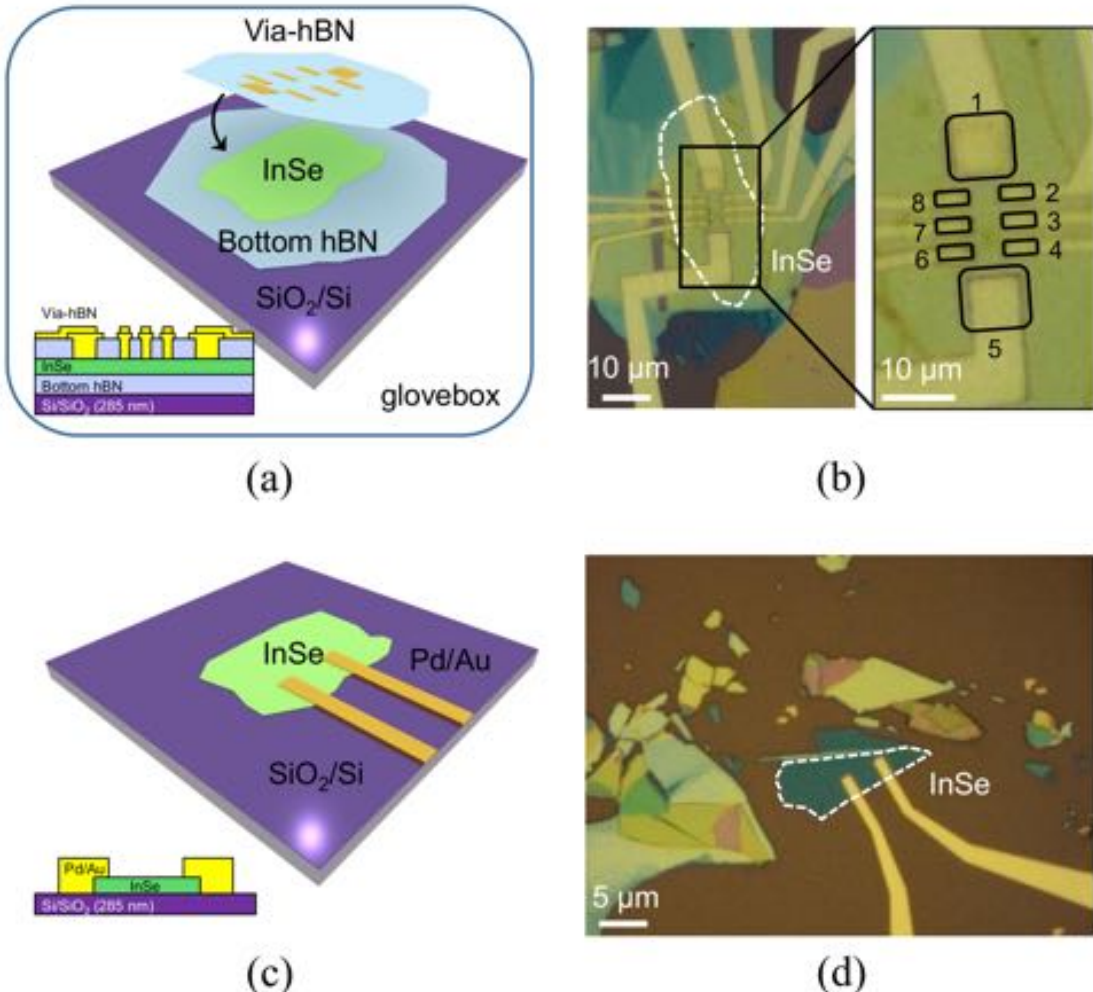


Figure 4.15: Device configurations of two InSe-based FETs. (a) Schematic of the InSe-via device when the via-hBN covers InSe to encapsulate it and to form an electrical connection. The stack is fabricated inside a glovebox, (b) optical image of an InSe-via device, ~ 9.6 nm thick InSe flake (white dashed line) is sandwiched between bottom hBN and top via-hBN. The black solid lines in the enlarged image highlight multiple Pd/Au metal contacts (numbered 1 to 8) embedded in hBN, forming a vdW contact with the underlying InSe layer, (c),(d) schematic and optical image of an unencapsulated device, respectively. The white dashed line indicates the InSe flake on SiO_2 substrate. The metal electrodes are fabricated by depositing Pd/Au metal. Adapted from Arora et al.^[6]

To investigate the performance of hBN encapsulated InSe FETs, the $I-V$ characteristics is measured in back-gate configuration. The transfer curve shown in Figure 4.16a shows an n -type conductivity because of intrinsic doping of InSe as predicted previously.^[11,12,66] Interestingly, the device shows negligible hysteresis compared to the unencapsulated device (Figure 4.8a) as well as to other encapsulation techniques of ALD^[17] and dry oxidation^[16], where substantial hysteresis was observed because of trapped charge carriers at the InSe/ SiO_2

interface. The output curve of the encapsulated device (Figure 4.16b) reveals a linear characteristics, indicating the formation of ohmic contacts between the Pd/Au metal used in the via-contact and the underlying 9.6 nm thick InSe layer. Whereas for the previously discussed unencapsulated devices (Figure 4.8b), ohmic contacts could not be produced because of the degradation of InSe prior to the metal deposition, leading to tunnel barriers at the metal/InSe interface. The improvement in the FET performance on employing hBN encapsulation is evident from Figure 4.16c,d, which show linear and semi-log transfer curves (at $V_{DS} = 0.5$ V) of both device configurations. The reliability in the performance of encapsulated devices is seen in terms of smaller hysteresis and higher current levels than unencapsulated devices which showed large hysteresis in all measured devices.

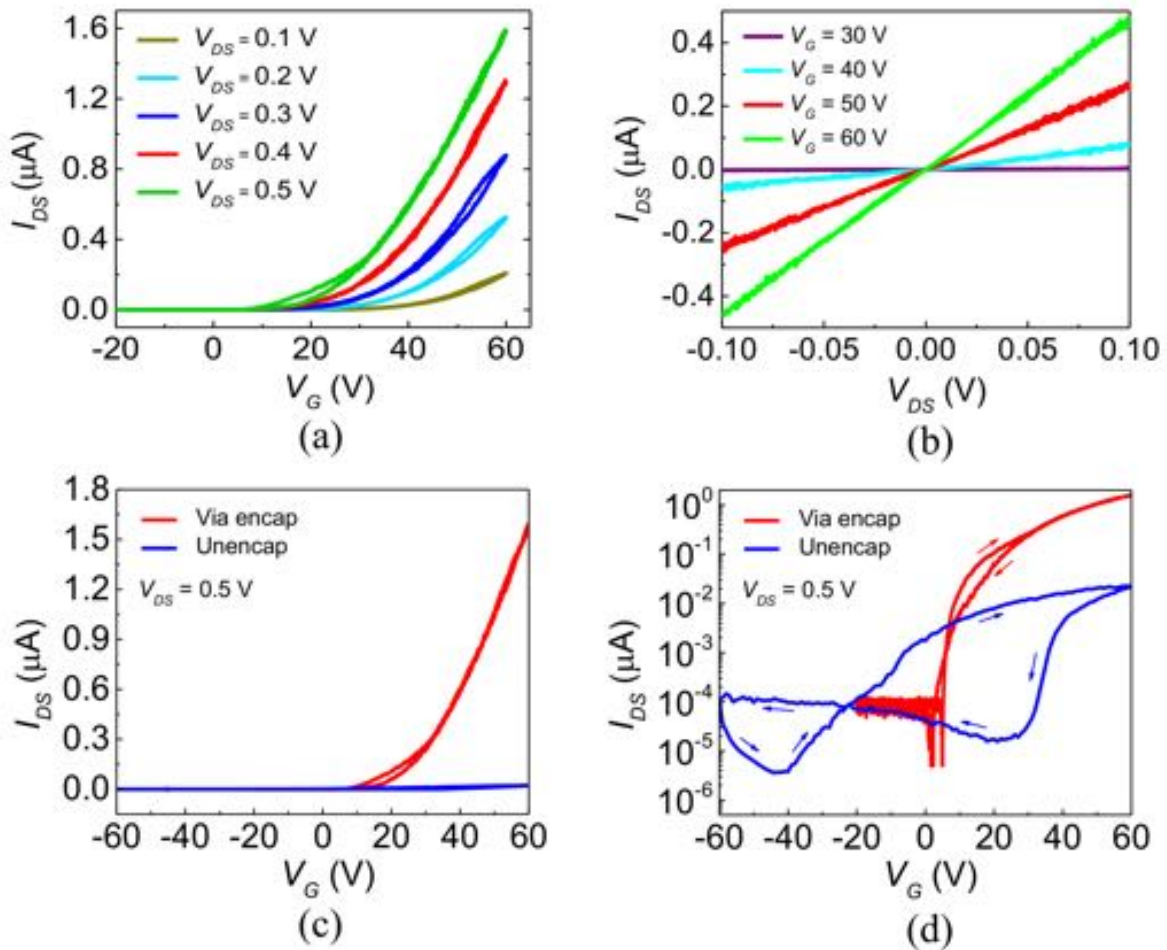


Figure 4.16: Transfer and output characteristics of the InSe-via device and its comparison with the unencapsulated InSe device, both shown in Figure 4.15. (a) Transfer characteristics of the InSe-via device at various V_{DS} , (b) output characteristics of the InSe-via encapsulated device for V_G varying from 30 V to 60 V, showing a linear characteristic and ohmic behavior, (c),(d) transfer characteristics for both devices at $V_{DS} = 0.5$ V in linear and semi-log scale, respectively, measured in back-gate configuration. The small arrows show the direction of the gate sweep. Adapted from Arora et al.^[6]

The performance of the devices is quantified by calculating on/off ratio and μ_{FE} . The bottom dielectric in the encapsulated device consists of 285 nm SiO₂ and 30 nm hBN layer. The capacitance (C_i) is obtained by adding the individual capacitances of both layers in series, assuming a parallel plate capacitor.

$$\frac{1}{C_i} = \frac{1}{C_{SiO_2}} + \frac{1}{C_{hBN}}; \quad C_{SiO_2} = \frac{\epsilon_0 \epsilon_{SiO_2}}{d_{SiO_2}}, \quad C_{hBN} = \frac{\epsilon_0 \epsilon_{hBN}}{d_{hBN}} \quad (4.2)$$

where $\epsilon_{SiO_2} = 3.9$ and $\epsilon_{hBN} = 3.5$.^[40,67,137] By using Equation 4.2, C_i is calculated to be 0.108×10^{-7} F cm⁻². The μ_{FE} for this device is extracted to be $30 \text{ cm}^2 \text{ V}^{-1} \text{ s}^{-1}$ with an on/off ratio of 10^4 , which compared to the unencapsulated device ($\mu_{FE} = 0.47 \text{ cm}^2 \text{ V}^{-1} \text{ s}^{-1}$, on/off = 500) is a significant improvement. For other InSe-via devices with InSe thicknesses of 8–12 nm, mobility ranging between $30\text{--}120 \text{ cm}^2 \text{ V}^{-1} \text{ s}^{-1}$ is obtained. The I – V characteristics of another InSe-via device is presented in Figure 4.17. The device is fabricated from a 12 nm thick InSe layer and demonstrates μ_{FE} of $85 \text{ cm}^2 \text{ V}^{-1} \text{ s}^{-1}$. Thus, as evident from the results, full hBN encapsulation is an effective passivation technique for InSe and yields smaller hysteresis, greatly enhanced μ_{FE} and larger on/off ratio as compared to the unencapsulated devices.

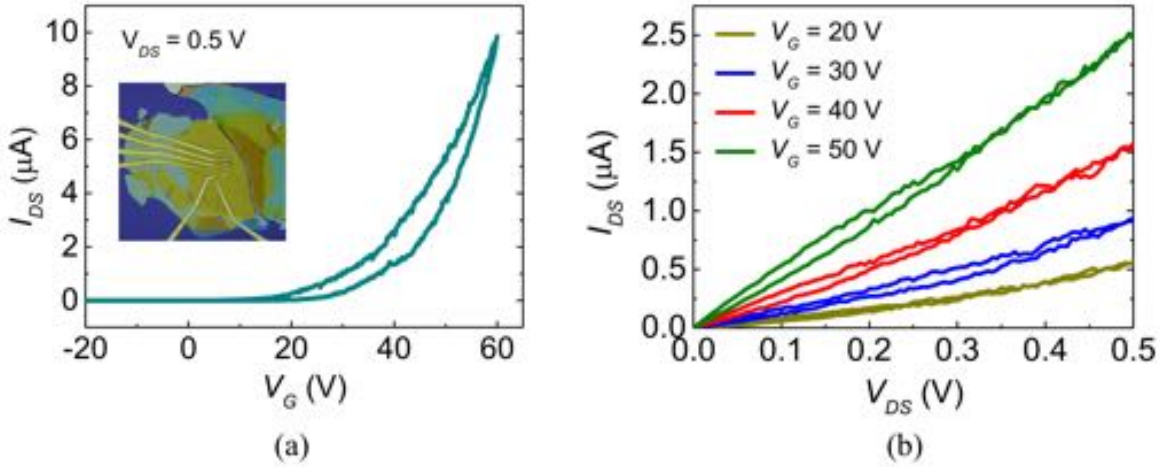


Figure 4.17: I – V characteristics of another InSe-via device. (a) Transfer curve of InSe-via device at $V_{DS} = 0.5$ V, yielding μ_{FE} of $85 \text{ cm}^2 \text{ V}^{-1} \text{ s}^{-1}$. Inset shows the optical image of the device, (b) output characteristic of the device at various V_G .

Following the demonstration of high performance, the encapsulated devices are measured over time to investigate their long-term stability. To do so, the samples are stored and measured in air for 15 days. The transfer curves of the encapsulated device (Figure 4.18a) show a stable and consistent charge transport for over 2 weeks, whereas the unencapsulated device has larger hysteresis and lower on-currents (Figure 4.18b). The large hysteresis and shift in the threshold voltage of the unencapsulated InSe device are attributed to the charge traps at the InSe/SiO₂ interface and to continuous adsorption/desorption of the gases because the samples are stored and measured in air. For the encapsulated sample, some changes in its transfer characteristics are observed after few days, which might be because of small amounts of moisture and gases getting trapped during the fabrication process. To completely

mitigate these issues, fabrication of the devices can be carried out under stringent atmospheric conditions, e.g. using an argon-filled glovebox instead of nitrogen.

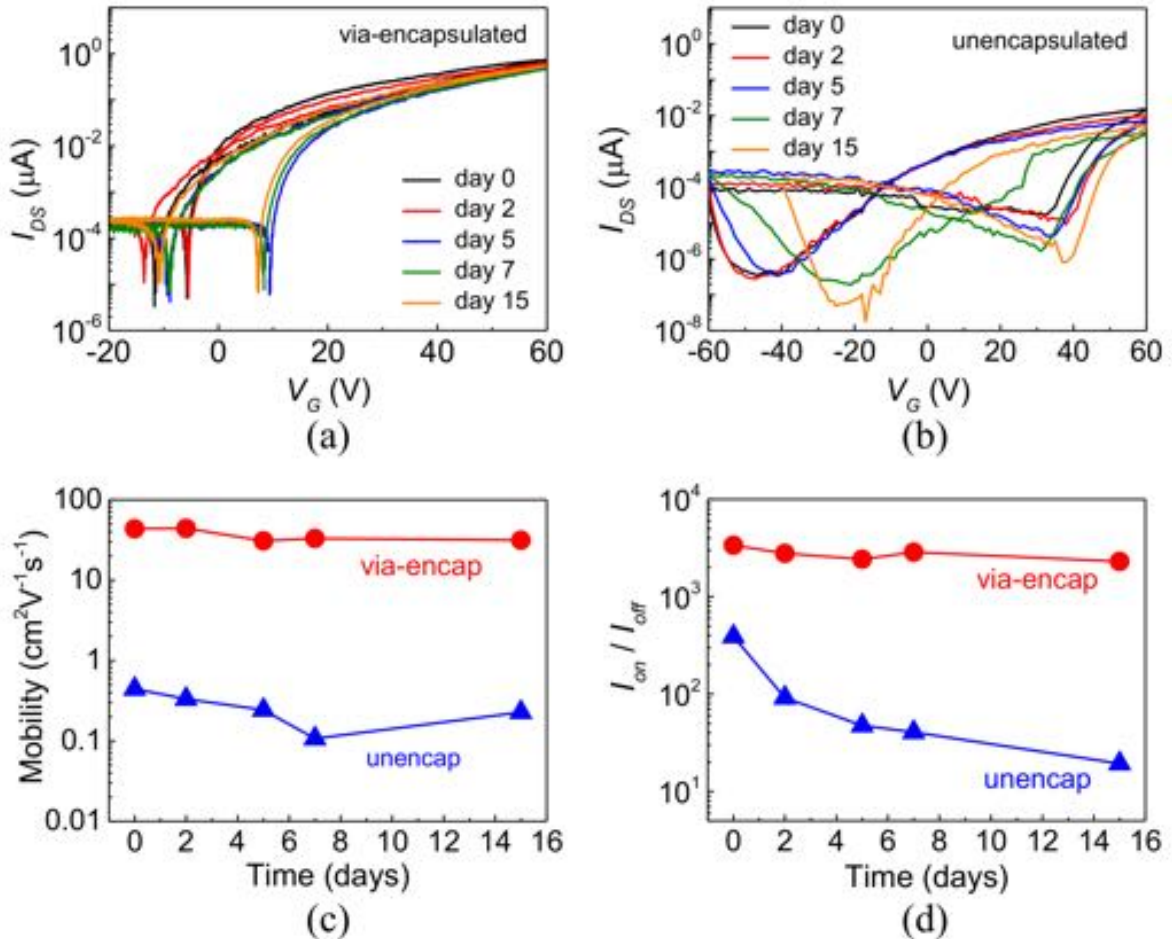


Figure 4.18: Transfer characteristics and FET parameters measured over time to investigate the stability of via-encapsulated and unencapsulated InSe devices. (a) Semi-log transfer curves of a via-encapsulated device at $V_{DS} = 0.5$ V, measured over 15 days. The on- and off-currents are reproducible with time indicating an ambient-stable device, (b) semi-log transfer curves of an unencapsulated device measured under the same conditions as the encapsulated device. Large hysteresis and unstable current demonstrates unreliable device characteristics. Evolution of (c) mobility, and (d) on/off ratio with time for both device configurations. Both parameters are unchanged for the encapsulated device, while the unencapsulated device degrades at a fast pace. Adapted from Arora et al.^[6]

The evolution of the field-effect mobility and on/off ratio for both devices over time is shown in Figure 4.18c,d, respectively. The unencapsulated device shows poor mobility and low on/off ratio as compared to the encapsulated device from the beginning and continues to deteriorate further with time. The performance of the encapsulated device, on the other hand, stays intact throughout the measured time period. It is important to mention that the unencapsulated device is fabricated and measured within a few hours from the time of exfoliation. This indicates that InSe is susceptible to degradation in air and during standard process steps of device fabrication. During the whole process, InSe layers come in contact

with various pre- and post-lithographic solvents, which may induce structural damage, tunnel barriers and pinning of the Fermi-level.^[144] The presence of tunnel barriers and Fermi-level pinning results in non-ohmic contacts, low on-current, and poor mobility as seen for the unencapsulated devices.^[17,152] Wei et al.^[14] have shown that adsorption of oxygen atoms into the InSe structure causes serious hampering of the electronic properties with mobility and other FET parameters to decrease 2–3 orders in magnitude. Therefore, it is essential to passivate InSe from air and other detrimental processes where its structural integrity can be compromised. In this regard, the top and bottom hBN encapsulation scheme is extremely useful as it protects InSe from various forms of degradation and disorder, and allows us to study its intrinsic properties.

5.4 Optoelectronic properties of GaSe-via devices

The full hBN encapsulation is subsequently integrated into GaSe, another emerging 2D material belonging to the same family as InSe, but far more sensitive under ambient conditions. The effectiveness of hBN encapsulation in suppressing GaSe degradation is supported by low-temperature micro-PL measurements as shown in Figure 4.19. On measuring various thicknesses of GaSe layers (18–28 nm), 10 times higher PL peak intensity is observed on full hBN encapsulation, whereas unencapsulated GaSe shows significant PL reduction within 3 hours from the time of exfoliation. In addition, a slight blue-shift of the PL peak is also observed in the encapsulated samples, which can be attributed to the aforementioned reasons causing the peak to shift to higher energies in multi-layered structures. Another possible reason for the blue-shift can be the strain between the layers. A recent study by Han et al.^[153] shows that the hBN encapsulation can cause tensile strain in the 2D layers, arising during the vdW heterostructure assembly process. When different layers are pressed onto each other and could not relax fully, deformation can arise in the stack. Though this strain should be less pronounced in multi-layered structures, the possibility cannot be fully ruled out.

Figure 4.20a shows one of the GaSe-via devices fabricated in this study. The Pd/Au via-contact forms an ohmic contact with GaSe layers, as seen from the output curves of four different devices in Figure 4.20b. The difference in the I_{DS} levels is attributed to different thicknesses of GaSe and via-contact geometries. For all GaSe-via devices, a *p*-type conductance and μ_{FE} of $\sim 0.5\text{--}0.8 \text{ cm}^2 \text{ V}^{-1} \text{ s}^{-1}$ is obtained, which is comparable to the previously reported values.^[72,79,80] Since GaSe finds a majority of its applications in optics, the large bandgap of hBN ($\sim 5.7 \text{ eV}$)^[90] is highly advantageous, as it stays transparent for the wavelengths where GaSe is optically active. The photoresponse obtained for the GaSe-via device under global illumination by a blue laser (405 nm) at various power settings is shown in Figure 4.20c,d. As the device is illuminated by higher laser power, I_{DS} increases monotonically because of the increased number of electron-hole pairs generated. In response to a pulsed illumination at 405 nm, the device shows a reproducible photoswitching behavior and maintains long-term stability of its photoresponse (Figure 4.20c). The rise in current from off to steady-state on light illumination occurs within a 20 ms time interval, which is the resolution of the measurement setup. It is probable that the photoresponse time is less than

20 ms, which is comparable to the response times of 10–20 ms reported previously with top Au contacts.^[73,75] The photocurrent, $I_{PH} = I_{light} - I_{dark}$ (plotted in Figure 4.20d), increases with increasing incident power densities.

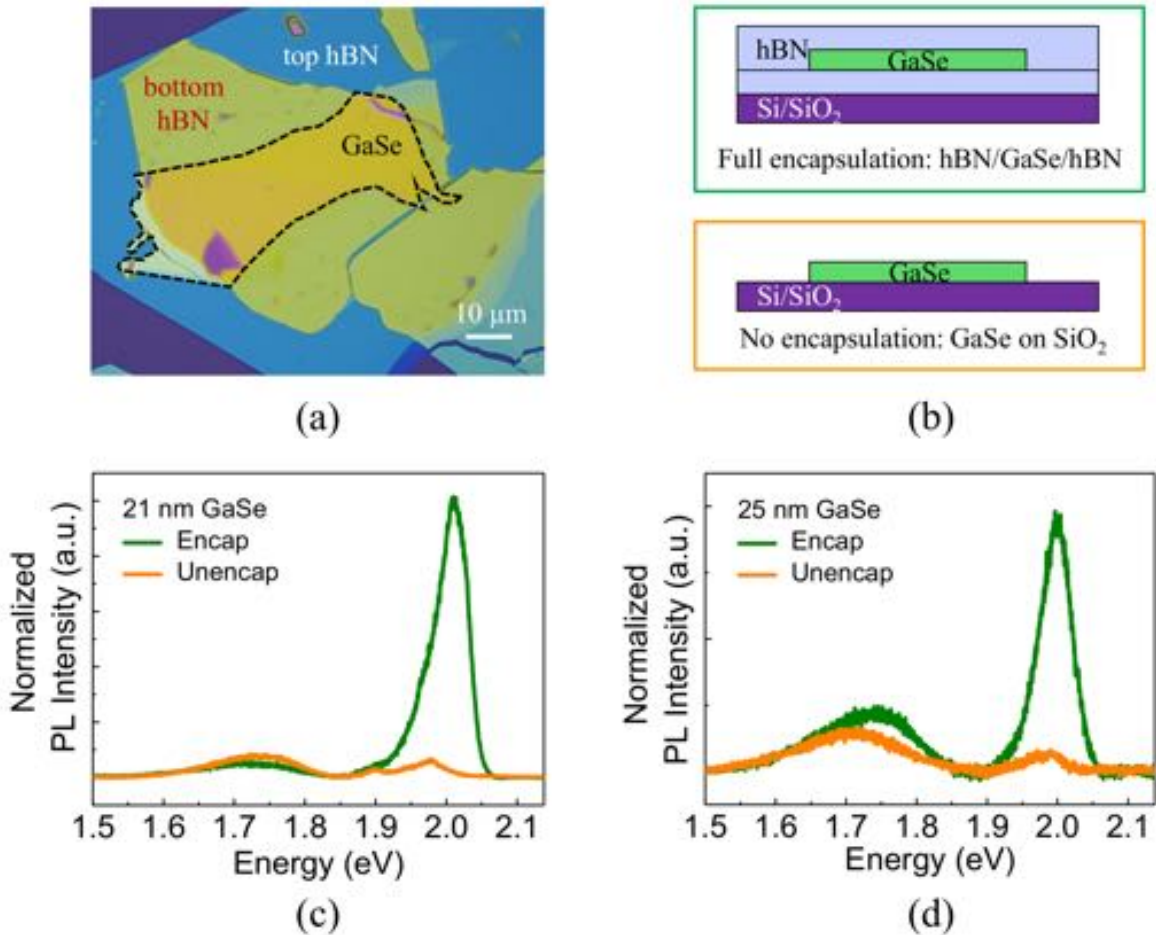


Figure 4.19: Low-temperature micro-PL measurements of few-layered GaSe. (a) Optical micrograph of the stack used for PL measurements (~ 21 nm GaSe sandwiched between top and bottom hBN), (b) schematics of two GaSe based stack configurations, measured and compared to analyze the effect of hBN on GaSe degradation, (c),(d) PL spectra measured at 4.2 K for 21 nm and 25 nm thick GaSe, respectively, with and without encapsulation. Adapted from Arora et al.^[6]

Responsivity, defined as the amount of photocurrent generated per unit incident illumination and calculated as the ratio of the photocurrent density to the incident power density ($R = I_{PH}/PA$; P is incident power density, A is exposed device area), is found to be decreasing as the incident power increases. This trend is frequently observed in photoconductive photodetectors and is attributed to the reduced numbers of photogenerated carriers available for extraction at higher power illuminations (due to the Auger process or the saturation of recombination/trap states, the lifetime of the generated carriers reduces at higher powers).^[154] It should be noted that a direct comparison between responsivity of different photodetectors should be done only under similar environmental conditions. At an incident power density of 0.3 mW cm⁻² ($V_G = -80$ V and $V_{DS} = 2$ V), a responsivity of 84.2 A W⁻¹ is achieved,

which is a major improvement over the top encapsulated GaSe photodetectors reported previously under same conditions.^[81]

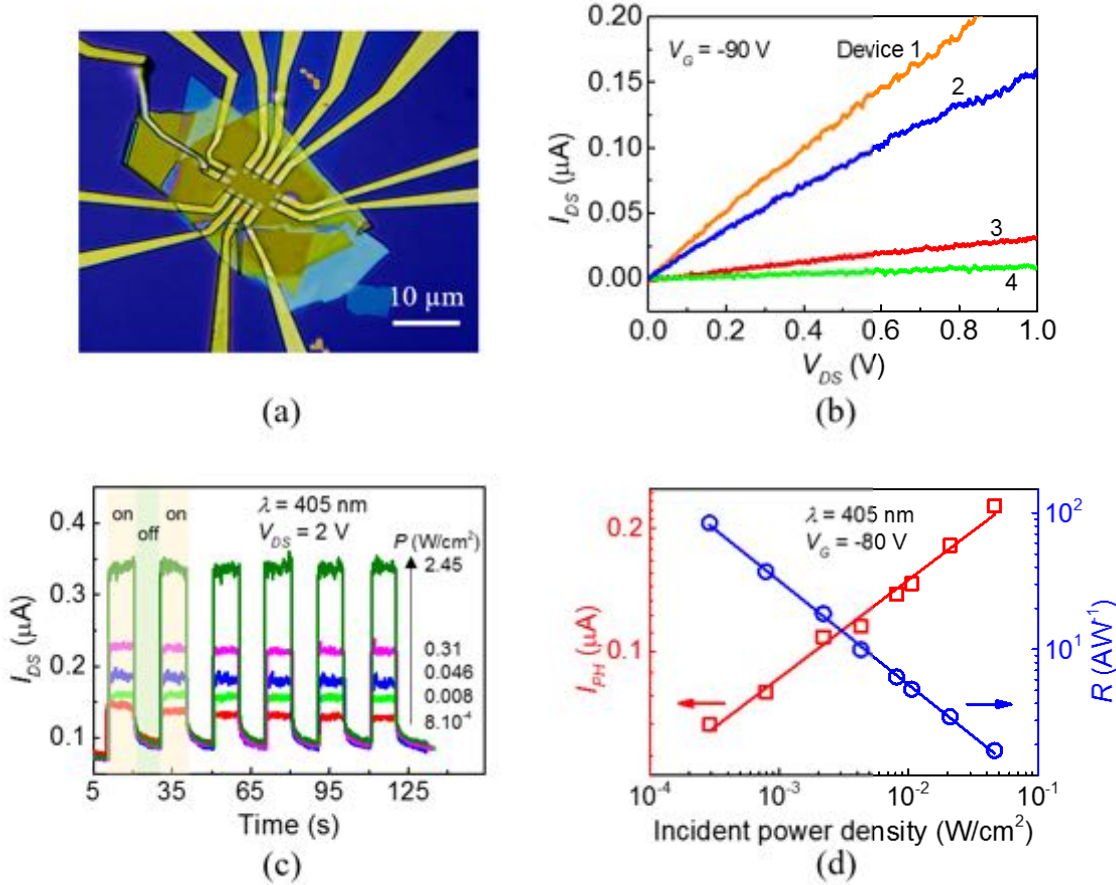


Figure 4.20: Electronic and optoelectronic properties of fully encapsulated GaSe devices. (a) Optical image of a GaSe-via device, (b) output characteristics of four different GaSe-via devices labeled as Device 1, 2, 3 and 4 at $V_G = -90$ V, (c) photoswitching response obtained for pulsed illumination of 405 nm at $V_G = -80$ V, $V_{DS} = 2$ V and various laser power densities, (d) photocurrent (red open squares) and responsivity (blue open dots) as a function of incident power density (at $V_G = -80$ V, $V_{DS} = 2$ V). Red and blue straight lines are obtained by fitting the measured data. Adapted from Arora et al.^[6]

For optoelectronic properties of GaSe, Table 4.2 is formulated, comparing the key parameters with previously published reports. The photoswitching performance of the devices fabricated in this work is comparable to state-of-the-art values reported by others. The high photoconductive gain of our device could be related to its transistor operation. Due to large gate bias applied to the device, the channel is accumulated with majority charge carriers, which results in high photocurrent and in turn high responsivity.

Table 4.2
Comparison of the key parameters for GaSe-photodetectors

GaSe thickness	V_G (V)	Mobility ($\text{cm}^2\text{V}^{-1}\text{s}^{-1}$)	Wavelength (nm)	Response time	Responsivity (A W^{-1})	Reference
20–30 nm	−80	0.5–0.8	405	20 ms	84.2	this work ^[6]
Nanosheet	−60	—	white light	—	8	[82]
Nanosheet	—	—	254	20 ms	2.8	[73]
45 nm	−18	0.13	532	—	0.9	[79]
20–30 nm	0	5×10^{-3}	410	10–20 ms	1200	[75]

5.5 Conclusions

The sensitivity of few-layered InSe and GaSe towards air, bottom dielectrics and lithography processes makes the assessment of their intrinsic properties difficult. We demonstrate that in order to obtain high-quality and stable devices, their full encapsulation in hBN layers is extremely advantageous as it protects the 2D layers from ambient degradation as well as from the charge disorder at the SiO_2 surface. The fully encapsulated InSe and GaSe devices show greatly enhanced and ambient-stable performance as compared to their unencapsulated counterparts. In contrast to previous studies, where either good performance or long-term stability was reported, we demonstrate a combination of both in our devices. hBN, due to its inertness, atomically flat surface and absence of charge traps, is an optimal encapsulation for fabricating reliable InSe- and GaSe-based devices. Our encapsulation technique is robust and easily transferable to other complex 2D materials which might not be compatible to the chemistry of ALD and dry oxidation techniques. Thus, this method opens up new avenues for the investigation of 2D materials which have been restricted so far in their fundamental study and applications because of their environmental sensitivity.

Chapter 5

Charge transport in 2D metal-organic frameworks

In this chapter, we investigate the electronic properties of a novel π -d conjugated semiconducting $\text{Fe}_3(\text{THT})_2(\text{NH}_4)_3$ (THT: 2,3,6,7,10,11-hexathioltriphenylene) 2D MOF. To understand the charge transport mechanisms, we performed the very first Hall-effect measurements on a MOF system. The thin films under investigation are developed by Dr. Renhao Dong in the group of Prof. Xinliang Feng at Technische Universität Dresden. The structural and morphological characterization of the material are carried out solely by them, whereas the temperature-dependent electrical characterization using conductivity measurements (two-probe and four-probe) and Hall-effect measurements are conducted by myself at HZDR.

The findings presented in this chapter have been published as:

- R. Dong, P. Han, **H. Arora**, M. Ballabio, M. Karakus, Z. Zhang, C. Shekhar, P. Adler, P. S. Petkov, A. Erbe, S. C. B. Mannsfeld, C. Felser, T. Heine, M. Bonn, X. Feng, and E. Cánovas, “High-mobility band-like charge transport in a semiconducting two-dimensional metal-organic framework”, *Nature Materials* **17**, 1027–1032 (2018).

1 Introduction

MOFs represent a class of hybrid materials where metal ions or clusters coordinate with organic linkers to form long-range ordered crystalline structures with tunable pore sizes (<1 nm to 10 nm).^[103,104] Due to their tunable porosity, large surface-to-volume ratios have been developed. As a result, MOFs have been primarily considered for application in gas storage/separation,^[108,109,155] drug delivery,^[110,111] and catalysis^[112,113] so far.

The recent discovery of electrically conductive MOFs has opened new areas of potential applications of MOFs in optoelectronics and chemiresistive sensing.^[114,119,125,156] The first report on a conductive π -conjugated 2D MOF based on triphenylene-fused metal-catecholates demonstrated a conductivity of 0.1 S cm^{-1} .^[117] Since then, much improved conductivities up to 1580 S cm^{-1} in benzene-fused metal-bis(dithiolene) based on Ni and Cu complexes

have been reported.^[121,122] These conductivity values are measured at room temperature using two-probe, four-probe and van der Pauw methods.^[125] In all cases, reducing the temperature of the sample resulted in a decrease of the conductivity, an effect that can be tentatively attributed to a hopping-type thermally activated transport. From these conventional conductivity measurements, it is challenging to address the nature of the transport in semiconducting MOFs. This is primarily because these techniques measure the conductivity, which is defined by the product of charge carrier density and mobility that can both vary with temperature. Therefore, the true nature of charge transport in semiconducting MOFs, e.g. whether a hopping or band-like transport mechanism is operative, has remained unresolved.^[114,125] Addressing the fundamentals of charge transport in semiconducting MOFs is essential for further MOF designing as well as to allow this class of materials to be exploited in optoelectronic applications.

2 A novel 2D MOF: $\text{Fe}_3(\text{THT})_2(\text{NH}_4)_3$

Here, we investigate charge transport mechanisms in a novel, π -d conjugated semiconducting $\text{Fe}_3(\text{THT})_2(\text{NH}_4)_3$ or Fe-THT (THT: 2,3,6,7,10,11-hexathioltriphenylene) 2D MOF. To address the nature of charge transport in these MOF films, four-probe conductivity and Hall-effect measurements are carried out. The findings show that the thin films of $\text{Fe}_3(\text{THT})_2(\text{NH}_4)_3$ support band-like charge transport and a room temperature Hall mobility of $\sim 230 \text{ cm}^2 \text{ V}^{-1} \text{ s}^{-1}$, which to the best of our knowledge, represents a record-high mobility in MOFs.^[114,125]

2.1 Synthesis

The synthesis and structural characterization of $\text{Fe}_3(\text{THT})_2(\text{NH}_4)_3$ MOF films are performed by the group of Prof. Xinliang Feng at Technische Universität Dresden. However, to facilitate better understanding of the results obtained from an in-depth electrical characterization, a detailed summary of synthesis protocol and the key findings obtained from the material's characterization is included in the following sections.

The $\text{Fe}_3(\text{THT})_2(\text{NH}_4)_3$ MOF films are synthesized by an interfacial reaction protocol. Water and CHCl_3 phases host THT and iron precursors (iron acetylacetone, $\text{Fe}(\text{acac})_2$), respectively. The incorporation of THT ligands with Fe centers provides a means to achieve charge transfer and enhance conductivity. A cylindrical glass vial (80 ml, 5 cm in diameter) containing $\text{Fe}(\text{acac})_2/\text{CHCl}_3$ solution (20 ml, 0.5 mM) is used as the reaction container. Next, water (10 ml) is dropped onto the organic phase to form an oil/water interface. A solution (20 ml) containing THT monomers (1 mM) in water along with NH_4OH (10 mM) is injected onto the top water phase. A spontaneous metal coordination reaction takes place at the CHCl_3 /water interface under argon atmosphere at room temperature, resulting in the formation of a large-area free-standing film. The as-prepared films are either used directly or transferred onto various substrates (such as, SiO_2/Si). Depending on the reaction time, the film thickness can be tailored from 20 nm up to several μm . In this work, $\sim 1.7 \mu\text{m}$ thick films are employed, which are formed after 72 hours of the reaction time.

2.2 Structural characterization

The chemical structure of $\text{Fe}_3(\text{THT})_2(\text{NH}_4)_3$ MOF film is shown in Figure 5.1a, where the Fe metal and THT organic ligands are bonded in a honeycomb structure with a pore size of $\sim 1.9 \text{ nm}$. Figure 5.1b shows a monolayer of $\text{Fe}_3(\text{THT})_2(\text{NH}_4)_3$ MOF film, possessing a planar hexagonal geometry extended into two directions, thus, forming a 2D network. When these MOF monolayers superimpose via vdW interactions in a preferred stacking pattern, multi-layered structures are formed. Powder X-Ray diffraction demonstrates an in-plane hexagonal packing and an inclined AA stacking pattern perpendicular to the layer plane as shown in Figure 5.1c, with an interlayer distance of $\sim 0.33 \text{ nm}$. These results are independently confirmed by DFT, which also shows the inclined AA stacking pattern energetically favorable as compared to AA eclipsed and AB stacking.

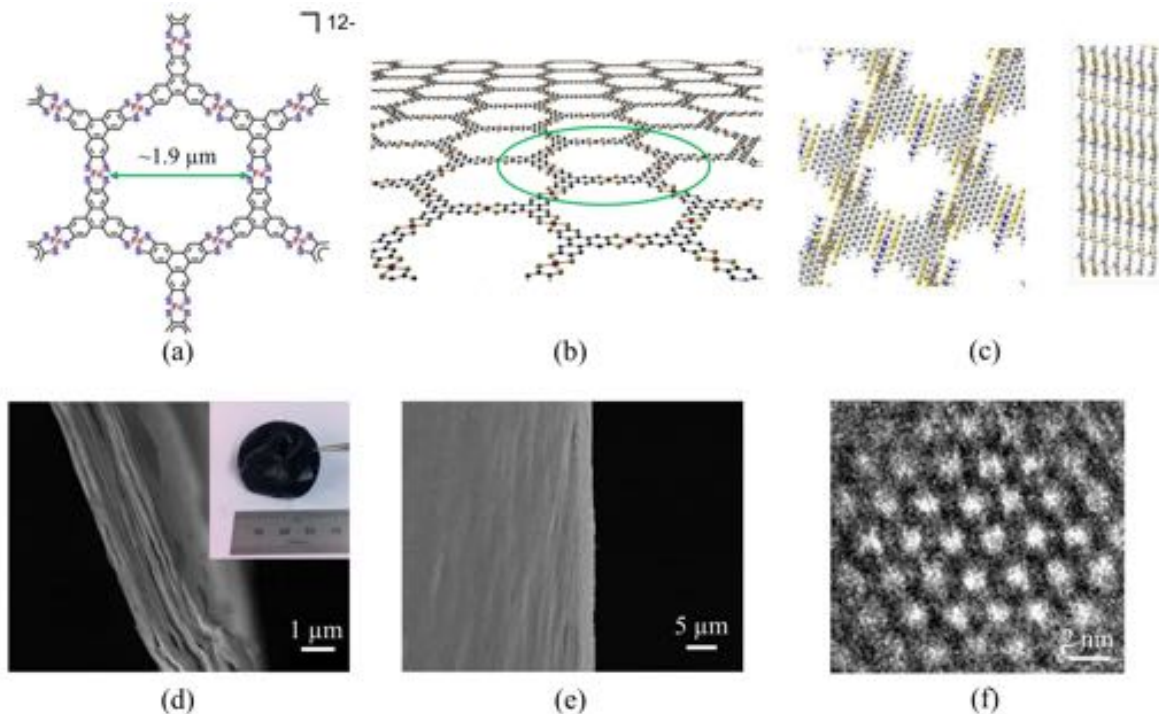


Figure 5.1: Structural characterization of $\text{Fe}_3(\text{THT})_2(\text{NH}_4)_3$ 2D MOF films. (a) Chemical structure of the MOF film, Fe metal and THT organic ligands are bonded via sulfur in a honeycomb structure with a pore size of $\sim 1.9 \text{ nm}$, (b) schematic of a monolayer of Fe-THT MOF film, (c) DFT calculated AA inclined stacking arrangement for the layers of Fe-THT MOF, (d) SEM image of the cross-section revealing multilayers stacked via vdW interactions. Inset: photograph of a large-area free-standing film, (e) SEM image of the top surface of $1.7 \mu\text{m}$ thick MOF film, showing a flat and crack-free surface, (f) HRTEM image of the honeycomb structure (scale bar: 2 nm). Adapted from Arora et al.^[3] and Dong et al.^[9]

An as-synthesized free-standing Fe-THT film is shown in the inset of Figure 5.1d and reveals a lateral dimension extending up to a few mm. SEM images in Figure 5.1d,e reveal vdW stacked films that are flat and crack-free over large areas. Such large and uniform film areas are a major advantage over inorganic 2D materials for scalability of the devices. Further characterization by high-resolution transmission electron microscopy (HRTEM) confirms the

high-quality polycrystalline nature of as-prepared $\text{Fe}_3(\text{THT})_2(\text{NH}_4)_3$ MOF films with grain sizes ranging from tens to hundreds of nanometres. A honeycomb lattice structure with a pore size of ~ 1.9 nm is also observed (Figure 5.1f). A long-range ordered crystalline structure with unit cell dimension of ~ 1.97 nm is revealed from selected area electron diffraction. In addition, the MOF films are found to be porous with a surface area of $526 \text{ m}^2 \text{ g}^{-1}$ as inferred by the Brunauer-Emmett-Teller method. Using X-ray photoelectron spectroscopy, a high degree of coordination between the Fe ions and thiol groups with an Fe:S ratio of 0.97:4 is observed, which is close to the theoretically expected ratio of 1:4. EDS mapping further confirms this large degree of iron-sulfur coordination with Fe:S ratios of 0.9:4 over the whole film area.

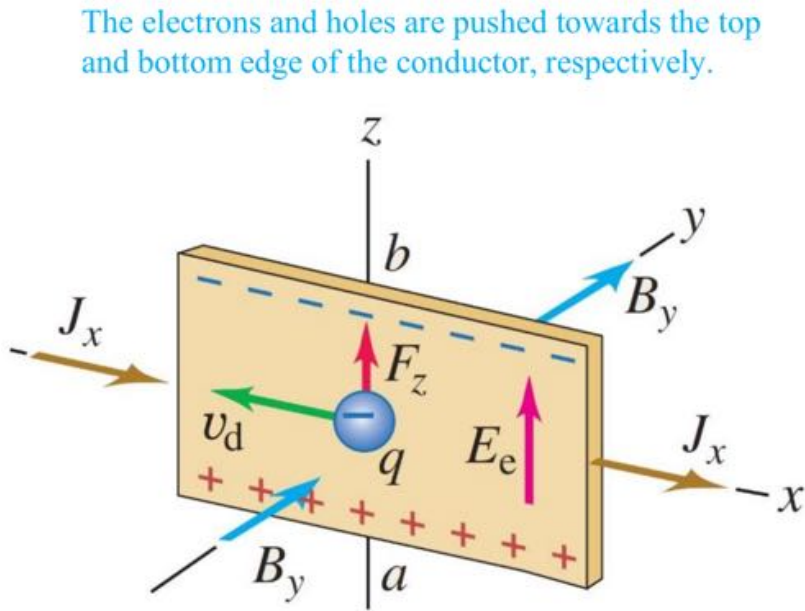
The presence of redox-active iron-bis(dithiolene) centers triggers the semiconducting nature of the MOF films. The DFT calculations estimate a bandgap of ~ 0.35 eV for the $1.7 \mu\text{m}$ thick film, which reduces to 0.30 eV for monolayers. Fourier-transform infrared spectroscopy (FTIR) of MOF films confirm a direct bandgap, with an absorption edge lying between 0.25–0.45 eV (the variability is likely to be associated with sample-to-sample variations in the local carrier concentration induced by doping). The DFT calculations further report a fully delocalized π -electron cloud over the conjugated plane. For the inclined AA stacked sample, the calculated effective mass of holes is found to be smaller than of electrons, suggesting higher hole mobility ($m_h^* = 0.78 m_0$, $m_e^* = 0.98 m_0$ for holes and electrons, respectively, m_0 is the electron rest mass).

3 Electronic transport in $\text{Fe}_3(\text{THT})_2(\text{NH}_4)_3$ 2D MOF films

Though high conductivities have been reported in 2D MOF structures, all previous reports demonstrated a hopping-type charge transport dominant in these materials rather than band-like transport.^[125,157–160] A systematic methodology to conclude a charge transport mechanism (hopping or band-like), is to perform temperature-dependent conductivity measurements. Generally, an increase in conductivity with rising temperature suggests hopping conduction; whereas a decrease in conductivity with temperature indicates band conduction. However, addressing the nature of charge transport only from the conductivity measurements can be misleading. This is because, as per Drude model (Equation 2.4), the conductivity (σ) is defined as the product of charge carrier density (N) and mobility (μ), that can both vary with temperature.

Temperature dependence of the conductivity provides only preliminary information on the nature of charge transport. A linear dependence of the natural logarithm of conductivity on the reciprocal of the absolute temperature is a tentative indication of band-like transport. On the other hand, hopping transport shows a linear relation between $\ln \sigma$ and T^{-n} ($n < 1$), where the value of n determines the hopping-model. A clear insight into the charge transport mechanism can be obtained by Hall-effect measurements. It also quantifies the material's properties by determining charge carrier density and intrinsic mobility with high accuracy.

Hall-effect Discovered in 1879 by the American physicist Edwin Hall, the Hall-effect is one of the most powerful techniques for measuring intrinsic electrical properties of a material. It provides an accurate estimation of charge carrier density, carrier mobility and type of doping.



An electric field builds up because point a is at a higher electric potential than point b .

Figure 5.2: Lorentz forces acting on the charge carriers in a magnetic field.^[161]

The Hall-effect is observed when a current-carrying conductor is placed in a perpendicular magnetic field. Because of Lorentz force $q\vec{v} \times \vec{B}$, charge carriers are deflected in a direction perpendicular to both current and magnetic field. Figure 5.2 shows the orientations of charge carriers experiencing Lorentz force in a conductor with length l , width w , and thickness t , when the current flows in the $+x$ -direction (I_x) and a uniform magnetic field is applied in $+y$ -direction (B_y). Electrons and holes, because of their opposite polarities, experience forces in upward and downward direction, respectively. Excess electrons then get accumulated at the top edge of the conductor, leaving holes at its lower edge. This reverses with the direction of the magnetic field. The excess accumulation of one type of charge carriers on one side of the conductor generates a transverse potential difference between the two edges, which counteracts the Lorentz force. After that, a steady state is reached and no net transverse force exists to deflect the moving charge carriers. This built-in potential is called “Hall voltage” (V_H) and is directly proportional to the magnetic field and the current as:^[162]

$$V_H = -\frac{I_x B_y}{e N t} \quad (5.1)$$

From Equation 5.1, the Hall coefficient (R_H) is defined as:

$$R_H = -\frac{1}{eNt} \quad (5.2)$$

R_H contains the information on the charge carrier density (N) and sign of the carriers, i.e. doping-type in the conductor. Once charge carrier density is known, mobility (μ) is determined from Drude model (Equation 2.4). For this, conductivity should be measured first, which is discussed in the next section.

Four-probe conductivity measurements The conductivity of the sample is measured in the absence of magnetic field by using the four-probe method. As the name suggests, this method utilizes four probes or contacts; two outer probes for passing the current and two inner probes for measuring the voltage difference. Since the potential difference is measured between different terminals than the ones carrying the current, this method excludes the role of contact resistances and therefore, provides a precise estimation of the intrinsic sample conductivity. Figure 5.3 shows the arrangement of the four probes to measure the sheet conductivity of a rectangular conductor. For a reliable measurement, the realization of ohmic contacts between the metal and the semiconductor is important. Ohmic contacts ensure an efficient and loss-free injection of the charge carriers. The four-probe conductivity (σ_{xx}) is deduced by using the following equation:^[162]

$$\sigma_{xx} = \frac{I_y b}{V_{xx} w t} \quad (5.3)$$

where b is the distance between the voltage probes, and w and t are width and thickness of the sample, respectively.

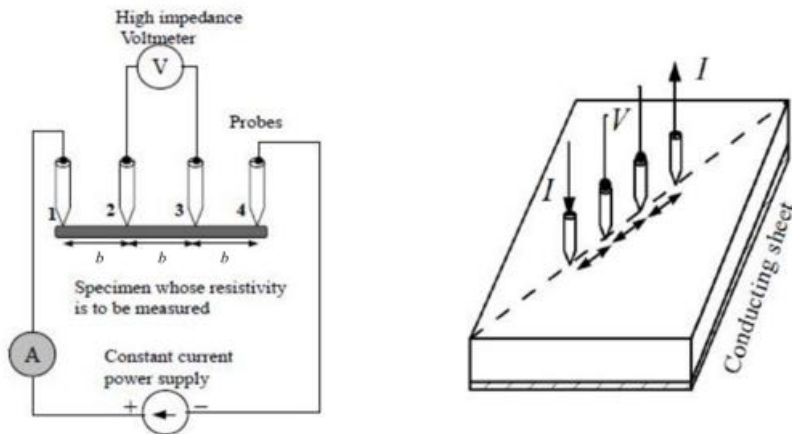


Figure 5.3: Principle of four-probe conductivity measurements of a rectangular conductor. Current is passed across probes 1 and 4, potential difference is measured across probes 2 and 3.^[161]

Sample geometry The Hall-effect and conductivity measurements illustrated before in a rectangular slab conductor provide an ideal case. In a real-case scenario, the experimental

determination of transport properties of a material requires significant consideration over the sample geometry and configuration. The sample geometry commonly employed for Hall-effect measurements is shown in Figure 5.4. In order to measure Hall voltage between the transverse contact pairs 2-6 or 3-5 and four-probe conductivity between parallel contact pairs 2-3 or 5-6, a minimum of six contacts is necessary. The length of the sample is generally kept about four times its width so that the electric current streamlines have an opportunity to become laminar or the electric potential lines to become parallel and perpendicular to the edges of the sample. The values of the Hall coefficient and the four-probe conductivity are highly sensitive to the sample geometry. An ideal Hall bar geometry consists of point contacts made at the end of the extended arms.^[163,164] However, because of experimental limitations, electrical contacts always have some finite width, which may give rise to geometrical resistances.^[163] To minimize these geometrical contributions, care should be taken with respect to the size and placement of electrical contacts and voltage probes to the sample.

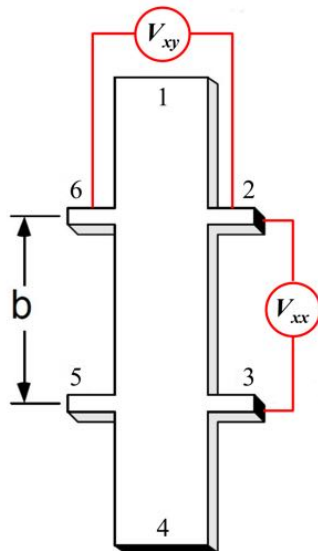


Figure 5.4: Hall bar geometry consisting of six electrical contacts required to measure the Hall voltage.^[163]

3.1 Two-probe conductivity measurements

To analyze the conductivity of $\text{Fe}_3(\text{THT})_2(\text{NH}_4)_3$ MOF films, two-probe I - V measurements are carried out for the MOF films with varying thicknesses (from 20 nm to 1.7 μm). Devices are fabricated by transferring the film onto a *p*-doped 300 nm SiO_2/Si substrate. With the help of a shadow mask, planar interdigitated finger electrodes are evaporated onto the sample using Au metal as shown in Figure 5.5.^a The channel length between the two electrodes is 100 μm and the width is 4.5 mm (Figure 5.5b). The electrical characterizations of the devices with different MOF thicknesses are carried out in the dark and under vacuum (10^{-8} mbar) using a parameter analyzer (Agilent 4156C, Agilent Technologies).

^a The top Au electrodes are thermally evaporated under 10^{-9} bar vacuum conditions at a rate of 1.5 \AA s^{-1} to a final thickness of 70 nm.

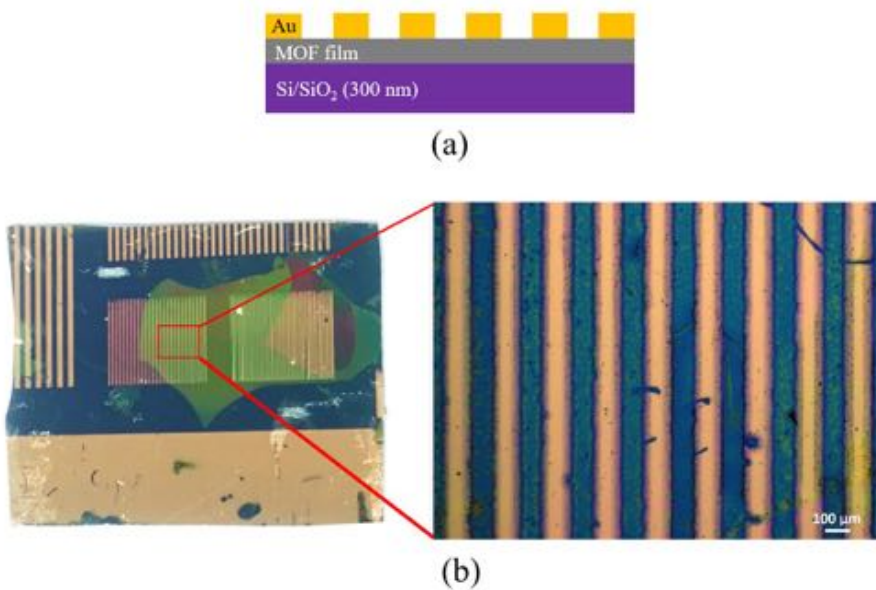


Figure 5.5: Two-terminal device based on a large-area MOF film. (a) Schematic of a MOF device with interdigitated finger electrodes, (b) photograph and optical image (enlarged image on the right) of a $\text{Fe}_3(\text{THT})_2(\text{NH}_4)_3$ MOF device on a 300 nm SiO_2/Si substrate. Au electrodes are deposited to form finger electrodes with a channel length of 100 μm and a width of 4.5 mm.

Figure 5.6 shows the I - V curves measured for different MOF film thicknesses. Ohmic responses are obtained in the measured voltage range, indicating efficient charge injection from Au electrodes into the MOF film. As expected, the conductance of the MOF film is increasing with the film thickness because of a higher amount of the conducting material.

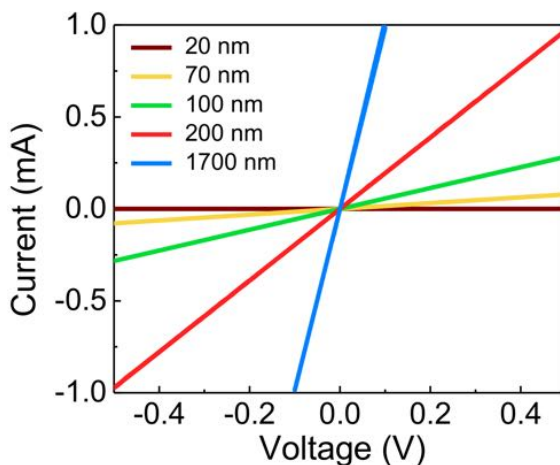


Figure 5.6: I - V curves measured at room temperature for Fe-THT MOF films with varying film thicknesses.

To gain deeper insight into the underlying charge transport mechanisms, temperature-dependent conductivity measurements for the 70 nm thick film in the temperature range of 320 K down to 4.2 K are carried out at regular temperature intervals of 5 K. A probe station (Model CPX-VF, *Lakeshore*) cooled by continuous flow of liquid He is used for

low-temperature measurements. Measurement of conductivity as a function of time at 10 K revealed weak thermal coupling of the MOF film to the environment and that the base temperature is achieved after a cooling period of about 10 min. Hence, to make sure that the sample is at the set temperature, a waiting time of 10 min is enforced before measuring the I - V curves. The temperature-dependent I - V characteristics plotted in Figure 5.7 reveals the formation of ohmic contacts between the metal and the MOF film for the temperature range of 70–320 K. In addition, no hysteresis is seen in the curves, which indicates the absence of interfacial states and a strong bonding between the metal and the MOF layer.

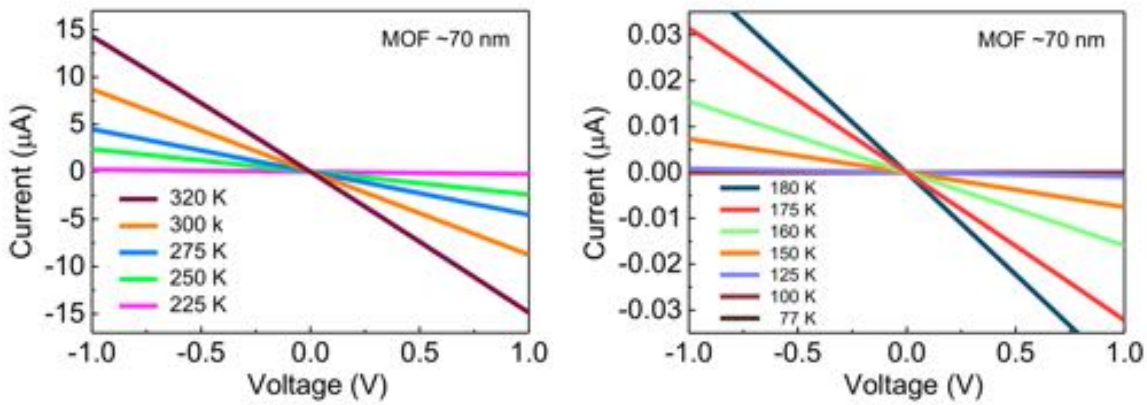


Figure 5.7: Temperature-dependent I - V curves for the 70 nm thick Fe-THT MOF film, displaying ohmic response between -1 and 1 V.

The electrical conductivity shows a strong temperature dependence as seen in Figure 5.8, decreasing by almost eight orders of magnitude from 0.47 S cm^{-1} at 320 K to $5.5 \times 10^{-9} \text{ S cm}^{-1}$ at 70 K, a fact confirming the intrinsic semiconducting nature of the MOF films. Within the same plot of $\log \sigma$ versus $1/T$ in Figure 5.8, a distinct linear region can be identified for temperatures above 150 K. The linear region in this temperature range is fitted with the Arrhenius distribution given as:

$$\sigma = \sigma_0 \exp \left(\frac{-E_a}{kT} \right) \quad (5.4)$$

where σ_0 is a prefactor, E_a is the activation energy, k is the Boltzmann constant and T is the absolute temperature. From Equation 5.4, $E_a = 0.202 \pm 0.008 \text{ eV}$ (slope of the red fitted line in Figure 5.8) is obtained. This value is in reasonable agreement with the bandgap value of 0.245 eV inferred optically for this sample, suggesting conduction via direct excitation of charge carriers from the valence band to the conduction band. At temperatures below 70 K, the MOF film shows negligible conductivity. The I - V characteristics demonstrates increasingly non-ohmic behavior and large hysteresis as seen in Figure 5.9. This can be tentatively attributed to the formation of highly localized states at such low temperatures. The strong variation of conductivity with temperature suggests a thermally activated charge carrier density in the samples and/or a reduction in sample's mobility induced by scattering sites, such as grain boundary scattering; the former and the latter being consistent with

the low bandgap of the analyzed MOFs and the polycrystalline nature of our samples, respectively. To disentangle the potential contribution of these two effects on the conductivity, we performed temperature-dependent Hall-effect measurements on the $\text{Fe}_3(\text{THT})_2(\text{NH}_4)_3$ 2D MOF films.

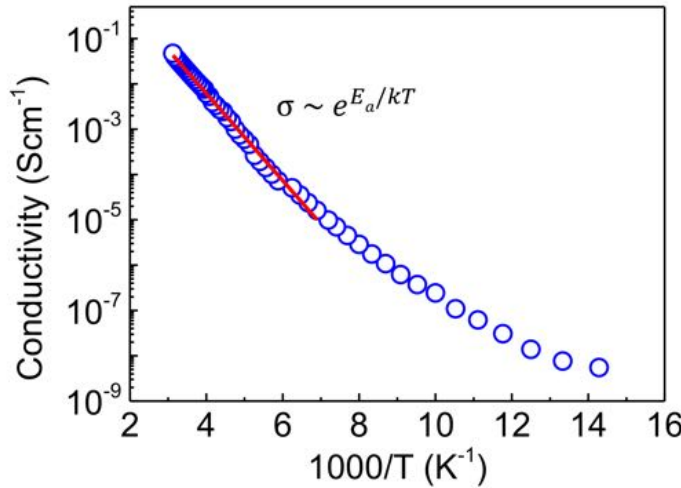


Figure 5.8: Logarithmic dependence of the two-probe conductivity on the reciprocal temperature. The red line represents a linear fit revealing Arrhenius-type activation within the temperature range of 150–320 K.

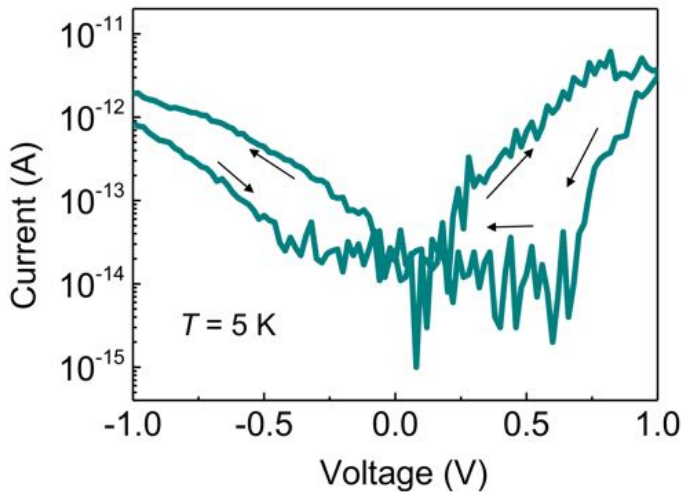


Figure 5.9: I - V curve at 5 K for the Fe-THT MOF sample, demonstrating a non-ohmic response and large hysteresis. The small arrows show the direction of the bias sweep.

3.2 Four-probe and Hall-effect measurements

In order to understand the underlying charge transport mechanisms and to quantify the intrinsic properties of the MOF film, four-probe conductivity and Hall-effect measurements

are carried out. As discussed before, samples in Hall bar geometry (schematic shown in Figure 5.10a) are required to perform reliable and accurate Hall-effect measurements. In this regard, the 1.7 μm thick MOF films are preferred over smaller thicknesses because of their relative easiness for handling during device fabrication (thinner samples are prone to break into small flakes during device processing). In addition, since the conductance of the MOF film increases with the film thickness (as seen in Figure 5.6), selecting thicker layers allows measuring larger currents in the developed devices. Furthermore, thicker samples have higher optical density, i.e. losses associated with light transmission are reduced and hence, larger photocurrents can be obtained (see chapter 6). Because of these practical reasons, the 1.7 μm thick MOF films are chosen for investigating the electronic properties and later on, are employed as an active element in the photodetectors.

3.2.1 Sample fabrication and characterization

The fabrication of Hall bars to the MOF layer (1.7 μm thick) deposited on a 300 nm SiO_2/Si substrate is performed by cold ablation via ultrafast laser pulses (LPKF ProtoLaser R, picosecond laboratory micromachining system). One of the Hall bar samples obtained after laser ablation is shown in Figure 5.10b. The Au contacts to the Hall bars are fabricated by e-beam lithography, using the procedure explained in Appendix B.1. The optical micrograph of the final Hall bar device is shown in Figure 5.10c.

To characterize the Hall bar samples, the cryogenic probe station equipped with a superconducting magnet system (Model 625, *Lakeshore*) with a vertical magnetic field reaching ± 2.5 T is used. All electrical measurements are carried out in the dark and under vacuum (10^{-8} mbar) using the parameter analyzer.

3.2.2 Results and discussion

To test the quality of the metal contacts, two-probe measurements on multiple contact pairs as a function of temperature are performed. Ohmic contacts with low contact resistance ($\sim 4 \text{ k}\Omega$) are realized between the MOF layer and the Cr/Au metal contact for the temperature range of 100–300 K. The ohmic response of the contact pair 1-5 of the Hall bar device is shown in Figure 5.11 as a function of temperature.

Four-probe conductivity of the sample is measured by sourcing the current from contact 1 to 5 and measuring the voltage difference across parallel contact pairs (here, 2-3 and 6-7). Considering the distance between the parallel contact pairs $b = 200 \mu\text{m}$, width of the sample $w = 300 \mu\text{m}$, and thickness of the MOF film $t = 1.7 \mu\text{m}$, four-probe conductivity (σ_{xx}) is obtained from Equation 5.3 and is plotted in Figure 5.12 as a function of temperature. The plot reveals the same qualitative response as obtained with two-probe measurements on the 70 nm thick sample in Figure 5.8. In addition, very small contact resistance is achieved, as indicated by the comparable values of two-probe and four-probe conductivity tabulated in Figure 5.12. This confirms that the resistance of the contacts does not constrain the measurements and also that reliable contacts and high-quality Hall bar devices are achieved.

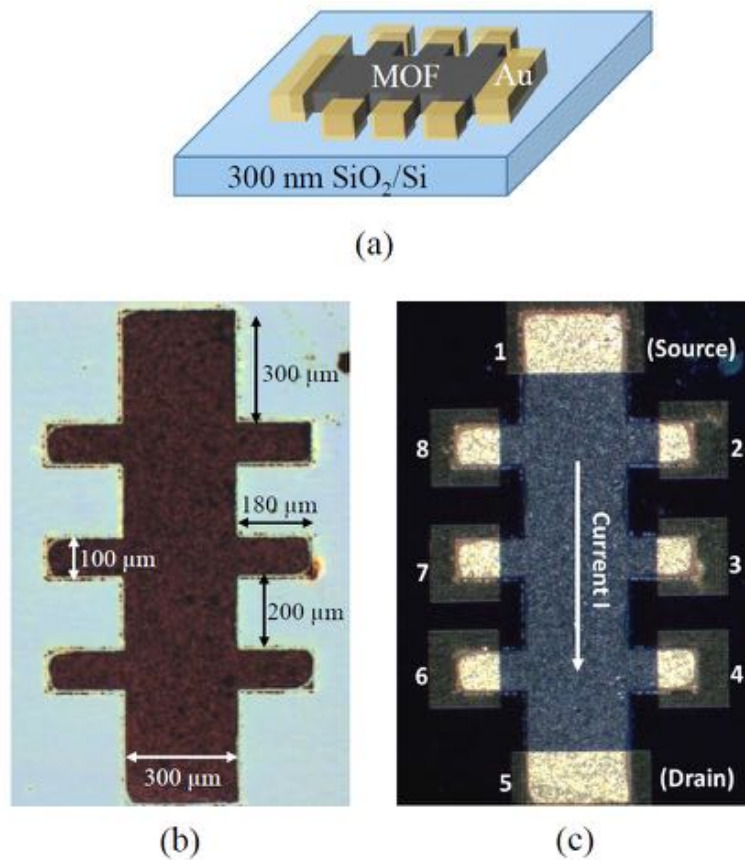


Figure 5.10: Hall bar geometry developed from the MOF film. (a) Schematic of the required Hall bar sample for Hall-effect measurements, (b) optical image of the Hall bar sample developed by laser ablation of 1.7 μm thick MOF film, (c) deposition of Au contacts to obtain the final Hall sample with eight Hall bars numbered from 1 to 8. Adapted from Dong et al.^[9]

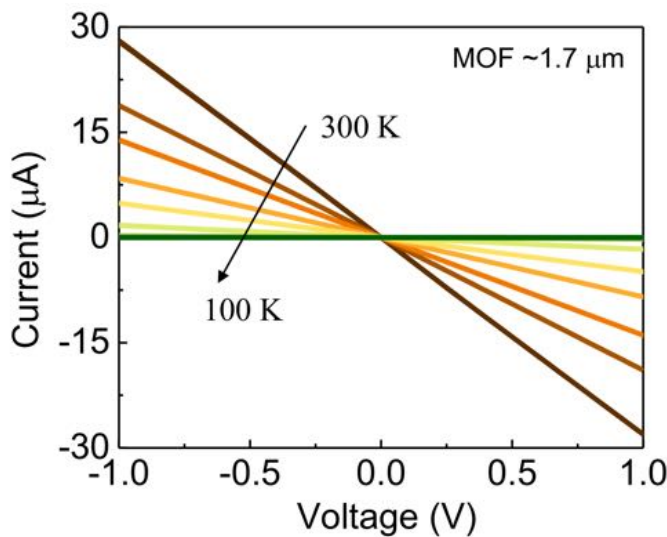


Figure 5.11: Temperature-dependent I - V characteristics of the Hall bar device shown in Figure 5.10, demonstrating ohmic behavior in the temperature range of 100–300 K.

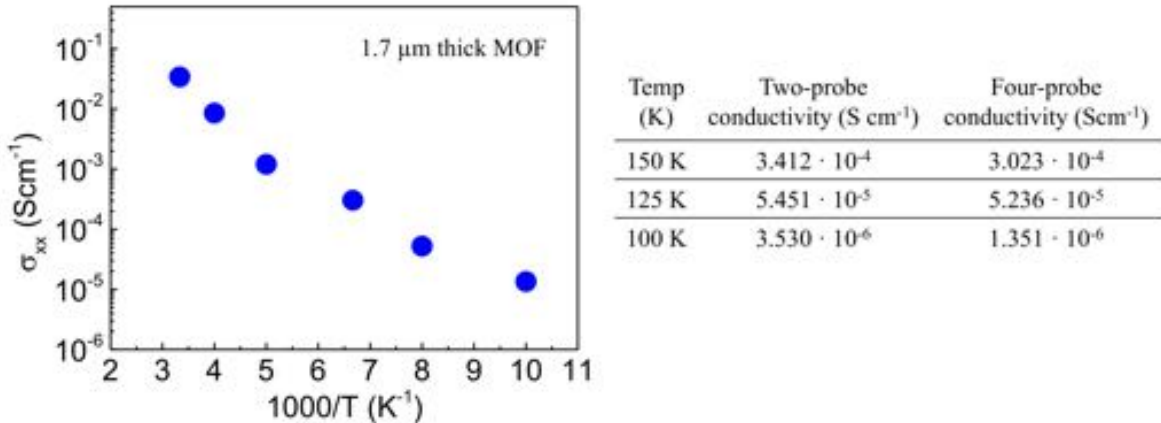


Figure 5.12: Logarithmic dependence of four-probe conductivity (σ_{xx}) on the reciprocal temperature, indicating a strong decrease in the conductivity as the temperature is reduced. Adapted from Dong et al.^[9]

The Hall-effect measurements are performed by sourcing the current from contact 1 to 5 and measuring the voltage difference (V_{xy}) between the opposite contacts, i.e. 2-8, 3-7, 4-6 (Figure 5.10), in the presence of a vertical magnetic field. In our experiments, rather than continuously measuring the Hall voltage (or Hall resistance) as a function of magnetic field, V - I curves at various magnetic fields are measured. Hall resistance (R_{xy}) is then extracted from the slope of the V - I curves and plotted as a function of magnetic field to obtain the Hall coefficient ($R_H = dR_{xy}/dB$). Figure 5.13a shows the as-measured data for the Hall bar device at manually varied magnetic fields from 0 to ± 0.8 T. R_{xy} is extracted from the slopes of the V - I curves and plotted as a function of magnetic field in Figure 5.13b. R_H is then calculated from the slope of R_{xy} versus B curve using Equation 5.2, which provides a measure of the charge carrier density (N). Once N is known, Hall mobility (μ_H) is inferred from the expression:^[165]

$$\mu_H = \frac{\sigma_{xx}}{eN} \quad (5.5)$$

For the sample shown in Figure 5.10 (Sample 1), $\sigma_{xx} = 0.034$ S cm⁻¹, $N = 9.24 \times 10^{14}$ cm⁻³, and $\mu_H = 230 \pm 34$ cm² V⁻¹ s⁻¹ is inferred at room temperature. In another sample at room temperature (Sample 2), $N = 4.2 \times 10^{15}$ cm⁻³ and $\mu_H = 265 \pm 56$ cm² V⁻¹ s⁻¹ is obtained (measurements shown in Figure 5.13c,d).

The Hall measurements are carried out at a regular temperature interval from 300 to 100 K at magnetic fields ranging from 0 to ± 0.8 T (R_{xy} versus B curves at different temperatures are shown in Appendix C.1). Before going into the details of the results, it is important to discuss the large offset at $B = 0$ T obtained in our Hall samples. The non-zero value of R_{xy} at $B = 0$ T is attributed to the deviation of the sample geometry from ideal Hall bar geometry. As seen in Figure 5.10, the Hall bars are rather wide than what is expected ideally to be a point contact. This results in an additional contribution of the longitudinal resistance of the sample to the Hall resistance at 0 T. V_{xy} depends on the sample geometry and alignment of the opposite voltage probes and can be affected by the asymmetries present in the probe element and in the voltage measurement contact. Since the Hall coefficient is not

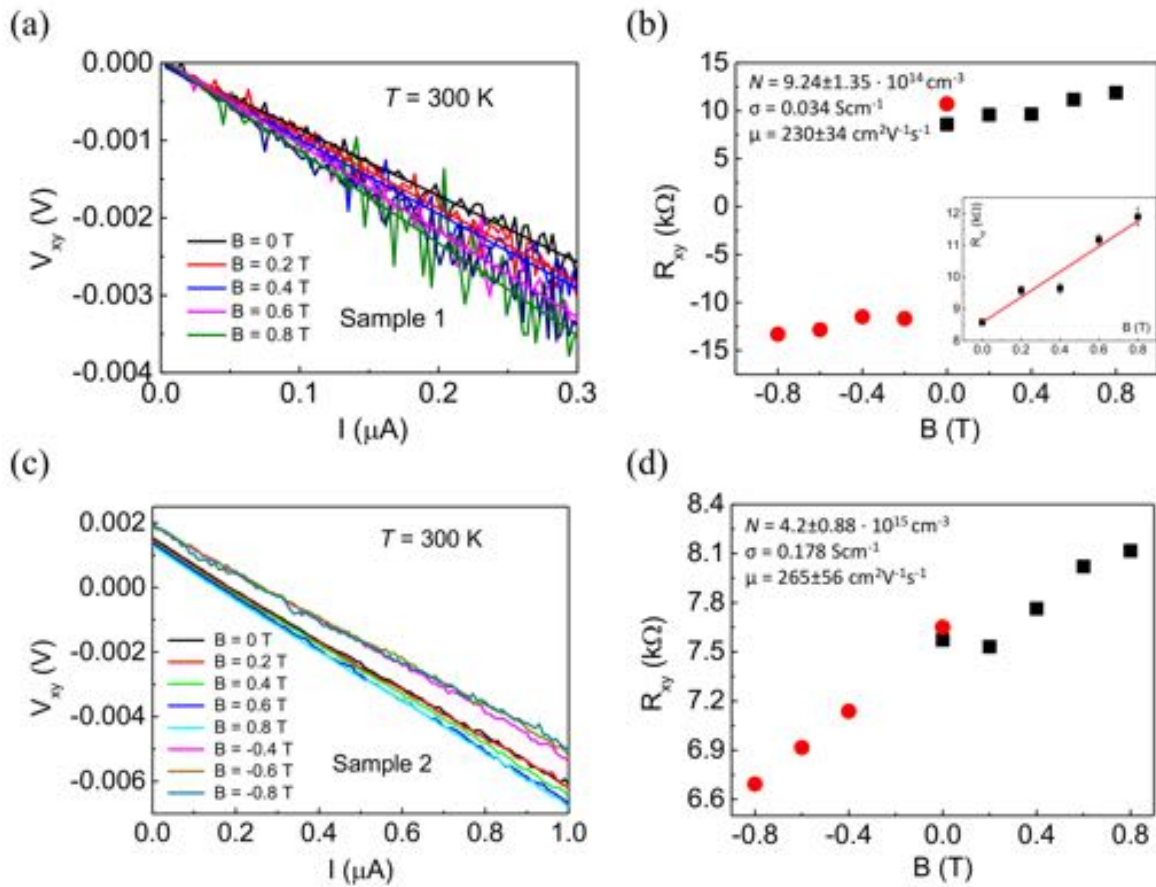


Figure 5.13: Hall-effect measurements on two Fe-THT MOF samples. (a),(c) Ohmic V - I curves obtained for both samples at various magnetic fields, (b),(d) R_{xy} is extracted from the slopes of V - I curves for the respective samples and plotted as a function of magnetic field. Inset of (b): Data zoomed for positive magnetic fields to show a linear dependence of R_{xy} on B . N is calculated from the slope dR_{xy}/dB and subsequently, μ_H is calculated. The values obtained for N and μ_H for both samples are reported in the graphs.

extracted from the direct R_{xy} - B sweeps, but from individual V - I sweeps, the probe position may change during the Hall-effect measurements. In Sample 1, this most likely happened at room temperature, causing the sign of R_{xy} to flip at 0 T, as seen in Figure 5.13b. The slope of the curve, however, does not change across the offset, giving a reliable measure of the mobility.^b In Sample 2, on the other hand, a more familiar R_{xy} - B curve at room temperature is observed, where no sign flip for R_{xy} at 0 T is seen. At lower temperatures, geometric magnetoresistance plays a significant role in our samples and contributes to the

^b The values of the slope dR_{xy}/dB vary slightly with the direction of applied magnetic field, which is attributed to the metal contacts fabricated to the MOF layer. In an ideal scenario, when opposite metal contacts (where V_{xy} is measured) are ideal, symmetric curves for positive and negative magnetic fields are observed. However, experimentally it is difficult to achieve ideal contacts, leading to the variations in the recorded voltage drop values when charge carriers change their direction of motion with the direction of the magnetic field. To incorporate this, the values of mobility and charge density obtained at positive and negative magnetic fields are averaged and reported as the final result.

Hall resistance. This may again be caused by changes in the measurement geometry or even by structural changes in the material. Since our sample geometry is somewhere in between ideal Hall bar geometry and pure magnetoresistance geometry, the mobility is expected to be between these two cases, with the magnetoresistance setting the lower limit of the mobility and Hall resistance the upper limit. By averaging the values of charge carrier density and mobility for both directions of the magnetic fields, these effects are compensated to a large extent.

The findings of the Hall-effect measurements are summarized in Figure 5.14 (and in Table C.1 in Appendix C.1). Using the right-hand rule, an intrinsic *p*-type doping (induced by Fe^{3+} centers) is confirmed in the MOF samples at all temperatures. Figure 5.14a,b present N and μ_H as a function of temperature. As evident from the plot, Hall mobility is barely affected over the analyzed temperature range (100–300 K), while a clear decay in the charge carrier density is found. This observation strongly supports the idea that a thermally activated charge carrier population is present in the samples. A clear correlation between the temperature decay in σ_{xx} (Figure 5.12) and N (Figure 5.14a) is seen. This indicates that the decay in conductivity is a direct consequence of thermally activated carrier density in the samples rather than a reduction in sample's mobility. Assuming that $\sigma(T)$ is proportional to $N(T) \propto \exp(-E_g/2kT)$, an estimate of the bandgap $E_g = 0.201 \pm 0.02$ eV is obtained, which is in reasonable agreement with the bandgap inferred optically (~ 0.245 eV) for these samples. The results obtained from Hall-effect measurements provide convincing evidence that band-like charge transport is operative in $\text{Fe}_3(\text{THT})_2(\text{NH}_4)_3$ 2D MOF films in the 100–300 K temperature range.

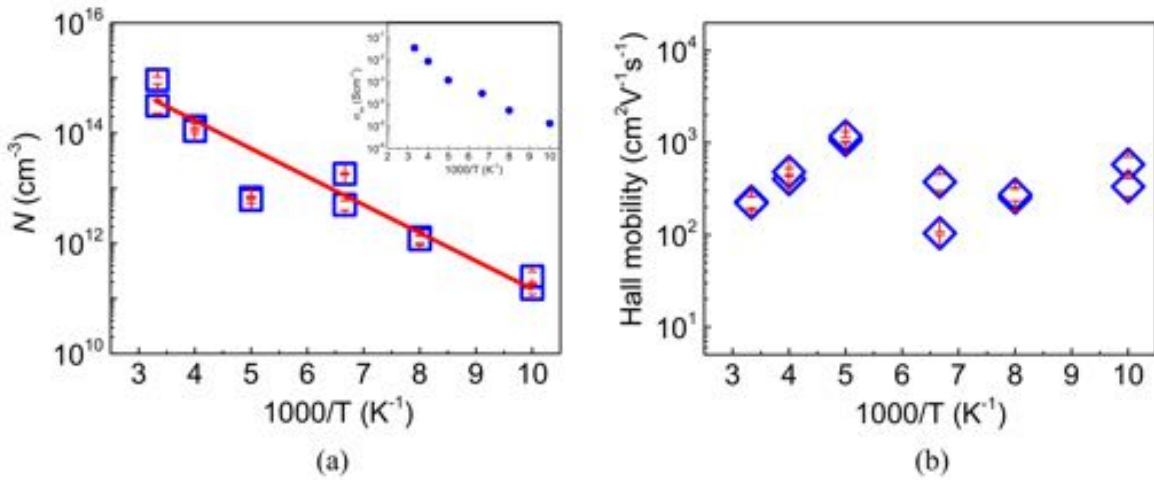


Figure 5.14: Temperature dependence of transport properties of Fe-THT MOFs measured by Hall-effect. (a) Dependence of charge density (N) on temperature. Inset: σ_{xx} versus $1/T$, here re-plotted to show that the temperature decay of sample's conductivity is because of the reduction in N with temperature, (b) dependence of Hall mobility on temperature. Each temperature contains two values obtained for the positive and negative magnetic fields. Error bars represent the standard error of the mean. Adapted from Dong et al.^[9]

Further proof into the conduction mechanism is obtained from Zabrodskii plots, which reveal the dependence of reduced activation energy $W = d(\log(\sigma))/d(\log(T))$ on temperature, as shown in Figure 5.15. The reduced activation energy is derived from the two-probe conductivity data in the temperature range of 320 K to 77 K. For a qualitative comparison, this plot is compared with the plot obtained for Ge ($E_g = 0.66$ eV), another narrow bandgap material.

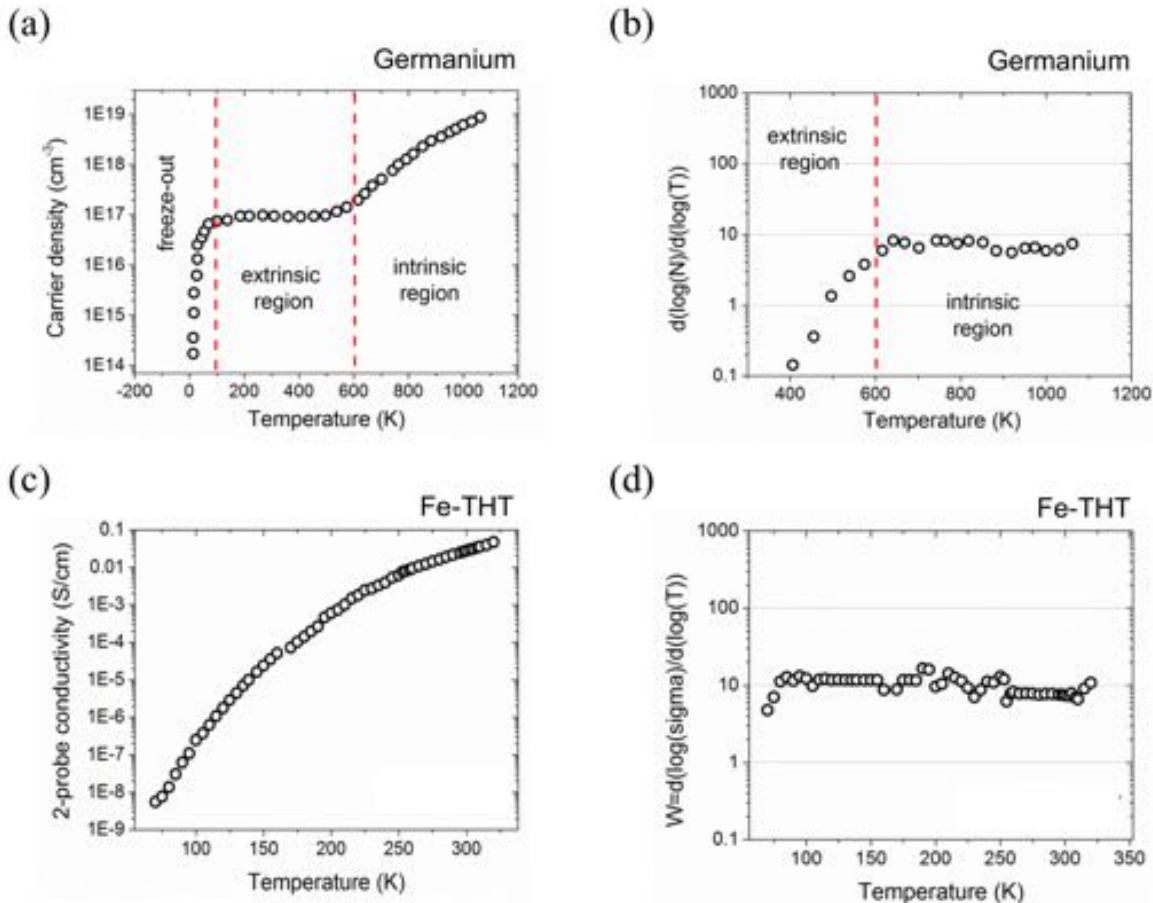


Figure 5.15: Zabrodskii plots for Ge and Fe-THT MOF to understand their conduction mechanism. (a) Charge carrier density in Ge as a function of temperature over the characteristic intrinsic, extrinsic, and freeze-out regions, (b) Zabrodskii plot for the same data,^[166] (c) the variation of the two-probe conductivity with temperature in our 2D MOF film, (d) Zabrodskii plot of the same data showing that the MOF samples are in the intrinsic region where the Fermi level lies in the middle of the energy gap.

Figure 5.15a reveals the variation of carrier density in Ge with temperature over the characteristic intrinsic, extrinsic, and freeze-out regions. In Figure 5.15b we replotted this data in a Zabrodskii plot. The plot indicates that the intrinsic region (thermally activated population of carriers across the bandgap and an invariant Fermi level, $E_F = E_g/2$) can be recognized as a constant reduced activation energy (W). Whereas the extrinsic region (onset at ~ 600 K) is associated with a negative slope, i.e. a reduced activation energy with reduced T (consistent with a displacement of the Fermi level from the center of the gap towards a dopant level near the valence band in p -type Ge). In close analogy to the Ge case, we can explain the

behavior observed in our $\text{Fe}_3(\text{THT})_2(\text{NH}_4)_3$ sample within the same scenario. Figure 5.15c,d show the two-probe conductivity of the MOF sample as a function of temperature. The trend of the curve is consistent with the sample being in the intrinsic region at least until 77 K, after which it enters in the extrinsic region where *p*-type doping associated with Fe centers is expected to dominate.

The results obtained with Hall-effect measurements are independently confirmed by time-resolved terahertz spectroscopy (TRTS) measurements. Unlike Hall-effect, the mobilities inferred using TRTS (THz mobility) are linked to charge displacements over very short length scales (~ 100 nm, for a thermal charge velocity of $\sim 10^5$ m s $^{-1}$). Since the THz mobility is less sensitive to scattering mechanisms that can impede mobility over larger distances (i.e. grain boundaries), it denotes the upper limit of mobility for a given material. Interestingly, the resolved THz mobility ($\mu_{THz} = 211 \pm 7$ cm 2 V $^{-1}$ s $^{-1}$) agrees very well with the room temperature Hall mobility ($\mu_H = 229 \pm 33$ cm 2 V $^{-1}$ s $^{-1}$) and points to impurity scattering as the common scattering mechanism impeding both a.c. and d.c. mobilities in $\text{Fe}_3(\text{THT})_2(\text{NH}_4)_3$ 2D MOF films. These results strongly suggest that grain boundaries are not constraining the long-range transport of free charge carriers in our samples. This observation can be explained by the strong doping in the samples, as reported previously.^[167]

3.3 Conclusions

In this work, we addressed the nature of charge transport in $\text{Fe}_3(\text{THT})_2(\text{NH}_4)_3$ 2D MOF samples using four-probe conductivity and Hall-effect measurements. This novel π -d conjugated MOF material exhibits a direct IR bandgap of 0.25–0.45 eV. The four-probe measurements of a 1.7 μm thick sample reveal a strong decrease in the conductivity on reducing the temperature. The Hall-effect measurements show that the temperature dependence of the conductivity is not because of hopping-type conduction, but due to thermally activated population of the energy bands, enabled by the narrow bandgap of these materials. The observed exponential decrease in the conductivity with decreasing temperature is thus fully compatible with band-like charge transport operative in Fe-THT MOFs. Furthermore, a record-high mobility of 230 cm 2 V $^{-1}$ s $^{-1}$ is inferred for the MOF film, which is barely affected over the analyzed temperature range.

Band-like transport and high mobilities in a MOF semiconductor are very desirable properties and directly open the path to exploit 2D MOFs in novel optoelectronic devices. In the next chapter, a proof of principle of a 2D MOF-based broadband photodetector is discussed at length.

Chapter 6

Broadband photodetectors based on $\text{Fe}_3(\text{THT})_2(\text{NH}_4)_3$ 2D MOF

A novel semiconducting $\text{Fe}_3(\text{THT})_2(\text{NH}_4)_3$ 2D MOF with record-high mobility and band-like charge transport has been introduced in the previous chapter, along with an in-depth characterization of the material's structure, electrical, and optical properties.

This chapter utilizes our previous results to focus on the application of the MOF films into active devices. Here, we demonstrate $\text{Fe}_3(\text{THT})_2(\text{NH}_4)_3$ MOF-based photodetectors capable of detecting a broad wavelength range from UV to NIR. Because of the small IR bandgap of MOF samples, the photodetectors are best operated at cryogenic temperatures by suppressing the noise from thermally activated charge carriers to obtain a clear signal from the optically generated ones. So far, only a handful of reports have addressed the photodetection properties of MOFs and our work reports the first proof-of-concept MOF-based photodetector.

The results discussed in this chapter are published as:

- **H. Arora**, R. Dong, T. Venanzi, J. Zscharschuch, H. Schneider, M. Helm, X. Feng, E. Cánovas, and A. Erbe, “Demonstration of a Broadband Photodetector Based on a Two-Dimensional Metal–Organic Framework”, *Advanced Materials* **32**, 1907063 (2020).

1 Introduction

The large degree of structural and chemical tunability and long-range crystalline order have made MOFs promising materials for a large variety of applications (prominently, gas storage/separation and catalysis). However, owing to the fact that the majority of MOFs reported to date are electrical insulators, their exploitation in electronics and optoelectronics have been severely constrained.

In the last years, advances in synthetic approaches have revealed several examples of (semi-)conductive MOFs, an aspect that allows their use in (opto)electronic applications as an active element.^[9,114,119,120,125,156–160,168–170] While some works demonstrate their semiconducting behavior with a defined bandgap,^[9,159,169,170] others have revealed them behaving as either metals or semi-metals,^[120,158,160,171] i.e. lacking a bandgap. Among them,

graphene-like MOF analogues, where 2D hexagonal lattices are obtained from trigonal organic ligands coordinated by square-planar atomic metal nodes, have emerged as a unique sub-class of electrically conducting materials. In general, these 2D MOF samples display a variety of electrical properties, which can be linked to intrinsic and/or extrinsic factors. In most cases, the samples are produced in powder form, and later pressed into pellets to characterize their conductive properties as a function of temperature.^[159,172] These powder synthesis routes usually result in low density and in a discontinuous structure of the MOF films with a large amount of grain boundaries, resulting in hopping-type charge transport and low charge carrier mobilities.^[125] MOFs with such features are particularly unsuitable for device prototyping, where large-area thin films displaying semiconducting properties (with a defined bandgap) and delocalized charge carrier transport are required. These ideal features for device development are revealed in the $\text{Fe}_3(\text{THT})_2(\text{NH}_4)_3$ 2D MOF, as discussed in the previous chapter. The 1.7 μm thick MOF films are characterized by a direct bandgap in the IR region and a charge carrier mobility of $230 \text{ cm}^2 \text{ V}^{-1} \text{ s}^{-1}$ at room temperature. These appealing characteristics of the reported samples open the path to exploit them as active elements in optoelectronic devices.

In this work, the ability of free-standing films of $\text{Fe}_3(\text{THT})_2(\text{NH}_4)_3$ MOF to serve as an active element in a two-terminal photodetector device is demonstrated. The fabricated MOF photodetectors are tested over the UV-to-NIR spectral range (400–1575 nm). Owing to the IR bandgap of the active layer, cooling of the devices suppresses thermally generated charge carriers, allowing us to obtain a clear signal from the optically generated charge carriers upon light illumination. Furthermore, the photoswitching performance of the MOF photodetector is evaluated by testing the response of the MOF device to light/dark cycles of the illumination at different wavelengths and temperatures. To the best of our knowledge, such broadband photoresponse is being reported for the first time for an entirely 2D MOF-based photodetector and demonstrates a reliable and robust device.

2 Photodetector operation and its figures of merit

A photodetector is an optoelectronic device with an electrically biased semiconductor which generates current upon photon absorption. The bandgap of the semiconductor plays an important role in governing the photon absorption process and the spectral range of photodetection. Depending on its mode of operation, a photodetector can be divided into two categories: (a) photovoltaic and (b) photoconductor.^[173,174]

2.1 Photovoltaic

A photovoltaic photodetector, commonly known as photodiode, is based on a *p-n* junction and produces a current or voltage signal upon light absorption. Its device structure consists of a semiconductor diode contacted by two metal electrodes as shown in Figure 6.1a. The photodiode operates in the reverse bias condition when the photogenerated carriers in the depletion region are accelerated in opposite directions by an internal electric field to produce

the photocurrent. The I - V characteristics of the photodiode is shown in Figure 6.1b. The increase of current in the reverse bias upon light illumination is noted.

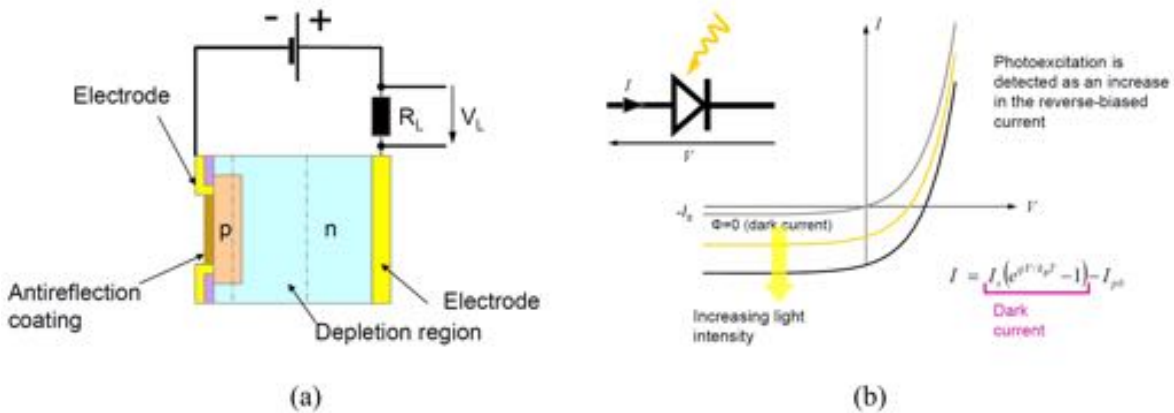


Figure 6.1: Device structure and characteristic curves of a photodiode under illumination. (a) Device schematic of a photodiode based on a p-n junction, (b) I - V curves of the photodiode in dark condition and under illumination. The reverse current increases on increasing the light intensity. The diode equation is modified by adding the photocurrent (I_{ph}).

2.2 Photoconductor

A photoconductor responds to the light by changing its resistance or conductance on photon absorption. The device configuration of a photoconductor consists of a semiconducting active layer contacted with two metal electrodes on the opposite ends to form a two-terminal device. Figure 6.2a shows the device schematic of a photoconductor connected to an external circuit for applying the bias. In the dark and under an applied bias (V), a dark current (I_{dark}) flows through the circuit. Under illumination, absorption of the photons with energy higher than the bandgap of the semiconductor ($E_{ph} \geq E_g$) generates electron-hole ($e-h$) pairs which are separated by the applied bias as shown in Figure 6.2b. The photogenerated electrons and holes drift in the opposite directions towards the metal contacts, resulting in an increase of the overall current (I_{light}). The current from the photogenerated carriers alone is called the photocurrent (I_{ph}) and is obtained by subtracting the dark current from the total current under illumination, i.e. $I_{ph} = I_{light} - I_{dark}$.^[3,6,174] Figure 6.2c shows the I - V characteristics of a photoconductor in the dark and light conditions. As the light intensity increases, photogenerated charge carrier density increases as well, thus producing higher photocurrent.^[173] A photoconductor can be further divided into two categories: (a) intrinsic, where electrons are excited from the valence band to the conduction band on photon absorption, thereby leaving holes behind and (b) extrinsic, where the photo-excitation involves energy levels formed by extrinsic doping of the material.^[173] The donor and acceptor levels are very close to the conduction and valence bands, respectively, resulting in a very small effective energy gap needed to overcome by the photon energy for photo-excitation. Therefore, extrinsic photoconductors can operate far into the IR region. However, because of the small effective bandgap, the population of thermally activated charge carriers is high, which results in large dark current.

In a photodetector, photogenerated charge carriers are the desired signal and not the thermally generated ones.^[173] To prevent the thermally activated charge carriers overshadowing the photogenerated signal, these photodetectors are operated at cryogenic temperatures. At low temperatures, the thermal charge carriers freeze out and a clear signal from the photogenerated charge carriers is obtained.

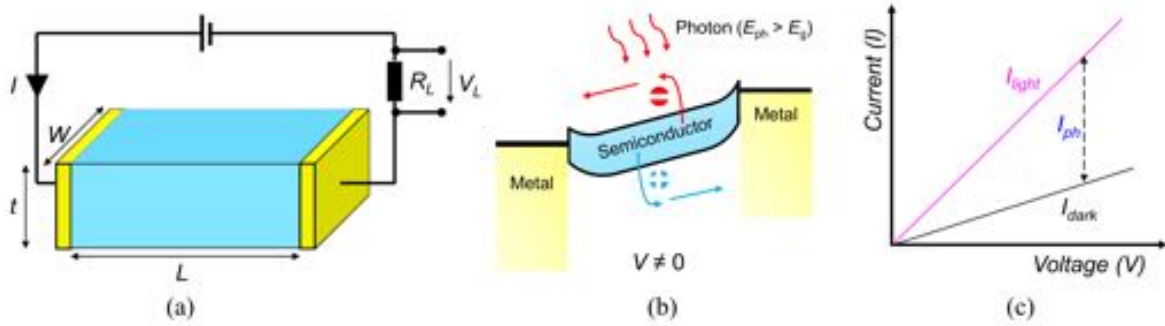


Figure 6.2: Operation of a photoconductor under illumination. (a) Device schematic of a photoconductor where the semiconducting active layer is contacted by two metal electrodes for charge collection and injection, (b) band diagram of a semiconducting channel under illumination and at an applied bias. The energy of the impinging photons is higher than the bandgap of the semiconductor. The absorption of a photon generates free charge carriers that are collected at the metal electrodes. (c) I - V curves of the photoconductor in dark condition and under illumination. The photocurrent is obtained by subtracting the dark current from the light current, $I_{ph} = I_{light} - I_{dark}$.

2.3 Figures of merit of a photodetector

Figures of merit are essential for characterizing the performance of a photodetector. They also facilitate the relative comparison between different photodetectors irrespective of geometry, mode of operation, and the active material used. In this section, an introduction to generic figures of merit is provided and their mathematical calculations are discussed.

In a photodetector, I_{ph} is calculated as:

$$I_{ph} = I_{light} - I_{dark} = \Delta\sigma EWt \quad (6.1)$$

where $\Delta\sigma$ is the change in the conductivity on illumination, E is the electric field, and W and t are the width and thickness of the material, respectively. From Drude's law (Equation 2.4), assuming that the mobility is independent of the carrier concentration, I_{ph} can be written as:

$$I_{ph} = \Delta\sigma EWt = e\mu\Delta nEWt \quad (6.2)$$

where μ is the mobility and Δn is the change in carrier concentration upon illumination.

As discussed before, for photo-excitation the energy of the photon ($h\nu$) must be equal to or greater than the bandgap of the active material (E_g):

$$h\nu \geq E_g \quad (6.3)$$

where h is Plank's constant, ν is the optical frequency of the photons (cycles s^{-1}) and can be expressed as $\nu = c/\lambda$, where c is the speed of light and λ is the wavelength of the radiation.

The lowest wavelength detectable by a photodetector is called the cut-off wavelength (λ_c) and is an important parameter of a photodetector. λ_c can be calculated by equating the energy associated with λ_c to the energy gap of the detector material:

$$\frac{hc}{\lambda_c} = E_g \quad (6.4)$$

$$\lambda_c(\mu\text{m}) = \frac{1238}{E_g(\text{eV})} \quad (6.5)$$

Therefore, the bandgap of the active layer determines the cut-off wavelength of the detector. If the bandgap is small, the cut-off wavelength will be large, e.g. for a material with $E_g = 0.25$ eV, the cut-off wavelength is $\lambda_c = 4.96 \mu\text{m}$.

1. Quantum efficiency (η), measured in %

The efficiency of converting a photon into free charge carriers is called quantum efficiency, normally expressed in percent. In a photodetector, it is calculated as the number of free charge carriers generated divided by the number of photons absorbed by the detector's active area.^[174,175]

$$\eta = \frac{\text{number free carriers}}{\text{number absorbed photons}} \quad (6.6)$$

Absorption quantum efficiency (η_{abs}) is defined as:^[173,174]

$$\eta_{abs} = (1 - r)(1 - \exp(-\alpha t)) \quad (6.7)$$

where r accounts for the surface reflection, α is the absorption coefficient and t is the thickness of the active layer. The absorption quantum efficiency is high if the surface reflectance is low and/or absorbance is high, because the radiations can enter into the detector material efficiently.

From Equation 6.6, the number of photogenerated charge carriers per unit volume can be derived as:

$$\Delta n = \frac{\tau \eta P}{E_{h\nu} L W t} \quad (6.8)$$

where P is the incident radiation power and τ is the lifetime of the free charge carriers.

From Equation 6.2 and Equation 6.8, the photocurrent can be re-written as:

$$I_{ph} = \left(\frac{\eta \lambda e}{hc} \right) \left(\frac{\mu E \tau}{L} \right) P = \left(\frac{\eta \lambda e}{hc} \right) \left(\frac{\mu V \tau}{L^2} \right) P \quad (6.9)$$

where V is the applied voltage bias.

2. (a) Responsivity (R), measured in A W^{-1}

The responsivity quantifies the amount of the output signal per unit watt of incident radiation. It is calculated as the ratio of the photocurrent (I_{ph}) and the optical power (P) incident on the photodetector.^[6] From Equation 6.9, one can write:

$$R = \frac{I_{ph}}{P} = \left(\frac{\eta \lambda e}{hc} \right) \left(\frac{\mu V \tau}{L^2} \right) \quad (6.10)$$

A high responsivity is an indication of a high output signal at a certain optical power. Although responsivity is a useful parameter for estimating the output, it is of limited significance from detector's sensitivity point of view, because it considers only the output signal and not the noise level. Moreover, as seen from Equation 6.10, responsivity is dependent on the applied bias (V) and the device length (L).^[176] In this respect, it is better to consider voltage responsivity (R_v), which is discussed next.

(b) **Voltage responsivity (R_v), measured in V W^{-1}**

Voltage responsivity is defined as the change in voltage per unit incident power across the detector. For a photoconductor, voltage responsivity is often regarded as a more appropriate figure of merit than responsivity, because it does not depend on geometrical factors, and moreover, takes into account the dark current.^[173]

$$R_v = \frac{RV}{I_{dark}} \quad (6.11)$$

3. Photoconductive gain (G)

Photoconductive gain is given by the number of electrons passing through the photoconductor per absorbed photon. The second term of the right side of Equation 6.10 gives the measure of G , which is also a unitless quantity.

$$G = \frac{\mu V \tau}{L^2} = \frac{\tau}{T_r} \quad (6.12)$$

where T_r is the transit time of a free electron from cathode to anode.

When electrons are excited into the conduction band from the valence band, they are either collected at the electrodes or they recombine. A gain is produced if the free carriers are collected at the electrodes before recombining, i.e. if the lifetime is larger than the transit time. On the other hand, if the lifetime is small, i.e. free carriers recombine before reaching the electrodes, gain is less than one.^[175,177] As seen from Equation 6.12, G is directly proportional to the applied voltage (V) and inversely to the square of the device length or electrode spacing (L). This is because at higher biases, the carriers are moving faster, and thus, the recombination rate decreases. However, if the distance they need to transit is longer, the chances of recombination will increase.^[178] Because electrons travel faster than holes, a higher gain is expected for materials with electrons as majority charge carriers.

4. Noise equivalent power (NEP), measured in $\text{W Hz}^{-1/2}$

Another important parameter to evaluate the performance of the photodetector is NEP. It is defined as the detection limit of the photodetector and is a function of the detector's noise level, expressed as:^[179,180]

$$\text{NEP} = \frac{\overline{I_n^2}^{1/2}}{R} \quad (6.13)$$

where $\overline{I_n^2}^{1/2}$ is the root mean square of the total noise current. A low NEP value is desirable for a sensitive photodetector. Therefore, in order to determine the NEP accurately, various noise mechanisms acting in the detector should be considered.

The fundamental noise sources in photoconductors are Johnson noise (I_j), generation-recombination (G-R) noise (I_{gr}), and $1/f$ noise (I_f), the latter being dominant at low frequencies.^[173,174]

The Johnson noise is calculated as:^[173]

$$I_j = \left(\frac{4kT\Delta f}{R_d} \right)^{1/2} \quad (6.14)$$

where k is the Boltzmann constant, T is the absolute temperature, Δf is the bandwidth, and R_d is the resistance of the device.

The G-R noise is calculated as:^[173,181]

$$I_{gr} = (4eGI_{dark}\Delta f)^{1/2} \quad (6.15)$$

where G is the photoconductive gain, $G = Rhc/\eta e\lambda$.

While the estimations of the Johnson noise and the G-R noise are straightforward, the analysis of $1/f$ noise requires noise measurements using more sophisticated equipment. With the existing instrumentation at our lab, we cannot estimate the $1/f$ noise in our MOF photodetectors, therefore, it is not included in the NEP calculations.

A major drawback of NEP is its dependence on device geometry, making a direct comparison with other photodetectors difficult. To circumvent this problem, specific detectivity (D^*) is used, which is discussed next.

5. Specific detectivity (D^*), measured in $\text{cm Hz}^{1/2} \text{ W}^{-1}$ or Jones

The specific detectivity (D^*) of a photodetector is derived as:^[180,182]

$$D^* = \frac{A^{1/2}}{\text{NEP}} \quad (6.16)$$

where A is the device area.

D^* measures the sensitivity of the detector irrespective of the device area, enabling a direct comparison between different photodetectors. A bigger value of D^* is desirable for a better performance of the photodetector. D^* can also be interpreted as signal-to-noise ratio (SNR) when 1 W of power is incident on 1 cm^2 detector area of 1 Hz bandwidth. The unit of D^* is $\text{cm Hz}^{1/2} \text{ W}^{-1}$ or Jones.

6. Response time, measured in s

As the name suggests, response time tells how fast a detector can respond to a pulse of optical radiation. The response time is measured for both rise and decay processes, i.e. when light is switched on and off, respectively. They are extracted as the time required by the photodetector to reach from 10% to 90% of the peak photocurrent after the illumination is turned on (rise time) and from 90% to 10% of the peak photocurrent after the illumination is turned off (decay time).^[183,184]

The response time is controlled by three basic phenomena: (a) transit time of the photogenerated carriers, (b) trapping of the photogenerated carriers, and (c) equivalent-circuit RC time constant.^[175,177] In a high-mobility material, the transit time is small since the charge carriers move at a high speed, leading to a fast response. However, in

the presence of traps, additional time-dependent processes, such as filling and emptying of the trap states when light is turned on and off, respectively, may increase the overall time of response.^[182,185]

3 Broadband photodetectors based on $\text{Fe}_3(\text{THT})_2(\text{NH}_4)_3$ 2D MOF films

3.1 Principle of operation

Small bandgap photodetectors are capable of detecting long wavelengths, far into the IR region. However, the small bandgap also causes thermally excited band-to-band charge carrier population, resulting in large dark current (or noise), while hampering the sensitivity of the detector. As discussed before, in a high performance photodetector, the dark current should be as low as possible, so that a high photocurrent can be obtained.

In the previous chapter, an in-depth analysis of the electrical properties of $\text{Fe}_3(\text{THT})_2(\text{NH}_4)_3$ 2D MOF as a function of temperature by using Hall-effect measurements is presented. The findings revealed that the charge carrier density decays exponentially with temperature, i.e. a thermally activated charge carrier population is present in the samples. This thermally activated population of charge carriers is described by $N(T) \propto \exp[-E_g/2kT]$, decreasing from $6.2 \times 10^{14} \text{ cm}^{-3}$ at 300 K to $2.0 \times 10^{11} \text{ cm}^{-3}$ at 100 K. These results provide convincing evidence that because of the small IR bandgap, MOF samples undergo a large amount of thermal transitions across the bandgap at high temperatures. By decreasing the temperature, this thermal generation of charge carriers can be suppressed and clear optical signals can be obtained, which formulates the fundamental working principle of our MOF photodetectors. Please note that this observation is common among low bandgap semiconductors, making it necessary for the IR detectors to be cooled down to cryogenic temperatures for their operation. The smaller the bandgap of the active layer, the longer the wavelength it can detect and the colder the detector should be to prevent the thermal generation of charge carriers.

The Zabrodskii plot (Figure 5.15 in chapter 5) reveals the MOF samples being in the intrinsic region for the temperature range of 77–320 K. This implies a thermally activated population of free carriers across the bandgap and an invariant Fermi level, $E_F = E_g/2$. Thus, the MOF photodetectors fall into the category of intrinsic photoconductors for the analyzed temperature range.

3.2 Experimental section

In this study, free-standing 1.7 μm thick $\text{Fe}_3(\text{THT})_2(\text{NH}_4)_3$ MOF films are used to fabricate the photodetector devices. The FTIR measurements are carried out to characterize the bandgap of the samples under investigation (FTIR details in Appendix A.3). From the Tauc plot shown in Figure 6.3a, the samples are characterized by a direct bandgap with an absorption edge at ~ 0.45 eV, which corresponds to a cut-off wavelength of 2.76 μm . Ideally,

all wavelengths smaller than the cut-off wavelength shall be detectable. A two-terminal device (schematic in Figure 6.3b) is fabricated from a MOF film bonded to an insulating glass substrate by using high-quality indium (In) metal electrodes (*chemPUR*, 99.99% purity). The optical micrographs of the actual devices are shown in Figure 6.3c,d.

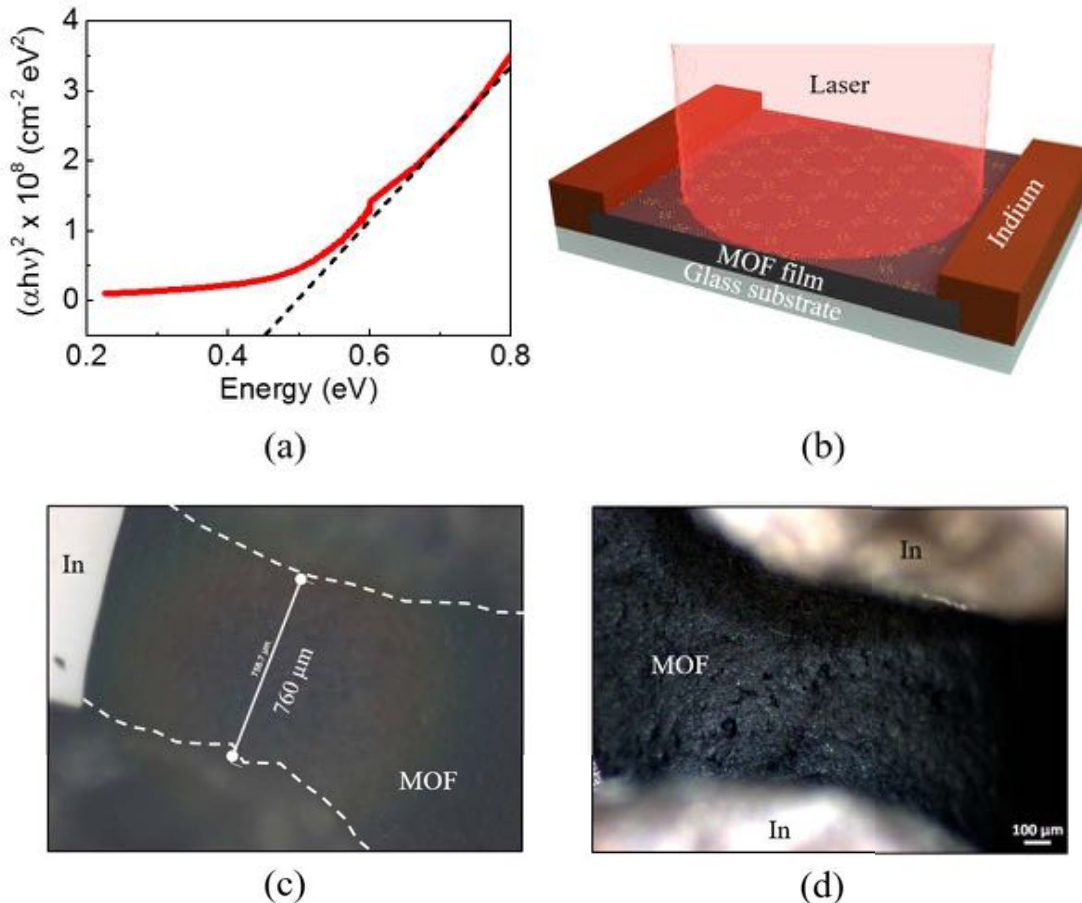


Figure 6.3: FTIR characterization of the MOF film and photodetector fabrication. (a) Tauc plot of the 1.7 μm thick MOF film at room temperature, revealing an optical bandgap of 0.45 eV, (b) schematic of a two-terminal MOF photodetector, (c),(d) optical images of MOF photodetectors fabricated from free-standing 1.7 μm thick MOF films (white dashed line) on an insulating glass substrate. Electrodes are fabricated from In metal. Adapted from Arora et al.^[3]

The photoresponse of the developed MOF-based photodetector is initially characterized under 785 nm laser irradiation, and subsequently at 405 nm, 633 nm and 1575 nm, at various laser power settings. The spot size of the laser is ~ 2 mm in diameter, assuring full illumination of the device's active area. All electrical characterizations with and without illumination are carried out in vacuum ($< 10^{-7}$ mbar) by applying a sweeping bias of ± 1 V for the temperature range of 77–300 K. For the whole temperature range, all analyzed MOF devices are found to yield hysteresis-free I – V characteristics both in dark condition and under illumination.

Effect of MOF thickness on light absorption characteristics In this work, only the 1.7 μm thick films are employed as the active element in photodetectors because of several practical reasons. First, the conductance of the MOF film increases with the film thickness (Figure 5.6), therefore, selecting thicker layers allows measuring larger currents in the developed devices. Another reason for choosing 1.7 μm thick samples is related to their higher optical density, i.e. losses associated with light transmission are reduced, and hence, larger photocurrents are obtained. Finally, since in our previous report we employed 1.7 μm thick MOF film, we aimed at keeping consistency in order to facilitate a direct correlation between the results conveyed in both reports. While the previous study revolves around material characterization and intrinsic charge transport mechanisms, the focus of this work is on the application of 1.7 μm thick MOF films into active devices.

Nevertheless, to understand the role of MOF thickness on the photodetector performance, optical spectroscopy on two MOF thicknesses, 130 nm and 1700 nm is performed. Figure 6.4a shows the absorbance of both samples, from which one can relate absorbance (A) with the sample thickness (t) using the expression $A = -\alpha t \log e$, as shown in Figure 6.4b.

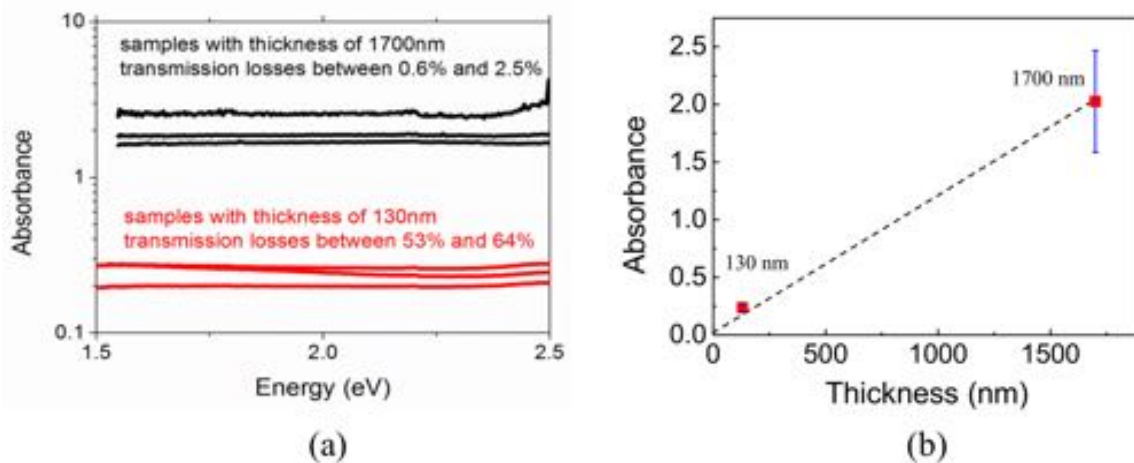


Figure 6.4: Effect of MOF thickness on light absorption characteristics. (a) Absorbance of Fe-THT samples with thicknesses 1700 nm (top) and 130 nm (below), (b) absorbance versus thickness plot for 130 nm and 1700 nm thick samples. The black dashed line connects the two data points and extrapolates to zero, indicating a linear relationship between absorbance and thickness.

In the plot, a linear connection between the two data points extrapolates to zero, indicating a linear dependency between absorbance and thickness. The absorption coefficient (α) is deduced from the slope of this curve and is found to be $26900 \pm 6400 \text{ cm}^{-1}$, which is in reasonable agreement with the absorption coefficient value of $24900 \pm 3000 \text{ cm}^{-1}$ obtained directly from the FTIR measurements (Tauc plot in Figure 6.3a). Because of the linear relationship between absorbance and thickness, the major effect of thickness variation on the device operation will be the generation of proportionate amounts of photocurrent upon irradiation. Most figures of merit estimated in this work, such as photosensitivity and voltage responsivity, do not depend on the sample thickness. However, NEP estimations include Johnson noise, which is a thickness-dependent term. This makes NEP and D^* weakly de-

pendent on the sample thickness ($\propto t^{1/2}$). Nevertheless, within the linear dependency of absorbance and thickness, Johnson noise can be extrapolated for other thicknesses using the data presented in this work for the 1.7 μm thick samples.

3.3 Photoresponse in the near-infrared region

3.3.1 785 nm illumination

The electrical characterization of the MOF photodetector consisting of a 1.7 μm thick MOF layer is shown in Figure 6.5. The photodetector has an active area $A \approx 0.7 \text{ mm}^2$, defined by a channel length $L \approx 1 \text{ mm}$ and a width $W \approx 0.7 \text{ mm}$. Figure 6.5a,b show the I - V characteristics of the MOF device as a function of incident laser power densities (P) at 785 nm wavelength at 300 K and 77 K, respectively. Both curves reveal an increase in the photocurrent with increasing photon density, demonstrating the operation of the active MOF layer as a photoconductor at both temperatures. In order to precisely determine the effect of temperature on the performance of the photodetector, we measured the photoresponse of the device in the temperature range of 77–300 K under various fluences of 785 nm illumination. Figure 6.5c shows current (at a bias of -1 V) as a function of inverse temperature ($1/T$) measured in the dark (black curve) and under different 785 nm light intensities ranging from 0.026 W cm^{-2} (red curve) to 0.60 W cm^{-2} (orange curve). The obtained trend is consistent with the narrow IR bandgap of the samples, enabling thermally activated charge carrier population of the conduction and valence bands at higher temperatures (in agreement with our previous findings). On fitting the curve to the exponential distribution $\exp(-E_a/kT)$, an activation energy $E_a = 0.35 \pm 0.1 \text{ eV}$ is extracted, which is comparable to the optical bandgap of 0.45 eV resolved for the samples. At higher temperatures ($T \geq 200 \text{ K}$), the increase of thermally induced electronic transitions across the narrow bandgap results in larger dark currents, overshadowing the detection of optically generated charge carriers upon light illumination. This reverses at lower temperatures ($77 \text{ K} \leq T < 200 \text{ K}$), where photocurrent tends to remain constant and clearly dominates the dark current. In the low temperature range, the photodetector performance is, thus, governed mainly by optically generated charge carriers for the analyzed range of incident laser powers. To quantify these effects, photodetector photosensitivity (I_{ph}/I_{dark})^[185,186] is plotted as a function of inverse temperature (Figure 6.5d). The photosensitivity is found to increase significantly with decreasing temperature; 6 at 77 K as opposed to 0.3 at 300 K ($P = 0.60 \text{ W cm}^{-2}$, $V = -1 \text{ V}$). While a notable change in the photosensitivity is observed at 77 K even for a low power density of 0.026 W cm^{-2} , at 300 K there is no measurable photocurrent until the incident power is increased tenfold, further affirming the improved photosensitivity at lower temperatures. In addition, photosensitivity also increases with the laser power density, owing to higher photocurrent generation.

To characterize the device performance, we measured other important figures of merit including voltage responsivity, NEP, and D^* . Due to the symmetric I - V characteristics, the MOF photodetector operates in photoconductive mode. The transmission spectroscopy measurements performed over the UV–NIR spectral range (Figure 6.4a) reveal an invari-

ant and high absorption with reflection losses of $5\% \pm 1\%$. The absorption coefficient $\alpha = 24900 \pm 3000 \text{ cm}^{-1}$ is extracted from the Tauc plot at $\lambda = 866 \text{ nm}$ (Figure 6.3a), which is assumed to be constant over the whole analyzed spectral range attributed to high absorbing properties of the MOF film (consistent with its black opaque appearance). Using these values in Equation 6.7, an absorption efficiency η_{abs} of $94\% \pm 1\%$ is obtained for the $1.7 \mu\text{m}$ thick sample. Assuming that all absorbed photons contribute to the photocurrent, the quantum efficiency (η) is considered the same as the absorption efficiency, i.e. $\eta = \eta_{abs}$.

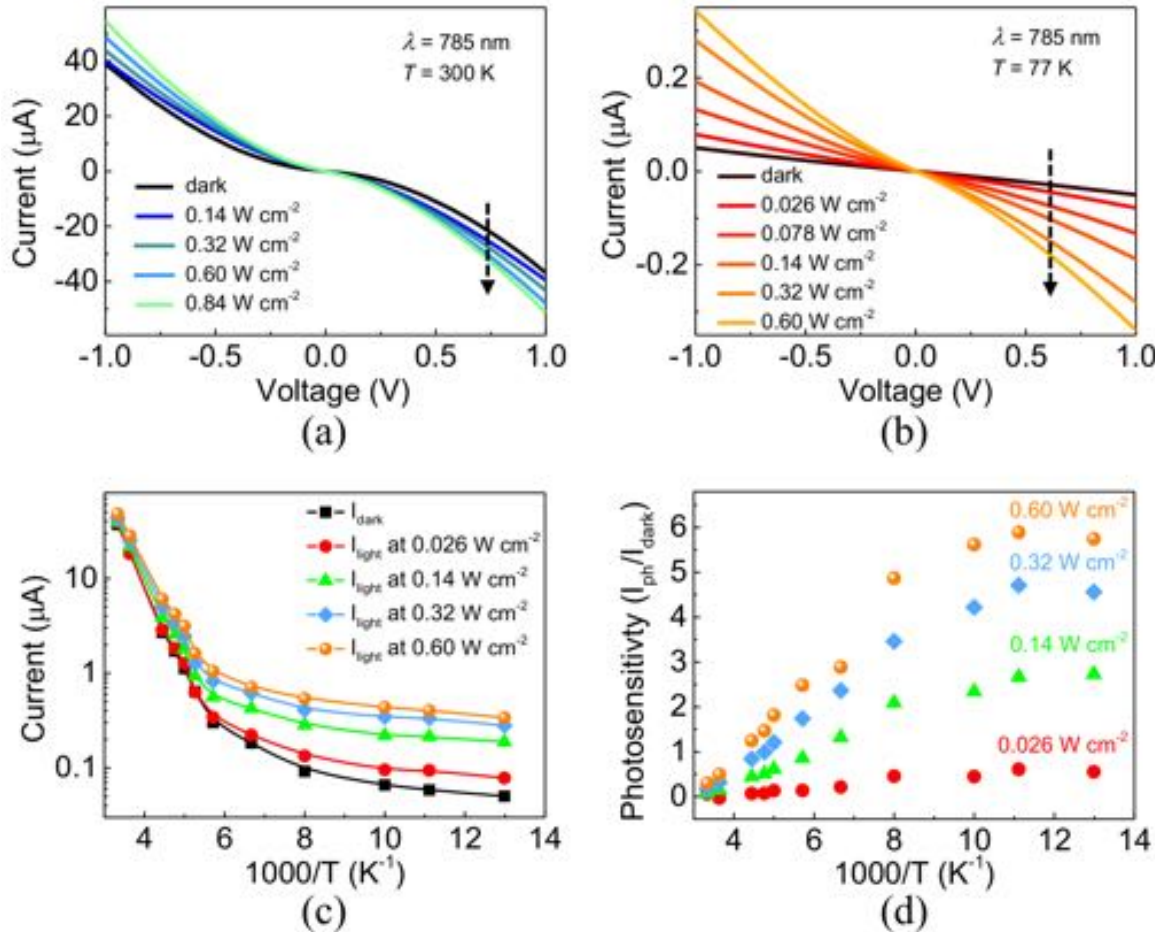


Figure 6.5: Electrical characterization of the MOF photodetector at 785 nm. (a),(b) I - V curves for different power densities of 785 nm wavelength at 300 K and 77 K, respectively, (c) temperature dependence of current in the dark (I_{dark}) and under illumination (I_{light}) at various power densities and at a bias of -1 V , (d) photosensitivity ($I_{\text{ph}}/I_{\text{dark}}$) versus temperature at various laser power densities and at an applied bias of -1 V . Adapted from Arora et al.^[3]

From Equation 6.10, responsivity (R) is calculated to be 4 mA W^{-1} at 300 K ($P = 0.14 \text{ W cm}^{-2}$, $V = -1 \text{ V}$). The responsivity of the MOF photodetector is comparable to the values obtained for the first demonstrations of photodetectors based on black phosphorus (4.8 mA W^{-1})^[184] and graphene ($< 6 \text{ mA W}^{-1}$)^[187,188] indicating a promising potential of MOFs in optoelectronics. However, in a photoconductor, responsivity is strongly

dependent on the device geometry and can vary significantly with the device active area.^[176] In this respect, we further analyzed voltage responsivity (R_v), since it is independent of the device area. An R_v of 2.5 kV W^{-1} and 0.07 kV W^{-1} at 77 K and 300 K , respectively, is inferred using Equation 6.11. The temperature dependence of R_v is plotted in Figure 6.6a and shows a continuous increase with decreasing temperature.

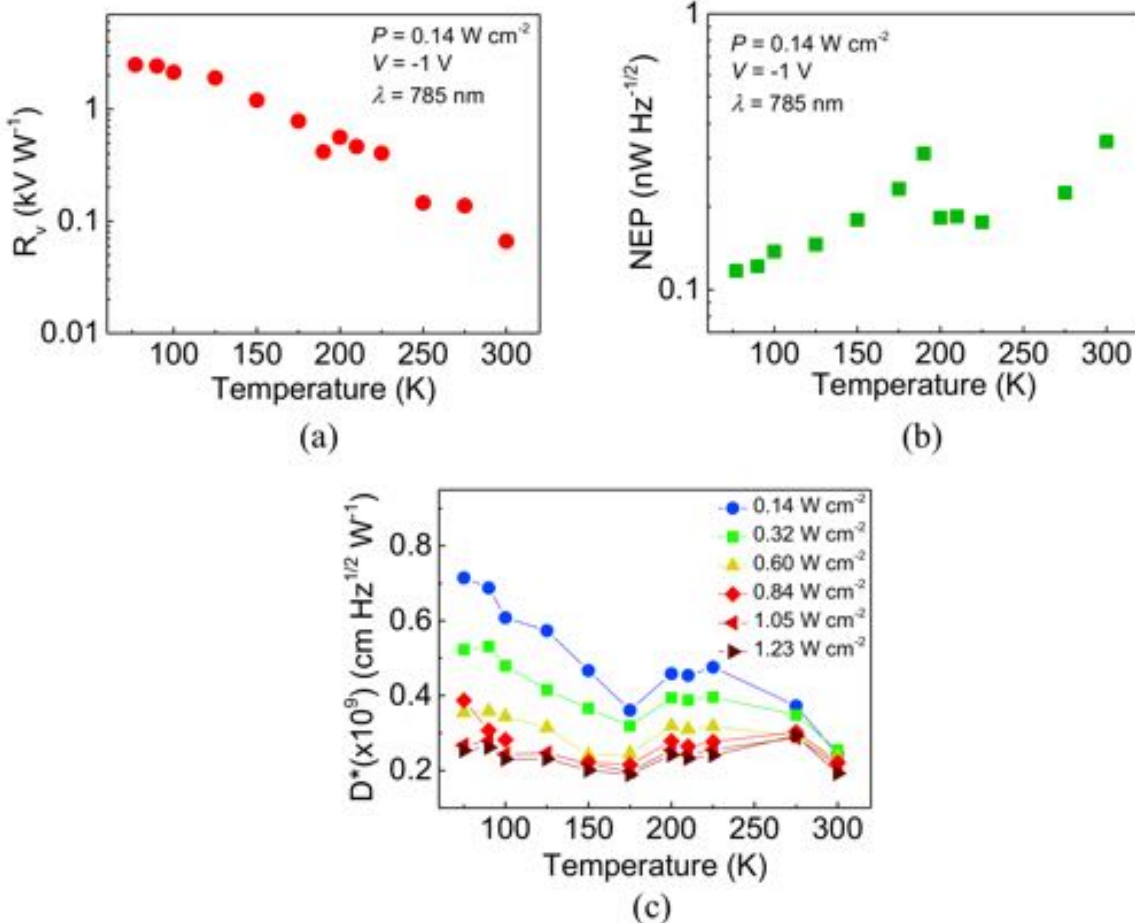


Figure 6.6: Figures of merit calculated at 785 nm to characterize the performance of the MOF photodetector as a function of temperature. (a),(b) temperature dependence of R_v and NEP, (c) temperature dependence of D^* for various power densities of 785 nm laser. Adapted from Arora et al.^[3]

Another important parameter to evaluate the performance of the photodetector is NEP, calculated by using Equation 6.13. From the photocurrent measurements, the Johnson noise is calculated using Equation 6.14. For the MOF device, the values of I_j are found to be $7.81 \times 10^{-13} \text{ A Hz}^{-1/2}$ at 300 K , which decreases to $1.44 \times 10^{-14} \text{ A Hz}^{-1/2}$ at 77 K ($P = 0.14 \text{ W cm}^{-2}$, $V = -1 \text{ V}$). The G-R noise, calculated from Equation 6.15, is found to be ranging from 3.11×10^{-13} at 300 K to $2.60 \times 10^{-15} \text{ A Hz}^{-1/2}$ at 77 K . While the Johnson and G-R noise estimations are straightforward, the $1/f$ noise is difficult to analyze analytically and is currently out of the scope of this work. Therefore, only Johnson noise and G-R noise are considered for the calculation of NEP. NEP as a function of temperature is plotted in Figure 6.6b. An NEP value as low as possible is desirable for an efficient

and sensitive photodetector, which for $\text{Fe}_3(\text{THT})_2(\text{NH}_4)_3$ MOF photodetectors is achieved by lowering the operating temperature. Finally, the influence of temperature on D^* is investigated for various laser power densities. Figure 6.6c shows an increase in D^* as the temperature decreases, with a peak value of $7 \times 10^8 \text{ cm Hz}^{1/2} \text{ W}^{-1}$ achieved at 77 K. It should be noted that the estimated NEP values (and hence, D^*) depend on the assumption that all absorbed photons generate free charge carriers. There is a possibility that a part of the absorption is “parasitic”, i.e. some photons are lost without contributing to any photocurrent, leading to additional (typically, $1/f$) noise. Such a scenario would imply a higher gain, larger NEP, and smaller D^* values. Since this scenario is currently neglected, the estimations of NEP and D^* are valid only under the assumptions that the total noise comprises of only Johnson noise and G-R noise, and that the quantum efficiency equals the absorption efficiency. Therefore, our calculations provide a lower limit estimate of NEP and an upper limit of D^* values for the developed MOF photodetectors.

Subsequently, the photoswitching performance of the MOF photodetector is evaluated by testing its response to light/dark cycles of illumination at 785 nm at various temperatures. Irrespective of temperature, a strong and reproducible switching behavior is revealed in Figure 6.7a, which demonstrates a stable operation of the MOF device under pulsed irradiation. The response times for both rise and decay processes are extracted. From Figure 6.7b, the rise and decay times at 77 K are found to be 2.3 s and 2.15 s, respectively, an increase from ~ 1.7 s for both at 300 K. On testing multiple samples, response times in the range of 1–3 s are obtained. These response times are affected severely by the types and density of defects either intrinsic to the material and/or arising during device fabrication processes.^[182,185,189] Previous reports have shown that by modulating these defects in a controlled manner, faster response times can be achieved.^[175,177,182,185,189] A brief discussion of potential defects present in our samples and ways to engineer them to obtain faster response time is provided next.

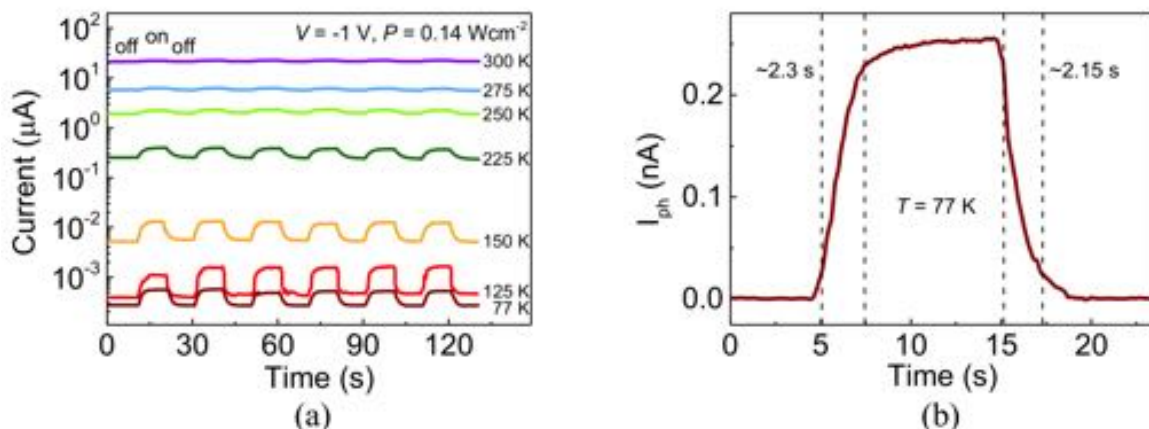


Figure 6.7: Photoswitching behavior of the MOF photodetector at 785 nm. (a) Photoresponse as a function of time at different temperatures. The device shows long-term stable photoswitching capability, (b) time-resolved response zoomed for 77 K showing a response time of ~ 2 s. Adapted from Arora et al.^[3]

Potential origins of defects Two types of defects are commonly present in MOF samples: point defects, such as vacancies associated with metal centers or organic ligands and extended defects associated with imperfections in the crystal structure.^[190] When samples are polycrystalline, like our MOF samples, grain boundaries will tend to be populated with a large density of defects, which can modulate energy barriers between the grains and affect the charge transport. Mid-gap states will also affect the response time by trapping/releasing photogenerated charge carriers when the light is switched on/off.^[182,185] An indication for the presence of such defects in our MOF samples can be traced back to the band-tail in the absorbance between 0.50–0.65 eV (Tauc plot in Figure 6.3a). In addition to these, defects can also arise during the device fabrication process, e.g. because of charge disorder at the substrate/MOF interface, tunnel barriers and Fermi level pinning at the metal/MOF contact, and/or surface barriers formed when the MOF film comes in contact with moisture and oxygen in air.^[6,8,10,185,189] A study on photoresponse of monolayer MoS₂ has demonstrated a strong influence of the bottom substrate in controlling the response times,^[189] whereas another report on WS₂ photoresponse has revealed that trap states at the metal/WS₂ junction can delay the response time substantially.^[185] Furthermore, the response time may also be affected by the large area-to-volume ratio of our samples, resulting in local bending, corrugations, and irregularities of the MOF films that can be associated with charge carrier localization. The porous and large areas of the samples also enable host molecules to eventually contribute to the charge transport, evidently revealed by the changes in resistances of these samples under different environments (chemiresistive behavior).^[168,191]

Defect engineering strategies Owing to the synthetic flexibility of MOFs, intrinsic defects could be modulated in a controlled manner either during or after synthesis. A proven effective strategy is to tune the metal centers and their valences, which can significantly affect their electronic properties.^[192–195] For example, a bi-metallic MOF structure of Fe/Cu or Fe/Ni with controlled metallic ratios can be synthesized to modulate the density of mid-gap states. Specific to Fe-THT MOFs, reducing Fe³⁺ into Fe²⁺ after synthesis can result in improved conjugation and enhanced transport properties. Grain boundaries can also be reduced by obtaining larger crystalline domains by either increasing the synthesis temperature or by post-synthesis thermal annealing of the MOF samples. From a device fabrication point of view, mechanically exfoliated MOF films can be employed into devices, which in the case of MoS₂ has yielded faster photoresponse because of improved quality and lower defect density of the samples as compared to bottom-up grown films.^[189,196,197] Opting for a substrate that is dangling bonds-free and has very low charge traps, such as hBN, is also an effective approach as discussed in chapter 4.^[6,8] Top encapsulation of the porous structures of MOFs from air can prevent the layers from surface defects. Further defect engineering can be performed by fabricating more reliable contacts, e.g. by using e-beam lithography or thermal probe lithography, which will also help reduce the edge states. The optimization of channel area and electrode spacing are other possibilities to improve response speed as well as performance.

3.3.2 1575 nm illumination

The photoresponse of the MOF device is further tested at longer wavelengths in the NIR region. Figure 6.8a shows the photoresponse of the device operated at 77 K under 1575 nm irradiation. The photocurrent is found to increase linearly with the laser power density as per the power law, $I_{ph} \propto P^\gamma$ (Figure 6.8b). The exponent (γ) in the power law is extracted to be 0.94. A quantitative analysis of the photoresponse with temperature shows that the MOF device is photoconductive at all temperatures in the range of 77–300 K. The photosensitivity in Figure 6.8c is found to increase substantially with decreasing temperature, resulting in an improved performance of the device at lower temperatures. At $P = 0.31 \text{ W cm}^{-2}$, photosensitivity increases from 1 at 300 K to 20 at 77 K. Other figures of merit, such as NEP and D^* are calculated to be $0.07 \text{ nW Hz}^{-1/2}$ and $2 \times 10^9 \text{ cm Hz}^{1/2} \text{ W}^{-1}$ at $P = 0.14 \text{ W cm}^{-2}$ and $V = -1 \text{ V}$. In addition, a strong and reproducible photoswitching behavior is observed (Figure 6.8d), which improves as the device is cooled down.

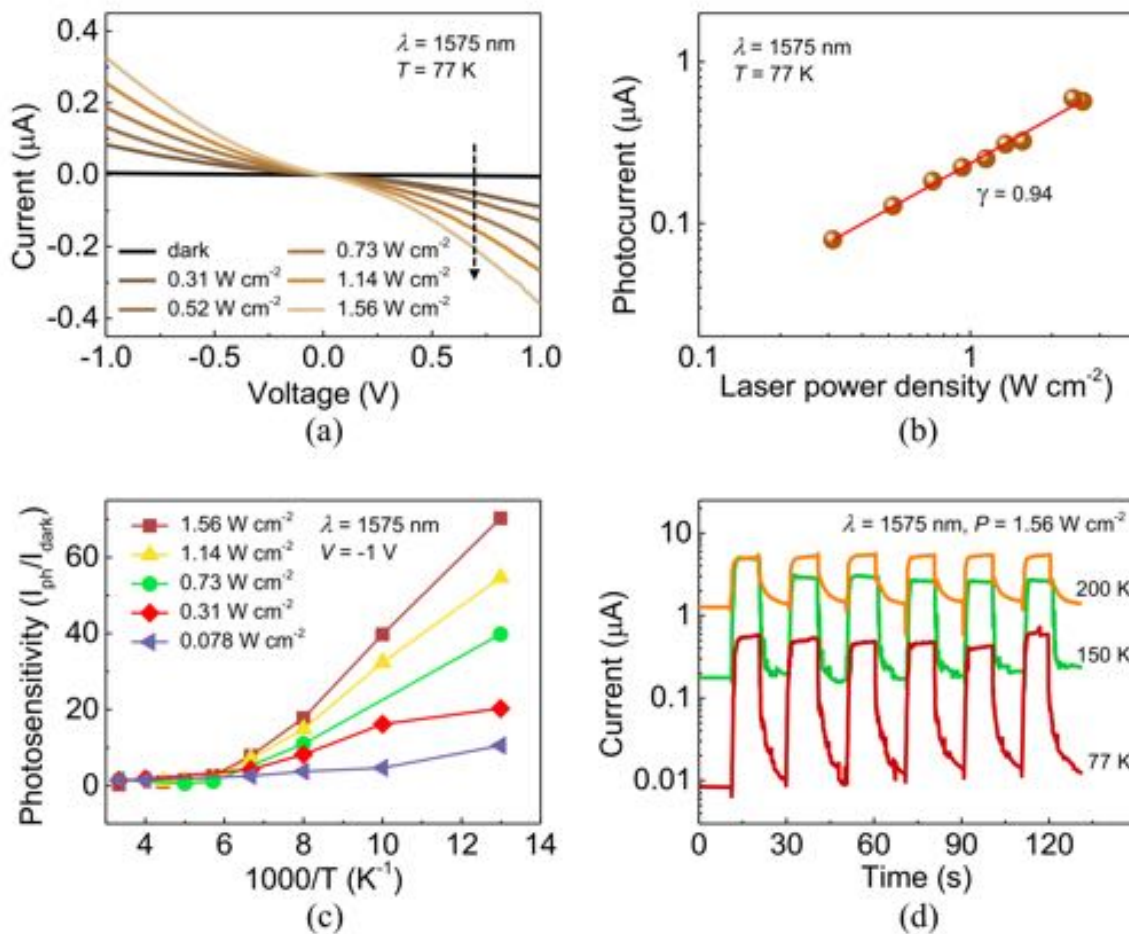


Figure 6.8: Performance characterization of the MOF photodetector at 1575 nm as a function of temperature. (a) I - V curves for different laser power densities at 77 K, (b) I_{ph} versus P at 77 K, showing linear dependence with $\gamma = 0.94$, (c) photosensitivity versus $1/T$ at various laser power densities at -1 V bias, (d) photoswitching behavior at various temperatures at $P = 1.56 \text{ W cm}^{-2}$ and -1 V bias. Adapted from Arora et al.^[3]

3.4 Photoresponse in the visible region

3.4.1 405 nm illumination

The photoresponse of the MOF device under 405 nm illumination at 100 K is summarized in Figure 6.9. An enhancement of the current on illumination in Figure 6.9a confirms the photodetection operation in the visible region. The laser power dependence of the photocurrent shows a sublinear increase with $\gamma = 0.84$ at 100 K (Figure 6.9b). The slight deviation of γ from unity is attributed to complex recombination processes associated with photogenerated carriers and traps.^[187,188] Consistent with previous findings at 785 nm and 1575 nm, a stable and reproducible photoswitching behavior is obtained at 405 nm, as revealed in Figure 6.9c. A significant improvement in photosensitivity and performance is obtained once the device is cooled down to lower temperatures. On testing multiple samples, the response times for both rise and decay processes are found to be within 1–3 s (Figure 6.9d). For the analyzed temperature range of 100–300 K, the lowest NEP and peak D^* values are obtained at 100 K, corresponding to $2.8 \text{ nW Hz}^{-1/2}$ and $3 \times 10^7 \text{ cm Hz}^{1/2} \text{ W}^{-1}$, respectively at $P = 0.14 \text{ W cm}^{-2}$ and $V = -1 \text{ V}$.

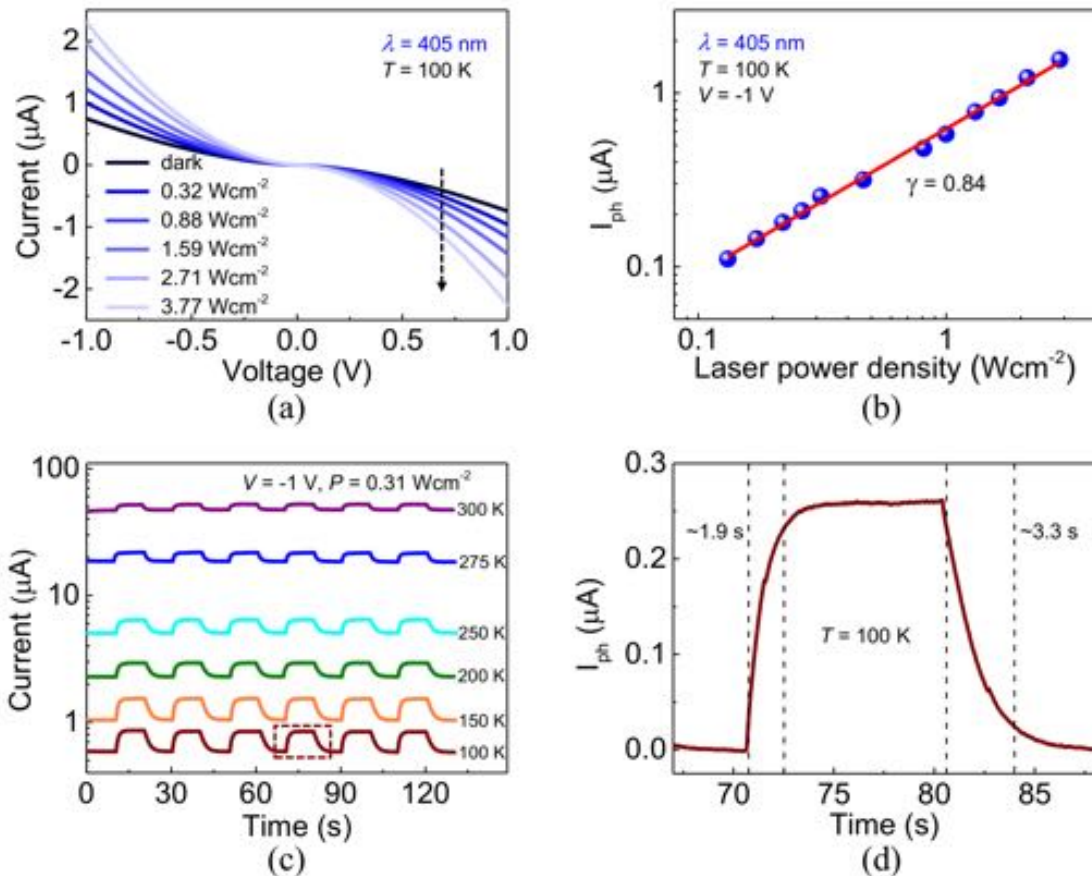


Figure 6.9: Performance characterization of the MOF photodetector at 405 nm. (a) I - V curves for different laser power densities at 100 K, (b) I_{ph} versus P at 100 K, showing linear dependence with $\gamma = 0.84$, (c) temperature-dependent photoresponse as a function of time, (d) time-resolved photoresponse zoomed for 100 K, showing a rise time of $\sim 1.9 \text{ s}$ and decay time of $\sim 3.3 \text{ s}$. Adapted from Arora et al.^[3]

3.4.2 633 nm illumination

The MOF device operated at 100 K shows a change in photoconductance when a 633 nm laser is irradiated on the detector area (Figure 6.10a). The photocurrent is found to increase linearly with the laser power density as per the power law $I_{ph} \propto P^\gamma$ with $\gamma = 1.01$, plotted in Figure 6.10b. The photosensitivity (Figure 6.10c) is found to increase with decreasing temperature, resulting in an improved performance of the device at lower temperatures. At $P = 0.05 \text{ W cm}^{-2}$, the photosensitivity increases by two orders of magnitude from 0.04 at 300 K to 4 at 100 K. Consistent with the trend at other wavelengths, the figures of merit improve at 100 K compared to 300 K; associated with the suppression of thermally activated charge carrier density with temperature. At 100 K, an NEP of $0.33 \text{ nW Hz}^{-1/2}$ and D^* of $3 \times 10^8 \text{ cm Hz}^{1/2} \text{ W}^{-1}$ at $P = 0.14 \text{ W cm}^{-2}$ and $V = -1 \text{ V}$ is achieved.

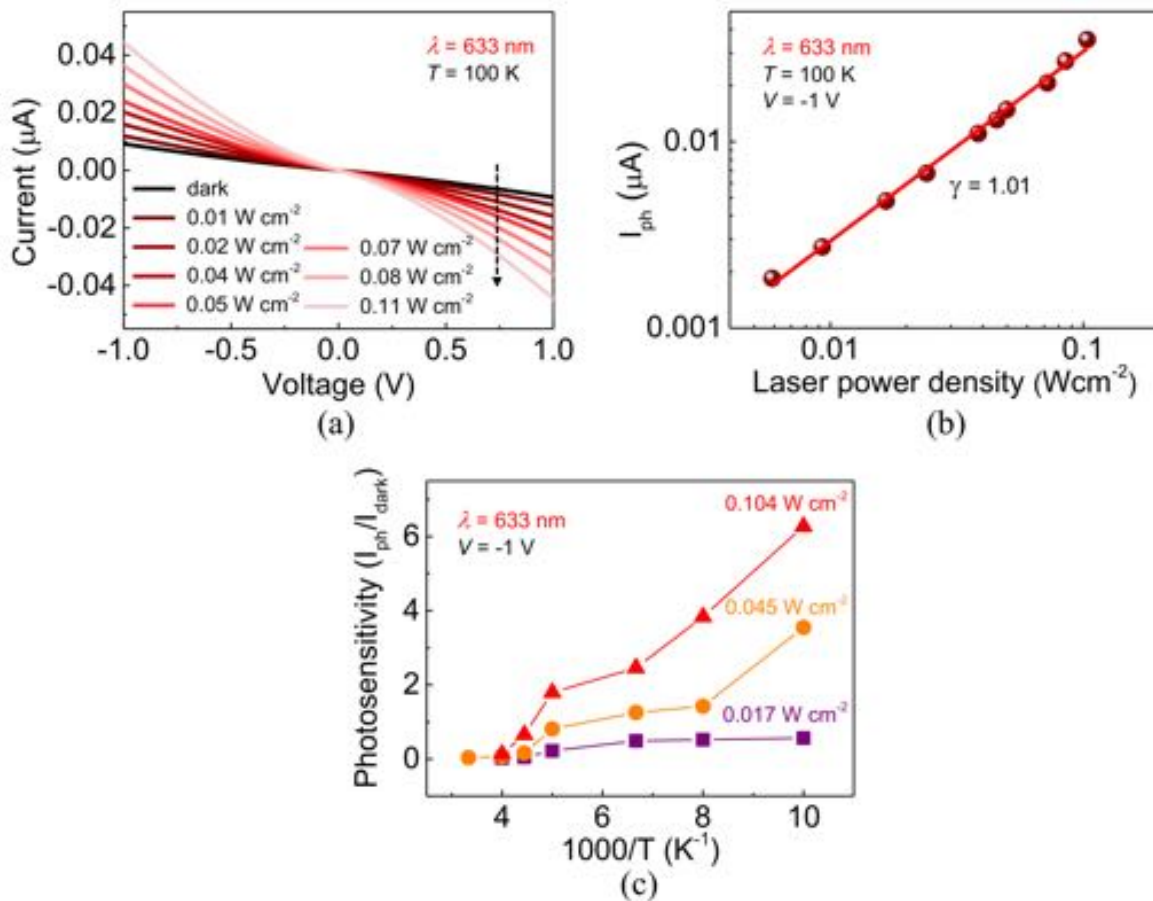


Figure 6.10: Performance characterization of the MOF photodetector at 633 nm. (a) I - V curves for different laser power densities of 633 nm wavelength at 100 K, (b) I_{ph} versus P at 100 K, showing a linear dependence with $\gamma = 1.01$, (c) photosensitivity versus $1/T$ at various laser power densities and at -1 V bias. Adapted from Arora et al.^[3]

In order to analyze the photoswitching capability, the response of the MOF device to pulsating illumination of 633 nm at various temperatures is tested. Figure 6.11a reveals a strong and reproducible switching behavior, confirming a robust and stable MOF photodetector. Furthermore, a significant improvement in photosensitivity is observed as the device is cooled

down to lower temperatures. In Figure 6.11b, the photoswitching characteristics at 300 K and 175 K have been enlarged. A noisy response at 300 K is obtained, which smooths out at 175 K. This observation is attributed to thermal transitions across the bandgap at higher temperatures, resulting in large dark current, making the device noisy and hampering its photosensitivity. With decreasing temperature the thermal generation of the charge carriers is suppressed below the optical generation to yield a photo-excitation dominated signal.

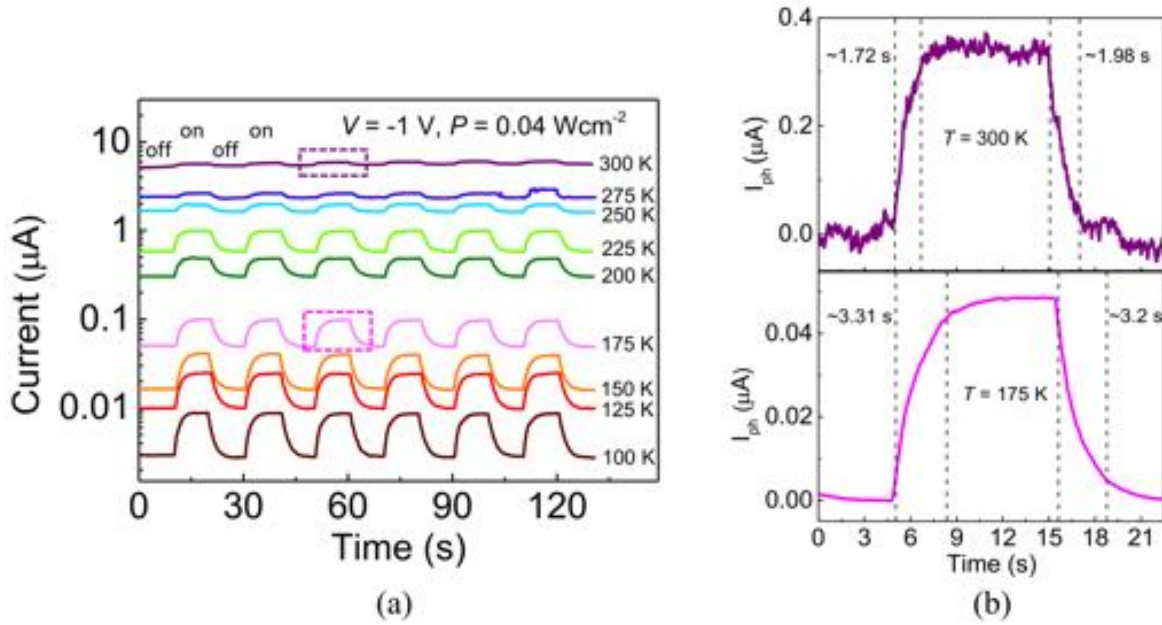


Figure 6.11: Photoswitching behavior of the MOF photodetector at 633 nm. (a) temperature-dependent photoresponse as a function of time at 633 nm, (b) temporal response at 300 K (upper panel) and 100 K (lower panel) at $P = 0.04 \text{ W cm}^{-2}$. A noisy response is obtained at room temperature, which smooths out at lower temperatures, yielding stable and reliable device performance.

An enhancement of the current at all analyzed wavelengths confirms the broadband photodetection in the UV-to-NIR range. The photocurrent increases with the laser power density in accordance with the power law, with the exponent $\gamma = 0.92 \pm 0.09$ for all analyzed wavelengths. Temperature-dependent photoswitching measurements further confirm a stable and robust device with response time in the range of 1–3 s. The responsivity calculated for all impinging wavelengths at 100 K is plotted in Figure 6.12. Since MOFs have high absorption in the UV–NIR region, no significant change in the quantum efficiency at these wavelengths is expected, which is consistent with the observed wavelength-independent responsivity.

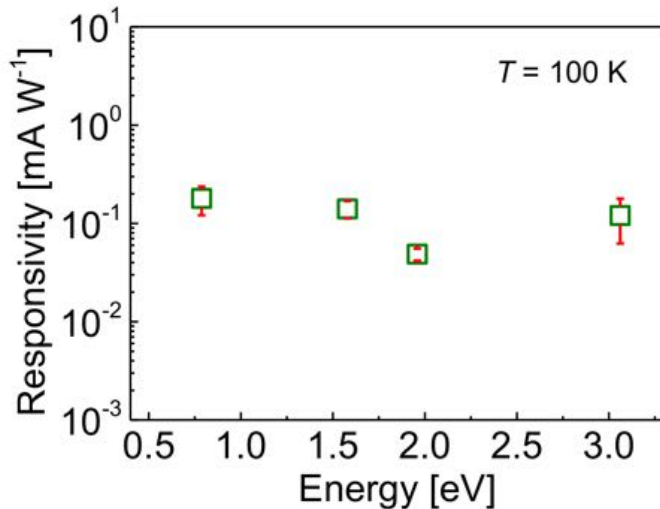


Figure 6.12: Responsivity at 100 K as a function of photon energy at a constant laser power density $P = 0.14 \text{ W cm}^{-2}$. Error bars represent the standard error of the mean. Adapted from Arora et al.^[3]

4 Conclusions

In summary, we report a proof-of-concept photodetector device based on semiconducting $\text{Fe}_3(\text{THT})_2(\text{NH}_4)_3$ 2D MOF films operating in a broad spectral range (400–1575 nm). A systematic study of the photoresponse dependence on temperature, wavelength, and incident laser power is carried out for the first time to fully address the performance of the MOF device. Significant improvements in the performance of the device are achieved by cooling the detector to cryogenic temperatures. These results are consistent with the low IR bandgap of the samples, which causes strong thermally activated band-to-band population of free charge carriers at room temperature. Cooling the devices suppresses this thermal generation of the charge carriers, which consequently leads to much improved device performance. Furthermore, the devices show stable and reproducible photoswitching behavior.

Our findings present the feasibility of integrating 2D MOFs as an active element into functional photodetectors, thus bridging the gap between materials' synthesis and technological applications. Owing to synthetic flexibility, large-area coverage and cost-effective production of the 2D conjugated MOFs, these materials are promising candidates for a plethora of optoelectronic applications.

Chapter 7

Summary and outlook

The field of 2D materials, despite being only a few decades old, has stimulated a lot of interest in the scientific community. The most fascinating opportunity is the possibility to replace silicon in next generation electronics. In this regard, the 2D semiconductors MoS₂ and WSe₂ have come quite close to the expectation. However, yet lower mobility than silicon, a direct bandgap available only in monolayers, and issues with large area growth have kept these materials from practical viability. With the research on conventional semiconducting TMDCs reaching a mature stage, the search for new materials beyond these traditional 2D materials is at a rapid pace. Another emerging frontier in 2D materials research is the fabrication of vdW heterostructures and devices. The possibility to “mix and match” various 2D layers in a vdW heterostructure provides a wide playground to explore a number of exciting physical phenomena, such as the study of twisted layers and Moiré patterns. Furthermore, such techniques allow to investigate the properties of materials which are unstable under ambient conditions by encapsulating them in inert layers.

The work presented in this thesis aims to explore charge transport in two different classes of 2D semiconducting materials: (a) inorganic InSe and GaSe and (b) organic-inorganic hybrid Fe₃(THT)₂(NH₄)₃ MOF. Though all are 2D semiconductors with appealing (opto)electronic properties, their integration into technological devices and applications has been highly constrained. On the one hand, the sensitivity of few-layered InSe and GaSe towards air, bottom dielectrics, and standard lithography processes has made the assessment of their intrinsic properties difficult. On the other hand, the majority of MOFs developed to date have been associated with large bandgap and lower mobilities. The poor compatibility of MOFs with standard device fabrication processes has added to further issues. Therefore, for both these classes, their usage at the device-level has remained a daunting challenge. In this work, we have attempted to tackle the limitations of these materials by understanding their charge transport mechanisms and developing novel techniques to better exploit their intrinsic properties for subsequent utilization into devices.

The demonstration of high mobilities in InSe, and of nonlinear optical properties as well as single-photon emission in GaSe has set them as emerging 2D semiconductors. Yet, their devices are lagging behind because of their sensitivity to the environment and to standard

device fabrication processes. The initial attempts to fabricate InSe FETs involved mechanically exfoliated few-layered InSe on a SiO₂/Si substrate with metal electrodes evaporated directly onto bare InSe. These InSe devices yielded much lower performance than expected and became non-functional within a few hours. This indicated that passivating these layers against the environment is necessary in order to preserve their intrinsic properties. In addition, novel contacting schemes are needed to obtain reliable and high-quality contacts to few-layered InSe and GaSe. In this regard, we developed a hBN-based encapsulation technique, where 2D layers of InSe and GaSe are covered entirely between two layers of hBN. The top hBN layer passivates the 2D layer from the environment and the bottom hBN prevents charge transfer to the 2D layer from the SiO₂ substrate. The vdW stack of hBN/InSe/hBN is fabricated inside a nitrogen-filled glovebox, which further ensures a contamination-free stacking and minimal exposure of InSe to ambient conditions. To fabricate devices out of fully encapsulated 2D layers, we employed the via-contacting scheme (metal contacts embedded within hBN flakes). Via-contacts allow to simultaneously achieve encapsulation and electrical connection to the underlying 2D layer without any direct lithographic patterning. Based on our results, we found that hBN acts as an excellent encapsulant and a near-ideal substrate for InSe and GaSe by passivating them from the environment and isolating them from the charge disorder at the SiO₂ surface. Consequently, the fully encapsulated InSe and GaSe devices showed greatly enhanced and ambient-stable performance. A two-terminal field-effect mobility of 30–120 cm² V⁻¹ s⁻¹ and an on/off ratio of 10⁴ is obtained at room temperature for fully encapsulated InSe device as compared to a mere \sim 1 cm² V⁻¹ s⁻¹ for unencapsulated devices.

Our results show that in order to study the unaltered properties of InSe and GaSe, their encapsulation is essential. To date, four major encapsulating techniques have been reported for InSe, one of which is developed in this project. In addition, this work provides a systematic study of *fully* encapsulated devices based on InSe and GaSe, which was missing until now. We believe that this technique can open ways for fundamental studies as well as towards the integration of these materials in technological applications.

Another 2D semiconductor studied in this thesis belongs to the class of MOFs, hybrid materials consisting of metal ions connected by organic ligands. Owing to tunable coupling between the organic and inorganic constituents and long-range crystalline order, electrically conductive MOFs are emerging as a new generation of electronic materials. However, to date, the nature of charge transport in the MOFs has remained elusive. Addressing these fundamental mechanisms in semiconducting MOFs is essential for further MOF designing as well as to allow this class of materials to be exploited for optoelectronic applications.

In this work, we address the charge transport mechanisms in a novel semiconducting Fe₃(THT)₂(NH₄)₃ 2D MOF. This new material exhibits a direct IR bandgap (0.25–0.45 eV) and is interesting from both fundamental and application point of view. To understand the charge transport mechanisms, we performed four-probe conductivity and Hall-effect measurements for the first time on a MOF system. Hall bar geometry is patterned on a 1.7 μ m thick MOF film deposited on a SiO₂/Si substrate, followed by metal contact

fabrication using e-beam lithography. Temperature-dependent conductivity measurements revealed a decrease in the conductivity on reducing the temperature. This strong variation of conductivity with temperature suggests a thermally activated charge carrier population in the samples and/or a reduction in the sample's mobility induced by scattering sites, such as grain boundaries; the former and latter being consistent with the low bandgap of the analyzed MOFs and the polycrystalline nature of our samples, respectively. To disentangle the potential contribution of these two effects on conductivity, we performed temperature-dependent Hall-effect measurements. While the Hall mobility was barely affected over the analyzed temperature range, the carrier density was found to decrease exponentially with temperature. This thermally activated charge carrier population is described by $N \propto \exp[-E_g/2kT]$ and is enabled by the narrow bandgap of the $\text{Fe}_3(\text{THT})_2(\text{NH}_4)_3$ MOF. Because conductivity is directly proportional to charge carrier density (from Drude's law), this also accounts for the decrease in the conductivity of the MOF sample with temperature. These findings confirm a band-like charge transport operating in the films. From the Hall measurements, a room temperature mobility of $230 \text{ cm}^2 \text{ V}^{-1} \text{ s}^{-1}$ is resolved for the samples, which is a record-high value reported for a MOF structure. In addition, *p*-type doping (induced by Fe^{3+} centers) is inferred from the Hall data.

With these attractive properties of high mobility, direct bandgap, and band-like charge transport, subsequently, we employed the 2D MOF films of $\text{Fe}_3(\text{THT})_2(\text{NH}_4)_3$ as an active element in a two-terminal photodetector device. The MOF-based photodetector operating in photoconductive mode is capable of detecting a broad wavelength range from UV to NIR (400–1575 nm). The narrow IR bandgap of the active layer constrains the performance of the photodetector at room temperature by band-to-band thermal excitation of charge carriers. To prevent thermally activated charge carriers from overshadowing the optically generated signal, the photodetectors are cooled to cryogenic temperatures. Over the analyzed wavelength range, the figures of merit of the photodetectors are found to improve drastically at 77 K as compared to room temperature; a two orders of magnitude higher voltage responsivity, lower noise equivalent power, and higher specific detectivity of $7 \times 10^8 \text{ cm Hz}^{1/2} \text{ W}^{-1}$ are achieved under 785 nm excitation. In addition, a long-term stable photoswitching behavior is obtained. These figures of merit are retained over the analyzed spectral region and are comparable to those obtained with the first demonstrations of graphene and black phosphorus based photodetectors. So far, only a handful of reports have addressed the photodetection properties of MOFs and our work reports the first proof-of-concept MOF-based photodetector, revealing MOFs as promising candidates for optoelectronic applications.

Along with material and device characterization, we also ventured into the area of vdW heterostructures to explore the properties and underlying physics of 2D materials. Various transfer techniques are optimized and utilized during the course of this work. Depending on the final structure, an appropriate transfer technique is then chosen. Special focus is given to vdW stacks of hBN/2DM/hBN, where the major role of hBN is to encapsulate the 2D layer. Other than this, we fabricated TEM samples with free-standing mono- and few-layers of hBN. The samples were used by our collaborators at IFW Dresden to develop an electron

holographic method, which facilitates high spatial resolution compared to conventional imaging techniques in the TEM. In the future, these techniques can be used to fabricate complex 2D- and quasi 2D-structures. An exciting opportunity is to explore twisted layers of similar or dissimilar materials. The study of Moiré patterns and their unique properties could be an interesting avenue.

Outlook An immediate continuation of this work could be to perform four-probe and Hall-effect measurements on fully encapsulated InSe-via devices. Because contact resistance does not contribute to the results obtained from these measurements, a more precise estimate of the transport properties could be obtained. Further improvements to these devices could be achieved by stacking the layers in more stringent environments, i.e. an argon-filled glovebox. Fabricating the heterostructures in argon atmosphere is expected to enhance the lifetime of the devices by minimizing the contaminants to the lowest. In the future, the whole process from exfoliation to vdW assembly and finally, electrical and structural characterization could be carried out inside a vacuum chamber. Assessing the properties of the layers without breaking the vacuum would be the ultimate challenge and could possibly reveal fascinating properties and physical phenomena. One such setup is currently under construction at the University of Manchester. Other than studying the electronic properties, encapsulation of InSe opens ways to study its unaltered optical properties. One such study is carried out by our collaborator at HZDR by performing thickness-dependent time-resolved photoluminescence measurements on hBN/InSe/hBN stacks. This work studies PL dynamics of few-layered InSe and reports two recombination processes, the direct bandgap electron-hole and defect-assisted radiative recombination. The ratio of the weights of the two processes varies with the number of layers, and confirms the direct-to-indirect bandgap transition below 6 nm in InSe.

The advances in terms of device engineering for InSe show an increasing inclination of the scientific community towards III–VI semiconductors for applications into next-generation high-speed electronic devices. However, the integration of these materials into devices is limited, attributed to their instability under ambient conditions. Based on this work, prototype devices including image sensors and photodetectors could be fabricated from encapsulated InSe and GaSe. Combining InSe (*n*-type) and GaSe (*p*-type) to fabricate lateral *p*-*n* junctions for the applications of photovoltaic and light emitting diodes is an interesting and yet unexplored endeavor. The direct bandgap of InSe and GaSe is a promising feature, especially for optoelectronic applications. In combination with vdW assembly techniques, multilayered vertical vdW structures, such as a *p*-*i*-*n* diode based on InSe and GaSe could be fabricated. The direct bandgaps of both materials are expected to offer high efficiency as well as large spectral tunability of the devices. The large bandgap of hBN (\sim 5.7 eV) is particularly advantageous here, as it does not interfere with the performance of the devices.

hBN due to its inertness, atomically flat surface and low defect density is compatible with most 2D materials. In the future, our encapsulation technique can be applied to other air-sensitive 2D materials that have been restricted so far in their fundamental study and applications because of their environmental sensitivity. Black phosphorus, a high-mobility

material ($6000 \text{ cm}^2 \text{ V}^{-1} \text{ s}^{-1}$) but extremely air-sensitive is one such material of interest. Because of its rapid degradation in air, most research has been done on few-layers rather than on atomically thin layers. In addition, due to its poor compatibility with other 2D materials, very few reports have addressed encapsulation techniques for black phosphorus. With this respect, the via-encapsulation technique could be an exciting opportunity to investigate the intrinsic properties of black phosphorus and to pave the way for its technological applications. While it is apparent that our via-encapsulation technique is beneficial for air-sensitive materials, it is not restricted only to them. Though TMDCs are known to be relatively stable, it has been found that even their electronic properties degrade over time on exposure to air. Encapsulating these materials in hBN would yield reliable and high-quality devices, which are stable for a prolonged period of time.

In case of MOFs, a number of future directions can be pursued. Owing to high tunability of the 2D MOFs, their conductivity, mobility and bandgap could be further improved through appropriate chemical designs. From a synthesis point of view, structural engineering could be pursued by tuning the metal centers and their valences, which can significantly affect their electronic properties. Specific to Fe-THT MOFs, reducing Fe^{3+} into Fe^{2+} during or after synthesis could result in improved conjugation and enhanced transport properties. Other approaches to modify their intrinsic properties include modification of the functional groups and organic ligands and selecting appropriate guest molecules within the pores. Specifically, developing single crystals and exfoliating them into monolayers would enable the development of high-quality MOF-based devices. These single-domain films will further help to control the grain boundaries which are a possible scattering site in our MOF samples because of its polycrystalline nature.

Our findings show a promising future for MOF-based photodetection, however, opportunities for further improvements by optimizing the device configuration, fabrication of reliable contacts, and structural engineering of the material still exist. From a device fabrication point of view, mechanically exfoliated MOF films, which are usually associated with improved quality and lower defect density as compared to bottom-up grown films, could be employed into devices. Opting for a substrate that is dangling bonds-free and has very low charge traps, such as hBN, could further enhance the device performance as discussed for InSe and GaSe in chapter 4. The optimization of channel area and electrode spacing are other possibilities to improve response speed as well as performance of the photodetector. Finally, designing 2D vdW heterostructures, e.g. by combining MOFs with other 2D materials are exciting avenues to be followed and yet unexplored. The controlled stacking of 2D MOF layers with other organic and/or inorganic 2D materials will allow the development of heterostructures with unique physical and chemical properties with a potential for various applications.

Bibliography

- [1] **H. Arora** and A. Erbe, “Recent progress in contact, mobility, and encapsulation engineering of InSe and GaSe”, InfoMat, 10.1002/inf2.12160 (2020).
- [2] **H. Arora**, S. Park, R. Dong, and A. Erbe, “2D MOFs: A New Platform for Optics?”, Optics and Photonics News **31**, 36–43 (2020).
- [3] **H. Arora**, R. Dong, T. Venanzi, J. Zscharschuch, H. Schneider, M. Helm, X. Feng, E. Cánovas, and A. Erbe, “Demonstration of a Broadband Photodetector Based on a Two-Dimensional Metal–Organic Framework”, Advanced Materials **32**, 1907063 (2020).
- [4] T. Venanzi, **H. Arora**, S. Winnerl, A. Pashkin, P. Chava, A. Patanè, Z. D. Kovalyuk, Z. R. Kudrynskyi, K. Watanabe, T. Taniguchi, A. Erbe, M. Helm, and H. Schneider, “Photoluminescence dynamics in few-layer InSe”, Physical Review Materials **4**, 044001 (2020).
- [5] F. Kern, M. Linck, D. Wolf, N. Alem, **H. Arora**, S. Gemming, A. Erbe, A. Zettl, B. Büchner, and A. Lubk, “Autocorrected off-axis holography of two-dimensional materials”, Physical Review Research **2**, 043360 (2020).
- [6] **H. Arora**, Y. Jung, T. Venanzi, K. Watanabe, T. Taniguchi, R. Hübner, H. Schneider, M. Helm, J. C. Hone, and A. Erbe, “Effective Hexagonal Boron Nitride Passivation of Few-Layered InSe and GaSe to Enhance Their Electronic and Optical Properties”, ACS Applied Materials & Interfaces **11**, 43480–43487 (2019).
- [7] F. Kern, M. Linck, D. Wolf, T. Niermann, **H. Arora**, N. Alem, A. Erbe, S. Gemming, and A. Lubk, “Direct Correction of Residual Symmetric Aberrations in Electron Holograms of Weak Phase Objects”, Microscopy and Microanalysis **25**, 98–99 (2019).
- [8] T. Venanzi, **H. Arora**, A. Erbe, A. Pashkin, S. Winnerl, M. Helm, and H. Schneider, “Exciton localization in MoSe₂ monolayers induced by adsorbed gas molecules”, Applied Physics Letters **114**, 172106 (2019).

- [9] R. Dong, P. Han, **H. Arora**, M. Ballabio, M. Karakus, Z. Zhang, C. Shekhar, P. Adler, P. S. Petkov, A. Erbe, S. C. B. Mannsfeld, C. Felser, T. Heine, M. Bonn, X. Feng, and E. Cánovas, “High-mobility band-like charge transport in a semiconducting two-dimensional metal-organic framework”, *Nature Materials* **17**, 1027–1032 (2018).
- [10] **H. Arora**, T. Schönherr, and A. Erbe, “Electrical characterization of two-dimensional materials and their heterostructures”, *IOP Conference Series: Materials Science and Engineering* **198**, 12002 (2017).
- [11] W. Feng, W. Zheng, W. Cao, and P. Hu, “Back Gated Multilayer InSe Transistors with Enhanced Carrier Mobilities via the Suppression of Carrier Scattering from a Dielectric Interface”, *Advanced Materials* **26**, 6587–6593 (2014).
- [12] S. Sucharitakul, N. J. Goble, U. R. Kumar, R. Sankar, Z. A. Bogorad, F. C. Chou, Y. T. Chen, and X. P. Gao, “Intrinsic Electron Mobility Exceeding 1000 cm²/(V s) in Multilayer InSe FETs”, *Nano Letters* **15**, 3815–3819 (2015).
- [13] L. Shi, Q. Zhou, Y. Zhao, Y. Ouyang, C. Ling, Q. Li, and J. Wang, “Oxidation Mechanism and Protection Strategy of Ultrathin Indium Selenide: Insight from Theory”, *Journal of Physical Chemistry Letters* **8**, 4368–4373 (2017).
- [14] X. Wei, C. Dong, A. Xu, X. Li, and D. D. Macdonald, “Oxygen-induced degradation of the electronic properties of thin-layer InSe”, *Physical Chemistry Chemical Physics* **20**, 2238–2250 (2018).
- [15] H. W. Yang, H. F. Hsieh, R. S. Chen, C. H. Ho, K. Y. Lee, and L. C. Chao, “Ultraefficient Ultraviolet and Visible Light Sensing and Ohmic Contacts in High-Mobility InSe Nanoflake Photodetectors Fabricated by the Focused Ion Beam Technique”, *ACS Applied Materials and Interfaces* **10**, 5740–5749 (2018).
- [16] P. H. Ho, Y. R. Chang, Y. C. Chu, M. K. Li, C. A. Tsai, W. H. Wang, C. H. Ho, C. W. Chen, and P. W. Chiu, “High-Mobility InSe Transistors: The Role of Surface Oxides”, *ACS Nano* **11**, 7362–7370 (2017).
- [17] S. A. Wells, A. Henning, J. Gish, V. K. Sangwan, L. J. Lauhon, and M. C. Hersam, “Supressing Ambient Degradation of Exfoliated InSe Nanosheet Devices via Seeded Atomic Layer Deposition Encapsulation”, *Nano Letters* **18**, 7876–7882 (2018).
- [18] P. R. Wallace, “The band theory of graphite”, *Physical Review* **71**, 622 (1947).
- [19] J. W. McClure, “Band structure of graphite and de Haas-van Alphen effect”, *Physical Review* **108**, 612 (1957).

- [20] S. H. El-Mahalawy and B. L. Evans, “Temperature Dependence of the Electrical Conductivity and Hall Coefficient in 2H-MoS₂, MoSe₂, WSe₂, and MoTe₂”, *Phys. Status Solidi B* **79**, 713–722 (1977).
- [21] Y. Hasegawa and Y. Abe, “Electrical and optical characteristics of a schottky barrier on a cleaved surface of the layered semiconductor InSe”, *Physica Status Solidi (a)* **70**, 615–621 (1982).
- [22] R. E. Peierls, “Bemerkungen über Umwandlungstemperaturen”, *Helvetica Physica Acta* **7**, 81–83 (1934).
- [23] R. E. Peierls, “Quelques propriétés typiques des corps solides”, *Annales de l'institut Henri Poincaré* **5**, 177–222 (1935).
- [24] L. D. Landau, “Zur Theorie der Phasenumwandlungen II”, *Phys. Z. Sowjetunion* **11**, 26–35 (1937).
- [25] K. S. Novoselov, A. K. Geim, S. V. Morozov, D. Jiang, Y. Zhang, S. V. Dubonos, I. V. Grigorieva, and A. A. Firsov, “Electric field in atomically thin carbon films”, *Science* **306**, 666–669 (2004).
- [26] K. S. Novoselov, D. Jiang, F. Schedin, T. J. Booth, V. V. Khotkevich, S. V. Morozov, and A. K. Geim, “Two-dimensional atomic crystals”, *Proceedings of the National Academy of Sciences of the United States of America* **102**, 10451–10453 (2005).
- [27] M. Ashton, J. Paul, S. B. Sinnott, and R. G. Hennig, “Topology-Scaling Identification of Layered Solids and Stable Exfoliated 2D Materials”, *Physical Review Letters* **118**, 106101 (2017).
- [28] W. Cao, J. Kang, D. Sarkar, W. Liu, and K. Banerjee, “2D Semiconductor FETs - Projections and Design for Sub-10 nm VLSI”, *IEEE Transactions on Electron Devices* **62**, 3459–3469 (2015).
- [29] D. Jariwala, V. K. Sangwan, D. J. Late, J. E. Johns, V. P. Dravid, T. J. Marks, L. J. Lauhon, and M. C. Hersam, “Band-like transport in high mobility unencapsulated singl-layer MoS₂ transistors”, *Applied Physics Letters* **102**, 173107 (2013).
- [30] B. Radisavljevic and A. Kis, “Mobility engineering and a metal-insulator transition in monolayer MoS₂”, *Nature Materials* **12**, 815–820 (2013).
- [31] R. R. Nair, P. Blake, A. N. Grigorenko, K. S. Novoselov, T. J. Booth, T. Stauber, N. M. R. Peres, and A. K. Geim, “Fine structure constant defines visual transparency of graphene”, *Science* **320**, 1308 (2008).
- [32] C. Lee, X. Wei, J. W. Kysar, and J. Hone, “Measurement of the elastic properties and intrinsic strength of monolayer graphene”, *Science* **321**, 385–388 (2008).

- [33] A. A. Balandin, “Thermal properties of graphene and nanostructured carbon materials”, *Nature Materials* **10**, 569–581 (2011).
- [34] J. S. Bunch, S. S. Verbridge, J. S. Alden, A. M. van der Zande, J. M. Parpia, H. G. Craighead, and P. L. McEuen, “Impermeable atomic membranes from graphene sheets”, *Nano Letters* **8**, 2458–2462 (2008).
- [35] M. Xu, T. Liang, M. Shi, and H. Chen, “Graphene-like two-dimensional materials”, *Chemical Reviews* **11**, 3766–3798 (2013).
- [36] S. Das Sarma, S. Adam, E. H. Hwang, and E. Rossi, “Electronic transport in two-dimensional graphene”, *Reviews of Modern Physics* **83**, 407–470 (2011).
- [37] K. I. Bolotin, K. J. Sikes, Z. Jiang, M. Klima, G. Fudenberg, J. Hone, P. Kim, and H. L. Stormer, “Ultrahigh electron mobility in suspended graphene”, *Solid State Communications* **146**, 351–355 (2008).
- [38] S. V. Morozov, K. S. Novoselov, M. I. Katsnelson, F. Schedin, D. C. Elias, J. A. Jaszczak, and A. K. Geim, “Giant intrinsic carrier mobilities in graphene and its bilayer”, *Physical Review Letters* **100**, 016602 (2008).
- [39] C. N. Lau, W. Bao, and J. Velasco Jr, “Properties of suspended graphene membranes”, *Materials Today* **15**, 238–245 (2012).
- [40] C. R. Dean, A. F. Young, I. Meric, C. Lee, L. Wang, S. Sorgenfrei, K. Watanabe, T. Taniguchi, P. Kim, K. L. Shepard, and J. Hone, “Boron nitride substrates for high-quality graphene electronics”, *Nature Nanotechnology* **5**, 722–726 (2010).
- [41] P. Miró, M. Audiffred, and T. Heine, “An atlas of two-dimensional materials”, *Chemical Society Reviews* **43**, 6537–6554 (2014).
- [42] K. S. Novoselov, A. Mishchenko, A. Carvalho, and A. H. Castro Neto, “2D materials and van der Waals heterostructures”, *Science* **353**, aac9439 (2016).
- [43] A. K. Geim and I. V. Grigorieva, “Van der Waals heterostructures”, *Nature* **499**, 419–425 (2013).
- [44] M. W. Lin, I. I. Kravchenko, J. Fowlkes, X. Li, A. A. Puretzky, C. M. Rouleau, D. B. Geohegan, and K. Xiao, “Thickness-dependent charge transport in few-layer MoS₂ field-effect transistors”, *Nanotechnology* **27**, 165203 (2016).
- [45] J. H. Kim, T. H. Kim, H. Lee, Y. R. Park, W. Choi, and C. J. Lee, “Thickness-dependent electron mobility of single and few-layer MoS₂ thin-film transistors”, *AIP Advances* **6**, 065106 (2016).
- [46] B. Radisavljevic, A. Radenovic, J. Brivio, V. Giacometti, and A. Kis, “Single-layer MoS₂ transistors”, *Nature Nanotechnology* **6**, 147–150 (2011).
- [47] O. V. Yazyev and A. Kis, “MoS₂ and semiconductors in the flatland”, *Materials Today* **18**, 20–30 (2015).

- [48] Y. Sun, S. Luo, X. G. Zhao, K. Biswas, S. L. Li, and L. Zhang, “InSe: a two-dimensional material with strong interlayer coupling”, *Nanoscale* **10**, 7991–7998 (2018).
- [49] J. F. Sánchez-Royo, A. Segura, O. Lang, E. Schaar, C. Pettenkofer, W. Jaegermann, R. Roa, and A. Chevy, “Optical and photovoltaic properties of indium selenide thin films prepared by van der Waals epitaxy”, *Journal of Applied Physics* **90**, 2818–2823 (2001).
- [50] V. K. Sangwan and M. C. Hersam, “Electronic Transport in Two-Dimensional Materials”, *Annual Review of Physical Chemistry* **69**, 299–325 (2018).
- [51] G. W. Mudd, S. A. Svatek, T. Ren, A. Patanè, O. Makarovsky, L. Eaves, P. H. Beton, Z. D. Kovalyuk, G. V. Lashkarev, Z. R. Kudrynskyi, and A. I. Dmitriev, “Tuning the bandgap of exfoliated InSe nanosheets by quantum confinement”, *Advanced Materials* **25**, 5714–5718 (2013).
- [52] D. A. Bandurin, A. V. Tyurnina, G. L. Yu, A. Mishchenko, V. Zólyomi, S. V. Morozov, R. K. Kumar, R. V. Gorbachev, Z. R. Kudrynskyi, S. Pezzini, Z. D. Kovalyuk, U. Zeitler, K. S. Novoselov, A. Patanè, L. Eaves, I. V. Grigorieva, V. I. Fal’Ko, A. K. Geim, and Y. Cao, “High electron mobility, quantum Hall effect and anomalous optical response in atomically thin InSe”, *Nature Nanotechnology* **12**, 223–227 (2017).
- [53] C. H. Ho, M. H. Lin, C. A. Chuang, B. X. Yeh, and Y. J. Chu, “2D multilayer InSe - An applicable 1000 nm light emitter and absorber”, *Imaging and Applied Optics 2016*, JT3A.5 (2016).
- [54] S. R. Tamalampudi, Y. Y. Lu, R. K. Ulaganathan, R. Sankar, C. D. Liao, K. Moorthy B., C. H. Cheng, F. C. Chou, and Y. T. Chen, “High performance and bendable few-layered InSe photodetectors with broad spectral response”, *Nano Letters* **14**, 2800–2806 (2014).
- [55] P. Tonndorf, S. Schwarz, J. Kern, I. Niehues, O. Del Pozo-Zamudio, A. I. Dmitriev, A. P. Bakhtinov, D. N. Borisenko, N. N. Kolesnikov, A. I. Tar takovskii, S. Michaelis de Vasconcellos, and R. Bratschitsch, “Single-photon emitters in GaSe”, *2D Materials* **4**, 021010 (2017).
- [56] W. Shi and Y. J. Ding, “A monochromatic and high-power terahertz source tunable in the ranges of 2.7–38.4 and 58.2–3540 μm for variety of potential applications”, *Applied Physics Letters* **84**, 1635 (2004).
- [57] W. Jie, X. Chen, D. Li, L. Xie, Y. Y. Hui, S. P. Lau, X. Cui, and J. Hao, “Layer-dependent nonlinear optical properties and stability of non-centrosymmetric modification in few-layer GaSe sheets”, *Angewandte Chemie - International Edition* **54**, 1185–1189 (2015).

- [58] A. Segura, “Layered indium selenide under high pressure: A review”, *Crystals* **8**, 206 (2018).
- [59] J. L. Verble and T. J. Wieting, “Lattice Mode Degeneracy in MoS₂ and Other Layer Compounds”, *Physical Review Letters* **25**, 362–365 (1970).
- [60] S. Lei, L. Ge, S. Najmaei, A. George, R. Kappera, J. Lou, M. Chhowalla, H. Yamaguchi, G. Gupta, R. Vajtai, A. D. Mohite, and P. M. Ajayan, “Evolution of the electronic band structure and efficient photo-detection in atomic layers of InSe”, *ACS Nano* **8**, 1263–1272 (2014).
- [61] N. Kuroda and Y. Nishina, “Resonance Raman scattering study on exciton and polaron anisotropies in InSe”, *Solid State Communications* **34**, 481–484 (1980).
- [62] Y. Yang, N. Huo, and J. Li, “Sensitized monolayer MoS₂ phototransistors with ultrahigh responsivity”, *Journal of Materials Chemistry C* **5**, 11614–11619 (2017).
- [63] S. L. Li, K. Tsukagoshi, E. Orgiu, and P. Samorì, “Charge transport and mobility engineering in two-dimensional transition metal chalcogenide semiconductors”, *Chemical Society Reviews* **45**, 118–151 (2016).
- [64] L. Gomez, I. Aberg, and J. L. Hoyt, “Electron transport in strained-silicon directly on insulator ultrathin-body n-MOSFETs with body thickness ranging from 2 to 25 nm”, *IEEE Electron Device Letters* **28**, 285–287 (2007).
- [65] L. Li, Y. Yu, G. J. Ye, Q. Ge, X. Ou, H. Wu, D. Feng, X. H. Chen, and Y. Zhang, “Black phosphorus field-effect transistors”, *Nature Nanotechnology* **9**, 372–377 (2014).
- [66] W. Feng, X. Zhou, W. Q. Tian, W. Zheng, and P. A. Hu, “Performance improvement of multilayer InSe transistors with optimized metal contacts”, *Physical Chemistry Chemical Physics* **17**, 3653–3658 (2015).
- [67] G. H. Lee, X. Cui, Y. D. Kim, G. Arefe, X. Zhang, C. H. Lee, F. Ye, K. Watanabe, T. Taniguchi, P. Kim, and J. Hone, “Highly Stable, Dual-Gated MoS₂ Transistors Encapsulated by Hexagonal Boron Nitride with Gate-Controllable Contact, Resistane and Threshold Voltage”, *ACS Nano* **9**, 7019–7026 (2015).
- [68] D. V. Rybkovskiy, N. R. Arutyunyan, A. S. Orekhov, I. A. Gromchenko, I. V. Vorobiev, A. V. Osadchy, E. Y. Salaev, T. K. Baykara, K. R. Allakhverdiev, and E. D. Obraztsova, “Size-induced effects in gallium selenide electronic structure: The influence of interlayer interactions”, *Physical Review B* **84**, 085314 (2011).
- [69] R. Le Toullec, M. Balkanski, J. M. Besson, and A. Kuhn, “Optical absorption edge of a new GaSe polytype”, *Physics Letters A* **55**, 245–246 (1975).
- [70] R. H. Bube and E. L. Lind, “Photoconductivity of gallium selenide crystals”, *Physical Review* **115**, 1159–1164 (1959).

- [71] A. Bergeron, J. Ibrahim, R. Leonelli, and S. Francoeur, “Oxidation dynamics of ultrathin GaSe probed through Raman spectroscopy”, *Applied Physics Letters* **110**, 241901 (2017).
- [72] W. Jie and J. Hao, “Two-Dimensional Layered Gallium Selenide: Preparation, Properties, and Applications”, in *Advanced 2d materials*, edited by A. Tiwari and M. Syväjärvi (John Wiley & Sons, 2016) Chap. 1, pp. 1–36.
- [73] P. Hu, Z. Wen, L. Wang, P. Tan, and K. Xiao, “Synthesis of few-layer GaSe nanosheets for high performance photodetectors”, *ACS Nano* **6**, 5988–5994 (2012).
- [74] Z. Zhu, Y. Cheng, and U. Schwingenschlögl, “Topological phase transition in layered GaS and GaSe”, *Physical Review Letters* **108**, 266805 (2012).
- [75] Y. Cao, K. Cai, P. Hu, L. Zhao, T. Yan, W. Luo, X. Zhang, X. Wu, K. Wang, and H. Zheng, “Strong enhancement of photoresponsivity with shrinking the electrodes spacing in few layer GaSe photodetectors”, *Scientific Reports* **5**, 8130 (2015).
- [76] S. I. Drapak, S. V. Gavrylyuk, Z. D. Kovalyuk, and O. S. Lytvyn, “Native oxide emerging of the cleavage surface of gallium selenide due to prolonged storage”, *Semiconductors* **42**, 414–421 (2008).
- [77] X. Zhang, Q. H. Tan, J. B. Wu, W. Shi, and P. H. Tan, “Review on the Raman spectroscopy of different types of layered materials”, *Nanoscale* **8**, 6435–6450 (2016).
- [78] R. Minder, G. Ottaviani, and C. Canali, “Charge transport in layer semiconductors”, *Journal of Physics and Chemistry of Solids* **37**, 417–424 (1976).
- [79] A. Abderrahmane, P.-G. Jung, N.-H. Kim, P. J. Ko, and A. Sandhu, “Gate-tunable optoelectronic properties of a nano-layered GaSe photodetector”, *Optical Materials Express* **7**, 587 (2017).
- [80] D. J. Late, B. Liu, J. Luo, A. Yan, H. S. S. R. Matte, M. Grayson, C. N. R. Rao, and V. P. Dravid, “GaS and GaSe ultrathin layer transistors”, *Advanced Materials* **24**, 3549–3554 (2012).
- [81] Q. Zhao, R. Frisenda, P. Gant, D. Perez de Lara, C. Munuera, M. Garcia-Hernandez, Y. Niu, T. Wang, W. Jie, and A. Castellanos-Gomez, “Toward Air Stability of Thin GaSe Devices: Avoiding Environmental and Laser-Induced Degradation by Encapsulation”, *Advanced Functional Materials* **28**, 1805304 (2018).

- [82] X. Li, M. W. Lin, A. A. Puretzky, J. C. Idrobo, C. Ma, M. Chi, M. Yoon, C. M. Rouleau, I. I. Kravchenko, D. B. Geohegan, and K. Xiao, “Controlled vapor phase growth of single crystalline, two-dimensional GaSe crystals with high photoresponse”, *Scientific Reports* **4**, 5497 (2014).
- [83] A. S. Mayorov, R. V. Gorbachev, S. V. Morozov, L. Britnell, R. Jalil, L. A. Ponomarenko, P. Blake, K. S. Novoselov, K. Watanabe, T. Taniguchi, and A. K. Geim, “Micrometer-scale ballistic transport in encapsulated graphene at room temperature”, *Nano Letters* **11**, 2396–2399 (2011).
- [84] X. Cui, G. H. Lee, Y. D. Kim, G. Arefe, P. Y. Huang, C. H. Lee, D. A. Chenet, X. Zhang, L. Wang, F. Ye, F. Pizzocchero, B. S. Jessen, K. Watanabe, T. Taniguchi, D. A. Muller, T. Low, P. Kim, and J. Hone, “Multi-terminal transport measurements of MoS₂ using a van der Waals heterostructure device platform”, *Nature Nanotechnology* **10**, 534–540 (2015).
- [85] J. Wang, F. Ma, and M. Sun, “Graphene, hexagonal boron nitride, and their heterostructures: properties and applications”, *RSC Advances* **7**, 16801–16822 (2017).
- [86] C. Zhi, Y. Bando, C. Tang, and D. Golberg, “Boron nitride nanotubes”, *Materials Science and Engineering: R: Reports* **70**, 92–111 (2010).
- [87] J. Xue, J. Sanchez-Yamagishi, D. Bulmash, P. Jacquod, A. Deshpande, K. Watanabe, T. Taniguchi, P. Jarillo-Herrero, and B. J. Leroy, “Scanning tunnelling microscopy and spectroscopy of ultra-flat graphene on hexagonal boron nitride”, *Nature Materials* **10**, 282–285 (2011).
- [88] L. H. Li and Y. Chen, “Atomically Thin Boron Nitride: Unique Properties and Applications”, *Advanced Functional Materials* **26**, 2594–2608 (2016).
- [89] K. Zhang, Y. Feng, F. Wang, Z. Yang, and J. Wang, “Two dimensional hexagonal boron nitride (2D-hBN): Synthesis, properties and applications”, *Journal of Materials Chemistry C* **5**, 11992–12022 (2017).
- [90] K. Watanabe, T. Taniguchi, and H. Kanda, “Direct-bandgap properties and evidence for ultraviolet lasing of hexagonal boron nitride single crystal”, *Nature Materials* **3**, 404–409 (2004).
- [91] F. Cadiz, E. Courtade, C. Robert, G. Wang, Y. Shen, H. Cai, T. Taniguchi, K. Watanabe, H. Carrere, D. Lagarde, M. Manca, T. Amand, P. Renucci, S. Tongay, X. Marie, and B. Urbaszek, “Excitonic linewidth approaching the homogeneous limit in MoS₂-based van der Waals heterostructures”, *Physical Review X* **7**, 021026 (2017).

- [92] F. Cadiz, C. Robert, G. Wang, W. Kong, X. Fan, M. Blei, D. Lagarde, M. Gay, M. Manca, T. Taniguchi, K. Watanabe, T. Amand, X. Marie, P. Renucci, S. Tongay, and B. Urbaszek, “Ultra-low power threshold for laser induced changes in optical properties of 2D molybdenum dichalcogenides”, *2D Materials* **3**, 045008 (2016).
- [93] C. H. Lui, L. Liu, K. F. Mak, G. W. Flynn, and T. F. Heinz, “Ultraflat graphene”, *Nature* **462**, 339–341 (2009).
- [94] L. H. Li, T. Xing, Y. Chen, and R. Jones, “Boron Nitride Nanosheets for Metal Protection”, *Advanced Materials Interfaces* **1**, 1300132 (2014).
- [95] Y. Liu, N. O. Weiss, X. Duan, H.-C. Cheng, Y. Huang, and X. Duan, “Van der Waals heterostructures and devices”, *Nature Reviews Materials* **1**, 16042 (2016).
- [96] X. Duan, C. Wang, J. C. Shaw, R. Cheng, Y. Chen, H. Li, X. Wu, Y. Tang, Q. Zhang, A. Pan, J. Jiang, R. Yu, Y. Huang, and X. Duan, “Lateral epitaxial growth of two-dimensional layered semiconductor heterojunctions”, *Nature Nanotechnology* **9**, 1024–1030 (2014).
- [97] Y. Gong, J. Lin, X. Wang, G. Shi, S. Lei, Z. Lin, X. Zou, G. Ye, R. Vajtai, B. I. Yakobson, H. Terrones, M. Terrones, B. K. Tay, J. Lou, S. T. Pantelides, Z. Liu, W. Zhou, and P. M. Ajayan, “Vertical and in-plane heterostructures from WS₂/MoS₂ monolayers”, *Nature Materials* **13**, 1135–1142 (2014).
- [98] A. Yan, J. Velasco Jr, S. Kahn, K. Watanabe, T. Taniguchi, F. Wang, M. F. Crommie, and A. Zettl, “Direct Growth of Single- and Few-Layer MoS₂ on h-BN with Preferred Relative Rotation Angles”, *Nano Letters* **15**, 6324–6331 (2015).
- [99] S. J. Haigh, A. Gholinia, R. Jalil, S. Romani, L. Britnell, D. C. Elias, K. S. Novoselov, L. A. Ponomarenko, A. K. Geim, and R. Gorbachev, “Cross-sectional imaging of individual layers and buried interfaces of graphene-based heterostructures and superlattices”, *Nature Materials* **11**, 764–767 (2012).
- [100] O. K. Farha, A. Ö. Yazaydin, I. Eryazici, C. D. Malliakas, B. G. Hauser, M. G. Kanatzidis, S. T. Nguyen, R. Q. Snurr, and J. T. Hupp, “De novo synthesis of a metal-organic framework material featuring ultrahigh surface area and gas storage capacities”, *Nature Chemistry* **2**, 944–948 (2010).
- [101] O. K. Farha, I. Eryazici, N. C. Jeong, B. G. Hauser, C. E. Wilmer, A. A. Sarjeant, R. Q. Snurr, S. T. Nguyen, A. Ö. Yazaydin, and J. T. Hupp, “Metal-organic framework materials with ultrahigh surface areas: Is the sky the limit?”, *Journal of the American Chemical Society* **134**, 15016–15021 (2012).
- [102] Q. L. Zhu and Q. Xu, “Metal-organic framework composites”, *Chemical Society Reviews* **43**, 5468–5512 (2014).

- [103] H. Deng, S. Grunder, K. E. Cordova, C. Valente, H. Furukawa, M. Hmadeh, F. G  ndara, A. C. Whalley, Z. Liu, S. Asahina, H. Kazumori, M. O'Keeffe, O. Terasaki, J. F. Stoddart, and O. M. Yaghi, "Large-Pore Aperatures in a Series of Metal-Organic Frameworks", *Science* **336**, 1018–1023 (2012).
- [104] E. Sharmin and F. Zafar, *Metal-organic frameworks* (IntechOpen, 2016).
- [105] N. L. Rosi, J. Eckert, M. Eddaoudi, D. T. Vodak, J. Kim, M. O'Keeffe, and O. M. Yaghi, "Hydrogen storage in microporous metal-organic frameworks", *Science* **300**, 1127–1129 (2003).
- [106] E. V. Perez, C. Karunaweera, I. H. Musselman, K. J. Balkus, and J. P. Ferraris, "Origins and evolution of inorganic-based and MOF-based mixed-matrix membranes for gas separations", *Processes* **4**, 32 (2016).
- [107] H. Furukawa, K. E. Cordova, M. O'Keeffe, and O. M. Yaghi, "The chemistry and applications of metal-organic frameworks", *Science* **341**, 1230444 (2013).
- [108] M. Eddaoudi, J. Kim, N. Rosi, D. Vodak, J. Wachter, M. O. Keeffe, O. M. Yaghi, J. Kimrn, and O. M. Yaghi, "Systematic Design of Pore Size and Functionality in Isoreticular MOFs and Their Application in Methane Storage Systematic Design and Functionality MOFs and Size Isoreticular in Application Storage", *Science* **295**, 469–472 (2002).
- [109] Z. Chen, K. Adil, L. J. Weselinski, Y. Belmabkhout, and M. Eddaoudi, "A supermolecular building layer approach for gas separation and storage applications: The eea and rtl MOF platforms for CO₂ capture and hydrocarbon separation", *Journal of Materials Chemistry A* **3**, 6276–6281 (2015).
- [110] P. Horcajada, C. Serre, M. Vallet-Reg  , M. Sebban, F. Taulelle, and G. F  rey, "Metal-organic frameworks as efficient materials for drug delivery", *Angewandte Chemie - International Edition* **45**, 5974–5978 (2006).
- [111] M. X. Wu and Y. W. Yang, "Metal-organic Framework (MOF)-Based Drug/Cargo Delivery and Cancer Therapy", *Advanced Materials* **29**, 1606134 (2017).
- [112] F. X. Llabr  s i Xamena, A. Abad, A. Corma, and H. Garcia, "MOFs as catalysts: Activity, reusability and shape-selectivity of a Pd-containing MOF", *Journal of Catalysis* **250**, 294–298 (2007).
- [113] J. Lee, O. K. Farha, J. Roberts, K. A. Scheidt, S. T. Nguyen, and J. T. Hupp, "Metal-organic framework materials as catalysts", *Chemical Society Reviews* **38**, 1450–1459 (2009).
- [114] I. Stassen, N. Burtch, A. Talin, P. Falcaro, M. Allendorf, and R. Ameloot, "An updated roadmap for the integration of metal-organic frameworks with electronic devices and chemical sensors", *Chemical Society Reviews* **46**, 3185–3241 (2017).

- [115] D. Banerjee, S. J. Kim, and J. B. Parise, “Lithium based metal-organic framework with exceptional stability”, *Crystal Growth and Design* **9**, 2500–2503 (2009).
- [116] J. H. Cavka, S. Jakobsen, U. Olsbye, N. Guillou, C. Lamberti, S. Bordiga, and K. P. Lillerud, “A New Zirconium Inorganic Building Brick Forming Metal Organic Frameworks with Exceptional Stability”, *Journal of the American Chemical Society* **130**, 13850–13851 (2008).
- [117] M. Hmadeh, Z. Lu, Z. Liu, F. Gándara, H. Furukawa, S. Wan, V. Augustyn, R. Chang, L. Liao, F. Zhou, E. Perre, V. Ozolins, K. Suenaga, X. Duan, B. Dunn, Y. Yamamoto, O. Terasaki, and O. M. Yaghi, “New Porous Crystals of Extended Metal-Catecholates”, *Chemistry of Materials* **24**, 3511–3513 (2012).
- [118] L. Sun, T. Miyakai, S. Seki, and M. Dinca, “Mn₂(2,5-disulfhydrylbenzene-1,4-dicarboxylate): A microporous metal-organic framework with infinite (-Mn-S-) chains and high intrinsic charge mobility”, *Journal of the American Chemical Society* **135**, 8185–8188 (2013).
- [119] A. A. Talin, A. Centrone, A. C. Ford, M. E. Foster, V. Stavila, P. Haney, R. A. Kinney, V. Szalai, F. El Gabaly, H. P. Yoon, F. Léonard, and M. D. Allendorf, “Tunable electrical conductivity in metal-organic framework thin-film devices”, *Science* **343**, 66–69 (2014).
- [120] D. Sheberla, L. Sun, M. A. Blood-forsythe, S. Er, C. R. Wade, C. K. Brozek, A. Aspuru-Guzik, and M. Dinca, “High Electrical Conductivity in Ni₃(2,3,6,7,10,11-hexaiminotriphenylene)₂, a Semiconducting Metal-Organic Graphene Analogue”, *J. Am. Chem. Soc.* **136**, 8859–8862 (2014).
- [121] T. Kambe, R. Sakamoto, T. Kusamoto, T. Pal, N. Fukui, K. Hoshiko, T. Shimojima, Z. Wang, T. Hirahara, K. Ishizaka, S. Hasegawa, F. Liu, and H. Nishihara, “Redox control and high conductivity of nickel bis(dithiolene) complex π-nanosheet: A potential organic two-dimensional topological insulator”, *Journal of the American Chemical Society* **136**, 14357–14360 (2014).
- [122] X. Huang, P. Sheng, Z. Tu, F. Zhang, J. Wang, H. Geng, Y. Zou, C.-a. Di, Y. Yi, Y. Sun, W. Xu, and D. Zhu, “A two-dimensional π–d conjugated coordination polymer with extremely high electrical conductivity and ambipolar transport behaviour”, *Nature Communications* **6**, 7408 (2015).
- [123] C. H. Hendon, D. Tiana, M. Fontecave, C. Sanchez, L. D'arras, C. Sassoye, L. Rozes, C. Mellot-Draznieks, and A. Walsh, “Engineering the optical response of the titanium-MIL-125 metal-organic framework through ligand functionalization”, *Journal of the American Chemical Society* **135**, 10942–10945 (2013).
- [124] M. Usman, S. Mendiratta, and K. L. Lu, “Semiconductor Metal–Organic Frameworks: Future Low-Bandgap Materials”, *Advanced Materials* **29**, 1605071 (2017).

- [125] L. Sun, M. G. Campbell, and M. Dinca, “Electrically Conductive Porous Metal-Organic Frameworks”, *Angewandte Chemie - International Edition* **55**, 3566–3579 (2016).
- [126] N. F. Mott, “Conduction in Non-crystalline Materials III. Localized States in a Pseudogap and Near Extremities of Conduction and Valence Bands”, in *Sir neville mott - 65 years in physics* (World Scientific, 1995), pp. 465–482.
- [127] F. Wang, Z. Wang, Q. Wang, F. Wang, L. Yin, K. Xu, Y. Huang, and J. He, “Synthesis, properties and applications of 2D non-graphene materials”, *Nanotechnology* **26**, 292001 (2015).
- [128] R. Schwarcz, M. A. Kanehisa, M. Jouanne, J. F. Morhange, and M. Eddrief, “Evolution of Raman spectra as a function of layer thickness in ultra-thin InSe films”, *Journal of Physics: Condensed Matter* **14**, 967–973 (2002).
- [129] A. Castellanos-Gomez, M. Buscema, R. Molenaar, V. Singh, L. Janssen, H. S. van der Zant, and G. A. Steele, “Deterministic transfer of two-dimensional materials by all-dry viscoelastic stamping”, *2D Materials* **1**, 011002 (2014).
- [130] L. Wang, I. Meric, H. P. Y., Q. Gao, Y. Gao, H. Tran, T. Taniguchi, K. Watanabe, L. M. Campos, D. A. Muller, J. Guo, P. Kim, J. Hone, K. L. Shepard, and C. R. Dean, “One-Dimensional Electrical Contact to a Two-dimensional Material”, *Science* **342**, 614–617 (2013).
- [131] R. Frisenda, E. Navarro-Moratalla, P. Gant, D. Pérez De Lara, P. Jarillo-Herrero, R. V. Gorbachev, and A. Castellanos-Gomez, “Recent progress in the assembly of nanodevices and van der Waals heterostructures by deterministic placement of 2D materials”, *Chemical Society Reviews* **47**, 53–68 (2018).
- [132] A. Jain, P. Bharadwaj, S. Heeg, M. Parzefall, T. Taniguchi, K. Watanabe, and L. Novotny, “Minimizing residues and strain in 2D materials transferred from PDMS”, *Nanotechnology* **29**, 265203 (2018).
- [133] D. G. Purdie, N. M. Pugno, T. Taniguchi, K. Watanabe, A. C. Ferrari, and A. Lombardo, “Cleaning interfaces in layered materials heterostructures”, *Nature Communications* **9**, 5387 (2018).
- [134] R. V. Gorbachev, I. Riaz, R. R. Nair, R. Jalil, L. Britnell, B. D. Belle, E. W. Hill, K. S. Novoselov, K. Watanabe, T. Taniguchi, A. K. Geim, and P. Blake, “Hunting for monolayer boron nitride: Optical and raman signatures”, *Small* **7**, 465–468 (2011).
- [135] J. Kang, S. A. Wells, V. K. Sangwan, D. Lam, X. Liu, J. Luxa, Z. Sofer, and M. C. Hersam, “Solution-Based Processing of Optoelectronically Active Indium Selenide”, *Advanced Materials* **30**, 1802990 (2018).

- [136] J. F. Sánchez-Royo, G. Muñoz-Matutano, M. Brotons-Gisbert, J. P. Martínez-Pastor, A. Segura, A. Cantarero, R. Mata, J. Canet-Ferrer, G. Tobias, E. Canadell, J. Marqués-Hueso, and B. D. Gerardot, “Electronic structure, optical properties, and lattice dynamics in atomically thin indium selenide flakes”, *Nano Research* **7**, 1556–1568 (2014).
- [137] G. H. Lee, Y. J. Yu, X. Cui, N. Petrone, C. H. Lee, M. S. Choi, D. Y. Lee, C. Lee, W. J. Yoo, K. Watanabe, T. Taniguchi, C. Nuckolls, P. Kim, and J. Hone, “Flexible and transparent MoS₂ field-effect transistors on hexagonal boron nitride-graphene heterostructures”, *ACS Nano* **7**, 7931–7936 (2013).
- [138] R. A. Doganov, E. C. O’Farrell, S. P. Koenig, Y. Yeo, A. Ziletti, A. Carvalho, D. K. Campbell, D. F. Coker, K. Watanabe, T. Taniguchi, A. H. Castro Neto, and B. Özyilmaz, “Transport properties of pristine few-layer black phosphorus by van der Waals passivation in an inert atmosphere”, *Nature Communications* **6**, 6647 (2015).
- [139] M. Egginger, S. Bauer, R. Schwödiauer, H. Neugebauer, and N. S. Sariciftci, “Current versus gate voltage hysteresis in organic field effect transistors”, *Monatshefte für Chemie - Chemical Monthly* **140**, 735–750 (2009).
- [140] G. W. Mudd, S. A. Svatek, L. Hague, O. Makarovsky, Z. R. Kudrynskyi, C. J. Mellor, P. H. Beton, L. Eaves, K. S. Novoselov, Z. D. Kovalyuk, E. E. Vdovin, A. J. Marsden, N. R. Wilson, and A. Patanè, “High Broad-Band Photoresponsivity of Mechanically Formed InSe-Graphene van der Waals Heterostructures”, *Advanced Materials* **27**, 3760–3766 (2015).
- [141] M. Rahaman, R. D. Rodriguez, M. Monecke, S. A. Lopez-Rivera, and D. R. Zahn, “GaSe oxidation in air: From bulk to monolayers”, *Semiconductor Science and Technology* **32**, 105004 (2017).
- [142] N. Balakrishnan, Z. R. Kudrynskyi, E. F. Smith, M. W. Fay, O. Makarovsky, Z. D. Kovalyuk, L. Eaves, P. H. Beton, and A. Patanè, “Engineering p-n junctions and bandgap tuning of InSe nanolayers by controlled oxidation”, *2D Materials* **4**, 025043 (2017).
- [143] A. Politano, G. Chiarello, R. Samnakay, G. Liu, B. Gürbulak, S. Duman, A. A. Balandin, and D. W. Boukhvalov, “The influence of chemical reactivity of surface defects on ambient-stable InSe-based nanodevices”, *Nanoscale* **8**, 8474–8479 (2016).
- [144] E. J. Telford, A. Benyamin, D. Rhodes, D. Wang, Y. Jung, A. Zangiabadi, K. Watanabe, T. Taniguchi, S. Jia, K. Barmak, A. N. Pasupathy, C. R. Dean, and J. Hone, “Via Method for Lithography Free Contact and Preservation of 2D Materials”, *Nano Letters* **18**, 1416–1420 (2018).

- [145] M. Manca, M. M. Glazov, C. Robert, F. Cadiz, T. Taniguchi, K. Watanabe, E. Courtade, T. Amand, P. Renucci, X. Marie, G. Wang, and B. Urbaszek, “Enabling valley selective exciton scattering in monolayer WSe₂ through upconversion”, *Nature Communications* **8**, 14927 (2017).
- [146] O. A. Ajayi, J. V. Ardelean, G. D. Shepard, J. Wang, A. Antony, T. Taniguchi, K. Watanabe, T. F. Heinz, S. Strauf, X. Y. Zhu, and J. C. Hone, “Approaching the intrinsic photoluminescence linewidth in transition metal dichalcogenide monolayers”, *2D Materials* **4**, 031011 (2017).
- [147] P. G. Eliseev, P. Perlin, J. Lee, and M. Osinski, “"Blue" temperature-induced shift and band-tail emission in InGaN-based light sources”, *Applied Physics Letters* **71**, 569–571 (1997).
- [148] Y. H. Cho, G. H. Gainer, A. J. Fischer, J. J. Song, S. Keller, U. K. Mishra, and S. P. DenBaars, “"S-shaped" temperature-dependent emission shift and carrier dynamics in InGaN/GaN multiple quantum wells”, *Applied Physics Letters* **73**, 1370–1372 (1998).
- [149] M. Buscema, G. A. Steele, H. S. J. van der Zant, and A. Castellanos-Gomez, “The effect of the substrate on the Raman and photoluminescence emission of single-layer MoS₂”, *Nano Research* **7**, 561–571 (2014).
- [150] O. Makkawi, Y. Qiu, W. Feng, and P. A. Hu, “The Modulation of Photoluminescences Band Gap of Two-Dimensional InSe Nanosheets on h-BN Substrate”, *Journal of Nanoscience and Nanotechnology* **16**, 9813–9819 (2016).
- [151] J. Wierzbowski, J. Klein, F. Sigger, C. Straubinger, M. Kremser, T. Taniguchi, K. Watanabe, U. Wurstbauer, A. W. Holleitner, M. Kaniber, K. Müller, and J. J. Finley, “Direct exciton emission from atomically thin transition metal dichalcogenide heterostructures near the lifetime limit”, *Scientific Reports* **7**, 12383 (2017).
- [152] K. J. Xiao, A. Carvalho, and A. H. Castro Neto, “Defects and oxidation resilience in InSe”, *Physical Review B* **96**, 054112 (2017).
- [153] X. Han, J. Lin, J. Liu, N. Wang, and D. Pan, “Effects of Hexagonal Boron Nitride Encapsulation on the Electronic Structure of Few-Layer MoS₂”, *Journal of Physical Chemistry C* **123**, 14797–14802 (2019).
- [154] R. Zhuo, S. Zuo, W. Quan, D. Yan, B. Geng, J. Wang, and X. Men, “Large-size and high performance visible-light photodetectors based on two-dimensional hybrid materials SnS/RGO”, *RSC Advances* **8**, 761–766 (2018).
- [155] D. Farrusseng, *Metal-Organic Frameworks: Applications from Catalysis to Gas Storage* (John Wiley & Sons, 2011).

- [156] M. G. Campbell, S. F. Liu, T. M. Swager, and M. Dinca, “Chemiresistive Sensor Arrays from Conductive 2D Metal-Organic Frameworks”, *Journal of the American Chemical Society* **137**, 13780–13783 (2015).
- [157] V. Stavila, A. A. Talin, and M. D. Allendorf, “MOF-based electronic and opto-electronic devices”, *Chemical Society Reviews* **43**, 5994–6010 (2014).
- [158] J. H. Dou, L. Sun, Y. Ge, W. Li, C. H. Hendon, J. Li, S. Gul, J. Yano, E. A. Stach, and M. Dinca, “Signature of metallic behavior in the metal-organic frameworks M₃(hexaiminobenzene)2 (M = Ni, Cu)”, *Journal of the American Chemical Society* **139**, 13608–13611 (2017).
- [159] R. Dong, Z. Zhang, D. C. Tranca, S. Zhou, M. Wang, P. Adler, Z. Liao, F. Liu, Y. Sun, W. Shi, Z. Zhang, E. Zschech, S. C. B. Mannsfeld, C. Felser, and X. Feng, “A coronene-based semiconducting two-dimensional metal-organic framework with ferromagnetic behavior”, *Nature Communications* **9**, 2637 (2018).
- [160] Y. Cui, J. Yan, Z. Chen, J. Zhang, Y. Zou, Y. Sun, W. Xu, and D. Zhu, “[Cu₃(C₆Se₆)_n]: The First Highly Conductive 2D π-d Conjugated Coordination Polymer Based on Benzenehexaselenolate”, *Advanced Science* **6**, 1802235 (2019).
- [161] M. C. Hels and T. K. Andersen, “Hall bar Measurements: Properties of Reduced Graphene Oxide and Au-Si-doped GaAs”, Bachelor Thesis (University of Copenhagen, 2012).
- [162] Supriyo Datta, *Electronic Transport in Mesoscopic Systems* (Cambridge University Press, Cambridge, 1997).
- [163] “Appendix A: Hall Effect Measurements”, in *Lake shore 7500/9500 series hall system user’s manual* (Lake Shore Cryotronics Inc., Westerville, OH, 1995).
- [164] R. Kinder, M. Mikolásek, D. Donoval, J. Kovác, and M. Tlaczala, “Measurement system with Hall and a four point probes for characterization of semiconductors”, *Journal of Electrical Engineering* **64**, 106–111 (2013).
- [165] H. H. Choi, Y. I. Rodionov, A. F. Paterson, J. Panidi, D. Saranin, N. Kharlamov, S. I. Didenko, T. D. Anthopoulos, K. Cho, and V. Podzorov, “Accurate Extraction of Charge Carrier Mobility in 4-Probe Field-Effect Transistors”, *Advanced Functional Materials* **28**, 1707105 (2018).
- [166] A. Zabrodskii and K. N. Zinov’eva, “Low-Temperature Conductivity and Metal-Insulator Transition in Compensate n-Ge”, *Zh. Eksp. Teor. Fiz.* **86**, 727–742 (1984).
- [167] J. Steinhauer, S. Fay, N. Oliveira, E. Vallat-Sauvain, and C. Ballif, “Transition between grain boundary and intragrain scattering transport mechanisms in boron-doped zinc oxide thin films”, *Applied Physics Letters* **90**, 142107 (2007).

- [168] M. G. Campbell, D. Sheberla, S. F. Liu, T. M. Swager, and M. Dinca, “Cu₃(hexaiminotriphenylene)2: An electrically conductive 2D metal-organic framework for chemiresistive sensing”, *Angewandte Chemie - International Edition* **54**, 4349–4352 (2015).
- [169] G. Wu, J. Huang, Y. Zang, J. He, and G. Xu, “Porous field-effect transistors based on a semiconductive metal-organic framework”, *Journal of the American Chemical Society* **139**, 1360–1363 (2017).
- [170] C. Yang, R. Dong, M. Wang, P. S. Petkov, Z. Zhang, M. Wang, P. Han, M. Ballabio, S. A. Bräuninger, Z. Liao, J. Zhang, F. Schwotzer, E. Zschech, H. H. Klauss, E. Cánovas, S. Kaskel, M. Bonn, S. Zhou, T. Heine, and X. Feng, “A semiconducting layered metal-organic framework magnet”, *Nature Communications* **10**, 3260 (2019).
- [171] A. J. Clough, J. M. Skelton, C. A. Downes, A. A. de la Rosa, J. W. Yoo, A. Walsh, B. C. Melot, and S. C. Marinescu, “Metallic Conductivity in a Two-Dimensional Cobalt Dithiolene Metal-Organic Framework”, *Journal of the American Chemical Society* **139**, 10863–10867 (2017).
- [172] K. P. Bera, G. Haider, M. Usman, P. K. Roy, H. I. Lin, Y. M. Liao, C. R. P. Inbaraj, Y. R. Liou, M. Kataria, K. L. Lu, and Y. F. Chen, “Trapped Photons Induced Ultrahigh External Quantum Efficiency and Photoresponsivity in Hybrid Graphene/Metal-Organic Framework Broadband Wearable Photodetectors”, *Advanced Functional Materials* **28**, 1804802 (2018).
- [173] E. L. Dereniak and G. D. Boreman, *Infrared Detectors and Systems* (John Wiley & Sons, New York, 1996).
- [174] A. Rogalski, *Infrared Detectors* (Gordon and Breach Science Publishers, Amsterdam, 2000).
- [175] A. Rose, *Concepts in Photoconductivity and Allied Problems* (Robert E. Krieger Publishing Company, Huntington, New York, 1978).
- [176] R. Singh and V. Mittal, “Mercury cadmium telluride photoconductive long wave infrared linear array detectors”, *Defence Science Journal* **53**, 281–324 (2003).
- [177] R. H. Bube, *Photoelectronic Properties of Semiconductors* (Cambridge University Press, Cambridge, 1992).
- [178] Q. Guo, A. Pospischil, M. Bhuiyan, H. Jiang, H. Tian, D. Farmer, B. Deng, C. Li, S. J. Han, H. Wang, Q. Xia, T. P. Ma, T. Mueller, and F. Xia, “Black phosphorus mid-infrared photodetectors with high gain”, *Nano Letters* **16**, 4648–4655 (2016).

- [179] **H. Arora**, P. E. Malinowski, A. Chasin, D. Cheyns, S. Steudel, S. Schols, and P. Heremans, “Amorphous indium-gallium-zinc-oxide as electron transport layer in organic photodetectors”, *Applied Physics Letters* **106**, 143301 (2015).
- [180] X. Qiu, X. Yu, S. Yuan, Y. Gao, X. Liu, Y. Xu, and D. Yang, “Trap Assisted Bulk Silicon Photodetector with High Photoconductive Gain, Low Noise, and Fast Response by Ag Hyperdoping”, *Advanced Optical Materials* **6**, 1700638 (2018).
- [181] V. D. Shadrin, V. V. Mitin, V. A. Kochelap, and K. K. Choi, “Photoconductive gain and generation-recombination noise in quantum well infrared photodetectors”, *Journal of Applied Physics* **77**, 1771 (1995).
- [182] B. Y. Zhang, T. Liu, B. Meng, X. Li, G. Liang, X. Hu, and Q. J. Wang, “Broadband high photoresponse from pure monolayer graphene photodetector”, *Nature Communications* **4**, 1811 (2013).
- [183] F. Gong, F. Wu, M. Long, F. Chen, M. Su, Z. Yang, and J. Shi, “Black Phosphorus Infrared Photodetectors with Fast Response and High Photoresponsivity”, *Physica Status Solidi - Rapid Research Letters* **12**, 1800310 (2018).
- [184] M. Buscema, D. J. Groenendijk, S. I. Blanter, G. A. Steele, H. S. J. van der Zant, and A. Castellanos-Gomez, “Fast and broadband photoresponse of few-layer black phosphorus field-effect transistors”, *Nano Letters* **14**, 3347–3352 (2014).
- [185] B. Cao, X. Shen, J. Shang, C. Cong, W. Yang, M. Eginligil, and T. Yu, “Low temperature photoresponse of monolayer tungsten disulphide”, *APL Materials* **2**, 116101 (2014).
- [186] A. F. Qasrawi and N. M. Gasanly, “Temperature effect on dark electrical conductivity, Hall coefficient, space charge limited current and photoconductivity of TlGaS₂ single crystals”, *Semiconductor Science and Technology* **20**, 446–452 (2005).
- [187] T. Mueller, F. Xia, and P. Avouris, “Graphene photodetectors for high-speed optical communications”, *Nature Photonics* **4**, 297–301 (2010).
- [188] F. Xia, T. Mueller, Y. M. Lin, A. Valdes-Garcia, and P. Avouris, “Ultrafast graphene photodetector”, *Nature Nanotechnology* **4**, 839–843 (2009).
- [189] O. Lopez-Sanchez, D. Lembke, M. Kayci, A. Radenovic, and A. Kis, “Ultrasensitive photodetectors based on monolayer MoS₂”, *Nature Nanotechnology* **8**, 497–501 (2013).
- [190] D. S. Sholl and R. P. Lively, “Defects in Metal-Organic Frameworks: Challenge or Opportunity?”, *Journal of Physical Chemistry Letters* **6**, 3437–3444 (2015).
- [191] W. T. Koo, J. S. Jang, and I. D. Kim, “Metal-Organic Frameworks for Chemiresistive Sensors”, *Chem* **5**, 1938–1963 (2019).

- [192] M. L. Aubrey, B. M. Wiers, S. C. Andrews, T. Sakurai, S. E. Reyes-Lillo, S. M. Hamed, C. J. Yu, L. E. Darago, J. A. Mason, J. O. Baeg, F. Grandjean, G. J. Long, S. Seki, J. B. Neaton, P. Yang, and J. R. Long, “Electron delocalization and charge mobility as a function of reduction in a metal-organic framework”, *Nature Materials* **17**, 625–632 (2018).
- [193] J. G. Park, M. L. Aubrey, J. Oktawiec, K. Chakarawet, L. E. Darago, F. Grandjean, G. J. Long, and J. R. Long, “Charge Delocalization and Bulk Electronic Conductivity in the Mixed-Valence Metal-Organic Framework Fe(1,2,3-triazolate)2(BF₄)_x”, *Journal of the American Chemical Society* **140**, 8526–8534 (2018).
- [194] M. E. Ziebel, L. E. Darago, and J. R. Long, “Control of Electronic Structure and Conductivity in Two-Dimensional Metal-Semiquinoid Frameworks of Titanium, Vanadium, and Chromium”, *Journal of the American Chemical Society* **140**, 3040–3051 (2018).
- [195] L. S. Xie, L. Sun, R. Wan, S. S. Park, J. A. DeGayner, C. H. Hendon, and M. Dinca, “Tunable Mixed-Valence Doping toward Record Electrical Conductivity in a Three-Dimensional Metal-Organic Framework”, *Journal of the American Chemical Society* **140**, 7411–7414 (2018).
- [196] S. Luo, X. Qi, L. Ren, G. Hao, Y. Fan, Y. Liu, W. Han, C. Zang, J. Li, and J. Zhong, “Photoresponse properties of large-area MoS₂ atomic layer synthesized by vapor phase deposition”, *Journal of Applied Physics* **116**, 164304 (2014).
- [197] F. Yu, M. Hu, F. Kang, and R. Lv, “Flexible photodetector based on large-area few-layer MoS₂”, *Progress in Natural Science: Materials International* **28**, 563–568 (2018).

Appendices

Appendix A

Material characterization

A.1 Energy-dispersive x-ray spectroscopy

EDS is carried out at an accelerating voltage of 20 kV by the means of a conventional Si(Li) detector with S-UTW window (*Oxford Instruments*) attached to a SEM. EDS spectra are obtained with the INCA software by scanning a specimen area of about $3 \times 5 \mu\text{m}^2$ for a duration of 1 hour and acquiring the data with an energy dispersion of 10 eV/channel in an energy range of 0–20 keV. Sample preparation is done by exfoliating thin layers of GaSe and InSe from their bulk crystals and depositing them onto $1 \times 1 \text{ cm}^2$ pieces of a Si wafer. These wafer pieces are then mounted onto an aluminum holder for SEM and EDS analysis. SEM analysis is performed using a S-4800 II microscope (*Hitachi*) operated at an accelerating voltage of 20 kV.

A.2 Raman and photoluminescence measurements

A commercial Raman setup LabRAM HR Evolution (*Horiba*) is used to measure the Raman and PL spectra of InSe and GaSe. The excitation pump is a cw frequency-doubled Nd:YAG laser at a wavelength of 532 nm. The power is 10 μW focused on a spot diameter of 3 μm . The Raman spectra are captured on a liquid nitrogen cooled silicon CCD deep-depletion camera after being dispersed in a 1800 lines/mm grating spectrometer. Low-temperature micro-PL measurements are carried out by using a liquid He cryostat system (*Oxford Instruments*) in conjunction with the LabRAM setup. The PL spectra are captured after being dispersed in a 300 lines/mm grating spectrometer.

A.3 Fourier-transform infrared spectroscopy

FTIR is performed using a Vertex 80v spectrometer (*Bruker*). The spectral range is from 0.20 to 1.44 eV. The infrared source is a Globar. The thermal radiation emitted from the Globar is focused on the sample with a spot of around $2 \times 2 \text{ mm}^2$. A nitrogen cooled MCT is used as the detector.

Appendix B

Device fabrication

B.1 Fabrication of metal electrodes

The metal electrodes to the semiconducting channel are fabricated by e-beam lithography (Raith150 TWO). A commercially available double layer resist is used. First, a layer of EL 11 is spin-coated on the samples at 3000 rpm for 60 s and post-baked at 180 °C for 10 min to obtain a thickness of 309 nm. Then, a layer of PMMA 950 A4 resist is spin-coated using the exact same recipe to obtain a thickness of 148 nm. The contacts are patterned by e-beam lithography at an electron dose of 100 $\mu\text{C cm}^{-2}$, an acceleration voltage of 10 kV, and an aperture of 30 μm . The samples are then developed by immersing first in isopropanol and water (7:3) solution for 45 s, followed by 15 s dip in isopropanol and nitrogen blow dry. The patterned contacts are deposited with Ti or Cr (5 nm) as an adhesive layer at a rate of 2 \AA s^{-1} , followed by Au (100–150 nm) at a rate of 5 \AA s^{-1} using thermal evaporation. After metallization, the lift off process is done by dipping the samples in acetone for few hours, followed by washing with isopropanol and drying in a stream of nitrogen.

B.2 Metal extensions to the via-contacts

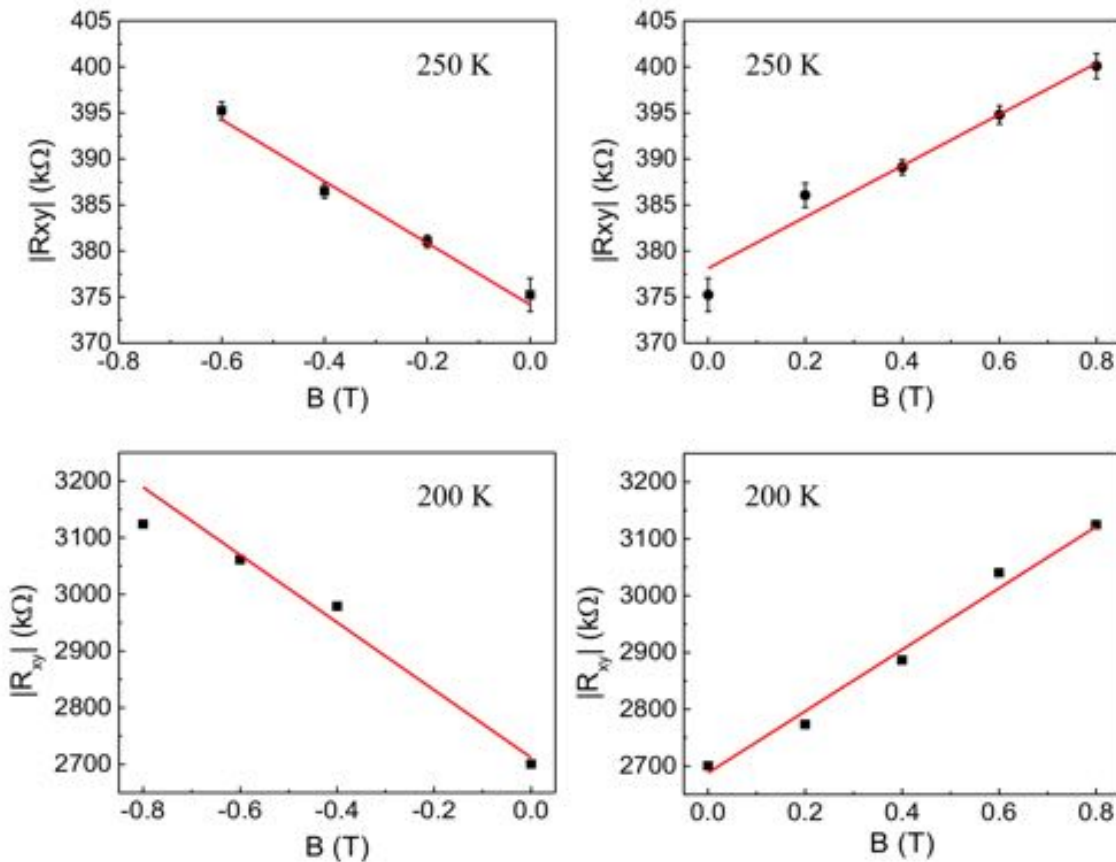
The metal extensions and contact pads are fabricated by e-beam lithography. The PMMA A6 resist layer is spin-coated onto the substrate at 2000 rpm for 1 min. After e-beam exposure, the sample is developed by dipping in MIBK and isopropanol (3:1) solution for 1 min followed by nitrogen blowing. The metals in the order of Cr (2 nm)/Pd (20 nm)/Au (40 nm) are deposited using e-beam evaporator at a deposition rate of 1 \AA s^{-1} . For the lift-off process, the sample is dipped into acetone followed by isopropanol rinsing and nitrogen blowing to obtain the final device.

Appendix C

Device characterization

C.1 R_{xy} versus B curves at different temperatures

The R_{xy} versus B curves measured for the MOF sample at different temperatures are shown below. The linear dependence of R_{xy} on B shows the Hall-effect in the $\text{Fe}_3(\text{THT})_2(\text{NH}_4)_3$ 2D MOF samples. The linearity can be seen in both positive and negative magnetic fields in the temperature range of 300 K to 100 K. The offset or the residual resistance obtained at $B = 0$ T is attributed to misalignment of the opposite voltage probes or asymmetries in the probe element and voltage measurement contacts.



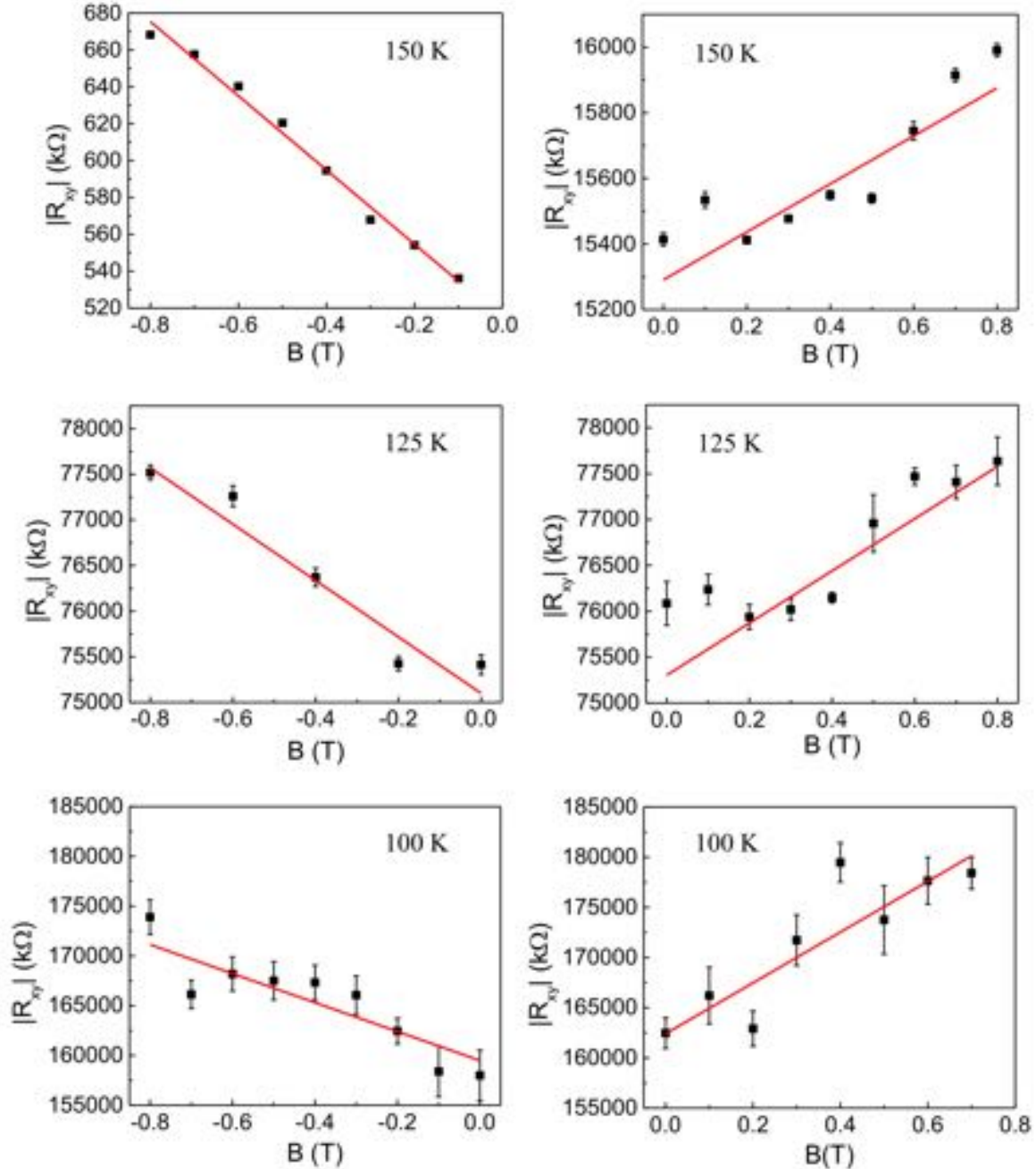


Figure C.1: Linear dependence of R_{xy} on B at all measured temperatures for the MOF sample. The sample temperature is indicated on each graph.

Table C.1
Summary of Hall data

Temperature (K)	four-probe conductivity (S cm ⁻¹)	charge density (cm ⁻³)	Mobility (cm ² V ⁻¹ s ⁻¹)
300 (+B)	3.400×10^{-2}	$9.24 \pm 1.35 \times 10^{14}$	229 ± 33
300 (-B)	3.400×10^{-2}	$3.16 \pm 0.86 \times 10^{14}$	222 ± 37
250 (+B)	8.500×10^{-3}	$1.32 \pm 0.15 \times 10^{14}$	402 ± 46
250 (-B)	8.500×10^{-3}	$1.10 \pm 0.11 \times 10^{14}$	482 ± 47
200 (+B)	1.200×10^{-3}	$6.79 \pm 0.45 \times 10^{12}$	1067 ± 71
200 (-B)	1.200×10^{-3}	$6.17 \pm 0.77 \times 10^{12}$	1175 ± 147
150 (+B)	3.023×10^{-4}	$5.03 \pm 0.99 \times 10^{12}$	375 ± 75
150 (-B)	3.023×10^{-4}	$1.83 \pm 0.07 \times 10^{13}$	104 ± 4
125 (+B)	5.236×10^{-5}	$1.29 \pm 0.35 \times 10^{12}$	253 ± 69
125 (-B)	5.236×10^{-5}	$1.19 \pm 0.18 \times 10^{12}$	274 ± 40
100 (+B)	1.351×10^{-5}	$1.50 \pm 0.30 \times 10^{11}$	581 ± 119
100 (-B)	1.351×10^{-5}	$2.52 \pm 0.56 \times 10^{11}$	334 ± 74

Eidesstattliche Versicherung

Hiermit versichere ich, Himani Arora, geboren am 22. Januar 1989 in Neu-Delhi, Indien, dass ich die vorliegende Arbeit ohne unzulässige Hilfe Dritter und ohne Benutzung anderer als der angegebenen Hilfsmittel angefertigt habe; die aus fremden Quellen direkt oder indirekt übernommenen Gedanken sind als solche kenntlich gemacht. Die Arbeit wurde bisher weder im Inland noch im Ausland in gleicher oder ähnlicher Form einer anderen Prüfungsbehörde vorgelegt.

Die Dissertation wurde in der Zeit von 10/2015 bis 02/2020 am Helmholtz-Zentrum Dresden-Rossendorf im Institut für Ionenstrahlphysik und Materialforschung unter der wissenschaftlichen Betreuung von PD Dr. habil. Artur Erbe und Prof. Dr. Gianaurelio Cuniberti angefertigt.

Himani Arora

Dresden, den 18. Februar 2020